

**PASSIVE VIBRATION MITIGATION VIA MECHANICAL NONLINEAR
BISTABLE OSCILLATORS**

by

Christian B. Grantz

A Thesis

Submitted to the Faculty of Purdue University

In Partial Fulfillment of the Requirements for the degree of

Master of Science in Mechanical Engineering



School of Mechanical Engineering

West Lafayette, Indiana

August 2019

**THE PURDUE UNIVERSITY GRADUATE SCHOOL
STATEMENT OF COMMITTEE APPROVAL**

Dr. Andres F. Arrieta, Chair

School of Mechanical Engineering

Dr. Shirley J. Dyke

School of Mechanical Engineering and School of Civil Engineering

Dr. Jeffrey Rhoads

School of Mechanical Engineering

Dr. Fabio Semperlotti

School of Mechanical Engineering

Approved by:

Dr. Jay P. Gore

Head of the Graduate Program

To Mom and Dad, the first engineers I ever met.

ACKNOWLEDGMENTS

A special thank you to Professor Andres Arrieta for guidance through my research and pushing me to maximize my understanding of a new field. Thank you to my colleagues at the Programmable Structures Lab at Purdue's Ray W. Herrick Laboratories for all the advice and contributions in this journey. Thank you to Professor Charles Krousgrill for his guidance through the transition from my BSME into my MSME and for suggesting courses that fit my passion. Finally, thank you to my parents for their encouragement and for giving me the thirst for knowledge.

TABLE OF CONTENTS

LIST OF TABLES	8
LIST OF FIGURES	10
LIST OF ABBREVIATIONS.....	15
ABSTRACT.....	16
1. INTRODUCTION	17
1.1 Vibration Suppression Techniques	18
1.1.1 Active Control Methods	18
1.1.2 Semi-Active Control Methods.....	19
1.1.3 Passive Control Methods	20
1.1.3.1 Passive Shunt Vibration Suppression.....	21
1.1.3.2 Passive Mechanical Vibration Absorbers.....	22
1.1.3.3 Nonlinear Energy Sinks.....	23
1.1.3.4 Application of Passive Control Methods to Turbomachinery and other Rotational Machinery.....	24
1.2 Resonance Avoidance.....	26
1.3 Research Needs.....	27
1.4 Goals and Detailed Research Objectives	28
1.5 Research Approach	29
1.6 Novel Contributions.....	30
1.7 Structure of the Thesis	30
2. BACKGROUND	31
2.1 Nonlinear Bistable Structures	31
2.1.1 Nonlinear Systems and the Duffing Equation	31
2.1.2 Linearization and Linearized Natural Frequencies	35
2.1.3 Potential Functions	36
2.1.4 Symmetric vs. Asymmetric Systems	37
2.1.5 The Nonlinear Mass Spring Model.....	39
2.2 Piezoelectric Materials and Electromechanical Coupling	41
2.2.1 The Piezoelectric Effect.....	42

2.2.2	Linear Constitutive Relations and Electromechanical Coupling.....	42
2.2.3	Electromechanical Boundary Conditions	43
2.3	Resonance Frequency Detuning (RFD).....	45
3.	MODAL REDUCTION.....	48
3.1	Verification Exercise	49
3.2	ROM Beam Model Case Study – Impact of Adding a Coupled DOF.....	52
4.	LINEAR MASS SPRING – BEAM SYSTEM	55
4.1	Analytical and Numerical Analysis Procedure	55
4.2	SDOF Linear Mass-Spring - Beam Model	57
4.2.1	Linear SDOF Mass Spring.....	57
4.2.2	Cantilevered Beam Model and its Eigenfunctions	58
4.2.3	Linear SDOF Mass Spring - Beam Model – Equations of Motion	63
4.3	Results.....	66
5.	NONLINEAR MASS SPRING – BEAM SYSTEM.....	68
5.1	NLMS – Beam Model.....	68
5.2	Nonlinear Frequency Response	77
5.2.1	Base Excitation	78
5.2.2	Viscous Damping.....	80
5.2.3	Results of Nonlinear Frequency Response Numerical Simulation.....	81
6.	COUPLED NONLINEAR MASS SPRING SYSTEM.....	99
6.1	Coupled Nonlinear Mass Spring Model	99
6.1.1	Model.....	100
6.1.2	Designing for Bistability.....	102
6.1.3	Base Excitation within Coupled NLMS Model.....	106
6.1.4	Addition of Asymmetry to Base Excited Model	112
6.2	Asymmetric Coupled NLMS System Added to Beam	121
6.3	Results.....	126
6.4	Generalization of Results: Sensitivity to System Imperfections.....	139
6.4.1	Impact of Detuning Mechanical Parameters.....	140
6.4.2	Effect of Modal Discretization: Higher Order Modes	149
6.4.3	Frequency Content within Displacement Time Response.....	152

7. CONCLUSIONS	156
7.1 Future Work	157
REFERENCES	158

LIST OF TABLES

Table 3.1 Abaqus vs ROM Eigenvalue Verification	51
Table 3.2 Beam Parameters used in Finite Element Model.....	52
Table 3.3 Squared Natural Frequencies of Cantilever Beam FEM ROM with Additional DOF .	54
Table 4.1 Cantilever Beam Mechanical Parameters	66
Table 4.2 Natural Frequencies of Combined SDOF LMS-Beam System	66
Table 4.3 Eigenvectors for Combined SDOF LMS-Beam System	67
Table 5.1 Mechanical Parameters for the Cantilever Beam	73
Table 5.2 Linearized Natural Frequencies of Beam and NLMS Modes for Various NLMS Parameters and $ma = 38.5 \text{ kg}$	75
Table 5.3 Linearized Natural Frequencies of Beam and NLMS Modes for Various NLMS Parameters and $ma = 77.0 \text{ kg}$	75
Table 5.4 Excitation Parameters Used in Numerical Simulation	82
Table 5.5 Excitation Parameters used for Numerical Simulation with Additional Damping.....	89
Table 5.6 Excitation Parameters used in Numerical Simulations.....	93
Table 6.1 Mechanical Parameters for Coupled NLMS Model – Equation 6.9.....	107
Table 6.2 Mechanical Parameters for Coupled NLMS Model – Equation 6.10.....	107
Table 6.3 Mechanical Parameters for Asymmetric Coupled NLMS Model – Equation 6.3	112
Table 6.4 Mechanical Parameters for Asymmetric Coupled NLMS Model – Equation 6.4	112
Table 6.5 Beam Parameters	127
Table 6.6 Mechanical Parameters for Asymmetric Coupled NLMS Model – Equation 6.3	127
Table 6.7 Mechanical Parameters for Asymmetric Coupled NLMS Model – Equation 6.4	127
Table 6.8 Mechanical Parameters for Asymmetric Coupled NLMS Model – Equation (6.1) ...	128
Table 6.9 Mechanical Parameters for Asymmetric Coupled NLMS Model – Equation (6.2) ...	128

Table 6.10 Linearized Natural Frequencies of Coupled NLMS – Beam System with Table 6.5 Beam Parameters	130
Table 6.11 Linearized Damping Ratios for the Coupled NLMS-Beam System.....	132
Table 6.12 Sampled Points for FFTs	153
Table 6.13 Frequencies Present at Various Points in the Displacement Time Response	154

LIST OF FIGURES

Figure 1.1 Restoring Force and Potential Energy Curves for a Bistable System	29
Figure 2.1 Characteristics of a nonlinear spring. (a) A model of a nonlinear spring with a stiffness that is a function of the displacement. (b) Force-displacement relationships for a linear spring (solid line), a hardening spring (dashed line), and a softening spring (dashed-dotted line).....	32
Figure 2.2 Stable states of a system exist at potential minima	37
Figure 2.3 (a) Symmetric and (b) Asymmetric Potential Functions	38
Figure 2.4 SDOF NLMS Model	40
Figure 2.5 Mechanical Compliance for Short Circuit and Open Circuit Boundary Conditions...	45
Figure 2.6 Campbell diagram: natural frequencies (solid lines) and speed lines (dashed lines) engine orders, figure reproduced from Ref. [42].....	46
Figure 2.7 Resonance frequency detuning concept: (a) two stiffness states ($2S_0$ and $2S_1$) with detuned stiffness (solid black line), and (b) short-circuit (SC) and open-circuit (OC) frequency response curves (dashed lines) and optimal response (solid line), figure reproduced from Ref. [42].....	47
Figure 3.1 (a) 32-Blade Blisk FEM Model (b) 2 nd Mode of Blisk (c) 6 th Mode of Blisk.....	50
Figure 3.2 (a) ROM Mass Matrix; (b) ROM Stiffness Matrix	51
Figure 3.3 Cantilever Beam FEM with Node Numbers	52
Figure 4.1 Analytical Procedure for Computing Fixed Points and Linearized Natural Frequencies	56
Figure 4.2 Linear SDOF Mass Spring - Beam System.....	57
Figure 4.3 SDOF Linear Mass Spring System.....	57
Figure 4.4 Isotropic Cantilever Beam with Deflection $w(x, t)$	58
Figure 5.1 SDOF NLMS added to Cantilever Beam	69
Figure 5.2 Potential Functions for Each Case of SDOF NLMS Parameters	76
Figure 5.3 NLMS - Beam Model with Base Excitation.....	78

Figure 5.4 Phase Portrait (Left) and Time Response (Right) of Numerical Simulation 1 where (a) Begins in State 1 and Sweeps Up, (b) Begins in State 1 and Sweeps Down, (c) Begins in State 2 and Sweeps Up, (d) Begins in State 2 and Sweeps Down	82
Figure 5.5 Frequency Response Function for Simulation 1, and Figure 5.4 Data.....	83
Figure 5.6 Phase Portrait (Left) and Time Response (Right) of Numerical Simulation 2 where (a) Begins in State 1 and Sweeps Up, (b) Begins in State 1 and Sweeps Down, (c) Begins in State 2 and Sweeps Up, (d) Begins in State 2 and Sweeps Down	84
Figure 5.7 Frequency Response Function for Simulation 2 and Figure 5.6 Data.....	85
Figure 5.8 Phase Portrait (Left) and Time Response (Right) of Numerical Simulation 3 where (a) Begins in State 1 and Sweeps Up, (b) Begins in State 1 and Sweeps Down, (c) Begins in State 2 and Sweeps Up, (d) Begins in State 2 and Sweeps Down	87
Figure 5.9 Frequency Response Function for Simulation 3 and Figure 5.8 Data.....	87
Figure 5.10 Phase Portrait (Left) and Time Response (Right) of Numerical Simulation 4 with too Much Damping.....	90
Figure 5.11 Phase Portrait (Left) and Time Response (Right) of Numerical Simulation 5 with too Much Damping.....	90
Figure 5.12 Potential Functions of Simulations 4 and 5	91
Figure 5.13 Potential Functions for Simulations 1, 2, and 3 and Simulations 6, 7, and 8.....	92
Figure 5.14 Phase Portrait (Left) and Time Response (Right) of Numerical Simulation 6 where (a) Begins in State 1 and Sweeps Up, (b) Begins in State 1 and Sweeps Down, (c) Begins in State 2 and Sweeps Up, (d) Begins in State 2 and Sweeps Down	94
Figure 5.15 Frequency Response Function for Simulation 6 and Figure 5.12 Data.....	94
Figure 5.16 Phase Portrait (Left) and Time Response (Right) of Numerical Simulation 7 where (a) Begins in State 1 and Sweeps Up, (b) Begins in State 1 and Sweeps Down, (c) Begins in State 2 and Sweeps Up, (d) Begins in State 2 and Sweeps Down	95
Figure 5.17 Frequency Response Function for Simulation 7 and Figure 5.14 Data.....	96
Figure 5.18 Phase Portrait (Left) and Time Response (Right) of Numerical Simulation 8 where (a) Begins in State 1 and Sweeps Up, (b) Begins in State 1 and Sweeps Down, (c) Begins in State 2 and Sweeps Up, (d) Begins in State 2 and Sweeps Down	97
Figure 5.19 Frequency Response Function for Simulation 8 and Figure 5.16 Data.....	98
Figure 6.1 Coupled NLMS Model	100
Figure 6.2 Desired Frequency Response	105

Figure 6.3 Frequency Response Curve of Base-Excited Coupled NLMS System with Mechanical Parameters Detailed in Table 6.1 and Table 6.2 – Starting with the Negative Fixed Point (State 1) for Both the Sweep Up and Sweep Down.....	108
Figure 6.4 Phase Portrait and Displacement Time Response of (a) m_1 with a Monostable Spring during a Sweep Up from 15 to 22 rad/s (b) m_1 with Monostable Spring during a Sweep Down from 22 to 15 rad/s (c) m_2 with the Bistable Spring during a Sweep Up from 15 to 22 rad/s (d) m_2 with Bistable Spring during a Sweep Down from 15 to 22 rad/s – Starting with the Negative Fixed Point (State 1) for Both the Sweep Up and Sweep Down.....	110
Figure 6.5 Frequency Response Curve of Base Excited Coupled NLMS System with Mechanical Parameters Detailed in Table 6.1 and Table 6.2 – Starting with the Positive Fixed Point (State 2) for Both the Sweep Up and Sweep Down.....	110
Figure 6.6 Phase Portrait and Displacement Time Response of (a) m_1 with a Monostable Spring during a Sweep Up from 15 to 22 rad/s (b) m_1 with Monostable Spring during a Sweep Down from 22 to 15 rad/s (c) m_2 with the Bistable Spring during a Sweep Up from 15 to 22 rad/s (d) m_2 with Bistable Spring during a Sweep Down from 15 to 22 rad/s – Starting with the Positive Fixed Point (State 2) for Both the Sweep Up and Sweep Down.....	111
Figure 6.7 Phase Portrait and Displacement Time Response of m_1 , Starting from the Negative Fixed Point (State 1) of the Monostable Spring for (a) a Sweep Up from 3 to 14 rad/s and (b) a Sweep Down from 14 to 3 rad/s.....	114
Figure 6.8 Phase Portrait and Displacement Time Response of m_2 , Starting from the Negative Fixed Point (State 1) of the Bistable Spring for (a) a Sweep Up from 3 to 14 rad/s and (b) a Sweep Down from 14 to 3 rad/s.....	115
Figure 6.9 Modified Frequency Response of m_2 – Starting from the Negative Fixed Point (State 1) of the Bistable Spring for Both the Sweep Up and Sweep Down in Frequency.	116
Figure 6.10 Phase Portrait and Displacement Time Response of m_1 , Starting from the Positive Fixed Point (State 2) of the Bistable Spring for (a) a Sweep Up from 3 to 14 rad/s and (b) a Sweep Down from 14 to 3 rad/s.....	118
Figure 6.11 Phase Portrait and Displacement Time Response of m_2 , Starting from the Positive Fixed Point (State 2) of the Bistable Spring for (a) a Sweep Up from 3 to 14 rad/s and (b) a Sweep Down from 14 to 3 rad/s.....	119
Figure 6.12 Modified Frequency Response of m_2 – Starting from the Positive Fixed Point (State 2) of the Bistable Spring for Both the Sweep Up and Sweep Down in Frequency.	120
Figure 6.13 Coupled NLMS System Attached to Beam.....	121
Figure 6.14 Coupled NLMS System Attached to Beam.....	125

- Figure 6.15 Linearized Natural Frequencies for Various Quadratic Nonlinearities, B_4 , in (a) the Coupled NLMS System and (b) the Coupled NLMS – Beam System (excluding the 2nd beam mode) 129
- Figure 6.16 Phase Portrait and Displacement Time Response for m_2 , Starting from the Positive Fixed Point (State 2) of the Bistable Spring, (a) Sweeping Up 5 to 12.4 rad/s and (b) Sweeping Down 12.4 to 5 rad/s with an Excitation Amplitude of 0.00563 m..... 133
- Figure 6.17 Modified Frequency Response for m_2 in the Coupled NLMS System and Beam – Starting from Positive Fixed Point (State 2) 134
- Figure 6.18 Frequency Response for 1st Beam Mode in the Coupled NLMS System and Beam – Starting from Positive Fixed Point (State 2) 134
- Figure 6.19 Phase Portrait and Displacement Time Response for m_2 , Starting from the Negative Fixed Point (State 1) of the Bistable Spring, (a) Sweeping Up 5 to 12.4 rad/s and (b) Sweeping Down 12.4 to 5 rad/s with an Excitation Amplitude of 0.00556 m and 0.00554 m respectively..... 136
- Figure 6.20 Modified Frequency Response for m_2 in the Coupled NLMS System and Beam – Starting from Negative Fixed Point (State 1) 137
- Figure 6.21 Modified Frequency Response for 1st Beam Mode in the Coupled NLMS System and Beam – Starting from Negative Fixed Point (State 1)..... 137
- Figure 6.22 Campbell Diagram Interpretation of Coupled-NLMS – Beam Switching Scheme (a) Starting in State 2 for both the Sweep Up and Sweep Down in Frequency (b) Starting in State 1 for both the Sweep Up and Sweep Down in Frequency. The Dashed, Black Line Indicates an Engine Order that would exist in a Rotating Environment 139
- Figure 6.23 Difference in Squared Eigenvalue Corresponding to 1st Beam Mode between State 1 and State 2 140
- Figure 6.24 Difference in Eigenvalue Corresponding to 1st Beam Mode between State 1 and State 2 141
- Figure 6.25 Phase Portrait and Displacement Time Response for m_2 , Starting from the Positive Fixed Point (State 2) of the Bistable Spring with +2% Stiffness Detuning, (a) Sweeping Up 5 to 12.4 rad/s and (b) Sweeping Down 12.4 to 5 rad/s with an Excitation Amplitude of 0.00564 m 142
- Figure 6.26 Phase Portrait and Displacement Time Response for m_2 , Starting from the Positive Fixed Point (State 2) of the Bistable Spring with -2% Stiffness Detuning, (a) Sweeping Up 5 to 12.4 rad/s and (b) Sweeping Down 12.4 to 5 rad/s with an Excitation Amplitude of 0.00562 m 143

- Figure 6.27 Phase Portrait and Displacement Time Response for m_2 , Starting from the Positive Fixed Point (State 2) of the Bistable Spring with +0.5% Length Detuning, (a) Sweeping Up 5 to 12.4 rad/s and (b) Sweeping Down 12.4 to 5 rad/s with an Excitation Amplitude of 0.00564 m 145
- Figure 6.28 Phase Portrait and Displacement Time Response for m_2 , Starting from the Positive Fixed Point (State 2) of the Bistable Spring with -0.5% Length Detuning, (a) Sweeping Up 5 to 12.4 rad/s and (b) Sweeping Down 12.4 to 5 rad/s with an Excitation Amplitude of 0.00564 m 146
- Figure 6.29 Phase Portrait and Displacement Time Response for m_2 , Starting from the Positive Fixed Point (State 2) of the Bistable Spring with +5% Length Detuning, Sweeping Up 5 to 12.4 rad/s with an Excitation Amplitude of 0.00564 m 147
- Figure 6.30 Phase Portrait and Displacement Time Response for m_2 , Starting from the Positive Fixed Point (State 2) of the Bistable Spring with +5% Stiffness Detuning, Sweeping Down 12.4 to 5 rad/s with an Excitation Amplitude of 0.00564 m 148
- Figure 6.31 Phase Portrait and Displacement Time Response for m_2 , Starting from the Positive Fixed Point (State 2) of the Bistable Spring with -5% Stiffness Detuning, Sweeping Up 5 to 12.4 rad/s with an Excitation Amplitude of 0.00564 m 148
- Figure 6.32 Points at which Periods were Sampled for Frequency Content 153
- Figure 6.33 FFTs of at Least 10 Periods at (a) Point A, (b) Point B, (c) Point C, (d) Point D, (e) Point E, and (f) Point F..... 154

LIST OF ABBREVIATIONS

2DOF	Two Degree of Freedom
BC	Boundary Condition
DOF	Degree of Freedom
EOM	Equation of Motion
FEA	Finite Element Analysis
FEM	Finite Element Model
FFT	Fast Fourier Transform
HCF	High-Cycle Fatigue
LMS	Linear Mass Spring
NLMS	Nonlinear Mass Spring
ROM	Reduced-Order Model
SDOF	Single Degree of Freedom

ABSTRACT

Author: Grantz, Christian, B. MSME

Institution: Purdue University

Degree Received: August 2019

Title: Passive Vibration Mitigation via Mechanical Nonlinear Bistable Oscillators

Committee Chair: Andres F. Arrieta

Passive vibration mitigation via multi-stable, mechanical means is relatively unexplored. In addition, achieving vibration suppression through avoiding resonance is at the forefront of up and coming research. This thesis investigates the application of a purely mechanical, bistable device as a passive method of vibration suppression. A purely mechanical device does not require power, multiple materials, or electrical circuits, and a passive device does not require external interaction or control. Therefore, a passive, mechanical device could be implemented with ease even in physically constrained environments with large dynamic loads, such as turbomachinery. The purely mechanical, bistable device presented herein replicates the two switches per resonance crossing evident in semi-active Resonance Frequency Detuning method. This work explores two different bistable, mass-spring models. The first is a single degree of freedom nonlinear mass spring model aiming to utilize asymmetry in the potential function to change the stiffness of the overall system. The second model is a coupled, two degree of freedom system that combines the nonlinear softening and hardening spring characteristics with the unique stiffnesses of two stable states. The performance is verified by targeting the first mode of a cantilever beam, with the device shifting the resonance away from the excitation frequency. Future research could apply these idealized models to complex, rotating structures and replicate the performance of the passive, mechanical devices in a physical geometry that could be manufactured as a part of a target structure.

1. INTRODUCTION

Fatigue is the weakening of a material due to repeatedly applied loads, known as stress cycles. In the life of a structure, High-Cycle Fatigue (HCF) indicates the fatigue endured by the structure after 10,000 stress cycles. The vibration response levels at or around resonance have the greatest potential to accumulate fatigue cycles on a structure, which could lead to failure. With the goal of reducing response levels and theoretically surviving for infinite life, extensive research has been conducted to suppress vibration levels in general and mitigate response levels around resonance. Conventional methods of suppressing vibration include active, semi-active, and passive control methods. In physically constrained environments with large dynamic loads, such as turbomachinery, both active and semi-active methods require external power and control, making them difficult to implement. However, a purely mechanical device does not require power, multiple materials, electrical circuits, or external control. Therefore, a passive, mechanical device could be implemented with ease.

Passive vibration mitigation via multi-stable, mechanical means is relatively unexplored. In addition, achieving vibration suppression by avoiding resonance is at the forefront of up and coming research. This thesis investigates the application of a purely mechanical, bistable device as a passive method of vibration suppression. The purely mechanical, bistable device presented herein replicates the two switches per resonance crossing utilized in the semi-active Resonance Frequency Detuning method. This work explores two different bistable, mass-spring models. The first is a single degree of freedom (SDOF) nonlinear mass spring (NLMS) model aiming to utilize asymmetry in the potential function to change the stiffness of the overall system. The second model is a coupled, two degree of freedom (2DOF) system that combines the nonlinear softening and hardening spring characteristics with the unique stiffnesses of two stable states. Each model was attached to cantilever beam and designed to avoid the resonance response levels around the beam's 1st natural frequency. Furthermore, each model was evaluated on its impact on the 1st natural frequency of the beam, its ability to switch between states to avoid resonance, and its ability to return to its original state for other resonance crossings. Future research could apply these idealized models to complex, rotating structures and replicate the performance of these passive, mechanical devices in a physical geometry that could be manufactured as a part of a target structure.

1.1 Vibration Suppression Techniques

Vibration suppression and mitigation, aiming to reduce or remove damaging response levels in dynamically loaded structures has been researched for many years. Reducing response amplitudes will decrease the number of fatigue cycles endured by a structure, extending its operational life and avoiding failure. Vibration suppression to date has been achieved using various control methods, which can be categorized into the following types: active control, semi-active control, and passive control. The following sections present a survey of these conventional techniques for suppressing vibration. This review includes active controllers such as lead compensators, direct velocity feedback controllers, positive position feedback controllers, and integral feedback controllers; semi-active controller such as state switching method and the skyhook method; and passive control methods involving piezoelectric shunts, vibrational absorbers, and nonlinear energy sinks. This section will also touch on the application of passive methods to turbomachinery.

1.1.1 Active Control Methods

Active controllers provide guaranteed stability by increasing the negative real part of a system's poles if the dynamics of the system are known and can be modeled accurately [1]. This increase in the negative real part of a pole adds damping to the system, while leaving the natural frequencies of the system relatively unchanged, and is referred to as active damping. Common examples of active controllers that utilize active damping include lead compensators, direct velocity feedback (DVF) controllers, positive position feedback (PPF) controllers, and integral force feedback (IFF) controllers. Lead compensators add a pole and zero to the overall system, with the pole placed much farther to the left in the left-hand plane (LHP) than the zero in a root locus plot of the system. The addition of a pole and zero introduces a phase lead within the frequency band, adding active damping to all the modes that exist between the added pole and zero of the controller. A DVF controller is a special kind of lead compensator in which the pole is placed at negative infinity and the zero is placed at the origin. A PPF controller provides a first or second order filter to add damping. The second order filter must be tuned to a targeted mode and has little impact on modes of other natural frequencies, but can be placed in parallel with other PPF controllers to target several modes. The first order filter does not require tuning, but provides less roll-off compared to the second order filter. Examining the root locus of both

PPF controllers, the real components can become unstable for large gains. Thus, these filters are not desirable in environments that require large control efforts. IFF controllers perform similarly to the lead controller but places the pole closer to the origin than the zero, and in alternating pole-zero configurations, the IFF controller begins with a zero rather than the pole. This restricts all the loops of the root locus in the left-hand plane and path along the real axis moves farther left as the gain is increased, guaranteeing unconditional stability. As there is only one tuning parameter for an IFF controller, the optimal value for one mode may not be the same for another mode. Therefore, a compromise must be made to target multiple modes. Active control schemes have also been performed using piezoelectric materials. Behrens [2] studied active shunt techniques for providing piezoelectric damping, Singh and Vizzini [3] demonstrated the reduction in interlaminar stress within composite laminates with embedded active actuators, and Melnykowycz [4] presented the fatigue reliability of piezoelectric fibers in active fiber composites. Active controllers can provide damping to a target bandwidth of frequencies, to single modes, and to several uncoupled modes. However, in some cases, like with PPF controllers, large gains can cause the system to go unstable. A controller required to provide large control efforts is also cumbersome to implement in systems with large dynamic loading. Furthermore, in a system that is difficult to model, the chance of exciting unmodeled or untargeted modes is high. This also increases the potential for undesired modes to drive the system unstable. To maintain stability and feasibility, researchers have looked towards methods that reduce the control effort required to add damping to a system.

1.1.2 Semi-Active Control Methods

Semi-active control methods, rather than always actively controlling the system, switch states to change the overall system at optimal times in order to minimize the response of the system while reducing the required control effort. There has been a large amount of research into semi-active damping methods such as state switching, synchronized switch damping (SSD), synchronized switch damping on an inductor (SSDI), and synchronized switch damping on a negative capacitor (SSDNC) to add more damping into the system. State switching implies switching between states, regardless of whether the switch is between stiffness states or two different boundary conditions. Larson et al [5] provided early research of state switching, switching piezoelectric boundary conditions within an underwater acoustic transducer to achieve

high powers at low frequencies. The paper demonstrated that with state switching, a high Q resonance could be maintained while avoiding slow response times and narrow bandwidth. Switching electrical boundary conditions would also allow for an effective change in the resonance of the acoustic transducer by more than 25%. In SSD, a piezoelectric patch is switched between an open-circuit configuration to an optimal impedance configuration for a rapid change in voltage [6]. Coor and Clark [7-8] investigated the damping capabilities of this semi-active, switching shunt, control law for piezoceramic actuators. An SSDI implements the SSD theory on a RL shunt equipped with a switch that closes at a point of zero velocity, remains closed for the half the electrical period, then opens again [1]. Closing and opening the switch changes the sign of the charge and keeps the sign opposed to the velocity for half of a period, effectively acting as dry friction. An SSDNC, proposed by Liu et al [9] for turbomachinery blisks, utilizes switching with a negative capacitor to improve the damping across all modes without altering the natural frequencies of the system. This method is insensitive to changes in mechanical parameters and able to suppress the amplification that occurs due to random variations between blades, known as mistuning. Another common semi-active control strategy is the sky-hook method. This method isolates a mass or structure from a support input using a semi-active damper. This damper is made to mimic a grounded passive damper by switching between a high and low damping value [10]. While semi-active methods can provide damping to systems with a smaller control effort than many active systems in the presence of large dynamic loads, there still exist some shortcomings. As in active control techniques, semi-active methods still require an external power source, which is difficult to implement in complicated structures, especially rotating machinery. In addition, semi-active control falters in high frequency environments, as switching multiple times per period is very challenging and requires large control efforts. In order to reduce complexity and any need for onboard control or power, researchers have turned towards passive control methods.

1.1.3 Passive Control Methods

Passive control methods dissipate or absorb energy without any external control. Current methods include passive piezoelectric shunts, vibration absorbers, and nonlinear energy sinks. Piezoelectric shunts convert mechanical energy to electrical energy to dissipate this energy with an electrical circuit, vibration absorbers use additional degrees of freedom to reduce vibration

response levels at a particular frequency, and nonlinear energy sinks transfer mechanical energy from a primary structure to a secondary structure in order to dissipate energy off-site without accumulating fatigue cycles on the primary structure. This section will survey each of these passive methods and touch on their application to a turbomachinery environment.

1.1.3.1 Passive Shunt Vibration Suppression

Piezoelectric shunts have been extensively researched as a method of reducing response amplitudes. Piezoelectric shunts utilize the electromechanical coupling characteristics of piezoelectric materials to convert mechanical energy to electrical energy to dissipate said energy with an electrical circuit [1]. Electric dipoles contained within the polarized crystals or electrical asymmetries within long polymer molecules produce the electromechanical coupling within piezoelectric materials. When the piezoelectric material is strained, the rotation of these dipoles causes a charge to flow, called electrical displacement [11]. Piezoelectric materials can also convert electrical energy to mechanical energy. When an electric field is applied at the electrodes of the piezoelectric material, the electric dipoles fixed in the crystals of the material rotate. The rotation produces strain in the material. The measure of the how well a piezoelectric material converts mechanical energy to electrical energy and vice versa is the called the electromechanical coupling coefficient. The dissipation of electrical energy through piezoelectric shunts adds effective damping that reduces the response of the overall system. Forward [12] was one of the earliest to use piezoelectric materials to dampen a structure. In his research, piezoelectric materials were used to dampen optical structures. Hagood and von Flotow [13] provide one of the earliest analytical formulations for passive shunts. These shunts require no additional sensors or power source, the only external element is the electrical shunt connected to the electrodes of the piezoelectric material. There exist purely resistive shunts, R-shunts, and shunts consisting of both a resistor and an inductor, called RL-shunts [11]. As the electromechanical coupling coefficient and the capacitance of the piezoelectric material are properties of the material, the shunt circuit contains the parameters available for optimization. While the purely resistive shunt can provide damping, small electromechanical coupling coefficients limit the amount of damping that can be introduced. Incorporating an inductor in series with the R-shunt and the piezoelectric material creates an RLC circuit. The coupling between the inductor and the piezoelectric material can be tuned to a particular natural

frequency. This coupling also acts like an electrical tuned-mass damper, creating two new peaks in place of the original mode. Similar to R-shunts, the resistance of the shunt is still optimized to maximize the damping on the targeted natural frequency. In fact, Belloli and Ermanni [14] optimized the size and placement of shunted piezoelectric systems within a composite layup for vibration suppression. Since R-shunts and RL-shunts contain optimized electrical parameters, both shunts are susceptible to the detuning of these parameters. The effectiveness of shunt damping is greatly reduced as the parameters shift away from their optimal values. As mentioned previously, Coor and Clark [7-8] used semi-active piezoelectric switching shunts to add damping. Delpero [6] compares adaptive and passive solutions in the design of a rotating blade, proposing that a compromise between stiffness and damping must be found. The adaptive, active or semi-active, outperform the passive solutions, especially when the excitation spectrum is broad band. However, the ease of implementation and advantages of requiring no external power or control may make passive control methods a more preferable option. In order to avoid the complexity of multiple materials involved with piezoelectric shunts and implementing shunt circuitry in addition to the piezoelectric material itself in a structure, a strictly mechanical solution could serve as a viable alternative.

1.1.3.2 Passive Mechanical Vibration Absorbers

Vibration absorbers have been researched and used to passively reduce resonance vibration with additional degrees of freedom for many years and come in a variety of shapes and sizes. A traditional tuned mass absorber consists of a mass and spring attached to the primary structure that creates an antiresonance at the targeted natural frequencies and two new resonances: one above and one below the antiresonance. Ormondroyd and Hartog [15] provided some of the earliest theory on vibration absorbers and Habib et al [16] provided a nonlinear generalization to Den Hartog's equal peak method [17]. Linear Lanchester dampers [18] consist of a small mass with a linear dashpot, while nonlinear Lanchester dampers are linked to the primary mass through dry friction forces. Babitsky and Veprik [19] demonstrate that an elastic beam with a sliding washer is a self-damping system that reduces its response to random stationary and impulsive excitation. Miller et al [20] also verified that a beam with a sliding proof mass had the passive self-tuning capabilities to match the frequencies of input vibrations between 45 and 140 Hz for beams of 6 cm and 30 cm in length. These self-tuning resonators

maintained their tuned condition as the frequency was stepped up or down for a bandwidth of 6 to 40 Hz. Xu et al [21] studied the effect of dynamic vibration absorbers on the nonlinear behavior and stability of fluid-induced vibration within a rotor-seal system. The research concluded that the synchronous and instability vibrations still exist in the rotor-seal system even with the dynamic vibration absorber and the instability frequency is changed from the rotor natural frequency to the first or second order natural frequency of the overall system. The study also noted that for some parameters, the instability threshold is decreased by the addition of the absorber, meaning less energy is required to drive the system unstable. With the exception of self-tuning absorbers, mechanical vibration absorbers are susceptible to mistuning. When mistuning drive the system parameters away from the designed or optimized values, the effectiveness of these absorbers greatly decreases. To increase the bandwidth of the effective performance of vibration absorbers and to reduce sensitivity to mistuning, researchers have turned towards nonlinear systems. Nonlinear energy sinks, in particular, are less sensitive to mistuning and use nonlinear frequency characteristics to increase the bandwidth of effective performance beyond that of vibration absorbers.

1.1.3.3 Nonlinear Energy Sinks

Nonlinear energy sinks (NES) are another passive control method. A nonlinear energy sink is a device added to a structure that becomes the recipient of targeted energy transfer (TET) from a primary structure. The energy received is then dissipated through this nonlinear attachment rather than causing large response levels in the primary structure. Grinberg et al [22] demonstrate that a 2DOF NES can provide better vibration absorption than a SDOF NES of equal mass, broadening the range of amplitudes at which effective performance is plausible. The 2DOF NES, however, does exhibit chaotic nature for moderate excitation amplitudes. Ahmadabadi et al [23] investigated the ability a coupled NES has to suppress the energy in a cantilever beam under shock excitation. The paper determined that energy transfer occurs effectively for an NES configuration that is ungrounded, providing 89% energy dissipation and that nonlinear normal modes possess the one-way irreversible energy transfer desired for NES. In addition, Georgiades et al [24] examined the capacity of a NES to passively absorb and locally dissipate broadband shock energy from a plate. The paper found that the highest efficiency was achieved when the NES was placed close to the clamped end of the plate or close to nodal lines

of the plate modes. The efficiency of the NES is also sensitive to the damping coefficient, where the largest damping is desired without providing so much as to limit the NES from achieving high relative displacements. Multiple SDOF NESs can operate with synergy to increase efficiency and MDOF NES systems can be used when they are strongly coupled with the plate. For successive shocks, fatigue and joint degradation would cause the natural frequencies to change, however, unlike the tuned mass dampers, an NES will remain tuned and maintain efficiency. Bab et al [25] found that a NES could also be effective in reducing the lateral vibration of a rotor since changing the linear stiffness of the NES can tune the NES to a desired rotational speed of the rotor. In addition, the appropriate range of detuning within the NES is negative, but for medium mass eccentricity force magnitudes, the strongly modulated responses occur for a wider range of the detuning parameter.

1.1.3.4 Application of Passive Control Methods to Turbomachinery and other Rotational Machinery

Sections 1.1.3.1 to 1.1.3.3 reviewed a variety of passive control methods. This section surveys their application to the physically constrained environments of turbomachinery and other types of rotating machinery. Many researches have applied piezoelectric shunts to turbomachinery in order to add damping and reduce vibration within bladed disks. Agnes [26] utilized piezoelectric materials to couple the blades of turbomachinery bladed-disk assemblies, creating a virtual shroud while avoiding aerodynamic interference, and reducing the sensitivity of the blades to mode localizations. The study also noted that the use of multiple shunts could prevent localization completely. Mokrani et al [27] use piezoelectric RL-shunted circuits to achieve the reduction in the response vibration of blades on a bladed drum by a factor of 4 in the bandwidth of the blade modes. The use of passive shunts was to avoid the need for external power in a rotating structure. In another paper, Mokrani et al [28] used loops of piezoelectric transducers to group several transducers onto a single inductor for additional damping performance in rotationally periodic structures. The damping was also most effective when the target mode was approximately harmonic circumferentially. As with other tuned shunts or tuned mass dampers, it was noted that the damping effectiveness does degrade with detuning, but is still applicable under moderate blade mistuning, which was shown numerically and experimentally in a separate paper [29]. In addition, this is one of the few studies to address the implementation challenges of the piezoelectric shunts, as the piezoelectric patches were installed

on the inner side of the blade support rim to avoid disturbing the flow of the compressor. Zhou [30] also installed passive shunts on the disk to reduce vibration in turbomachinery blades. In this case, however, Zhou exploited the coupling between the blade and the disk to target the vibration in the blades. The paper proposed introducing controllable mistuning in the inductor of the piezoelectric shunt to adjust for the mistuning in the blades and maintain optimal vibration levels. Yu et al [31] used negative capacitance to enhance the coupling of piezoelectric damper-absorber circuitry and improve its ability to suppress the vibration in mistuned bladed disks. Loop et al [32] mention that the boundary condition the blade root should be incorporated in the design of the piezoelectric system, as the optimization of the piezoelectric material for a stand-alone blade may be no longer optimal. Liu et al [33] use parallel piezoelectric networks (PPNs) along the disk of a bladed-disk to suppress blisk vibration. PPNs consisting either of strictly R-shunts or RL-shunts provide damping to the blisk, but the RL-shunts were proven to have better performance, still eliminating amplitude magnification in the case of 20% mistuning. The PPN impacts the mechanical frequencies by less than about 0.5%, and only when the frequencies lie near the clusters of electrical frequencies. As the piezoelectric patches are attached to the disk, the blade-disk coupling plays an important role in the damping performance of the PPN. The paper also notes that as the disk is much stiffer than the piezoelectric patch, the distribution and geometry of said patches should be optimized to ensure an acceptable electromechanical coupling coefficient, or better than 1.14%, the coupling coefficient used in this study. While research into using piezoelectric patches on the bladed disks in turbomachinery is extensive, only a few papers consider using blade-disk coupling to keep the piezoelectric patches on the disk and out of the flow of the compressor or turbine. In addition, the use of circuitry and wiring in a rotating environment is still undesirable, something which is not addressed. Moving towards a more mechanical system could remove the dependence on wiring and the shunt circuit.

For rotating machinery, one of the earlier rotating absorbers was studied by Campos et al [34] to reduce the lateral vibration of a vertical washing machine. Campos determined better tuning of an absorber can provide more reduction and in cases of low damping, a slightly detuned absorber was used to avoid overwhelming the strength of other components in the primary structure. Shaw et al [35-36] investigated features of centrifugal pendulum vibration absorbers that can provide effective performance over a wide torque range. The study concluded that the perfectly tuned cycloidal paths were preferred as no jumps or non-synchronous

responses will occur. In addition, a small amount of positive mistuning could help alleviate any localization within the absorbers, while any amount of negative mistuning should be avoided, as it will cause an increase in vibration levels. Hu et al [37] studied the impact of a rotor dynamic vibration absorber (RDVA) at different positions along the length of the rotor. Using an on-off control of an electromagnet to alter the natural frequency of the RDVA between two values, the two peaks of a traditional dynamic vibration absorber can be eliminated. Hu et al also determined the best performance was achieved when the RDVA was placed close to a support. Theurich et al [38] address passive vibration mitigation of a system under harmonic near-resonant forcing with impact absorbers. The impact absorbers are effective when energy transfer to off-resonant modes occurs and the energy is dissipated in these off-resonant modes. These absorbers have the capability of targeting multiple modes in a wide bandwidth of excitation levels. In rotating machinery, resonance conditions depend on both the rotation speed of the structure as well as the structures natural frequencies and modes. Bladed disk turbomachinery is also susceptible to random mistuning and the localized increase of vibration among these blades. This mistuning causes deviations from optimal parameters, which can reduce the effectiveness of tuned absorbers. Thus, Olson et al [39-40] proposed vibration absorbers tuned to an order of rotation rather than a single frequency in turbomachinery and structures with cyclic symmetry. These absorbers are still sensitive to small perturbations, but intentional detuning can improve robustness. In fact, specific undertuning can eliminate responses near orders of interest. Ghaderi et al [41] used a damped, centrifugally driven, order tuned absorber to reduce vibration in rotating flexible structures. This absorber can only target one resonance within a system and its performance was measured by the area under the frequency response curve, with a minimal area indicating good reduction performance.

1.2 Resonance Avoidance

Substantial research has gone into adding damping to the overall structure or to add effective damping around a concerning resonance, but much less research has been conducted into adaptively changing the resonance conditions to avoid resonance altogether. If resonance conditions could be avoided, the large, and possibly damaging, response levels could also be avoided, thus not requiring any additional damping. Kauffman and Lesieutre [42-43] introduced resonance frequency detuning (RFD), a new kind of state switching method to avoid resonance.

RFD is a semi-active state switching method for systems subject to swept frequency excitation which utilizes the open- and short-circuit boundary conditions of piezoelectric materials to create two stiffness states. With an optimal switch between states, the natural frequency of the targeted system will shift away from the excitation frequency, thus avoiding resonance, then switch back to the original stiffness state to preserve the designed stiffness for future resonance crossings. Compared to other state switching devices, RFD only requires two switches per resonance crossing rather than four switches per period. At high vibration frequencies, executing multiple switches per period requires significant effort from a controller, so while RFD provides less vibration reduction, it does not require high frequency switching constraints. Loop and Kauffman [44-45] investigated the effectiveness of RFD in regions with high modal density. The papers found that ample vibration reduction was present for most cases with the exception of overlapping peaks. When the single overlapping peak is larger than the target resonance peak, the reduction capabilities of the RFD method are decreased, and the optimal switching may be no switching at all. Comparing RFD to other state switching methods in regions of high modal density, SSDI would be the preferred semi-active method, but physical constraints and power requirements make implementation difficult in a turbomachinery environment. The ease of implementation and switching only twice per resonance crossing compared to four switches per vibration cycle can outweigh the cost of less vibration reduction in systems with large dynamic loads, operating at high frequencies. Despite these advantages, RFD still uses piezoelectric elements that require external control to switch between electrical boundary conditions. A purely mechanical, passive system could avoid resonance without these constraints.

1.3 Research Needs

There is a need for a system to avoid resonance using purely passive mechanical elements. While active control methods can provide additional damping by increasing the negative real part of a system's poles, they require an accurate model of the system's dynamics, require external power, and encounter difficulties maintaining stability for large control efforts. Semi-active methods aim to reduce the control effort with various state switching methods, but still require an external controller and external power. Passive methods are not restricted by external control or external power, but possess their own downsides in physically constrained environments. Passive piezoelectric shunts deal with the interaction and implementation of

multiple materials and add the electrical complexity of shunt circuits. Passive vibration absorbers avoid the electrical complexity by mechanically suppressing vibration with additional DOF, they are very sensitive to mistuning, in which optimal parameters are no longer very effective. Nonlinear energy sinks can reduce the sensitivity of the system to mistuning at the cost of sensitivity to damping and can introduce chaos into the system for moderate to large excitation amplitudes. All these methods, from active to passive control methods, aim to add damping and suppress vibration at or around resonance, while methods such as RFD avoid resonance conditions altogether. RFD is a promising method at avoiding resonance to avoid high response levels, but RFD is subject to the external power, control, and the complexity of piezoelectric circuitry as with other semi-active methods. Thus, the objective of this thesis is to avoid resonance in a passive and purely mechanical fashion.

1.4 Goals and Detailed Research Objectives

The goal of this thesis is to provide a passive, purely mechanical solution to mitigating resonance vibration of a structure. This research focuses on a bistable model, using the capability to switch between two stiffness states to mitigate the resonance of the targeted structure. This provides a solution that would decrease the potential for high-cycle fatigue and avoid the complexity of adding electrical components in a physically constrained environment, such as turbomachinery. This would also allow for the efforts of saving weight and cost to progress without raising concerns when sweeping through resonance conditions. To fulfill the aforementioned goals, this thesis has the following objectives:

1. Develop a methodology to reduce mass and stiffness matrices, exported from a finite element software, from thousands of degrees of freedom down to a subset of DOF to simplify the analysis. DOF that produce the largest response levels and are most likely to accumulate fatigue cycles on the structure should be included in this reduced order model.
2. Design a model of a linear system with an additional DOF to illustrate how a change of stiffness within a single DOF will alter the entire system.
3. Modify the linear stiffness to a bistable nonlinear stiffness to numerically investigate the dynamics of switching stiffness around a targeted natural frequency.

4. Apply the model to a targeted structure, attempting to mitigate the resonance vibration around a targeted natural frequency.

1.5 Research Approach

This research provides a purely mechanical, passive system to perform a switching scheme similar to that of RFD. In this approach, the system switches between stiffness states twice per resonance crossing. The mechanical system presented utilizes bistability and energy transfer from the beam to passively switch between states. A stable state is a configuration of a structure or system in which the internal forces of the system are zero and the potential energy of the system is at a minimum. Both of these traits are illustrated in Figure 1.1 below. Bistability in a structure implies two stable configurations, and these two configurations could each have a unique stiffness. More information regarding bistability is provided in Chapter 2 of this work.

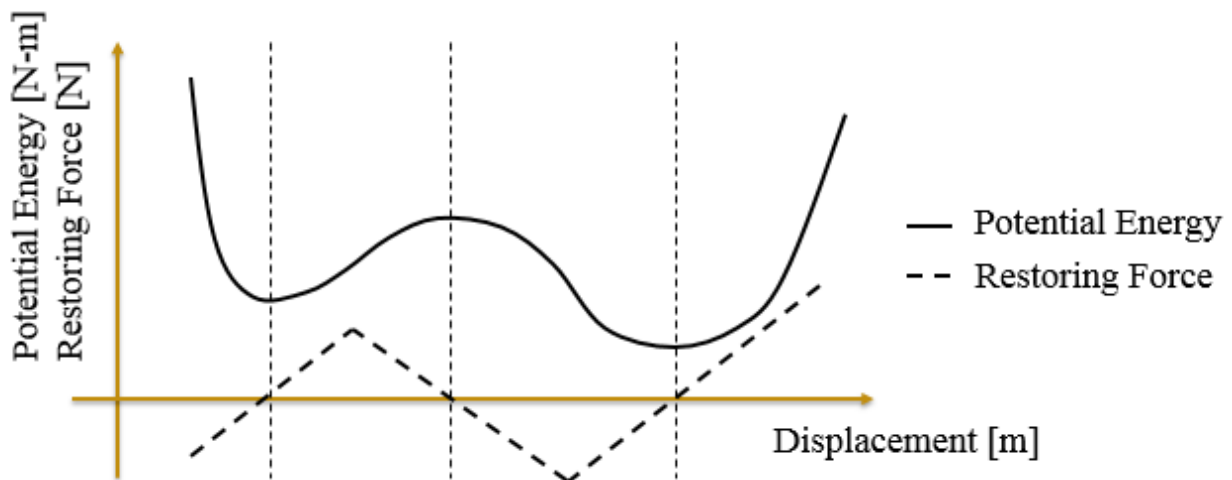


Figure 1.1 Restoring Force and Potential Energy Curves for a Bistable System

An attached bistable structure could switch between stiffness states to replicate the two-switch scheme of RFD. This bistable structure will remain purely mechanical to avoid the complexity of electrical circuits and dealing with multiple materials inherent in the implementation of piezoelectric materials. Bistable, mechanical devices designed to avoid resonance of a target structure is relatively unexplored. This proposed approach will provide a purely mechanical solution that fulfills the need to avoid resonance and to reduce the number of fatigue cycles endured by a structure.

1.6 Novel Contributions

This research explores the use of nonlinear, bistable, mechanical attachments to avoid resonance within a target structure. This thesis provides formulations for two different bistable models, targeting a resonance within a cantilevered beam. The results presented herein demonstrate a passive, mechanical solution to avoid resonance that can switch before the system enters resonance and then return to its original state for future resonance crossing, similar to RFD. In addition, the applications of these findings to turbomachinery is presented for potential future research.

1.7 Structure of the Thesis

This thesis is comprised of seven chapters. Chapter 1 reviews vibration suppression techniques, their application to turbomachinery and rotational machinery, and presents the need for a purely mechanical, passive system. Chapter 2 provides some additional background into multi-stable structures, specifically bistable structures, features associated with nonlinear dynamics, and a broader introduction to RFD. Chapter 3 presents a modal reduction to create a reduced set of degrees of freedom from the thousands to millions generated in present day finite element models. The impact of adding an additional DOF, coupled to a pre-existing DOF, is also studied. Chapter 4 begins with a traditional SDOF mass spring model and introduces the modeling and analytical scheme of a mass-spring attached to a cantilevered beam. This cantilevered beam will serve as the target structure of this work. Chapter 5 shifts the focus from a linear model to a nonlinear model. A nonlinear, bistable spring with quadratic and cubic stiffnesses is substituted for the linear spring and Chapter 5 studies its impact on the target resonance of the beam. Chapter 6 introduces a 2DOF coupled nonlinear mass-spring system representative of a bistable plate to target resonance. This chapter also demonstrates the coupled systems' effectiveness at avoiding resonance. Chapter 7 presents the conclusions of this thesis and reveals potential topics for future research on this subject.

2. BACKGROUND

2.1 Nonlinear Bistable Structures

A structure exists in a stable state when there are no internal forces within the system, implying zero restoring is exerted into the surroundings. A system with two statically stable states is called a bistable structure. A common example of a bistable structure would be a snap bracelet. This bracelet transitions from a straight metal tape spring to a curved bracelet by slapping it against another object. Its straight and curved configurations are two unique stable states that require a force or displacement induce “snap-through” to its other state. In nature, a Venus flytrap is not strictly bistable in the structure sense, but spatially distributed pre-stress within its leaves allows this plant to quickly snap from its open configuration to a closed configuration to trap prey. This section provides a brief introduction into nonlinear dynamics and uses the classical Duffing equation to guide the reader through the process of determining the existence and stability of equilibrium points, along with the linearized natural frequencies associated with each stable state.

2.1.1 Nonlinear Systems and the Duffing Equation

A system is considered nonlinear when the change of the output is not proportional to the change in the input. In linear mass-spring oscillators, the force-displacement curve of the spring has a linear relationship with the spring’s linear stiffness acting as the proportionality constant.

$$F_s = kx \tag{2.1}$$

As a larger deflection occurs, the force-displacement curve begins to drift away from the linear relationship as the deformation, whether it be in tension or compression, increases. This can be clearly shown using an example of a spring with a cubic nonlinearity. The force-displacement of this nonlinear spring is the following:

$$F_s = k_1x + k_3x^3 \tag{2.2}$$

When the cubic term of spring is positive, the spring is said to be hardening because the spring becomes stiffer as the displacement increases. When the cubic term of the spring is negative, the spring is said to be softening because the spring becomes softer as the displacement increases. This relationship is illustrated in Figure 2.1. If the restoring force, F_s , is integrated with respect to the displacement, x , the strain energy in the structure can be obtained. More details regarding the strain potential energy of a structure are given in Section 2.1.3.

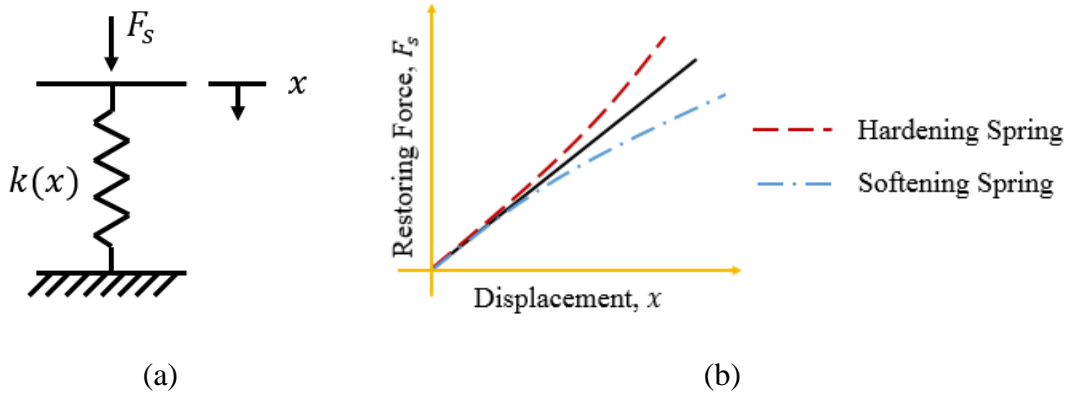


Figure 2.1 Characteristics of a nonlinear spring. (a) A model of a nonlinear spring with a stiffness that is a function of the displacement. (b) Force-displacement relationships for a linear spring (solid line), a hardening spring (dashed line), and a softening spring (dashed-dotted line).

A classical model used to describe many systems featuring nonlinear stiffness is the Duffing equation [47]. The Duffing equation possesses the same cubic nonlinearity as Equation (2.2), and the undamped, unforced form has been provided below.

$$m\ddot{x} + k_1x + k_3x^3 = 0 \quad (2.3)$$

To study the equilibrium and stability of this equation, a state space form is derived. The state space form is defined by two states variables: $x_1 = x(t)$ and $x_2 = \dot{x}(t)$, corresponding to the position and velocity of the mass respectively. In state space form, the Duffing equation becomes

$$\begin{aligned} \dot{x}_1 &= x_2 \\ \dot{x}_2 &= -\frac{k_1}{m}x_1 - \frac{k_3}{m}x_1^3 \end{aligned}$$

Defining the state vector, $\{\mathbf{x}\}$, and a nonlinear vector function \mathbf{F} , as the following

$$\{\mathbf{x}\} = \begin{Bmatrix} x_1 \\ x_2 \end{Bmatrix}, \quad \mathbf{F} = \begin{bmatrix} x_2 \\ -\frac{k_1}{m}x_1 - \frac{k_3}{m}x_1^3 \end{bmatrix}$$

The state space model becomes the vector equation $\{\dot{\mathbf{x}}\} = \mathbf{F}(\mathbf{x})$, or

$$\begin{Bmatrix} \dot{x}_1 \\ \dot{x}_2 \end{Bmatrix} = \begin{bmatrix} x_2 \\ -\frac{k_1}{m}x_1 - \frac{k_3}{m}x_1^3 \end{bmatrix} \quad (2.4)$$

An equilibrium point, or fixed point, of a system, x_{eq} , is defined as any vector $\{\mathbf{x}\}$ for which \mathbf{F} is identically zero, also called zero phase velocity [48]. Vanishing \mathbf{F} indicates there are no internal forces for the given system. For the Duffing equation, the equilibrium points are found to be

$$x_{eq} = (x_1, x_2) = (0, 0) \quad (2.5)$$

$$x_{eq} = (x_1, x_2) = \left(\pm \sqrt{\frac{-k_1}{k_3}}, 0 \right) = \left(\pm i \sqrt{\frac{k_1}{k_3}}, 0 \right) \quad (2.6)$$

The equilibrium points are physical characteristics of a system, and thus, complex equilibrium points will not manifest themselves in the physical system. However, the two fixed points defined in Equation (2.6) are not complex for all values of k_1 and k_3 . If either k_1 or k_3 are less than zero, the ratio between the linear and cubic stiffness terms becomes positive, and the equilibrium point becomes purely real. Therefore, if either k_1 or k_3 are less than zero, there will be three fixed points instead of a single fixed point at the origin.

The existence of multiple fixed points brings stability into question, as solutions around each fixed point may have different stability behavior. The Jacobian, a matrix of all first order partial derivatives of a vector-valued function, and its eigenvalues are used to determine stability. If the nonlinear vector function, F , is written as

$$\mathbf{F} = \begin{bmatrix} f_1(x_1, x_2) \\ f_2(x_1, x_2) \end{bmatrix} \quad (2.7)$$

Then the Jacobian for the Duffing equation is

$$J|_{(x_1, x_2)} = \begin{bmatrix} \partial f_1 / \partial x_1 & \partial f_1 / \partial x_2 \\ \partial f_2 / \partial x_1 & \partial f_2 / \partial x_2 \end{bmatrix} = \begin{bmatrix} 0 & 1 \\ -\frac{k_1}{m} - \frac{3k_3}{m} x_1^2 & 0 \end{bmatrix} \quad (2.8)$$

Computing the eigenvalues of the Jacobian evaluated at each equilibrium point will determine the stability of each fixed point. Regardless of the value of either k_1 or k_3 , the fixed point at the origin exists. The eigenvalues of the Jacobian for this fixed point are,

$$J|_{x_{eq}=(0,0)} = \begin{bmatrix} 0 & 1 \\ -\frac{k_1}{m} & 0 \end{bmatrix}$$

$$\det(J - \lambda I) = \begin{bmatrix} -\lambda & 1 \\ -\frac{k_1}{m} & -\lambda \end{bmatrix} = \lambda^2 + \frac{k_1}{m} = 0$$

$$\lambda = \pm i \sqrt{\frac{k_1}{m}} \quad (2.9)$$

If all the eigenvalues of the Jacobian contain negative real parts, the system is said to be stable at that fixed point. If $k_1 > 0$, the eigenvalues are purely complex. This lies on the imaginary axis of a real-imaginary plot, usually defined as marginally stable. However, if any amount of damping was included within Duffing system, one will find that the eigenvalues will have negative real parts and this fixed point will be stable. If $k_1 < 0$, the eigenvalues of the Jacobian become purely real with one positive and one negative eigenvalue. Thus, the fixed point does not contain only eigenvalues with negative real parts and is unstable.

If either k_1 or k_3 are less than zero, the other two possible fixed points must be considered. For the fixed points defined by Equation (2.6),

$$J|_{x_{eq}=\left(+\sqrt{\frac{-k_1}{k_3}}, 0\right)} = \begin{bmatrix} 0 & 1 \\ -\frac{k_1}{m} - \frac{3k_3}{m} \left(\frac{-k_1}{k_3}\right) & 0 \end{bmatrix} = \begin{bmatrix} 0 & 1 \\ -\frac{k_1}{m} + \frac{3k_1}{m} & 0 \end{bmatrix} = \begin{bmatrix} 0 & 1 \\ \frac{2k_1}{m} & 0 \end{bmatrix} \quad (2.10)$$

$$J|_{x_{eq}=\left(-\sqrt{\frac{-k_1}{k_3}}, 0\right)} = \begin{bmatrix} 0 & 1 \\ -\frac{k_1}{m} - \frac{3k_3}{m} \left(\frac{-k_1}{k_3}\right) & 0 \end{bmatrix} = \begin{bmatrix} 0 & 1 \\ -\frac{k_1}{m} + \frac{3k_1}{m} & 0 \end{bmatrix} = \begin{bmatrix} 0 & 1 \\ \frac{2k_1}{m} & 0 \end{bmatrix} \quad (2.11)$$

$$\begin{aligned} \text{Det}(J - \lambda I) &= \begin{bmatrix} -\lambda & 1 \\ \frac{2k_1}{m} & -\lambda \end{bmatrix} = \lambda^2 - \frac{2k_1}{m} = 0 \\ \lambda &= \pm \sqrt{\frac{2k_1}{m}} \end{aligned} \quad (2.12)$$

If $k_1 > 0$, there exists an eigenvalue with a positive real part, meaning both fixed points are unstable. If $k_1 < 0$, both eigenvalues become complex. As mentioned previously, purely complex eigenvalues are considered marginally stable, but any amount of damping can be shown to provide a negative real component and prove both fixed points to be stable. In summary, a positive linear stiffness will possess a single stable fixed point at the origin, and a negative linear stiffness will possess three equilibrium points, two of which are stable and one of which is an unstable fixed point. The transition from one to three fixed points as a single parameter is varied is classified as a pitchfork bifurcation. In this case, the varied parameter is the linear stiffness of the nonlinear spring. A system with a single stable fixed point is said to be monostable and a system with two stable fixed points on either side of an unstable fixed point is said to be bistable. At each stable equilibrium point, a system can be linearized to determine an effective linear stiffness and a corresponding linearized natural frequency.

2.1.2 Linearization and Linearized Natural Frequencies

The partial derivatives within the Jacobian provide linear gradients of the nonlinear vector function, \mathbf{F} , with respect to the states x_1 and x_2 [10]. If linearized states, y_1 and y_2 , are defined as an approximation of the nonlinear system around a fixed point, the linearized system can be defined as the following relation, where the Jacobian is evaluated at the same fixed point.

$$\{\dot{y}\} = [J]\{y\} \quad (2.13)$$

For the trivial fixed point at the origin, the linearized system is found to be

$$m\dot{y} + k_1 y = 0 \quad (2.14)$$

For this fixed point, the effective linear stiffness is the linear stiffness of the nonlinear system. The natural frequency of this fixed point is determined to be the following expression.

$$\omega_n = \sqrt{\frac{k_1}{m}} \quad (2.15)$$

For the non-trivial fixed points, the linearized system and the linearized natural frequency are

$$m\ddot{y} - 2k_1y = 0 \quad (2.16)$$

$$\omega_n = \sqrt{\frac{-2k_1}{m}} \quad (2.17)$$

Remember, for both non-trivial fixed points to exist, $k_1 < 0$, thus, the linearized natural frequency will also be a real value. Notice that the linearized natural frequency is the same for both the positive and negative fixed point. This is result of a symmetric system [48], in which the characteristics of the spring is the same in both tension and in compression. The force-displacement curve of a symmetric nonlinear spring can be approximated by a series of x with odd exponents of x . A comparison between symmetric and asymmetric nonlinear systems is provide later in this chapter. While the force-displacement equations are useful in visualizing the stiffness characteristics of the nonlinear spring, the potential function of the spring provides a clear picture of the system's stability at every fixed point.

2.1.3 Potential Functions

A good way to visualize bistability is by inspecting the potential function. The potential function of a nonlinear system can be found by integrating the force-displacement curve. In the case of the Duffing equation, whose force-displacement curve is defined by Equation (2.2), the 4th order potential function is

$$V(x) = \frac{k_1}{2}x^2 + \frac{k_3}{4}x^4 \quad (2.18)$$

The local maxima and minima of the potential function correspond to the fixed points of the nonlinear system because the fixed points are also zeros in the force-displacement curve. It is easy to visualize the stability at each fixed point by imagining a ball sitting atop the potential function. The ball will oscillate as the system is excited by an external force. The ball can decay into any local minima, implying those fixed points are stable. If the ball was placed perfectly

atop the local maxima, it would stay at rest, but if any perturbation should occur, the ball would fall into the potential “wells” containing the local minima. Thus, local maxima are unstable fixed points. Figure 2.2 illustrates this concept.

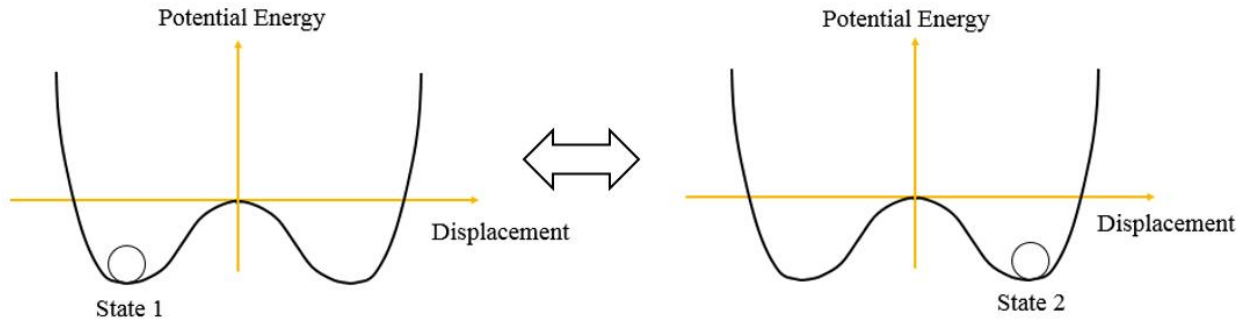


Figure 2.2 Stable states of a system exist at potential minima

Section 2.1.2 demonstrated that a linearized natural frequency can be found for every stable fixed point. If the system is excited near one of these natural frequencies, the mass could eventually possess enough energy to cross over to the other potential well or the other stable fixed point, through the unstable fixed point. This phenomenon is called “snap-through.” Given an excessive amount of excitation, inter-well oscillations would begin to take place, where the mass would be snapping between each stable state constantly, existing above either well. The depth of the potential well helps to visualize the amount of energy required to snap-through to another potential well. The Duffing equation presented here is a symmetric system, and thus, the potential function is symmetric about the y-axis and the potential wells have the same depth. Adding asymmetry into the system can alter the shape of the potential function and create a difference between the positive fixed point and the negative fixed point.

2.1.4 Symmetric vs. Asymmetric Systems

When shaping the potential functions of bistable systems, there exist two distinct choices: a symmetric or an asymmetric potential function. A symmetric potential function is symmetric around the unstable fixed point, also known as the potential boundary. Each potential well has the same depth, as seen in Figure 2.3a, and thus require the same amount of energy to escape the well and cross the potential boundary into the other well.

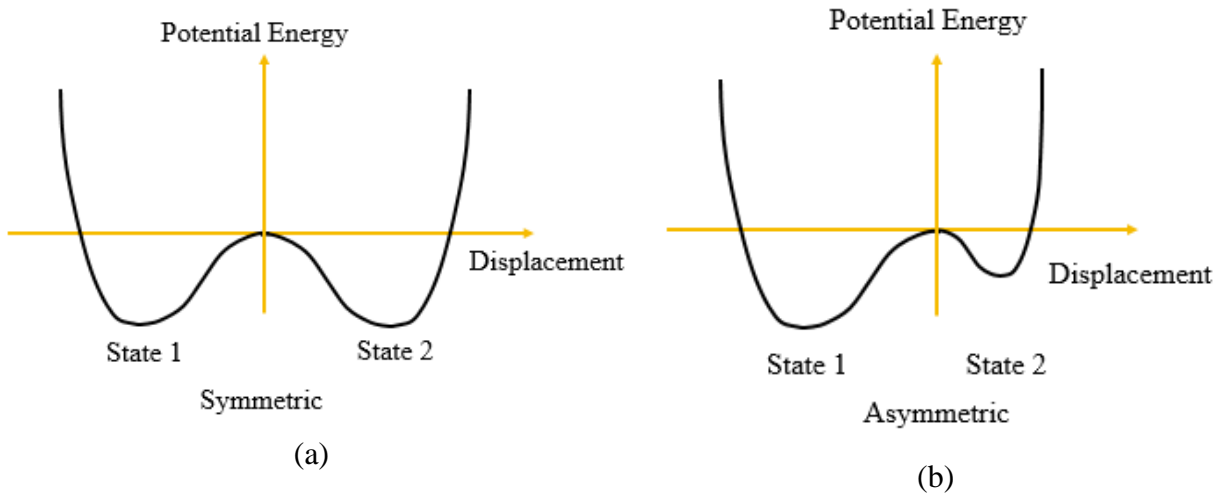


Figure 2.3 (a) Symmetric and (b) Asymmetric Potential Functions

The linearized natural frequencies of both stable states will also exist at the same frequency due to this symmetry, as seen in Section 2.1.2. In the case of this research, symmetric potential wells do not help avoid resonance since there is no difference between either of the stable states. In this condition, there is no control over the natural frequencies of the system.

This leads us to an asymmetric potential function. Adding a quadratic nonlinearity stiffness to the Duffing equation introduces asymmetry into the potential function, which appears in the form of a deeper and shallower well. With the addition of the quadratic nonlinearity, the force-displacement and potential function of the Duffing equation become

$$F_s = k_1x + k_2x^2 + k_3x^3 \quad (2.19)$$

$$V(x) = \frac{k_1}{2}x^2 + \frac{k_2}{3}x^3 + \frac{k_3}{4}x^4 \quad (2.20)$$

To which side of the potential boundary the deeper well appears in Figure 2.3b is dependent on the sign of the quadratic non-linearity. The difference in depth affects both the fixed point of each well and the associated natural frequency. Solving the state equations of the Duffing equation with the additional quadratic nonlinearity, the fixed points of the system are now

$$x_{eq} = (x_1, x_2) = (0, 0) \quad (2.21)$$

$$x_{eq} = (x_1, x_2) = \left(\frac{-k_2 \pm \sqrt{k_2^2 - 4k_1k_3}}{2k_3}, 0 \right) \quad (2.22)$$

Following the same procedure as Section 2.1.2, the effective stiffness and linearized natural frequencies can be determined. Assuming that $k_1 < 0$,

$$m\ddot{y} + \left[k_1 + 2k_2 \left(\frac{-k_2 \pm \sqrt{k_2^2 - 4k_1k_3}}{2k_3} \right) + 3k_3 \left(\frac{-k_2 \pm \sqrt{k_2^2 - 4k_1k_3}}{2k_3} \right)^2 \right] y = 0 \quad (2.23)$$

$$\omega_n = \sqrt{\frac{k_1 + 2k_2 \left(\frac{-k_2 \pm \sqrt{k_2^2 - 4k_1k_3}}{2k_3} \right) + 3k_3 \left(\frac{-k_2 \pm \sqrt{k_2^2 - 4k_1k_3}}{2k_3} \right)^2}{m}} \quad (2.24)$$

Plugging in values for k_1 , k_2 , and k_3 will produce different effective stiffness values and different linearized natural frequencies for different fixed points. For this 4th order potential function, if the potential boundary is centered at zero, the shallower potential well will have a lower natural frequency than that of the deeper potential well. This asymmetry can be applied to a physical system designed to passively avoid resonance within a primary structure.

2.1.5 The Nonlinear Mass Spring Model

A bistable spring with an asymmetric potential function forms the foundation for the SDOF NLMS system that will target the natural frequency of the first beam mode. A simple schematic of the SDOF NLMS model can be seen in Figure 2.4.

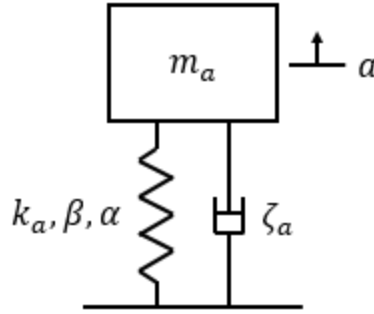


Figure 2.4 SDOF NLMS Model

The EOM for this NLMS model has the same form as the Duffing equation with a quadratic nonlinear stiffness term.

$$m_a \ddot{a} + \zeta_a \dot{a} + k_a a + \beta a^2 + \alpha a^3 = 0 \quad (2.25)$$

Where m_a is the mass, ζ_a is the damping coefficient, k_a is the linear stiffness, β is the quadratic stiffness, and α is the cubic stiffness. Following the derivation provided in Sections 2.1.2, the fixed points, linearized EOMs, and the linearized natural frequencies will be similar to that of Equations (2.21) to (2.24), only Equation (2.25) is written such that $m = m_a$, $k_1 = k_a$, $k_2 = \beta$, and $k_3 = \alpha$. The fixed points of Equation (2.25) are

$$x_{eq} = (x_1, x_2) = (0, 0) \quad (2.26)$$

$$x_{eq} = (x_1, x_2) = \left(\frac{-\beta \pm \sqrt{\beta^2 - 4k_a\alpha}}{2\alpha}, 0 \right) \quad (2.27)$$

The Jacobian of the SDOF NLMS system can be derived from the

$$J|_{(x_1, x_2)} = \begin{bmatrix} 0 & 1 \\ -\frac{k_a}{m_a} - \frac{2\beta}{m_a}x_1 - \frac{3\alpha}{m_a}x_1^2 & -\frac{\zeta_a}{m_a} \end{bmatrix} \quad (2.28)$$

Plugging the stable fixed points into the Jacobian, the linearized EOM and the linearized natural frequencies can then be determined, assuming $k_a < 0$.

$$m_a \ddot{y} + \zeta_a \dot{y} + \left[k_a + 2\beta \left(\frac{-\beta \pm \sqrt{\beta^2 - 4k_a \alpha}}{2\alpha} \right) + 3\alpha \left(\frac{-\beta \pm \sqrt{\beta^2 - 4k_a \alpha}}{2\alpha} \right)^2 \right] y = 0 \quad (2.29)$$

$$\omega_n = \sqrt{\frac{k_a + 2\beta \left(\frac{-\beta \pm \sqrt{\beta^2 - 4k_a \alpha}}{2\alpha} \right) + 3\alpha \left(\frac{-\beta \pm \sqrt{\beta^2 - 4k_a \alpha}}{2\alpha} \right)^2}{m_a}} \quad (2.30)$$

This SDOF NLMS model will be attached to the end of a cantilever beam. One of the two stable states will be designed to match the natural frequency of the 1st bending mode of the beam, while the other stable state will be used to snap as the combined system rises into resonance. The combination of these two states were used to passively avoid resonance conditions. More details regarding the effectiveness of the SDOF NLMS system at avoiding resonance within the cantilever beam is provided in Chapter 5. This difference in linearized natural frequency between states can also be seen in the electromechanical coupling of piezoelectric materials and different electrical boundary conditions can be used to change the stiffness of the structure.

2.2 Piezoelectric Materials and Electromechanical Coupling

Piezoelectricity is a property of materials that demonstrate electromechanical coupling. This coupling is characterized by the conversion of mechanical energy to electrical energy, known as the direct piezoelectric effect, and the conversion of electrical energy to mechanical energy, known as the converse piezoelectric effect [11]. The direct piezoelectric effect is the apparent charge flow measured across two electrodes occurs when a mechanical stress is applied to the material. The converse piezoelectric effect is the strain produced under the application of an electric field. Piezoelectric materials also exhibit a thermomechanical coupling known as the pyroelectric effect, but that is not the focus of this thesis. This section will present the physical basis behind the piezoelectric effect, the piezoelectric constitutive equations relating stress and strain as well as electric field and electric displacement, and the electromechanical boundary conditions defined by the electromechanical coupling within piezoelectric materials. The derivations provided herein closely follow the formulations presented by Leo [11].

2.2.1 The Piezoelectric Effect

Piezoelectricity is found mostly in crystalline solids, such quartz, Rochelle salt, and lead-zirconium-titanate (PZT), but can also be found in polymers, such as polyvinylidene (PVDF) [6]. The key property is electric polarization. Originally, piezoelectric materials have randomly distributed electric dipoles that do not exhibit any macroscopic polarization, however, a poling process is used to create polarization. At room temperature or just below the Curie temperature, the dipoles can freely rotate. A state electric field is then used to align the dipoles along the direction of the electric field. Upon reducing the temperature and removing the electric field, the dipoles will remain oriented. Now that the electric dipoles are aligned and parallel along the polarization direction, the piezoelectric effect will be observed. An electric field will attract the electric dipoles with opposing charges, causing movement in dipoles and strain in the material. Furthermore, a mechanical strain will force the dipoles to move and this movement of charges produces an apparent charge flow at the faces of the material. This is the physical basis for the converse and direct piezoelectric effects respectively. The direct and converse piezoelectric effects can also be expressed mathematically in the form of constitutive relations, as shown in the following section 2.2.2.

2.2.2 Linear Constitutive Relations and Electromechanical Coupling

A constitutive equation relates two physical quantities specific to a material. Piezoelectric materials contain four physical quantities: stress, strain, electric field, and electrical displacement. Constitutive equations of a mechanical material relate stress to strain and constitutive equations of an electric material relate electric field to electric displacement. The direct and converse piezoelectric effects also relate electrical displacement to stress and strain to electric field respectively. These four relations can be combined into following matrix equation:

$$\begin{Bmatrix} S \\ D \end{Bmatrix} = \begin{bmatrix} s & d \\ d & \varepsilon \end{bmatrix} \begin{Bmatrix} T \\ E \end{Bmatrix} \quad (2.31)$$

In this equation, S is the strain, D is the electrical displacement, T is the stress, and E is the electrical field. Notice the diagonal terms of the matrix represent the linear mechanical and electrical constitutive relations, where s is the mechanical compliance, the reciprocal of Young's Modulus, and ε is the dielectric permittivity. The piezoelectric strain coefficient, d , sits in the

off-diagonal, relating strain to electric field and electrical displacement to stress. At low levels of applied stress or electric field, these relations will remain linear [11]. Equation (2.31) can also be inverted to get the following form:

$$\begin{Bmatrix} T \\ E \end{Bmatrix} = \begin{bmatrix} \frac{1}{s} \left(\frac{1}{1 - d^2/s\varepsilon} \right) & -\frac{d/s\varepsilon}{1 - d^2/s\varepsilon} \\ -\frac{d/s\varepsilon}{1 - d^2/s\varepsilon} & \frac{1}{\varepsilon} \left(\frac{1}{1 - d^2/s\varepsilon} \right) \end{bmatrix} \begin{Bmatrix} S \\ D \end{Bmatrix} \quad (2.32)$$

This form expresses the stress and electric field as independent variables and the electrical displacement and strain as dependent variables. The frequent appearance of $d^2/s\varepsilon$ in piezoelectric materials led to the definition piezoelectric electromechanical coupling coefficient.

$$k = \frac{d}{\sqrt{s\varepsilon}} \quad (2.33)$$

The electromechanical coupling coefficient is always positive and is between 0 and 1, implying that only a fraction of the total energy is converted between the mechanical and electrical domains [11].

2.2.3 Electromechanical Boundary Conditions

This electromechanical coupling also implies the response of the material depends on electrical and mechanical boundary conditions [6]. For example, the mechanical stiffness of the piezoelectric material is dependent upon the open circuit or short circuit electrical boundary condition [11]. Short-circuit conditions occur when the electrodes of the piezoelectric material are connected directly. This results in zero electric field across the material, $E=0$, but charge is still allowed to flow from the positive to negative terminal. Plugging $E=0$ into Equation (2.31) results in the following equations,

$$S = sT \quad (2.34)$$

$$D = dT \quad (2.35)$$

Open circuit conditions occur when the electric terminals are opened and no charge is allowed to flow between terminals. Thus, no electrical displacement is seen in the material. Plugging $D=0$ in Equation (2.32) and incorporating the definition for the electromechanical coupling coefficient, Equation (2.33), results in the following equations,

$$T = \frac{1}{s(1 - k^2)} S \quad (2.36)$$

$$E = \frac{k^2}{d(1 - k^2)} S \quad (2.37)$$

Inverting Equation (2.36) reveals the difference in mechanical compliance between electrical boundary conditions.

$$S = \begin{cases} s^T & \text{short circuit} \\ s(1 - k^2)T & \text{open circuit} \end{cases} \quad (2.38)$$

Given that k and k^2 are always positive, the mechanical compliance decreases in the switch from the short circuit boundary condition and open circuit boundary condition. Thus, the compliance associated with each electrical boundary condition can be denoted with either the superscript E for constant electric field or D for constant electric displacement. Therefore, the following relationship between short-circuit and open-circuit compliance can be found.

$$s^D = s^E(1 - k^2) \quad (2.39)$$

Figure 2.5 illustrates this relationship on a strain-stress curve for a given electromechanical coupling coefficient.

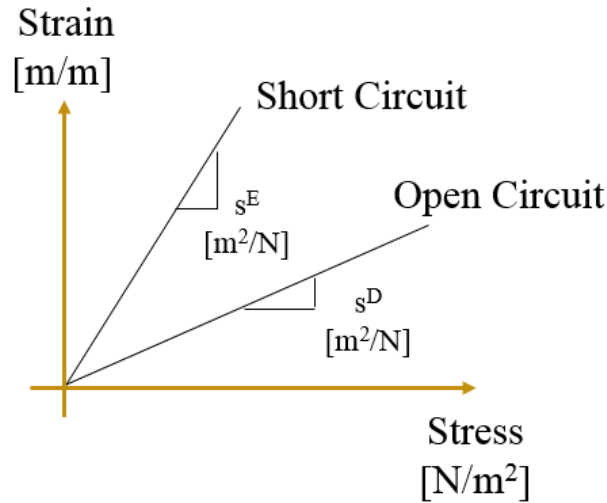


Figure 2.5 Mechanical Compliance for Short Circuit and Open Circuit Boundary Conditions

Examining the difference in electrical permittivity between the stress-free and strain-free mechanical boundary conditions, the following relationship can be found.

$$\varepsilon^S = \varepsilon^T(1 - k^2) \quad (2.40)$$

In this relationship, the superscript S represents the strain-free boundary condition and the superscript T represents the stress-free boundary condition. In this work, special attention will be given to the difference in mechanical compliance that results from the electrical boundary conditions. This difference in compliance plays a role in creating two states with unique natural frequencies that can be exploited to avoid resonance.

2.3 Resonance Frequency Detuning (RFD)

As defined by Kauffman and Lesieutre [42], “resonance frequency detuning provides vibration reduction by altering the stiffness of a structure to avoid resonant excitation condition.” Kauffman et al alters the stiffness of a turbomachinery blade with piezoelectric patches, using the difference in mechanical compliance between short-circuit and open-circuit boundary conditions. As stated before, the electromechanical coupling coefficient is the fraction of energy that can be converted from mechanical to electrical energy and vice versa. The square of this coefficient is the ratio of converted energy to the total work imposed on the material. Solving

the two eigenvalue problems, the square of the coupling coefficient can be written in a more convenient form that depends only on short-circuit and open-circuit natural frequencies.

$$k^2 = \frac{d^2}{s\varepsilon} = \frac{\omega_{OC}^2 - \omega_{SC}^2}{\omega_{OC}^2} \quad (2.41)$$

However, the natural frequencies of rotational machinery are a function of rotational speed and rotational machinery is also subject to excitation frequencies that are multiples of blade rotation speed. These conditions are best illustrated in a Campbell diagram, in which the crossing of natural frequencies and speed lines indicate resonant conditions. Figures 2.6 and 2.7 have been explicitly taken from Kauffman et al [42] to help develop an understanding of the turbomachinery environment and the resonance frequency detuning method.

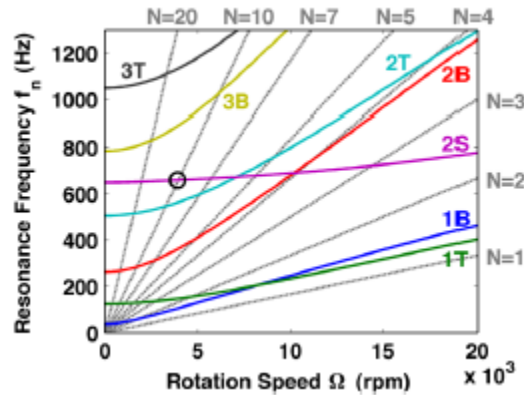


Figure 2.6 Campbell diagram: natural frequencies (solid lines) and speed lines (dashed lines) engine orders, figure reproduced from Ref. [42]

In Figure 2.6, the target resonance lies at the intersection between the 2nd stripe mode and the 10th engine order. The piezoelectric material begins in the open-circuit configuration, and a switch to the short-circuit boundary condition changes the mechanical compliance, and thus, the stiffness of the overall system. Switching to short-circuit conditions at the optimal frequency would avoid resonance conditions and minimize the response amplitude. This optimal switching frequency is determined by the intersection between short-circuit and open-circuit frequency response curves. This frequency can be derived from Equation (2.41),

$$\omega_{switch} = \sqrt{1 - \frac{k^2}{2}} \quad (2.31)$$

After avoiding resonance, a switch to the original open-circuit preserves the designed structural stiffness of the system. Figure 2.7a illustrates this switching scheme. Figure 2.7b illustrates the optimal switching frequency and the decay of the response magnitude following the switch.

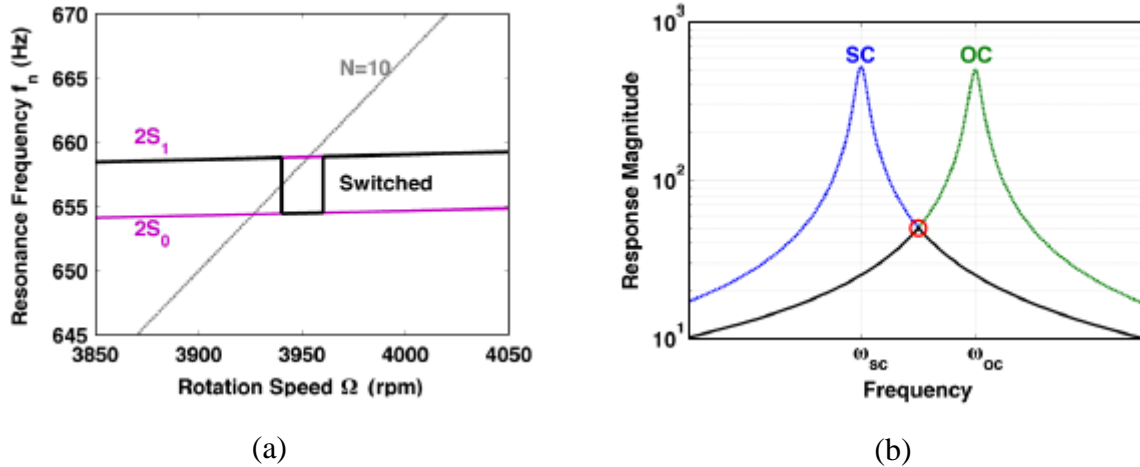


Figure 2.7 Resonance frequency detuning concept: (a) two stiffness states ($2S_0$ and $2S_1$) with detuned stiffness (solid black line), and (b) short-circuit (SC) and open-circuit (OC) frequency response curves (dashed lines) and optimal response (solid line), figure reproduced from Ref. [42]

The frequency domain analysis used by Kauffman et al is limited by the assumption of harmonic motion, which holds for very slow speeds, but swept frequency-domain excitation does violate this assumption. Their study is applied to a single blade of a turbomachinery disk, which would interfere with the flow of the bladed disk. This issue is addressed by Mokrani and Preumant [29], in which the piezoelectric patches are attached to the disk or drum of the bladed disk for manufacturability. In addition, this detuning method uses electrical components, still adding installation complexity in a rotating environment. The objective of this research is to achieve a similar detuning strategy of Kauffman; however, following a purely passive and mechanical approach. Keeping the model strictly mechanical also removes the complexity provided by electrical components. The next chapter presents the premise and modeling behind a reduced-order model and the impact of an additional coupled DOF on the natural frequencies of the entire system.

3. MODAL REDUCTION

The modeling of a complicated system is key when looking to reduce the response at resonance in turbomachinery. Accurately analyzing the stress and dynamic environment of a complex structure involves a finite element model. However, a typical finite element model can have thousands to millions of DOF. Creating a reduced-order model can reduce a mass and stiffness matrix with thousands of DOF down to a smaller, more manageable, number of DOF. This will allow the analysis to focus on the natural frequencies that produce the largest response levels and are most likely to accumulate fatigue cycles on the structure.

Consider the general form of a multi-DOF system.

$$M\ddot{x} + C\dot{x} + Kx = 0 \quad (3.1)$$

The matrices M, C, and K are generally coupled, and diagonalizing each of these matrices would simplify the model. Therefore, if the substitution $x = \psi q$ [10] is made, where ψ is defined as the modal matrix, and both side of the equation are pre-multiplied by ψ^T , then Equation (3.1) becomes,

$$\psi^T M \psi \ddot{q} + \psi^T C \psi \dot{q} + \psi^T K \psi q = 0 \quad (3.2)$$

Assuming a sinusoidal solution for each DOF, the eigenvalues relate to the natural frequencies and the eigenvectors form the columns of the modal matrix ψ . Since the eigenvectors are not unique, the modal matrix is normalized with respect to the mass matrix [49]. Therefore, the decoupled mass matrix becomes the identity matrix and the stiffness matrix becomes a diagonal matrix of the squared natural frequencies of the structure.

$$M_d = \psi^T M \psi = I \quad (3.3)$$

$$K_d = \psi^T K \psi = \text{diag}(\omega_n^2) \quad (3.4)$$

This method diagonalizes both the mass and stiffness matrices and decouples the DOF of the structure into its modal components.

In order to avoid analyzing thousands to millions of degrees of freedom, a modal reduction is performed on the expansive mass and stiffness matrices. This is performed by determining a subset of the eigenvectors of $M^{-1}K$. This subset should include the eigenvectors corresponding to the natural frequencies that need to be examined in the reduced-order model. The subset then serves as the modal matrix ψ when decoupling the mass and stiffness matrices. Thus, if M and K are n by n matrices, the matrix of eigenvalues will take the form

$$[\psi]_{n \times n} = [[\psi_1]_{n \times 1} \quad [\psi_2]_{n \times 1} \quad \dots \quad [\psi_n]_{n \times 1}] \quad (3.5)$$

Taking a subset of m eigenvectors,

$$[\psi]_{n \times m} = [[\psi_1]_{n \times 1} \quad [\psi_2]_{n \times 1} \quad \dots \quad [\psi_m]_{n \times 1}] \quad (3.6)$$

Now perform the diagonalization procedure defined by Equation (3.2), except using the subset of eigenvectors instead of the complete set.

$$([\psi]_{n \times m})^T [M]_{n \times n} [\psi]_{n \times m} = [\psi^T]_{m \times n} [M]_{n \times n} [\psi]_{n \times m} = [M_{red}]_{m \times m} \quad (3.7)$$

$$([\psi]_{n \times m})^T [K]_{n \times n} [\psi]_{n \times m} = [\psi^T]_{m \times n} [K]_{n \times n} [\psi]_{n \times m} = [K_{red}]_{m \times m} \quad (3.8)$$

This produces a diagonal set of mass and stiffness matrices where the mass matrix is still the identity matrix and the stiffness matrix is still a set of squared natural frequencies; however, there are only m natural frequencies corresponding to the m mode shapes that were selected above. This system is designated as the reduced-order model (ROM) of the system. The ROM allows for analysis on, for example, 10 modes compared to the innumerable amount of DOF within the structure's finite element model.

3.1 Verification Exercise

A simple verification of this procedure was performed on a finite element model of a bladed disk with 32 simplified blades created within Abaqus. This model contained around

14,000 DOF and served as an example of a complex structure. A frequency analysis was run within Abaqus and the first 10 natural frequencies were recorded. Examples of some of the observed mode shapes can be seen in Figures 3.1b and 3.1c. The mass and stiffness matrices were exported from the Abaqus software and imported into both MATLAB and Spyder, a scientific development environment that uses the Python programming language. In Spyder, a sparse matrix eigensolver used the Rayleigh-Ritz method to determine the first 10 eigenvalues of $M^{-1}K$. In MATLAB, the first 10 eigenvectors were used in Equations (3.7) and (3.8) to reduce and diagonalize the system. The resulting mass and stiffness matrices can be seen in Figure 3.2. Notice the mass matrix is the identity matrix and the stiffness matrix is composed of the eigenvalues along the diagonal. Computationally small numbers smaller than 10^{-7} were replaced by zero in the mass and stiffness matrix for clarity.

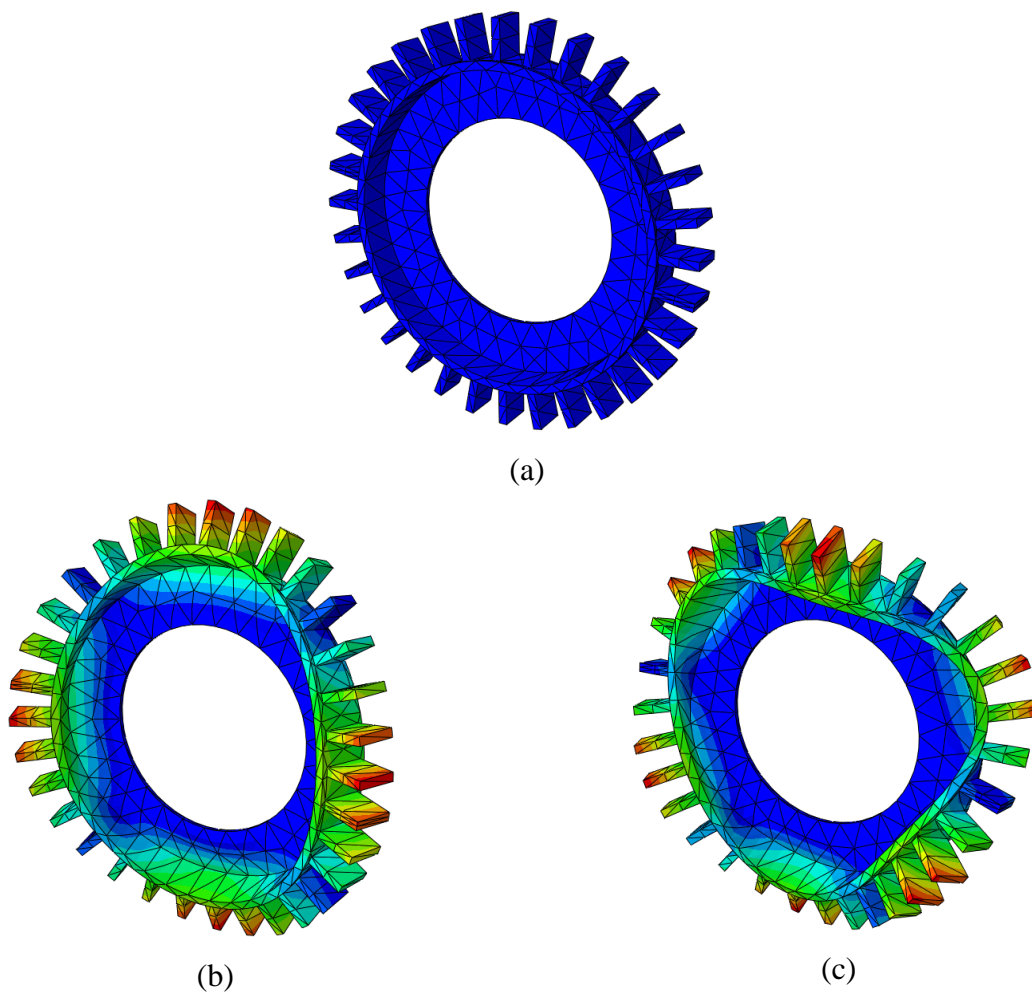


Figure 3.1 (a) 32-Blade Blisk FEM Model (b) 2nd Mode of Blisk (c) 6th Mode of Blisk

$$\begin{bmatrix}
 1.0000 & 0 & 0 & 0 & 0 & 0 & 0 & 0 & 0 & 0 \\
 0 & 1.0000 & 0 & 0 & 0 & 0 & 0 & 0 & 0 & 0 \\
 0 & 0 & 1.0000 & 0 & 0 & 0 & 0 & 0 & 0 & 0 \\
 0 & 0 & 0 & 1.0000 & 0 & 0 & 0 & 0 & 0 & 0 \\
 0 & 0 & 0 & 0 & 1.0000 & 0 & 0 & 0 & 0 & 0 \\
 0 & 0 & 0 & 0 & 0 & 1.0000 & 0 & 0 & 0 & 0 \\
 0 & 0 & 0 & 0 & 0 & 0 & 1.0000 & 0 & 0 & 0 \\
 0 & 0 & 0 & 0 & 0 & 0 & 0 & 1.0000 & 0 & 0 \\
 0 & 0 & 0 & 0 & 0 & 0 & 0 & 0 & 1.0000 & 0 \\
 0 & 0 & 0 & 0 & 0 & 0 & 0 & 0 & 0 & 1.0000
 \end{bmatrix}$$

(a)

$$\begin{bmatrix}
 4.8448 & 0 & 0 & 0 & 0 & 0 & 0 & 0 & 0 & 0 \\
 0 & 4.8565 & 0 & 0 & 0 & 0 & 0 & 0 & 0 & 0 \\
 0 & 0 & 6.8467 & 0 & 0 & 0 & 0 & 0 & 0 & 0 \\
 0 & 0 & 0 & 6.9249 & 0 & 0 & 0 & 0 & 0 & 0 \\
 0 & 0 & 0 & 0 & 11.9525 & 0 & 0 & 0 & 0 & 0 \\
 0 & 0 & 0 & 0 & 0 & 25.0209 & 0 & 0 & 0 & 0 \\
 0 & 0 & 0 & 0 & 0 & 0 & 25.2810 & 0 & 0 & 0 \\
 0 & 0 & 0 & 0 & 0 & 0 & 0 & 73.9489 & 0 & 0 \\
 0 & 0 & 0 & 0 & 0 & 0 & 0 & 0 & 74.6723 & 0 \\
 0 & 0 & 0 & 0 & 0 & 0 & 0 & 0 & 0 & 147.2598
 \end{bmatrix}$$

(b)

Figure 3.2 (a) ROM Mass Matrix; (b) ROM Stiffness Matrix

A complete summary of the eigenvalues found between Abaqus, Spyder, and the ROM in MATLAB can be found in Table 3.1. It is clear that eigenvalues of the ROM match the eigenvalues produced by the frequency analysis in Abaqus and the eigensolver in Spyder.

Table 3.1 Abaqus vs ROM Eigenvalue Verification

Abaqus Eigenvalues (rad/s) ²	Spyder Eigenvalues (rad/s) ²	MATLAB ROM Eigenvalues (rad/s) ²
4.845	4.845	4.845
4.857	4.857	4.857
6.847	6.847	6.847
6.925	6.925	6.925
11.953	11.953	11.953
25.021	25.021	25.021
25.281	25.281	25.281
73.949	73.949	73.949
74.949	74.672	74.672
147.260	147.260	147.260

3.2 ROM Beam Model Case Study – Impact of Adding a Coupled DOF

Once a ROM has been found for a system, the impact of an additional DOF, coupled has on the mode of interest, can be analyzed. This addition creates a coupled system of equations, which can be decoupled a second time to reveal how the targeted DOF has shifted. In this case study, a FEM model of a cantilever beam was used. Table 3.2 summarizes the geometrical and material properties of the cantilever beam shown in Figure 3.3.

Table 3.2 Beam Parameters used in Finite Element Model

Young's Modulus, E [N/m ²]	Second Area Moment of Inertia, I [m ⁴]	Density, ρ [kg/m ³]	Cross-Sectional Area, A [m ²]	Length, L [m]	Poisson's Ratio
180,000,000,000	0.0833	7700	1	2	0.305

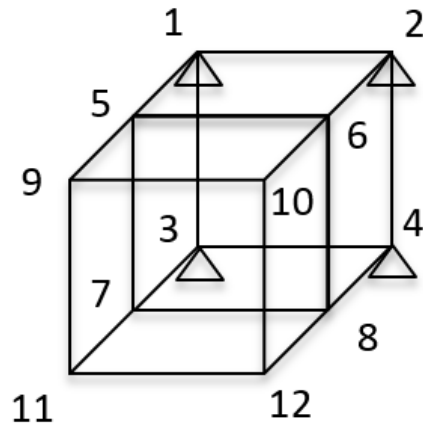


Figure 3.3 Cantilever Beam FEM with Node Numbers

This model originally has 12 nodes, implying 36 DOF accounting for the 3D displacement of each node. By defining fixed BCs on nodes 1 to 4, the 36 DOF reduces to 24 DOF. Analysis of a system with 24 DOF still has the possibility of 24 different modes which correspond to 24 different natural frequencies. To simplify the analysis to a more manageable 3 DOF, a ROM is generated for the first 3 modes of this FEM model.

$$\begin{bmatrix} 1 & 0 & 0 \\ 0 & 1 & 0 \\ 0 & 0 & 1 \end{bmatrix} \ddot{q} + \begin{bmatrix} 11086.6 & 0 & 0 \\ 0 & 11086.6 & 0 \\ 0 & 0 & 49465.2 \end{bmatrix} q = 0 \quad (3.9)$$

For the sake of this study, designate the second mode of this beam to be the targeted mode. Therefore, the additional DOF has the same natural frequency as the beam's 2nd mode and a coupled term, $-\alpha$, comes into the row and column of the 2nd mode to couple these two DOF together.

$$\begin{bmatrix} 1 & 0 & 0 & 0 \\ 0 & 1 & 0 & 0 \\ 0 & 0 & 1 & 0 \\ 0 & 0 & 0 & 1 \end{bmatrix} \ddot{q} + \begin{bmatrix} 11086.6 & 0 & 0 & 0 \\ 0 & 11086.6 & 0 & -\alpha \\ 0 & 0 & 49465.2 & 0 \\ 0 & -\alpha & 0 & 11086.6 \end{bmatrix} q = 0 \quad (3.10)$$

To accurately visualize the impact of this coupled DOF, the now augmented ROM is decoupled once more. For this example, $\alpha = 1$.

$$\begin{bmatrix} 1 & 0 & 0 & 0 \\ 0 & 1 & 0 & 0 \\ 0 & 0 & 2 & 0 \\ 0 & 0 & 0 & 2 \end{bmatrix} \ddot{q} + \begin{bmatrix} 49465.2 & 0 & 0 & 0 \\ 0 & 11086.6 & 0 & 0 \\ 0 & 0 & 22175.2 & 0 \\ 0 & 0 & 0 & 22171.2 \end{bmatrix} q = 0 \quad (3.11)$$

Which be rewritten into four EOMs,

$$\begin{aligned} \ddot{q}_1 + 49465.2q_1 &= 0 \\ \ddot{q}_2 + 11086.6q_2 &= 0 \\ \ddot{q}_3 + 11087.6q_3 &= 0 \\ \ddot{q}_4 + 11085.6q_4 &= 0 \end{aligned}$$

This process was conducted for several different values of the coupling coefficient, α . Table 3.3 summarizes the eigenvalues, or squared natural frequencies, of the decoupled ROM with an additional coupled DOF. The eigenvalues were ordered largest to smallest for clarity.

It is clear that as the coupling coefficient is increased, the impact of the additional DOF has on the original structure increases, increasing the shift in frequencies above and below the original value. It is also important to note that if the coupling coefficient becomes greater than the targeted eigenvalue, the structure will be unstable, as it possesses a negative eigenvalue. The one issue with this analysis and its application to a real system outside of this example is that blindly adding a DOF in a modal decoupled system adds an additional eigenvector that cannot be determined. Therefore, the reduced mass and stiffness matrices could not be expanded back into

the original mass and stiffness matrices with the additional DOF because of this missing eigenvector.

Table 3.3 Squared Natural Frequencies of Cantilever Beam FEM ROM with Additional DOF

Coupling, α	ω_{n1}^2	ω_{n2}^2	ω_{n3}^2	ω_{n4}^2
0	49465.2	11086.6	11086.6	11086.6
1	49465.2	11087.6	11086.6	11085.6
2	49465.2	11088.6	11086.6	11084.6
100	49465.2	11186.6	11086.6	10986.6
1000	49465.2	12086.6	11086.6	10086.6
$5543.3 = 0.5\omega_n^2$	49465.2	16629.9	11086.6	5543.3
10000	49465.2	21086.6	11086.6	1086.6
$11086.6 = \omega_n^2$	49465.2	22173.2	11086.6	$7.52e-24$
11100	49465.2	22186.6	11086.6	-13.4
$22173.2 = 2\omega_n^2$	49465.2	33259.6	11086.6	-11086.6

4. LINEAR MASS SPRING – BEAM SYSTEM

Chapter 3 established that the addition of another DOF to a structure can greatly affect the natural frequencies of the original structure when the additional DOF is coupled to a particular, pre-existing natural frequency. Chapter 4 applies this theory to a linear model attached to a cantilevered beam to better understand the impact an additional DOF has on a physical system. The linear system presented here is a single degree of freedom (SDOF) linear mass-spring (LMS) system. It will be attached to the end of a cantilevered beam with the aim of altering the first natural frequency of the beam. This chapter begins with the general procedure used to generate equations of motion (EOMs), to determine equilibrium points and their stability, and to find the linearized natural frequencies. After which, the models for the SDOF LMS system and the cantilevered beam will be introduced individually. Then, the equations of motion, equilibrium points, and linearized natural frequencies for the SDOF LMS attached to the end of the beam will be derived. The linearized natural frequencies will be compared to the original natural frequencies of the cantilevered beam to see the impact made by the addition of the SDOF LMS on the overall structure. The objective of this chapter is to demonstrate that with a change in stiffness, the natural frequencies of the combined system will shift. This shift will prove the possibility of switching and manipulating the natural frequencies of a structure to avoid resonance, thus mitigating the usual vibration endured during resonance.

4.1 Analytical and Numerical Analysis Procedure

A general procedure is followed to determine the EOMs and the linearized natural frequencies of a system, as well as the system's equilibrium points and their stability. This procedure applies to the SDOF LMS-Beam, the SDOF NLMS-Beam, and the Coupled 2DOF NLMS-Beam systems. The latter two models will be described in greater detail in Chapter 5 and Chapter 6, respectively. The flowchart in Figure 4.1 illustrates this general process. Analysis of a system (or subsystem) begins with defining the potential and kinetic energies of the structure. Using Lagrange's Equations, the EOMs can be derived for each generalized coordinate within the system. In this research, each generalized coordinate represents a DOF of the system.

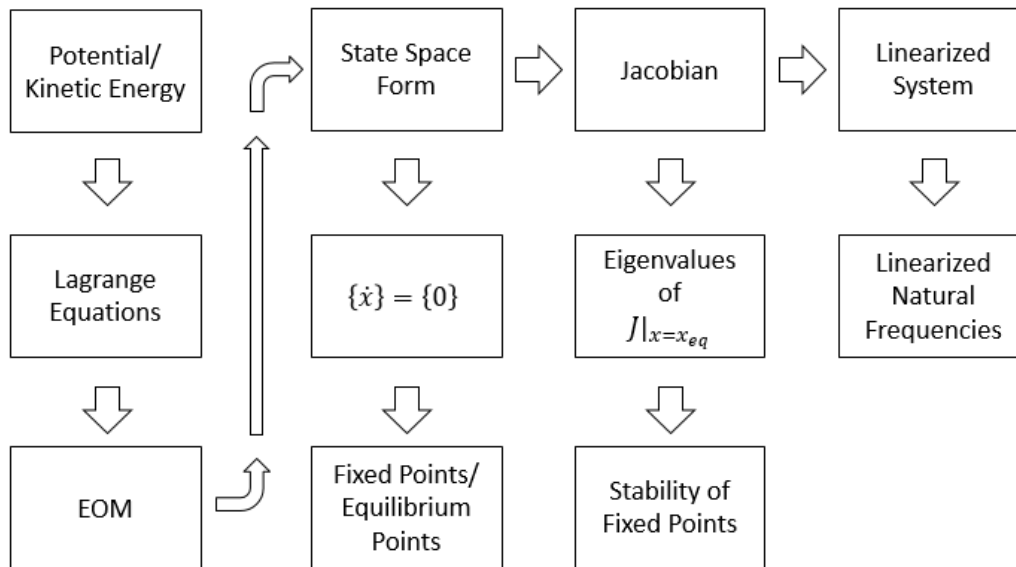


Figure 4.1 Analytical Procedure for Computing Fixed Points and Linearized Natural Frequencies

The EOMs of the system can then be rewritten in state space form. As described in Section 2.1.1, solving the state vector equation $\{\dot{\mathbf{x}}\} = \{\mathbf{0}\}$ will reveal the equilibrium points of the structure, which are also known as the system's fixed points. In addition, the Jacobian can be derived from the state equations. Solving for the eigenvalues of the Jacobian at each equilibrium point will determine which fixed points are stable and which are unstable. The Jacobian, evaluated at each fixed point, also linearizes the system's behavior around each fixed point, from which new linear EOMs can be determined. These EOMs contain an equivalent linear stiffness that, along with the mass associated with that EOM, was used to find linearized natural frequencies for each stable state.

To find the frequency response of the system, a numerical approach was used. A 4th order Runge-Kutta numerical solver can numerically determine the response of each state in the state equations for a variety of frequencies for a given excitation amplitude. A post-processing script determines the steady state response amplitude at each frequency and constructs a frequency response curve for each state equation. This frequency response curve can be used to see resonance, nonlinear hysteresis, jumps from low to high or high to low energy branches, and switching from state to state. Now that a general method for analyzing a system has been introduced, the SDOF LMS-Beam model will be presented.

4.2 SDOF Linear Mass-Spring - Beam Model

As previously mentioned, the targeted system will be a cantilever beam. The attached structure will be a SDOF, linear mass-spring system, placed at the end of the beam, targeting the first natural frequency of the beam. The following figure illustrates the model configuration.

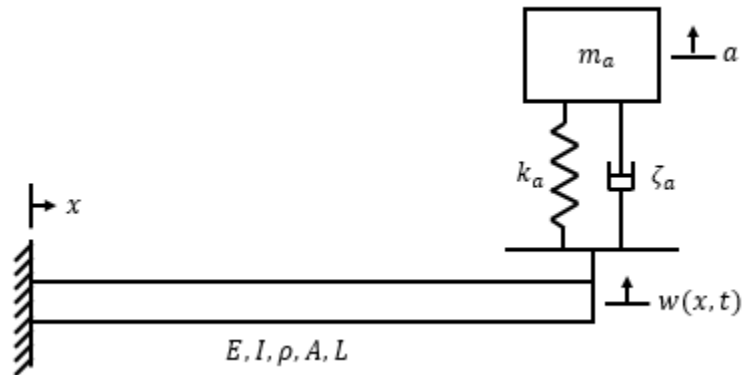


Figure 4.2 Linear SDOF Mass Spring - Beam System

The models for the SDOF LMS and the cantilevered beam will be introduced separately and then the EOM of the combined system will be derived.

4.2.1 Linear SDOF Mass Spring

The aim of this thesis is to show that the response levels at a particular natural frequency of a structure can be targeted and passively mitigated. For simplicity, this analysis used a SDOF LMS system to provide the additional DOF that will target the first natural frequency of the cantilever beam. A simple schematic can be seen in the following figure.

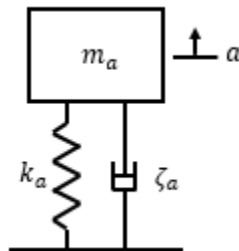


Figure 4.3 SDOF Linear Mass Spring System

The equation of motion for this system is of the commonly known form:

$$m_a \ddot{a} + \zeta_a \dot{a} + k_a a = 0 \quad (4.1)$$

In Equation (4.1), m_a is the mass, ζ_a is the damping coefficient, and k_a is the spring constant of the mass-spring system. The variable a describes the displacement of the mass m_a . In this linear system, only the spring constant describes the overall stiffness of the system. While this linear system does not have two stable states, the stiffness can be artificially changed to observe the change in the linearized natural frequencies of the entire structure.

4.2.2 Cantilevered Beam Model and its Eigenfunctions

A cantilever beam will serve as the target structure. For the purposes of this research, the beam is an Euler-Bernoulli beam, made of isotropic material and with a homogenous, rectangular cross section. Per the Euler-Bernoulli assumptions, the beam is subject to small deformations and pure bending [50].

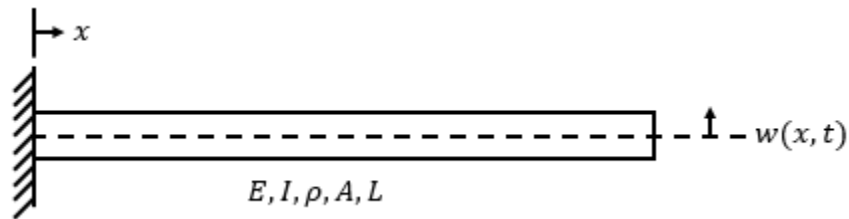


Figure 4.4 Isotropic Cantilever Beam with Deflection $w(x, t)$

Equation (4.2) is used to describe the dynamics of an Euler-Bernoulli beam. This equation can be derived from the force-diagram of an infinitesimal beam element, which is provided in greater detail within Inman's text [50].

$$\frac{\partial^2}{\partial x^2} \left(EI(x) \frac{\partial^2 w(x, t)}{\partial x^2} \right) + \rho A(x) \left(\frac{\partial^2 w(x, t)}{\partial t^2} \right) = f(x, t) \quad (4.2)$$

In this equation, x is the position along the length of the beam, with $x = 0$ representing the fixed end of the beam, $w(x, t)$ describes the deflection of the beam, $f(x, t)$ is the transverse load applied to the beam, E is the Young's Modulus, I is the second area moment of the beam cross section, ρ is the density, and A is the cross-sectional area of the beam. For this research, E , I , and A are assumed to be independent of x , reducing Equation (4.2) to the following form.

$$EI \left(\frac{\partial^4 w(x, t)}{\partial x^4} \right) + \rho A \left(\frac{\partial^2 w(x, t)}{\partial t^2} \right) = f(x, t) \quad (4.3)$$

Assuming there are no external lateral loads, $f(x, t) = 0$, the fixed-free boundary conditions characteristic of a cantilever beam are the following,

$$\begin{aligned} w(0, t) &= 0 \\ \frac{\partial w}{\partial x}(0, t) &= 0 \\ \frac{\partial^2 w}{\partial x^2}(L, t) &= 0 \\ \frac{\partial^3 w}{\partial x^3}(L, t) &= 0 \end{aligned} \quad (4.4)$$

The separation-of-variables method can be used to solve this partial differential equation for $w(x, t)$. This method uses a solution assumed to be of the form $w(x, t) = W(x)T(t)$. Substituting this expression into Equation (4.3) yields the following equation,

$$\frac{EI}{\rho A} \frac{W^{(4)}(x)}{W(x)} = -\frac{\ddot{T}(t)}{T(t)} = \omega^2 \quad (4.5)$$

Where the partial derivatives have now become total derivatives

$$\begin{aligned} W^{(4)}(x) &= \frac{d^4 W(x)}{dx^4} \\ \ddot{T}(t) &= \frac{d^2 T(t)}{dt^2} \end{aligned}$$

The separation constant, ω^2 , is selected so that the natural frequency comes from temporal equation,

$$\ddot{T}(t) + \omega^2 T(t) = 0 \quad (4.6)$$

The solution to the temporal equation has the form,

$$T(t) = A \sin \omega t + B \cos \omega t \quad (4.7)$$

Where A and B are constants determined by initial conditions after the spatial and temporal solutions have been combined.

Shifting focus to the second expression of Equation (4.5), the spatial equation and its fixed-free boundary conditions associated with a cantilever beam are expressed in Equations (4.8) and (4.9).

$$EIW^{(4)}(x) - \omega^2 \rho A W(x) = 0 \quad (4.8)$$

$$\begin{aligned} W(0) &= 0 \\ W'(0) &= 0 \\ W''(L) &= 0 \\ W'''(L) &= 0 \end{aligned} \quad (4.9)$$

Equation (4.3) can be rewritten in the form

$$W^{(4)}(x) - \frac{\omega^2 \rho A}{EI} W(x) = 0$$

The term β is defined as

$$\beta^2 = \sqrt{\frac{\omega^2 \rho A}{EI}}$$

And the solution is assumed to be of the form

$$W(x) = B_1 \cos(\beta x) + B_2 \sin(\beta x) + B_3 \cosh(\beta x) + B_4 \sinh(\beta x) \quad (4.10)$$

Plugging in the boundary conditions of Equation (4.4) into Equation (4.5) results in the following equations:

$$B_1 + B_3 = 0 \quad (4.11)$$

$$B_2 + B_4 = 0 \quad (4.12)$$

$$-B_1 \cos(\beta L) - B_2 \sin(\beta L) + B_3 \cosh(\beta L) + B_4 \sinh(\beta L) = 0 \quad (4.13)$$

$$B_1 \sin(\beta L) - B_2 \cos(\beta L) + B_3 \sinh(\beta L) + B_4 \cosh(\beta L) = 0 \quad (4.14)$$

A simple observation of Equations (4.11) and (4.12) reveals the following:

$$B_3 = -B_1 \quad (4.15)$$

$$B_4 = -B_2 \quad (4.16)$$

Equations (4.15) and (4.16) can be substituted into Equations (4.13) and (4.14) and rewritten to produce the following relations

$$\begin{bmatrix} \cos(\beta L) + \cosh(\beta L) & \sin(\beta L) + \sinh(\beta L) \\ \sin(\beta L) - \sinh(\beta L) & -\cos(\beta L) - \cosh(\beta L) \end{bmatrix} \begin{Bmatrix} B_1 \\ B_2 \end{Bmatrix} = \begin{Bmatrix} 0 \\ 0 \end{Bmatrix} \quad (4.17)$$

For non-trivial solutions, the determinant of this matrix must vanish. Therefore,

$$\begin{aligned} \det \left(\begin{bmatrix} \cos(\beta L) + \cosh(\beta L) & \sin(\beta L) + \sinh(\beta L) \\ \sin(\beta L) - \sinh(\beta L) & -\cos(\beta L) - \cosh(\beta L) \end{bmatrix} \right) &= 0 \\ -(\cos(\beta L) + \cosh(\beta L))^2 - (\sin(\beta L)^2 - \sinh(\beta L)^2) &= 0 \\ -\cos(\beta L)^2 - 2 \cos(\beta L) \cosh(\beta L) - \cosh(\beta L)^2 - \sin(\beta L)^2 + \sinh(\beta L)^2 &= 0 \end{aligned} \quad (4.18)$$

To reduce this expression to a more solvable form, the following trigonometric identities were used.

$$\begin{aligned} \cos(\beta L)^2 + \sin(\beta L)^2 &= 1 \\ \cosh(\beta L)^2 - \sinh(\beta L)^2 &= 1 \end{aligned}$$

From these two identities, the final relation can be determined.

$$\begin{aligned} -2 \cos(\beta L) \cosh(\beta L) - 1 - 1 &= 0 \\ \cos(\beta L) \cosh(\beta L) &= -1 \end{aligned} \quad (4.19)$$

The roots of Equation (4.19) can be identified as the intersection between two curves with β acting as the independent variable.

$$\beta_1 = \frac{1.875}{L}, \beta_2 = \frac{4.694}{L}, \beta_n = \frac{\pi \left(n - \frac{1}{2} \right)}{L}, n = 3, 4, \dots \quad (4.20)$$

From the 2nd equation in Equation (4.17), the coefficient B_2 , B_3 , and B_4 can be found in terms of B_1 .

$$B_2 = B_1 \frac{\sin(\beta L) - \sinh(\beta L)}{\cos(\beta L) + \cosh(\beta L)} \quad (4.21)$$

$$B_4 = -B_2 = -B_1 \frac{\sin(\beta L) - \sinh(\beta L)}{\cos(\beta L) + \cosh(\beta L)} \quad (4.22)$$

$$B_3 = -B_1 \quad (4.23)$$

Therefore, the eigenfunctions, or mode shapes, for a cantilevered beam can be written as the following expression.

$$W_n(x) = \phi_n(x) = B_1 \left[\cos(\beta_n x) + \frac{\sin(\beta_n L) - \sinh(\beta_n L)}{\cos(\beta_n L) + \cosh(\beta_n L)} \sin(\beta_n x) - \cosh(\beta_n x) - \frac{\sin(\beta_n L) - \sinh(\beta_n L)}{\cos(\beta_n L) + \cosh(\beta_n L)} \sinh(\beta_n x) \right] \quad (4.24)$$

Where B_1 is an arbitrary constant. For simplicity, it was chosen that $B_1 = 1$ for this research.

Now that both the spatial and temporal solutions have been derived for the cantilever beam, the complete solution can be determined. The series solution for the deflection of the beam is shown in Equation (4.25).

$$w(x, t) = \sum_{n=1}^{\infty} (A_n \sin \omega_n t + B_n \cos \omega_n t) \phi_n(x) \quad (4.25)$$

Where the orthogonality of the modes shapes and the initial conditions can be used to determine A_n and B_n [50].

The separation of variables method could also be used to determine the EOM of the beam with a linear or nonlinear mass spring system attached to the end of the beam. In this case, the additional system would be incorporated into the shear force boundary condition in Equation (4.4) at the end of the beam.

$$\frac{\partial^3 w}{\partial x^3}(L, t) = P(t) \quad (4.26)$$

$P(t)$ is the force exerted on the beam from the additional mass-spring system. However, in the general case where the mass-spring system is not placed at the end of the beam, the beam must be divided into multiple domains to define its boundary conditions. Solving a nonlinear multi-domain partial-differential equation becomes very complicated quickly, so the Lagrange's Equations were chosen to keep the DOF discrete in the form of generalized coordinates. The beam's eigenfunctions were still used to approximate the deflection of the beam in the Lagrange's Equations using the assumed modes method [51], which describes the deflection of the beam as a sum of the beam's mode shapes multiplied by generalized coordinates.

$$w(x, t) = \sum_{i=1}^n \phi_i(x) q_i(t) \quad (4.27)$$

Where $\phi_i(x)$ represents the i^{th} mode shape and i^{th} eigenfunction of a cantilever beam and $q_i(t)$ is the i^{th} generalized coordinate. It is clear from Equation (4.25) that an infinite number of modes are necessary to completely capture the deflection of the cantilever beam. To reduce the computational effort when analyzing the models used in this research, a two-mode expansion will be used to approximate the deflection of the beam. This minimizes the number of generalized coordinates, and thus the number of DOF, introduced into the system and will simplify the derivation of the EOMs.

4.2.3 Linear SDOF Mass Spring - Beam Model – Equations of Motion

The Lagrange's Equations were used to derive the EOM for the SDOF LMS attached to an isotropic Euler-Bernoulli beam with a homogenous cross section. This derivation begins by defining the potential and kinetic energies of the entire structure. The potential and kinetic energy for the SDOF LMS attached to an isotropic Euler-Bernoulli beam with a homogenous cross section are defined in Equations (4.28) and (4.29),

$$V = \frac{1}{2} \int_0^L EI \left(\frac{\partial^2 w(x, t)}{\partial x^2} \right)^2 dx + \frac{1}{2} k_a (a(t) - w(L, t))^2 \quad (4.28)$$

$$T = \frac{1}{2} \int_0^L \rho A \left(\frac{d}{dt} w(x, t) \right)^2 dx + \frac{1}{2} m_a \left(\frac{d}{dt} a(t) \right)^2 \quad (4.29)$$

Using the spatial discretization from Equation (4.27) into Equations (4.28) and (4.29),

$$V = \frac{1}{2} \int_0^L EI \left(\sum_{i=1}^n q_i(t) \phi_i''(x) \right)^2 dx + \frac{1}{2} k_a \left[a(t)^2 - 2a(t) \sum_{i=1}^n \phi_i(L) q_i(t) + \left(\sum_{i=1}^n \phi_i(L) q_i(t) \right)^2 \right] \quad (4.30)$$

$$T = \frac{1}{2} \int_0^L \rho A \left(\sum_{i=1}^n \phi_i(x) \dot{q}_i(t) \right)^2 dx + \frac{1}{2} m_a \dot{a}(t)^2 \quad (4.31)$$

The Lagrange's equations, defined in Equation (4.32), can be used to derive an EOM for every generalized coordinate of the structure.

$$\frac{d}{dt} \left(\frac{\partial L}{\partial \dot{q}_i} \right) - \frac{\partial L}{\partial q_i} = 0 \quad (4.32)$$

Where

$$L = T - V$$

For the structure in Figure 4.1, there exist n DOF from the modal expansion of the beam into its eigenfunctions and one DOF from the linear SDOF mass spring addition, in which Equation (4.32) will result in $n + 1$ EOMs. These EOMs can be written in the form.

$$[M]\ddot{q} + [K]q = 0 \quad (4.33)$$

Where

$$q = \begin{Bmatrix} q_1 \\ q_2 \\ \vdots \\ q_n \\ q_{n+1} \end{Bmatrix} = \begin{Bmatrix} q_1 \\ q_2 \\ \vdots \\ q_n \\ a \end{Bmatrix} \text{ and } \ddot{q} = \begin{Bmatrix} \ddot{q}_1 \\ \ddot{q}_2 \\ \vdots \\ \ddot{q}_n \\ \ddot{a} \end{Bmatrix} = \begin{Bmatrix} \ddot{q}_1 \\ \ddot{q}_2 \\ \vdots \\ \ddot{q}_n \\ \ddot{a} \end{Bmatrix}$$

$$[M] = \begin{bmatrix} \int_0^L \rho A \phi_1(x) \phi_1(x) dx & \cdots & \int_0^L \rho A \phi_1(x) \phi_n(x) dx & 0 \\ \vdots & \ddots & \vdots & \vdots \\ \int_0^L \rho A \phi_n(x) \phi_1(x) dx & \cdots & \int_0^L \rho A \phi_n(x) \phi_n(x) dx & 0 \\ 0 & \cdots & 0 & m_a \end{bmatrix}$$

$$[K] = \begin{bmatrix} \int_0^L EI\phi_1''(x)\phi_1''(x)dx + k_a\phi_1(L)\phi_1(L) & \cdots & \int_0^L EI\phi_1''(x)\phi_n''(x)dx + k_a\phi_1(L)\phi_n(L) & -k_a\phi_1(L) \\ & \vdots & \vdots & \vdots \\ \int_0^L EI\phi_n''(x)\phi_1''(x)dx + k_a\phi_n(L)\phi_1(L) & \cdots & \int_0^L \phi_n''(x)\phi_n''(x)dx + k_a\phi_n(L)\phi_n(L) & -k_a\phi_n(L) \\ & -k_a\phi_1(L) & \cdots & -k_a\phi_n(L) & k_a \end{bmatrix}$$

As previously mentioned, a two-term modal expansion was used for the cantilevered beam to simplify the analysis. Thus, Equation (4.27) becomes the following:

$$w(x, t) = \sum_{i=1}^2 \phi_i(x)q_i(t) = \phi_1(x)q_1(t) + \phi_2(x)q_2(t) \quad (4.34)$$

The mass and stiffness matrices are then reduced to the form of Equations (4.35) and (4.36)

$$[M]_2 = \begin{bmatrix} \int_0^L \rho A \phi_1(x)\phi_1(x)dx & \int_0^L \rho A \phi_1(x)\phi_2(x)dx & 0 \\ \int_0^L \rho A \phi_2(x)\phi_1(x)dx & \int_0^L \rho A \phi_2(x)\phi_2(x)dx & 0 \\ 0 & 0 & m_a \end{bmatrix} \quad (4.35)$$

$$[K]_2 = \begin{bmatrix} \int_0^L EI\phi_1''(x)\phi_1''(x)dx + k_a\phi_1(L)\phi_1(L) & \int_0^L EI\phi_1''(x)\phi_2''(x)dx + k_a\phi_1(L)\phi_2(L) & -k_a\phi_1(L) \\ \int_0^L EI\phi_2''(x)\phi_1''(x)dx + k_a\phi_2(L)\phi_1(L) & \int_0^L EI\phi_2''(x)\phi_2''(x)dx + k_a\phi_2(L)\phi_2(L) & -k_a\phi_2(L) \\ -k_a\phi_1(L) & -k_a\phi_2(L) & k_a \end{bmatrix} \quad (4.36)$$

After achieving the EOM in this form, the first and second eigenfunctions of the beam can be incorporated to capture the dynamics of the SDOF LMS-Beam system. Note that as a two-mode expansion was used, this is still an approximation of the beam deflection. Coupling can be seen between the beam and the SDOF LMS in the form of the eigenfunctions multiplied by spring constant of the LMS. The coupled EOM could be diagonalized into a set of decoupled equations using the decoupling procedure described in Chapter 3. Regardless of whether the EOM are coupled or decoupled, the EOM can be then converted into state space form, and the Jacobian can be used to compute fixed points and linearized natural frequencies.

4.3 Results

The following sets of parameters were used for the cantilever beam with the SDOF LMS system is attached.

Table 4.1 Cantilever Beam Mechanical Parameters

Young's Modulus, E [N/m ²]	Second Area Moment of Inertia, I [m ⁴]	Density, ρ [kg/m ³]	Cross-Sectional Area, A [m ²]	Length, L [m]
180,000,000	0.0833	7700	1	5

For comparison, it is important to note that with the parameters of Table 4.1, the natural frequencies for the first and second beam modes, without the addition of the SDOF system, are 6.20 rad/s and 38.90 rad/s respectively. Table 4.2 details the natural frequencies for the combined system of the cantilevered beam and the linear SDOF system for different mechanical parameters of the SDOF system. The mass and stiffness values of the SDOF LMS system were chosen to match the natural frequency corresponding to the first beam mode. The masses 38.5 kg and 77.0 kg were examined because those masses correlate with 0.1% and 0.2% of the beam's mass respectively.

Table 4.2 Natural Frequencies of Combined SDOF LMS-Beam System

k_a [N/m]	m_a [kg]	Mass m_a Natural Frequency [rad/s]	1 st Beam Natural Frequency [rad/s]	2 nd Beam Natural Frequency [rad/s]
38.39	1	6.17	6.23	38.90
1478.09	38.5	6.01	6.40	38.90
2956.18	77.0	5.93	6.48	38.91

The addition of a DOF splits the original target natural frequency into two, one above and below the original value. Artificially increasing the mass, m_a , shifts the 1st beam mode to a higher natural frequency and the natural frequency of the SDOF LMS to a lower natural frequency. While both natural frequencies excite both the 1st beam mode and the mode of the SDOF LMS, the lower natural frequency is primarily exciting the SDOF LMS mode and the higher natural frequency is primarily exciting the 1st beam mode. This behavior can be seen in the eigenvectors corresponding to each natural frequency. In a system defined by a mass and

stiffness matrix, an eigenvector describes the mode shape that occurs at its associated eigenvalue, which is the squared natural frequency. As there are three degrees of freedom in the overall structure, the eigenvectors will have the form,

$$v = \begin{pmatrix} x_1 \\ x_3 \\ x_5 \end{pmatrix} = \begin{pmatrix} 1st \text{ Beam Mode} \\ 2nd \text{ Beam Mode} \\ SDOF \text{ LMS Mode} \end{pmatrix}$$

The eigenvectors of the entire system for each set of mass and stiffness is summarized in Table 4.3.

Table 4.3 Eigenvectors for Combined SDOF LMS-Beam System

k_a [N/m]	m_a [kg]	Mass m_a Mode Eigenvector	1 st Beam Mode Eigenvector	2 nd Beam Mode Eigenvector
38.39	1	$v = \begin{pmatrix} 0.64 \\ 0 \\ 0.77 \end{pmatrix}$	$v = \begin{pmatrix} -0.77 \\ 0 \\ 0.64 \end{pmatrix}$	$v = \begin{pmatrix} 0 \\ -1 \\ 0 \end{pmatrix}$
1478.09	38.5	$v = \begin{pmatrix} 0.69 \\ 0 \\ 0.73 \end{pmatrix}$	$v = \begin{pmatrix} -0.73 \\ 0 \\ 0.69 \end{pmatrix}$	$v = \begin{pmatrix} 0 \\ -1 \\ 0 \end{pmatrix}$
2956.18	77.0	$v = \begin{pmatrix} -0.68 \\ 0 \\ -0.73 \end{pmatrix}$	$v = \begin{pmatrix} 0.73 \\ 0 \\ -0.68 \end{pmatrix}$	$v = \begin{pmatrix} 0 \\ -1 \\ 0 \end{pmatrix}$

By inspecting Table 4.2 and Table 4.3, it is clear that increasing the mass further would have greater impact on the first beam mode; however, a larger mass would become more difficult to physically implement on the structure and would greatly change the designed mass and stiffness of the target structure. This is counter-productive to any weight saving efforts, and may impact modes other than the targeted natural frequency. Therefore, this research kept the maximum mass of any attachment configuration at 2% of the beam's mass. Furthermore, a linear SDOF mass-spring system has only one stable state. Once this attachment is installed onto the beam, the new natural frequency of the 1st beam mode is fixed. The goal of this research was to avoid resonances altogether, which is impossible if the 1st beam mode is fixed. Therefore, a bistable, nonlinear system is needed to be able to change the first beam mode and avoid resonance conditions.

5. NONLINEAR MASS SPRING – BEAM SYSTEM

In Chapter 4, matching the linearized natural frequency of a SDOF LMS system to that of the cantilever beam's 1st bending mode was shown to increase the natural frequency of the 1st beam mode. However, the 1st beam mode is fixed once the SDOF LMS is implemented. The goal of this research was to avoid resonances altogether, which is impossible if the 1st beam mode is fixed. Chapter 5 substitutes a SDOF NLMS system for the SDOF LMS system attached to the end of the beam in order to introduce the possibility of multiple stable states. The chapter begins by deriving the EOM of the cantilever beam with a SDOF NLMS attached to the free end. Then, the Jacobian was used to determine the linearized natural frequencies of the combined system at each fixed point. The linearized natural frequencies were found for various sets of SDOF NLMS parameters to observe the effect of increasing the mass or asymmetry of the potential energy of the SDOF NLMS system on the complete structure. After which, numerical simulations were performed to verify the performance of the SDOF NLMS-Beam system. The objective of this chapter is to evaluate the SDOF NLMS system's capability to avoid resonance conditions around the 1st mode of the cantilever beam. The SDOF NLMS system presented in this chapter has two stable states with a different linearized natural frequency in each state. Thus, each state will have a unique impact on the 1st mode of the cantilever beam and switching between these states could avoid the large response levels experienced near resonance.

5.1 NLMS – Beam Model

Similar to the Linear SDOF mass spring system, the NLMS system is added to the targeted structure represented by the cantilever beam throughout this thesis. Note that the NLMS is added to the end of the beam. Since the target mode is the 1st bending mode of the cantilever beam, the end of the beam is the point of maximum deflection for the targeted mode and thus is the position where the NLMS can have the greatest coupling to the beam. For modes that contain a node at which no deflection occurs, applying the subsystem in this position would have no effect on the vibration and deflection of the beam.

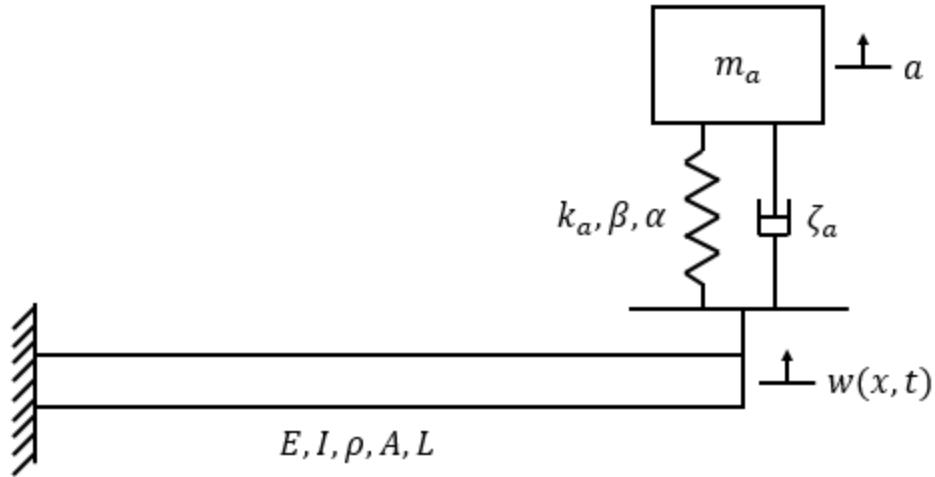


Figure 5.1 SDOF NLMS added to Cantilever Beam

The general process described in Section 4.1 is followed here to obtain the nonlinear EOMs using the eigenfunctions of the cantilever beam for the discretization of the displacement, as shown in Equation (4.34). The potential and kinetic energies of the entire structure are

$$V = \frac{1}{2} \int_0^L EI \left(\frac{\partial^2 w(x, t)}{\partial x^2} \right)^2 dx + \frac{1}{2} k_a (a(t) - w(L, t))^2 + \frac{1}{3} \beta (a(t) - w(L, t))^3 + \frac{1}{4} \alpha (a(t) - w(L, t))^4 \quad (5.1)$$

$$T = \frac{1}{2} \int_0^L \rho A \left(\frac{d}{dt} w(x, t) \right)^2 dx + \frac{1}{2} m_a \left(\frac{d}{dt} a(t) \right)^2 \quad (5.2)$$

The EOM will have both linear and nonlinear terms due to the nonlinear stiffness in the NLMS system. The linear terms can be arranged into a matrix and the nonlinear terms will be a vector function of the state variables. Recall, the beam displacement is approximated by Equation (4.34) in the Assumed Modes Method [51], where $q_1(t)$ and $q_2(t)$ are two discrete DOF. These two DOF are also two time-dependent generalized coordinates that describe the dynamics of the 1st and 2nd cantilever beam mode shapes, $\phi_1(x)$ and $\phi_2(x)$, respectively. The motion of the SDOF NLMS system attached to the beam is described by $a(t)$. These generalized coordinates can be arranged in the following vector form and used to compute the EOM of the entire system.

$$\{q\} = \begin{Bmatrix} q_1 \\ q_2 \\ a \end{Bmatrix} \quad (5.3)$$

Using Lagrange's Equations, the following EOMs can be found:

$$\begin{aligned} & \int_0^L \rho A (\phi_1(x) \ddot{q}_1(t) + \phi_2(x) \ddot{q}_2(t)) (\phi_1(x)) dx \\ & + \int_0^L EI (\phi_1''(x) q_1(t) + \phi_2''(x) q_2(t)) (\phi_1''(x)) dx \\ & + k_a (a(t) - \phi_1(L) q_1(t) - \phi_2(L) q_2(t)) (-\phi_1(L)) \\ & + \beta (a(t) - \phi_1(L) q_1(t) - \phi_2(L) q_2(t))^2 (-\phi_1(L)) \\ & + \alpha (a(t) - \phi_1(L) q_1(t) - \phi_2(L) q_2(t))^3 (-\phi_1(L)) = 0 \end{aligned} \quad (5.4)$$

$$\begin{aligned} & \int_0^L \rho A (\phi_1(x) \ddot{q}_1(t) + \phi_2(x) \ddot{q}_2(t)) (\phi_2(x)) dx \\ & + \int_0^L EI (\phi_1''(x) q_1(t) + \phi_2''(x) q_2(t)) (\phi_2''(x)) dx \\ & + k_a (a(t) - \phi_1(L) q_1(t) - \phi_2(L) q_2(t)) (-\phi_2(L)) \\ & + \beta (a(t) - \phi_1(L) q_1(t) - \phi_2(L) q_2(t))^2 (-\phi_2(L)) \\ & + \alpha (a(t) - \phi_1(L) q_1(t) - \phi_2(L) q_2(t))^3 (-\phi_2(L)) = 0 \end{aligned} \quad (5.5)$$

$$\begin{aligned} & m_a \ddot{a}(t) + k_a (a(t) - \phi_1(L) q_1(t) - \phi_2(L) q_2(t)) \\ & + \beta (a(t) - \phi_1(L) q_1(t) - \phi_2(L) q_2(t))^2 \\ & + \alpha (a(t) - \phi_1(L) q_1(t) - \phi_2(L) q_2(t))^3 = 0 \end{aligned} \quad (5.6)$$

The preceding three equations are arranged in matrix form as:

$$[M]\{\ddot{q}\} + [K]\{q\} + f(q) = \{0\} \quad (5.7)$$

Where $[M]$, $[K]$, and $f(q)$, are the mass matrix, the stiffness matrix, and a nonlinear function of the state variables, respectively

$$[M] = \begin{bmatrix} \int_0^L \rho A \phi_1^2(x) dx & \int_0^L \rho A \phi_1(x) \phi_2(x) dx & 0 \\ \int_0^L \rho A \phi_1(x) \phi_2(x) dx & \int_0^L \rho A \phi_2^2(x) dx & 0 \\ 0 & 0 & m_a \end{bmatrix}$$

$$\begin{aligned}
& [K] = \\
& \begin{bmatrix} \int_0^L EI(\phi_1''(x))^2 dx + k_a \phi_1^2(L) & \int_0^L EI\phi_1''(x)\phi_2''(x)dx + k_a \phi_1(L)\phi_2(L) & -k_a \phi_1(L) \\ \int_0^L EI\phi_1''(x)\phi_2''(x)dx + k_a \phi_1(L)\phi_2(L) & \int_0^L EI(\phi_2''(x))^2 dx + k_a \phi_2^2(L) & -k_a \phi_2(L) \\ -k_a \phi_1(L) & -k_a \phi_2(L) & k_a \end{bmatrix} \\
& f(q) = \\
& \left\{ \begin{array}{l} \beta \left[(a(t) - \phi_1(L)q_1(t) - \phi_2(L)q_2(t))^2 (-\phi_1(L)) \right] + \alpha \left[(a(t) - \phi_1(L)q_1(t) - \phi_2(L)q_2(t))^3 (-\phi_1(L)) \right] \\ \beta \left[(a(t) - \phi_1(L)q_1(t) - \phi_2(L)q_2(t))^2 (-\phi_2(L)) \right] + \alpha \left[(a(t) - \phi_1(L)q_1(t) - \phi_2(L)q_2(t))^3 (-\phi_2(L)) \right] \\ \beta \left[(a(t) - \phi_1(L)q_1(t) - \phi_2(L)q_2(t))^2 \right] + \alpha \left[(a(t) - \phi_1(L)q_1(t) - \phi_2(L)q_2(t))^3 \right] \end{array} \right\}
\end{aligned}$$

Using the orthogonality of modes shapes [50],

$$\int_0^L \phi_n(x)\phi_m(x) dx = 0, n \neq m \quad (5.8)$$

The mass matrix of Equation (5.7) becomes

$$[M] = \begin{bmatrix} \int_0^L \rho A \phi_1^2(x) dx & 0 & 0 \\ 0 & \int_0^L \rho A \phi_2^2(x) dx & 0 \\ 0 & 0 & m_a \end{bmatrix} \quad (5.9)$$

The EOM shown in Equation (5.7) are transformed into state space form to study the fixed points of the system. In addition, this form is amenable to direct numerical simulation. Equation (5.10) summarizes the six state variables for this system.

$$\{\mathbf{x}\} = \begin{Bmatrix} x_1 \\ x_2 \\ x_3 \\ x_4 \\ x_5 \\ x_6 \end{Bmatrix} = \begin{Bmatrix} q_1 \\ \dot{q}_1 \\ q_2 \\ \dot{q}_2 \\ a \\ \dot{a} \end{Bmatrix} \quad (5.10)$$

Thus, the state equations become

$$\{\dot{x}\} = \begin{Bmatrix} \dot{x}_1 \\ \dot{x}_2 \\ \dot{x}_3 \\ \dot{x}_4 \\ \dot{x}_5 \\ \dot{x}_6 \end{Bmatrix} = g(x, t) = [A] \begin{Bmatrix} x_1 \\ x_2 \\ x_3 \\ x_4 \\ x_5 \\ x_6 \end{Bmatrix} + F(x) \quad (5.11)$$

Where

$$[A] = \begin{bmatrix} 0 & 1 & 0 & 0 & 0 & 0 \\ \frac{-\int_0^L EI(\phi_1''(x))^2 dx - k_a \phi_1^2(L)}{\int_0^L \rho A \phi_1^2(x) dx} & 0 & \frac{-\int_0^L EI \phi_1''(x) \phi_2''(x) dx - k_a \phi_1(L) \phi_2(L)}{\int_0^L \rho A \phi_1^2(x) dx} & \frac{k_a \phi_1(L)}{\int_0^L \rho A \phi_1^2(x) dx} & 0 & 0 \\ 0 & 0 & 0 & 1 & 0 & 0 \\ \frac{-\int_0^L EI \phi_1''(x) \phi_2''(x) dx - k_a \phi_1(L) \phi_2(L)}{\int_0^L \rho A \phi_2^2(x) dx} & 0 & \frac{-\int_0^L EI(\phi_2''(x))^2 dx - k_a \phi_2^2(L)}{\int_0^L \rho A \phi_2^2(x) dx} & 0 & \frac{k_a \phi_2(L)}{\int_0^L \rho A \phi_2^2(x) dx} & 0 \\ 0 & 0 & 0 & 0 & 0 & 1 \\ \frac{k_a \phi_1(L)}{m_a} & 0 & \frac{k_a \phi_2(L)}{m_a} & 0 & \frac{-k_a}{m_a} & 0 \end{bmatrix}$$

$$F(x) = \begin{pmatrix} 0 \\ \frac{-\beta \left[(x_5 - \phi_1(L)x_1 - \phi_2(L)x_3)^2 (-\phi_1(L)) \right] - \alpha \left[(x_5 - \phi_1(L)x_1 - \phi_2(L)x_3)^3 (-\phi_1(L)) \right]}{\int_0^L \rho A \phi_1^2(x) dx} \\ 0 \\ \frac{-\beta \left[(x_5 - \phi_1(L)x_1 - \phi_2(L)x_3)^2 (-\phi_2(L)) \right] - \alpha \left[(x_5 - \phi_1(L)x_1 - \phi_2(L)x_3)^3 (-\phi_2(L)) \right]}{\int_0^L \rho A \phi_2^2(x) dx} \\ 0 \\ \frac{-\beta \left[(x_5 - \phi_1(L)x_1 - \phi_2(L)q_2(t))^2 \right] - \alpha \left[(x_5 - \phi_1(L)x_1 - \phi_2(L)x_3)^3 \right]}{m_a} \end{pmatrix}$$

The state space equations (5.11) sets the system in first order form allowing us to inspect its fundamental stability behavior using Lyapunov's (first) indirect method [52]. This enables us to determine the fixed points and their stability. The Jacobian of the system can be further utilized to linearize the nonlinear equations of motion about each fixed point, from which the linearized natural frequencies can be determined. The Jacobian can be determined using the following expression.

$$G(x) = \begin{bmatrix} f_1(x_1, x_2, x_3, x_4, x_5, x_6) \\ f_2(x_1, x_2, x_3, x_4, x_5, x_6) \\ f_3(x_1, x_2, x_3, x_4, x_5, x_6) \\ f_4(x_1, x_2, x_3, x_4, x_5, x_6) \\ f_5(x_1, x_2, x_3, x_4, x_5, x_6) \\ f_6(x_1, x_2, x_3, x_4, x_5, x_6) \end{bmatrix} = [A] \begin{Bmatrix} x_1 \\ x_2 \\ x_3 \\ x_4 \\ x_5 \\ x_6 \end{Bmatrix} + F(x) \quad (5.12)$$

$$J|_{(x_1, x_2, x_3, x_4, x_5, x_6)} = \begin{bmatrix} \frac{\partial f_1}{\partial x_1} & \frac{\partial f_1}{\partial x_2} & \frac{\partial f_1}{\partial x_3} & \frac{\partial f_1}{\partial x_4} & \frac{\partial f_1}{\partial x_5} & \frac{\partial f_1}{\partial x_6} \\ \frac{\partial f_2}{\partial x_1} & \frac{\partial f_2}{\partial x_2} & \frac{\partial f_2}{\partial x_3} & \frac{\partial f_2}{\partial x_4} & \frac{\partial f_2}{\partial x_5} & \frac{\partial f_2}{\partial x_6} \\ \frac{\partial f_3}{\partial x_1} & \frac{\partial f_3}{\partial x_2} & \frac{\partial f_3}{\partial x_3} & \frac{\partial f_3}{\partial x_4} & \frac{\partial f_3}{\partial x_5} & \frac{\partial f_3}{\partial x_6} \\ \frac{\partial f_4}{\partial x_1} & \frac{\partial f_4}{\partial x_2} & \frac{\partial f_4}{\partial x_3} & \frac{\partial f_4}{\partial x_4} & \frac{\partial f_4}{\partial x_5} & \frac{\partial f_4}{\partial x_6} \\ \frac{\partial f_5}{\partial x_1} & \frac{\partial f_5}{\partial x_2} & \frac{\partial f_5}{\partial x_3} & \frac{\partial f_5}{\partial x_4} & \frac{\partial f_5}{\partial x_5} & \frac{\partial f_5}{\partial x_6} \\ \frac{\partial f_6}{\partial x_1} & \frac{\partial f_6}{\partial x_2} & \frac{\partial f_6}{\partial x_3} & \frac{\partial f_6}{\partial x_4} & \frac{\partial f_6}{\partial x_5} & \frac{\partial f_6}{\partial x_6} \end{bmatrix} \quad (5.13)$$

The linearized equations of motion and the linearized natural frequencies can be determined by incorporating the eigenfunctions of the cantilever beam into the system and evaluating the Jacobian at each fixed point.

Having derived the nonlinear EOM, the linearized EOM, and the linearized natural frequencies of the SDOF NLMS-Beam system, we can now investigate the impact both stable states of the SDOF NLMS system have on the linearized natural frequencies of the combined system. As mentioned in Section 4.3, the original natural frequencies of the 1st and 2nd modes of the cantilevered beam, without the SDOF NLMS system, are 6.20 rad/s and 38.90 rad/s respectively. The linearized natural frequencies for both fixed points of the combined SDOF NLMS-Beam system were determined using the mechanical parameters specified in Table 5.1 for the cantilever beam.

Table 5.1 Mechanical Parameters for the Cantilever Beam

Young's Modulus, E (N/m ²)	Second Area Moment of Inertia, I (m ⁴)	Density, ρ (kg/m ³)	Cross-Sectional Area, A (m ²)	Length, L (m)
180,000,000	0.0833	7700	1	5

The linearized natural frequencies of the SDOF NLMS system and the 1st mode of the cantilever beam were compared for various sets of mechanical parameters. Since the SDOF NLMS system is bistable, the comparison was performed for both stable states. In Tables 5.2 and 5.3, four sets of mechanical parameters for the SDOF NLMS-Beam system were used to calculate linearized natural frequencies. In particular, two sets with a mass of $m_a = 38.5 \text{ kg}$ and two sets with a mass of $m_a = 77.0 \text{ kg}$, which correspond to 0.1% and 0.2% of the beam's mass respectively. For each mass, the second case (Case 2 and Case 4) exhibits a more asymmetric potential function than the first (Case 1 and Case 3, respectively). As mentioned previously in Section 2.1.4, an increase in the asymmetry of the potential function will increase the difference in linearized natural frequency between the two states of the SDOF NLMS system. In addition, an asymmetric potential function has a shallow potential well and a deep potential well. For all the cases in Tables 5.2 and 5.3, the deep well exist at a negative displacement and the shallow well exists at a positive displacement relative to the unstable fixed point, the potential hill top, at $a = 0$. For this chapter and Chapter 6, the deep well or negative fixed point will be referred to as state 1 and the shallow well or positive fixed point will be referred to as state 2, which can be seen in Figure 5.2.

Given the desire to achieve switching close to the target resonance of the target structure, one of these wells will need to match its linearized natural frequency with the linearized natural frequency of the 1st beam mode to couple the SDOF NLMS system to the 1st beam mode and substantially shift the linearized natural frequency of the 1st beam mode. The linearized natural frequency corresponding to the shallow potential well, state 2, was chosen to match the frequency of the 1st beam mode in order to place the linearized natural frequency of the deep potential well, state 1, above the 1st beam mode. This would allow the system to switch when the system approaches resonance, and then switch again afterwards, back to its original state. If the deep potential well is chosen to match the linearized natural frequency of the 1st beam mode, the linearized natural frequency of the shallow potential well will be below the 1st beam mode. Thus, the parameters were chosen so that there was no change in the linearized natural frequencies for state 2 regardless of the asymmetry within the potential function. Generally, lower modes are more damaging to a system, therefore, matching the linearized natural frequency to that of the deep potential well, should be avoided.

Table 5.2 and Table 5.3 show the linearized natural frequencies of the overall system for each stable state for each set of SDOF NLMS parameters. The percent difference in natural frequency between states is given for both the 1st beam mode, q_1 , and for the SDOF NLMS mode, m_a . This measures the impact of switching between states in the SDOF NLMS systems on the linearized natural frequency of the 1st beam mode, q_1 . In addition, the percent difference in the squared natural frequency is given for each set of parameters. Recall, the electromechanical coupling coefficient of the piezoelectric patches used by Kauffman et al [42] was related to the percent difference in squared natural frequency of each state, shown in Equation (2.41). In Kauffman's case, each state was created with either the open-circuit or short-circuit boundary conditions. Thus, the performance of SDOF NLMS system could be compared to the electromechanical coupling coefficients Kauffman et al present.

Table 5.2 Linearized Natural Frequencies of Beam and NLMS Modes for Various NLMS Parameters and $m_a = 38.5 \text{ kg}$

Case	$k_a \left[\frac{N}{m} \right]$	$\beta \left[\frac{N}{m^2} \right]$	$\alpha \left[\frac{N}{m^3} \right]$	Mode	State 1 $\omega_n \left[\frac{rad}{s} \right]$	State 2 $\omega_n \left[\frac{rad}{s} \right]$	$\Delta\omega_n$ [%]	$\Delta\omega_n^2$ [%]
1	-871.25	316.82	817.25	q_1	6.17	6.40	3.78	7.70
				m_a	7.47	6.01	19.58	35.32
2	-1069.55	1069.55	1069.55	q_1	6.19	6.40	3.45	7.01
				m_a	10.06	6.01	40.25	64.30

Table 5.3 Linearized Natural Frequencies of Beam and NLMS Modes for Various NLMS Parameters and $m_a = 77.0 \text{ kg}$

Case	$k_a \left[\frac{N}{m} \right]$	$\beta \left[\frac{N}{m^2} \right]$	$\alpha \left[\frac{N}{m^3} \right]$	Mode	State 1 $\omega_n \left[\frac{rad}{s} \right]$	State 2 $\omega_n \left[\frac{rad}{s} \right]$	$\Delta\omega_n$ [%]	$\Delta\omega_n^2$ [%]
3	-1742.49	663.63	1742.49	q_1	6.13	6.48	5.77	11.88
				m_a	7.71	5.93	23.11	40.88
4	-2139.11	2139.11	2139.11	q_1	6.17	6.48	5.14	10.54
				m_a	10.09	5.93	41.21	65.43

It is clear from Tables 5.2 and 5.3 that a larger mass in the SDOF NLMS system increases the percent difference between the linearized natural frequencies of the 1st beam mode, q_1 , in state 1 and in state 2 of the overall structure. In Chapter 4, the same result was also seen with the SDOF LMS-Beam system. Case 2 and Case 4 contain NLMS parameters that resemble a system

with a more asymmetric potential function than Case 1 and Case 3 respectively. This can be seen in Figure 5.2.

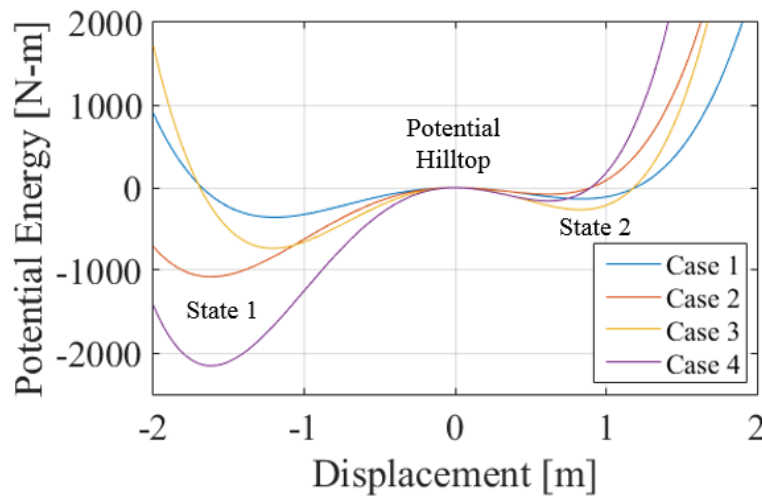


Figure 5.2 Potential Functions for Each Case of SDOF NLMS Parameters

Graphically, the potential hilltop is the local maximum at zero displacement for every case. The two stable states are local minima on either side of the potential hilltop, where state 1 is the local minimum at a negative displacement and state 2 is the local minimum at a positive displacement.

Both Case 2 and Case 4 indicate that a more asymmetric potential function in the SDOF NLMS system has a much greater impact on the linearized natural frequency of the SDOF NLMS mode, m_a , than on the linearized natural frequency of the 1st beam mode, q_1 , in the combined system. For Case 1, the linearized natural frequencies for the 1st beam mode and for the SDOF NLMS DOF are shifted by 3.78% and 19.58%, respectively, when switching from state 1 to state 2. For Case 2, the linearized natural frequencies are shifted by 3.45% and 40.25%. Thus, for the overall system, the increase in asymmetry within the potential function of the SDOF NLMS system actually slightly decreases the shift in the linearized natural frequency of the 1st beam mode. While there was a substantial increase in the difference in linearized natural frequency corresponding to the SDOF NLMS, the impact on the target structure is minimal, even counterproductive to the goal of increasing the difference between state 1 and state 2. This result is also seen when comparing Case 3 to Case 4, where the increase in asymmetry saw a decrease from 5.77% to 5.14%.

In Chapter 2, the difference in natural frequencies between states was shown to be related to the electromechanical coupling coefficient of piezoelectric materials. In a paper, Kauffman et al [43] considered coupling coefficients, k^2 , of 0.5%, 1.5%, and 5.0% because the highly-stressed nature of turbomachinery blades limits the amount of piezoelectric material that can be incorporated onto the blades. For the SDOF NLMS-Beam system, the percent difference between state 1 and state 2 in the squared linearized natural frequencies was also given for each parameter case. Between Case 1 and Case 2, the largest percent difference for the 1st beam mode was 7.70%, and the largest percent difference for Case 3 and Case 4 was 11.88%. The SDOF NLMS system thus shows that a mechanical solution can provide a greater difference in the target natural frequency of a structure while increasing the mass by only 0.1% or 0.2%. This increased difference opens the door to better performance when avoiding resonance. Figure 2.6 references a figure by Kauffman et al [42] that showed the optimal switching point was at the intersection between the resonance curves corresponding to the open-circuit and short-circuit boundary conditions. Increasing the distance between these curves will cause the intersection to occur at a lower response magnitude. The SDOF NLMS-Beam system proved effective at creating a substantial difference in the linearized natural frequencies of the 1st beam mode. However, the nonlinear frequency response of the overall system must be studied to verify the following performance aspects: the NLMS will actually receive enough energy to switch between states, the NLMS system will switch to avoid resonance conditions, and the NLMS system will switch a second time to return to its original state.

5.2 Nonlinear Frequency Response

Frequency response functions were obtained and used to understand the behavior of the overall system as a function of forcing frequency and the impact of adding the SDOF NLMS system. In order to obtain the frequency response function, the state equations were solved numerically using a 4th order Runge-Kutta numerical solver following a stepped frequency sweep in which the forcing is held constant for 500 seconds before proceeding to the next step. Holding each frequency constant for 500 seconds allows the system to reach steady state and ignores transient dynamics. The final values of each frequency step were also used as the initial conditions for the next step to allow any switching in the SDOF NLMS-Beam to be observed. When constructing the frequency response function at each frequency step, the amplitude of the

system was sampled from the displacement time response of the system at steady state. Furthermore, each stepped frequency sweep was performed stepping up and stepping down in frequency to reveal coexisting solutions that appear as hysteresis in the nonlinear frequency response function. In addition, a sweep up and a sweep down were each performed twice: once starting in state 1 and once starting in state 2. This aids in better understanding the capabilities of the SDOF NLMS system and its impact when attached to the beam.

5.2.1 Base Excitation

The forced excitation is applied to the NLMS – Beam system in the form of a harmonic displacement of the base of the beam. This can be visualized with a slight adjustment to Figure 5.1, shown in Figure 5.3.

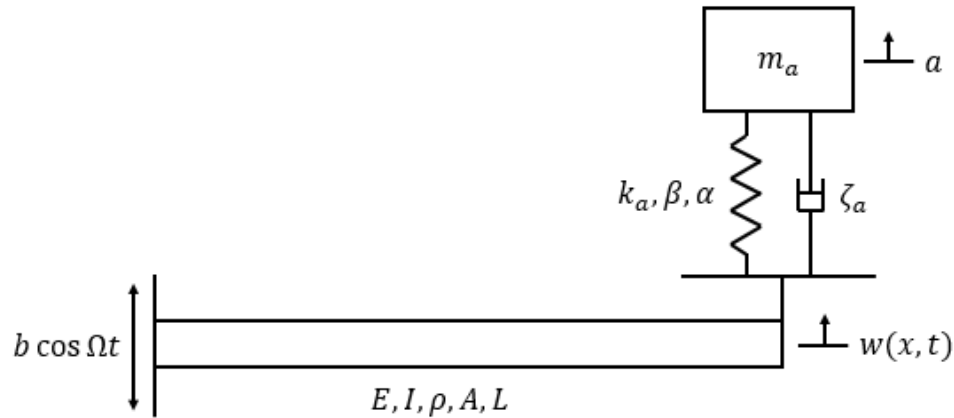


Figure 5.3 NLMS - Beam Model with Base Excitation

This harmonic excitation, with amplitude b and frequency Ω is incorporated into the beam deflection $w(x, t)$, forming $w_T(x, t)$, the total deflection of the beam, which is defined in the following expression.

$$w_T(x, t) = w(x, t) + b \cos \Omega t = \sum_{i=1}^2 \phi_i(x) q_i(t) + b \cos \Omega t = \phi_1(x) q_1(t) + \phi_2(x) q_2(t) + b \cos \Omega t \quad (5.14)$$

Incorporating this into the EOM for the SDOF NLMS-Beam system, the potential and kinetic energies become the following,

$$V = \frac{1}{2} \int_0^L EI \left(\frac{\partial^2 w_T(x, t)}{\partial x^2} \right)^2 dx + \frac{1}{2} k_a (a(t) - w_T(L, t))^2 + \frac{1}{3} \beta (a(t) - w_T(L, t))^3 + \frac{1}{4} \alpha (a(t) - w_T(L, t))^4 \quad (5.15)$$

$$T = \frac{1}{2} \int_0^L \rho A \left(\frac{d}{dt} w_T(x, t) \right)^2 dx + \frac{1}{2} m_a \left(\frac{d}{dt} a(t) \right)^2 \quad (5.16)$$

Proceeding through the Lagrange's equations, shown in Equation (4.32), the equations of motion of the overall system become

$$[M]\{\ddot{q}\} + [K]\{q\} + f(q) = E(q) \quad (5.17)$$

Where $[M]$, $[K]$, and $f(q)$ are identical to Equation 5.7, and $E(q)$, which contains all the terms associated with the excitation function, is the following

$$E(q) = \begin{Bmatrix} E_1(q) \\ E_2(q) \\ E_3(q) \end{Bmatrix} = \quad (5.18)$$

$$\left. \begin{aligned} & \int_0^L \rho A \phi_1(x) b \Omega^2 \cos \Omega t dx - k_a \phi_1(L) b \cos \Omega t - 2\beta \phi_1(L) a(t) b \cos \Omega t + 2\beta \phi_1^2(L) q_1(t) b \cos \Omega t + 2\beta \phi_1(L) \phi_2(L) q_2(t) b \cos \Omega t + \beta \phi_2(L) b^2 \cos^2 \Omega t \\ & \quad - 3\alpha \phi_1(L) a^2(t) b \cos \Omega t + 6\alpha \phi_1^2(L) a(t) q_1(t) b \cos \Omega t - 3\alpha \phi_1^3(L) q_1^2(t) b \cos \Omega t + 6\alpha \phi_1(L) \phi_2(L) a(t) q_2(t) b \cos \Omega t \\ & \quad - 6\alpha \phi_1^2(L) \phi_2(L) q_1(t) q_2(t) b \cos \Omega t - 3\alpha \phi_1(L) \phi_2^2(L) q_2^2(t) b \cos \Omega t + 3\alpha \phi_1(L) a(t) b^2 \cos^2 \Omega t - 3\alpha \phi_1^2(L) q_1(t) b^2 \cos^2 \Omega t \\ & \quad \quad - 3\alpha \phi_1(L) \phi_2(L) q_2(t) b^2 \cos^2 \Omega t - \alpha \phi_1(L) b^3 \cos^3 \Omega t \\ & \int_0^L \rho A \phi_2(x) b \Omega^2 \cos \Omega t dx - k_a \phi_2(L) b \cos \Omega t - 2\beta \phi_2(L) a(t) b \cos \Omega t + 2\beta \phi_1(L) \phi_2(L) q_1(t) b \cos \Omega t + 2\beta \phi_2^2(L) q_2(t) b \cos \Omega t + \beta \phi_2(L) b^2 \cos^2 \Omega t \\ & \quad - 3\alpha \phi_2(L) a^2(t) b \cos \Omega t + 6\alpha \phi_1(L) \phi_2(L) a(t) q_1(t) b \cos \Omega t - 3\alpha \phi_1^2(L) \phi_2(L) q_1^2(t) b \cos \Omega t + 6\alpha \phi_2^2(L) a(t) q_2(t) b \cos \Omega t \\ & \quad - 6\alpha \phi_1(L) \phi_2^2(L) q_1(t) q_2(t) b \cos \Omega t - 3\alpha \phi_2^3(L) q_2^2(t) b \cos \Omega t + 3\alpha \phi_2(L) a(t) b^2 \cos^2 \Omega t - 3\alpha \phi_1(L) \phi_2(L) q_1(t) b^2 \cos^2 \Omega t \\ & \quad \quad - 3\alpha \phi_2^2(L) q_2(t) b^2 \cos^2 \Omega t - \alpha \phi_2(L) b^3 \cos^3 \Omega t \\ & \quad k_a b \cos \Omega t + 2\beta a(t) b \cos \Omega t - 2\beta \phi_1(L) q_1(t) b \cos \Omega t - 2\beta \phi_2(L) q_2(t) b \cos \Omega t - \beta b^2 \cos^2 \Omega t \\ & \quad + 3\alpha a^2(t) b \cos \Omega t - 6\alpha \phi_1(L) a(t) q_1(t) b \cos \Omega t + 3\alpha \phi_1^2(L) q_1^2(t) b \cos \Omega t - 6\alpha \phi_2(L) a(t) q_2(t) b \cos \Omega t \\ & \quad + 6\alpha \phi_1(L) \phi_2(L) q_1(t) q_2(t) b \cos \Omega t + 3\alpha \phi_2^2(L) q_2^2(t) b \cos \Omega t - 3\alpha a(t) b^2 \cos^2 \Omega t + 3\alpha \phi_1(L) q_1(t) b^2 \cos^2 \Omega t \\ & \quad \quad + 3\alpha \phi_2(L) q_2(t) b^2 \cos^2 \Omega t + \alpha b^3 \cos^3 \Omega t \end{aligned} \right\}$$

Transforming this into state space we obtain,

$$\{\dot{x}\} = \begin{Bmatrix} \dot{x}_1 \\ \dot{x}_2 \\ \dot{x}_3 \\ \dot{x}_4 \\ \dot{x}_5 \\ \dot{x}_6 \end{Bmatrix} = [A] \begin{Bmatrix} x_1 \\ x_2 \\ x_3 \\ x_4 \\ x_5 \\ x_6 \end{Bmatrix} + F(x) + E(x) \quad (5.19)$$

Where $[A]$ and $F(x)$ are identical to Equation (5.11), and $E(x)$ is

$$E(x) = \left\{ \begin{array}{l} \frac{1}{\int_0^L \rho A \phi_1^2(x) dx} E_1(q) |_{q_1=x_1, q_2=x_3, a=x_5} \\ \frac{1}{\int_0^L \rho A \phi_2^2(x) dx} E_2(q) |_{q_1=x_1, q_2=x_3, a=x_5} \\ \frac{1}{m_a} E_3(q) |_{q_1=x_1, q_2=x_3, a=x_5} \end{array} \right\}$$

The state equations of Equation (5.19) are solved using the 4th order Runge-Kutta numerical solver to construct a frequency response function in the procedure detailed at the beginning of the section. As with any analytical model, the response levels at resonance are theoretically infinite without the presence of any damping. Therefore, damping was added to each DOF of the SDOF NLMS-Beam system in the form of viscous damping.

5.2.2 Viscous Damping

In order to avoid infinite peaks at resonance, viscous damping was added to the system. The EOM of the SDOF NLMS-Beam system would become,

$$[M]\{\ddot{q}\} + [C]\{\dot{q}\} + [K]\{q\} + f(q) = E(q) \quad (5.20)$$

Where $[C]$ is the damping matrix.

The following damping matrix was chosen to avoid having inter-well oscillations with very small excitation amplitudes

$$[C] = \begin{bmatrix} 1000 & 0 & 0 \\ 0 & 1000 & 0 \\ 0 & 0 & 10 \end{bmatrix} \quad (5.21)$$

This damping matrix was incorporated into the numerical simulations used to determine the frequency response of the SDOF NLMS-system. For a set of SDOF NLMS parameters, the damping matrix and the linearized stiffness matrix can be used to determine linearized damping ratios for each mode. For example, Simulations 1, 2, and 3, described below, use beam parameters from Table 5.1 and Case 2 parameters from Table 5.2. With these SDOF NLMS-Beam parameters, the linearized damping ratios can be determined for each state. The linearized

damping ratios for state 1 and state 2 are summarized in Equations (5.22) and (5.23), respectively.

$$[\zeta_{eq1}] = \begin{bmatrix} 0.001291 & 0 & 0 \\ 0 & 0.000334 & 0 \\ 0 & 0 & 0.020989 \end{bmatrix} \quad (5.22)$$

$$[\zeta_{eq2}] = \begin{bmatrix} 0.002029 & 0 & 0 \\ 0 & 0.000334 & 0 \\ 0 & 0 & 0.021614 \end{bmatrix} \quad (5.23)$$

For both states, the first, second, and third linearized damping ratios correspond to the 1st beam mode (q_1), the 2nd beam mode (q_2), and the SDOF NLMS mode (m_a) respectively. These damping ratios are provided for reference, as the damping matrix in Equation (5.21) was incorporated into the state equations and run in the numerical simulations.

5.2.3 Results of Nonlinear Frequency Response Numerical Simulation

As described in the general procedure of obtaining the frequency response function, each simulation was run four times. Each set of parameters was simulated stepping up and stepping down in frequency with initial conditions that start the system in state 1. Then, the same stepped frequency sweeps were performed with initial conditions that start the system in state 2. Each Simulation specified in Tables 5.4, 5.5 and 5.6 produced nine plots. For each of the four stepped frequency sweeps, a phase portrait plotting velocity vs. displacement and a displacement time response plot were generated. These plots track the motion of the SDOF NLMS mass, m_a , described by the generalized coordinate, a , in order to observe any nonlinear behavior or switching that may occur. The steady state amplitude was sampled for each frequency step to produce a frequency response function. As four stepped sweeps were conducted, there are four frequency response curves in each frequency response plot.

The sequence of simulations was performed using the excitation amplitude as the main parameter to reveal the nonlinear response of the system and to evaluate the potential of this approach to avoid resonance. Simulations 1 to 3 use the parameters defined in Table 5.4 for the cantilever beam, Case 2 parameters from Table 5.2 for the SDOF NLMS system, and the damping matrix in Equation (5.21). All these simulations were performed from 4.5 rad/s to 9.0 rad/s, stepping up or down in 0.1 rad/s increments. Simulations 1, 2, and 3 were excited with

amplitudes of 0.0005, 0.0025, and 0.00275 m respectively. A summary of the excitation parameters is given in Table 5.4.

Table 5.4 Excitation Parameters Used in Numerical Simulation

Simulation	Minimum Excitation Frequency $\Omega_{min} \left[\frac{rad}{s} \right]$	Step Excitation Frequency $\Omega_{step} \left[\frac{rad}{s} \right]$	Maximum Excitation Frequency $\Omega_{max} \left[\frac{rad}{s} \right]$	Excitation Amplitude $b [m]$
1	4.5	0.1	9.0	0.0005
2	4.5	0.1	9.0	0.0025
3	4.5	0.1	9.0	0.00275

Figures 5.4 and 5.5 present the numerical results using the parameters of Simulation 1.

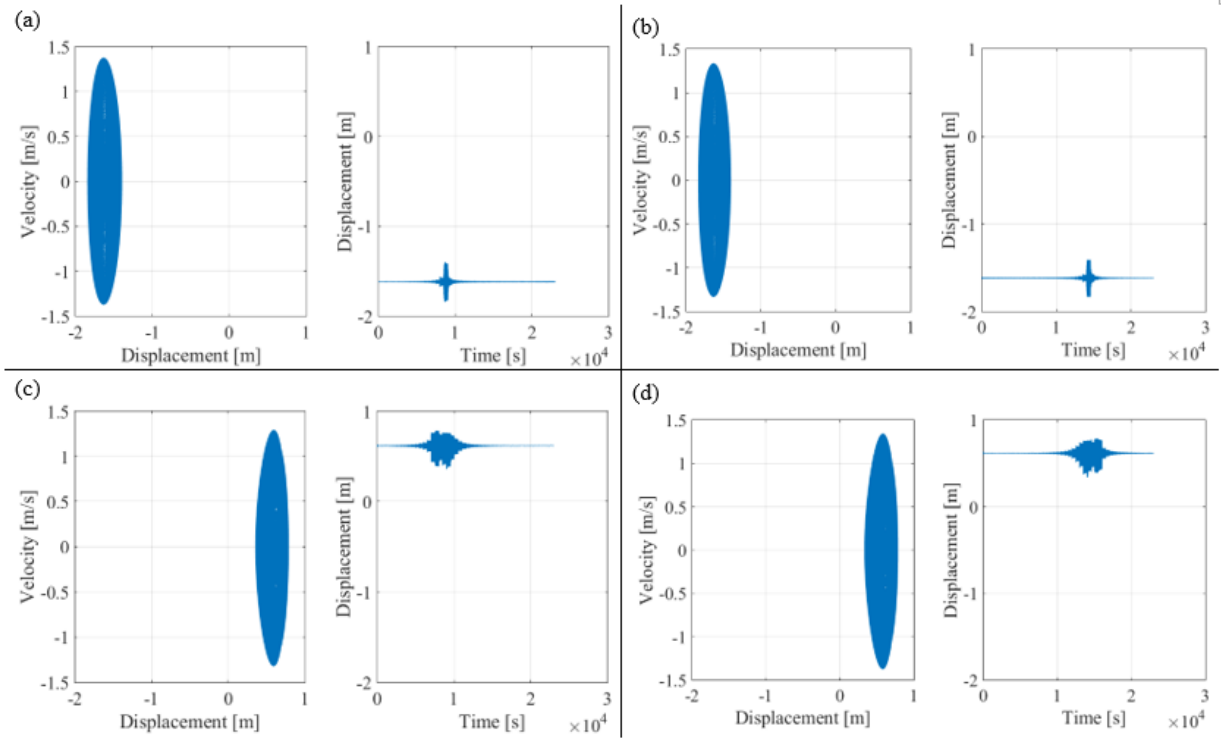


Figure 5.4 Phase Portrait (Left) and Time Response (Right) of Numerical Simulation 1 where (a) Begins in State 1 and Sweeps Up, (b) Begins in State 1 and Sweeps Down, (c) Begins in State 2 and Sweeps Up, (d) Begins in State 2 and Sweeps Down

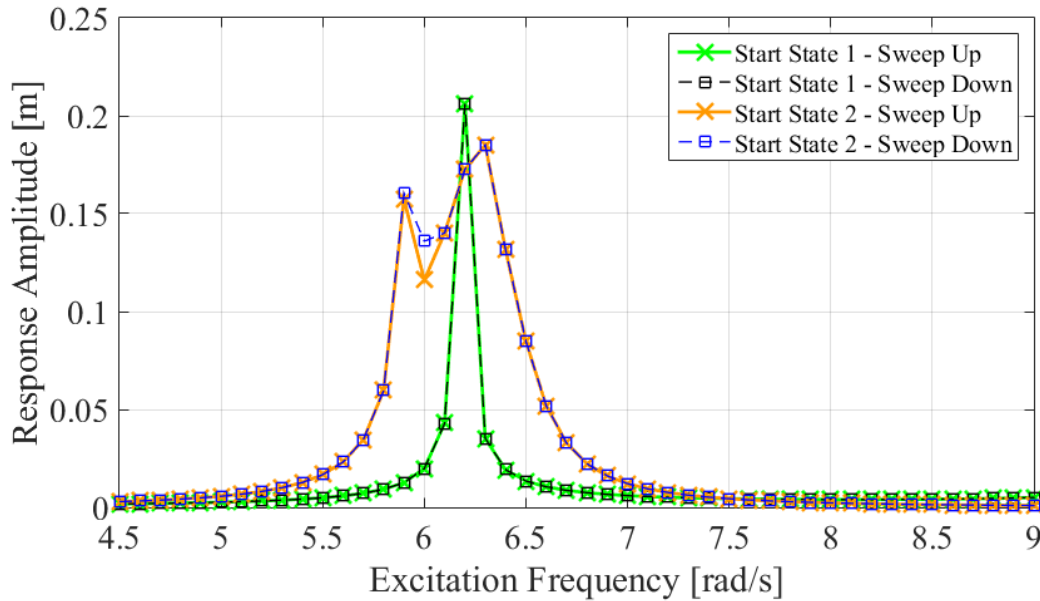


Figure 5.5 Frequency Response Function for Simulation 1, and Figure 5.4 Data

The excitation in Simulation 1 is small in amplitude, which allows the dynamics of each state to be observed with no switching and the least nonlinear behavior. Figure 5.4a show the phase portrait and displacement time response of the system starting in state 1 and stepping up in frequency. Figure 5.4b also shows the phase portrait and displacement time response of the system starting from state 1, but this run steps down in frequency. Figures 5.4c and 5.4d present the same frequency sweeps that 5.4a and 5.4b conducted, but the system is started in state 2 as opposed to state 1. The frequency response of these four stepped sweeps can be seen in Figure 5.5.

For each state of the SDOF NLMS-Beam system, the phase portraits and displacement time responses of Simulation 1 (Figure 5.4) corresponding to the sweep up and the sweep down in frequency are identical. This can be seen by comparing Figures 5.4a and 5.4b, as well as comparing Figures 5.4c and 5.4d. No snap-through was observed in Simulation 1 because the excitation amplitude does not provide sufficient energy to jump the unstable fixed point, the potential hilltop, at $a = x_5 = 0$. In addition, for this level of excitation, the obtained displacement time response (Figure 5.4) and frequency response plots (Figure 5.5) exhibit no hysteresis, implying a quasi-linear response. Two peaks are expected to appear for each state due to the coupling between the beam and the SDOF NLMS system: one for the 1st beam mode, q_1 ,

and one for the SDOF NLMS mode, m_a . The sweep up and sweep down in state 1 have linearized natural frequencies of 6.19 rad/s and 10.06 rad/s, corresponding to q_1 and m_a respectively. As the stepped sweeps were performed from 4.5 rad/s to 9 rad/s, the 10.06 rad/s peak is not seen. Since the focus of these sweeps is the impact on the linearized natural frequencies around the 1st beam mode, the SDOF NLMS peak does not need to be seen. The peak corresponding to the 1st beam mode, q_1 , can be observed at 6.2 rad/s in the frequency response. State 2, which was designed to match the linearized natural frequency of the 1st beam mode, has two peaks on either side of the original 1st beam mode. This was expected, as matching natural frequencies has this same result with vibration mass absorbers. As mentioned earlier, no switching was observed at this excitation amplitude. Therefore, the excitation was artificially increased to observe snap-through.

Figure 5.6 provides the phase portraits and displacement time responses of Simulation 2 for the sweep up and the sweep down for each state. These plots are also organized in the same structure as in Simulation 1 (Figure 5.4). Figure 5.7 presents the frequency response curves for each sweep of Simulation 2, as Figure 5.5 did for Simulation 1.

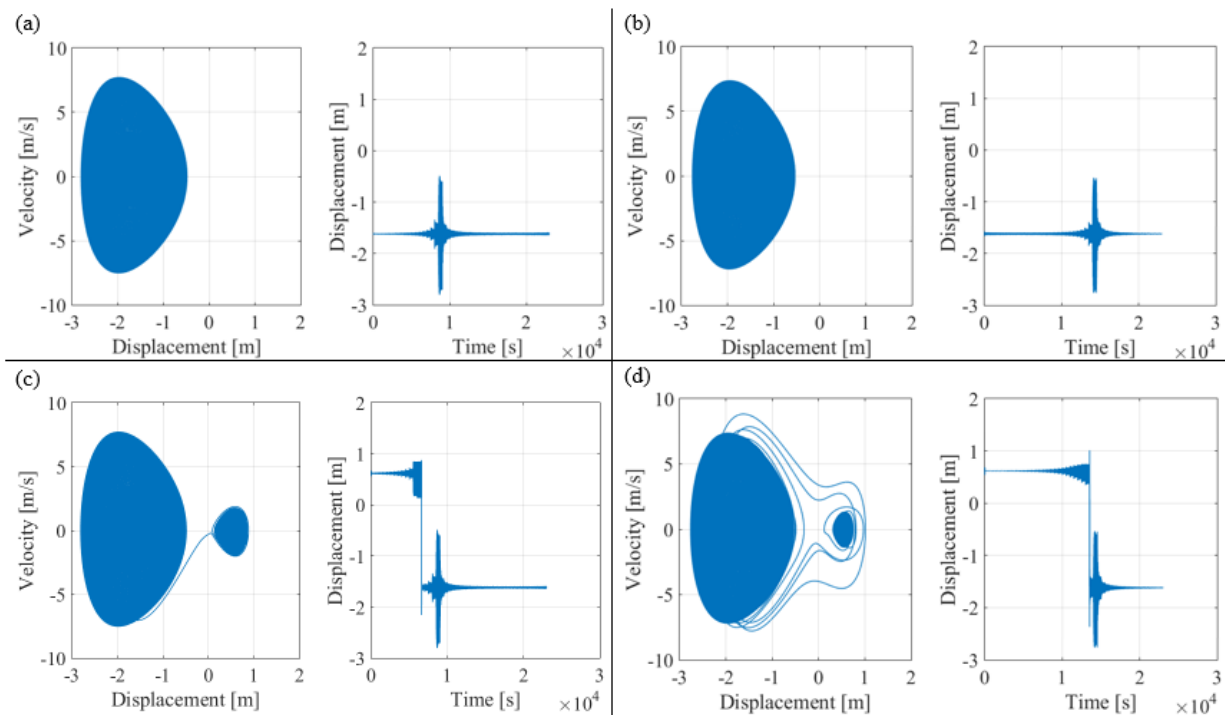


Figure 5.6 Phase Portrait (Left) and Time Response (Right) of Numerical Simulation 2 where (a) Begins in State 1 and Sweeps Up, (b) Begins in State 1 and Sweeps Down, (c) Begins in State 2 and Sweeps Up, (d) Begins in State 2 and Sweeps Down

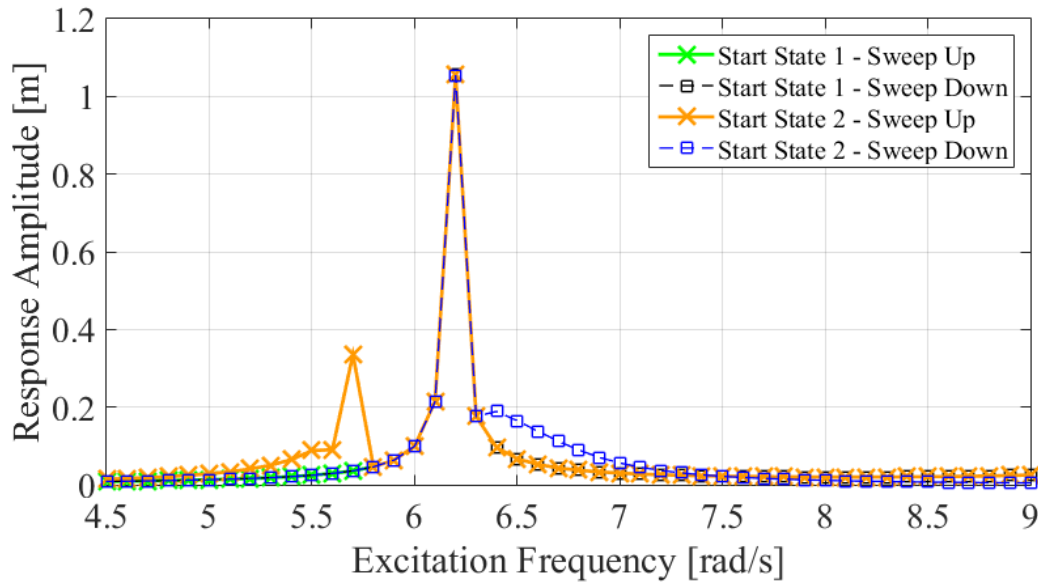


Figure 5.7 Frequency Response Function for Simulation 2 and Figure 5.6 Data

Simulation 2 uses the same simulation parameters as Simulation 1 with the exception of a larger excitation amplitude. This excitation amplitude causes switching between states, but only from the positive fixed point, state 2, to the negative fixed point, state 1. The displacement time responses shown in Figures 5.6a and 5.6b are similar to the time responses in Simulation 1 (Figures 5.4a and 5.4b). There still exists a single peak at 6.2 rad/s with no indication of nonlinear behavior. There is only a larger response amplitude that is due to the increasing excitation amplitude. However, when examining both phase portraits, the system can be observed oscillating closer to the potential boundary and the once elliptical shape is beginning to deform towards the unstable fixed point. As the system never crosses the potential boundary, no switching occurred for either the sweep up or the sweep down when starting from state 1. Recall, state 1 corresponds to the deep potential well, which requires more energy to jump the potential boundary than to jump from the shallow potential well. In fact, phase portraits in Figures 5.6c and 5.6d show the system switching from state 2 to state 1, or from the shallow potential well to the deep potential well. This snap-through is also observed in both displacement time responses in Figures 5.6c and 5.6d, where the system switches from oscillating around a positive displacement to a negative displacement. After this snap-through occurs, the displacement time response matches that of Figures 5.6a and 5.6b, the response of the system in state 1. The phase portrait in Figure 5.6c indicate that snap-through occurs only once

and no subsequent crossings of the unstable fixed point are observed. In Figure 5.6d, however, the phase portrait indicates that the system switches state multiple times before settling into state 1, the negative fixed point. These oscillations that oscillate around the basins of attraction that do not cross the potential boundary with zero velocity are referred to as inter-well oscillations.

In the frequency response function of Simulation 2 (Figure 5.7), the excitation amplitude in state 1 still has a peak at 6.2 rad/s. This same peak was observed in Simulation 1 (Figure 5.5), but the peak has a larger response amplitude in Simulation 2. In state 2, however, snap-through occurs on both the sweep up and sweep down where no snap-through was observed in state 2 during Simulation 1 (Figure 5.5). When sweeping up in state 2, snap-through switches the system from state 2 to state 1 at around 5.7 rad/s. After switching to state 1, the sweep up follows the frequency response curve seen when the sweep up began in state 1. A similar result is observed in the sweep down. When snap-through occurs at 6.3 rad/s, the system switches from state 2 to state 1 and proceeds along the curve that began sweeping down in state 1. With an excitation amplitude of 0.0025m, snap-through was observed from state 2 to state 1, but not from state 1 to state 2. This result was expected, as the shallow potential well requires less energy to jump the potential boundary than the deep potential well. Therefore, in order to observe snap-through from the deep well to the shallow well, or a jump from state 1 to state 2, the excitation amplitude was artificially increased again to 0.00275m for Simulation 3.

The excitation amplitude used in Simulation 3 causes switching to occur from either state, giving rise to the possibility of switching back to the original state after avoiding resonance. The results for Simulation 3 are summarized in Figures 5.8 and 5.9. Figures 5.8a through 5.8d present the phase portraits and displacement time response for each stepped frequency sweep. Figure 5.9 shows the frequency response function for each frequency sweep. Increasing the excitation amplitude to 0.00275m provided sufficient energy to cause snap-through to occur from state 1 to state 2. However, a large amount of inter-well oscillations are seen in every stepped sweep regardless of which state the system begins in. In the displacement time responses of Figures 5.8a and 5.8b, the snapping occurs at 6.2 rad/s, but the phase portraits indicate that these oscillations exist above either potential well. When the excitation frequency moves out of this peak, the system settles in the deep potential well, or the negative fixed point. While it is more likely that the system will settle in the deep potential well, these inter-well oscillations are chaotic, making the system unpredictable in practice.

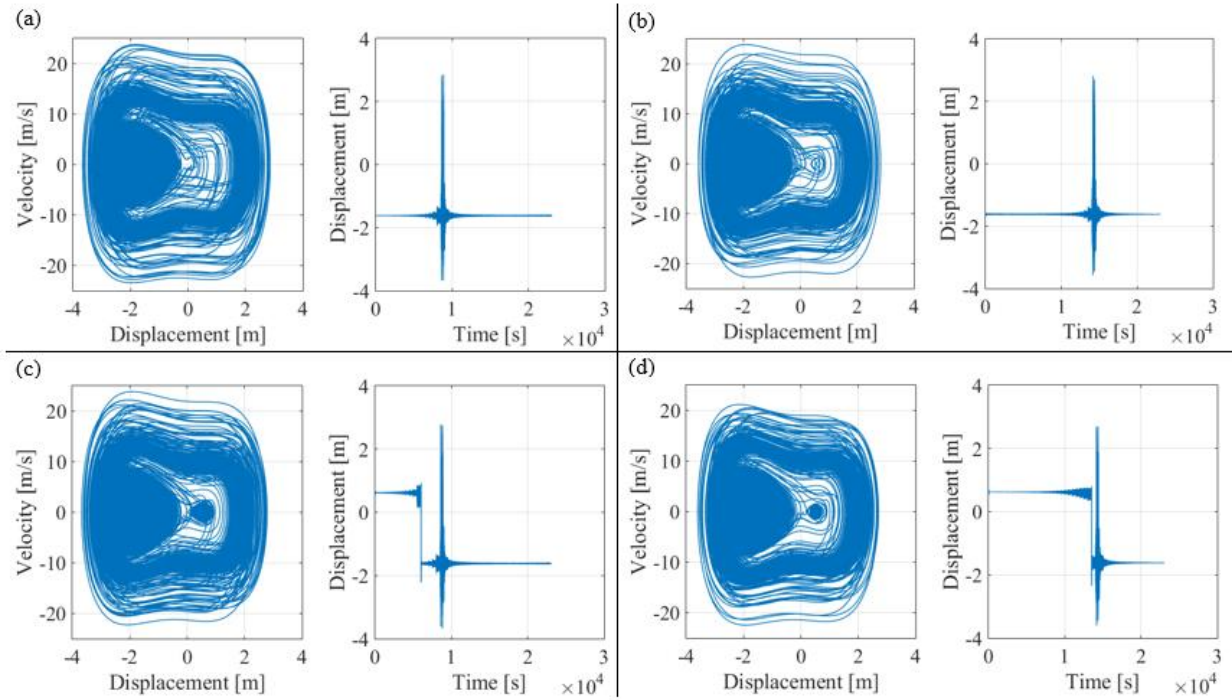


Figure 5.8 Phase Portrait (Left) and Time Response (Right) of Numerical Simulation 3 where (a) Begins in State 1 and Sweeps Up, (b) Begins in State 1 and Sweeps Down, (c) Begins in State 2 and Sweeps Up, (d) Begins in State 2 and Sweeps Down

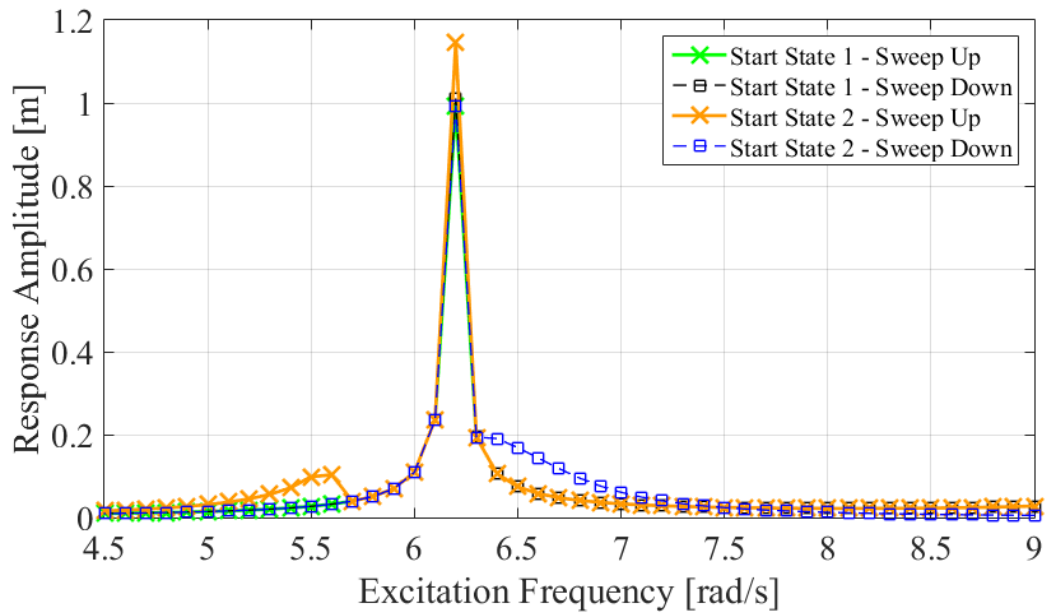


Figure 5.9 Frequency Response Function for Simulation 3 and Figure 5.8 Data

Figures 5.8c and 5.8d demonstrate that the system can still dependently snap-through from state 2 to state 1, but once the system sits in state 1, the large inter-well oscillations occur at the 6.2 rad/s peak. The frequency response function in Simulation 3 (Figure 5.9) is very similar to the response in Simulation 2 (Figure 5.7). The difference between Simulation 3 (Figure 5.9) and Simulation 2 (Figure 5.7) is that the snap-through from state 2 to state 1 occurs at 5.6 rad/s in the sweep up, earlier than with an excitation amplitude of 0.0025m. In addition, the peak at 6.2 rad/s has a larger response amplitude than the same peak in the frequency response of Simulation 2 (Figure 5.7) due to the increase in excitation amplitude.

With the increase in the excitation amplitude, there exists a particular amplitude for which switching will begin to occur. This amplitude indicates a bifurcation point that signals the switching from one well to another. This process is referred to in the nonlinear dynamics community as the point of escape from a potential well. In consequence, as the excitation is increased well beyond this bifurcation point, inter-well oscillations are more likely to occur. With excitation amplitudes of 0.0025m and 0.00275m, the switch from the shallow potential well to the deep well is dependable, but the switch from the deep well to the shallow well is difficult to control. Once the system has accumulated enough energy to jump to the shallow well, the system also has enough energy to immediately snap back to the deep well. The lack of control when switching from the deep well to the shallow well and the presence of inter-well oscillations means this configuration of the NLMS-Beam system is not satisfactory and will not be able to effectively avoid resonance.

In an effort to reduce the inter-well oscillations and to remain in the shallow potential well after switching from the deep well, the damping in the SDOF NLMS system was increased. The increase in damping of the SDOF NLMS system is reflected in the damping matrix,

$$[C] = \begin{bmatrix} 1000 & 0 & 0 \\ 0 & 1000 & 0 \\ 0 & 0 & 100 \end{bmatrix} \quad (5.24)$$

Two simulations, referred to as 4 and 5, were conducted using this increased damping with the parameters given in Table 5.5.

Table 5.5 Excitation Parameters used for Numerical Simulation with Additional Damping

Simulation	Minimum Excitation Frequency $\Omega_{min} \left[\frac{rad}{s} \right]$	Step Excitation Frequency $\Omega_{step} \left[\frac{rad}{s} \right]$	Maximum Excitation Frequency $\Omega_{max} \left[\frac{rad}{s} \right]$	Excitation Amplitude $b [m]$
4	4.5	0.1	9.0	0.005
5	0.5	0.25	15.0	0.005

Simulation 4 used the same Case 2 parameters from Table 5.2 for the SDOF NLMS system as with Simulations 1, 2, and 3. This provides a direct comparison between Simulation 1, 2, and 3 and Simulation 4 as to the impact of this additional damping on the overall dynamics of the system. Therefore, for Simulation 4, the increase in damping produces the linearized damping ratios shown in Equations (5.25) and (5.26) for state 1 and state 2, respectively.

$$[\zeta_{eq1}] = \begin{bmatrix} 0.001291 & 0 & 0 \\ 0 & 0.000334 & 0 \\ 0 & 0 & 0.209892 \end{bmatrix} \quad (5.25)$$

$$[\zeta_{eq2}] = \begin{bmatrix} 0.002029 & 0 & 0 \\ 0 & 0.000334 & 0 \\ 0 & 0 & 0.216138 \end{bmatrix} \quad (5.26)$$

Simulation 5 was conducted using the following parameters for the SDOF NLMS system: a linear stiffness of -380 N/m, a quadratic stiffness of 138.05 N/m², and a cubic stiffness of 380 N/m³. The linearized damping ratios for Simulation 5's parameters for state 1 and state 2 are described by Equations (5.27) and (5.28), respectively.

$$[\zeta_{eq1}] = \begin{bmatrix} 0.002085 & 0 & 0 \\ 0 & 0.000334 & 0 \\ 0 & 0 & 0.265773 \end{bmatrix} \quad (5.27)$$

$$[\zeta_{eq2}] = \begin{bmatrix} 0.002089 & 0 & 0 \\ 0 & 0.000334 & 0 \\ 0 & 0 & 0.317845 \end{bmatrix} \quad (5.28)$$

This set of parameters was greatly impacted by the increase in damping and provides another good example of how large amounts of damping skew the dynamics of the system. Figure 5.10 shows the phase portrait and displacement time response for the system starting in State 2 and stepping down in frequency. Figure 5.11 shows the same plots of the system starting in state 1 and sweeping up in frequency for the other set of SDOF NLMS parameters.

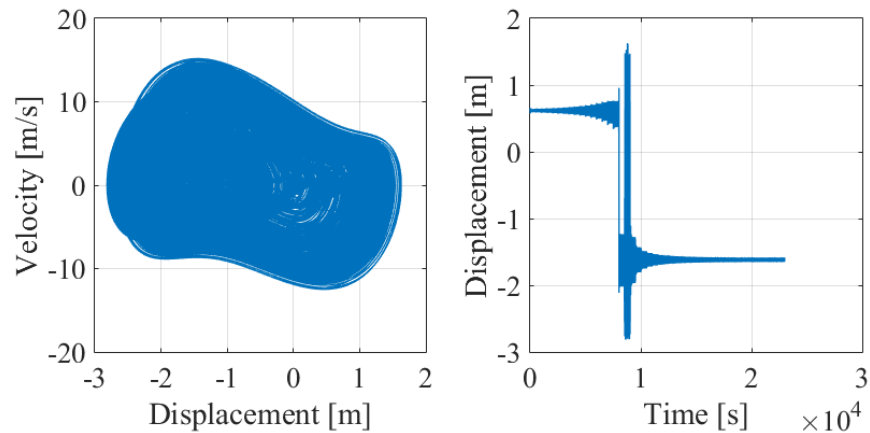


Figure 5.10 Phase Portrait (Left) and Time Response (Right) of Numerical Simulation 4 with too Much Damping

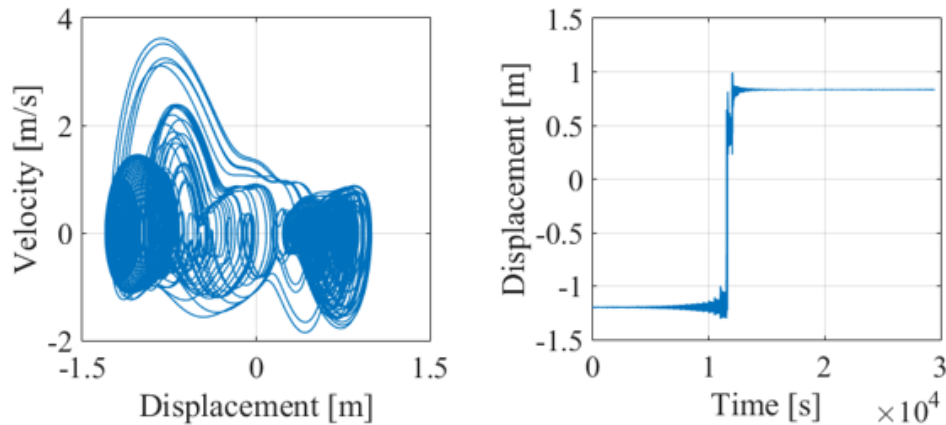


Figure 5.11 Phase Portrait (Left) and Time Response (Right) of Numerical Simulation 5 with too Much Damping

The displacement time response in Simulation 4 (Figure 5.10) is very similar to that in Simulation 3 (Figure 5.8c) despite the increase in damping on the SDOF NLMS system. The snap through occurs from state 2 and state 1, entering into inter-well oscillations exists at the

peak response frequency. Consequently, the system switches between states multiple times before still settling back in to the deep potential well. Thus, the damping did not improve the switch from state 1 to state 2. In addition, the phase portrait in Simulation 4 (Figure 5.10) is distorted from the phase portrait in Simulation 3 (Figure 5.8c) and does not accurately represent the true dynamics at play. This distortion is even more dramatic in the phase portrait of Simulation 5 (Figure 5.11). Any shape that the basins of attraction had has been lost. Switching from the deep potential well to the shallow well was observed in the displacement time response of Simulation 5 (Figure 5.11). While this switch did occur, the dynamics observed during snap-through are strange, oscillating around an unknown displacement before reaching the positive fixed point.

From Simulations 4 and 5, it is clear that an increase in the damping in the SDOF NLMS system is not the solution to control the switch from the deep potential well to the shallow well. The parameters used in Simulation 5, however, represent a system with less asymmetry in its potential function. Figure 5.12 illustrates the difference in asymmetry of the potential function.

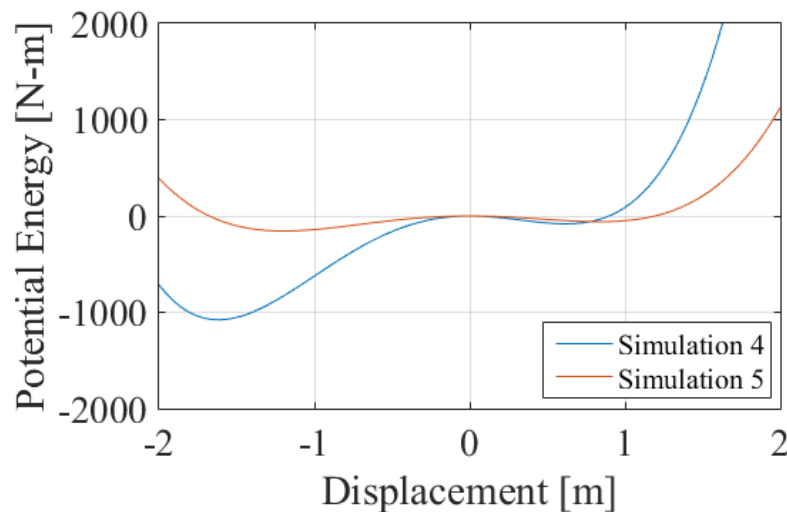


Figure 5.12 Potential Functions of Simulations 4 and 5

Reducing the asymmetry in the potential function of the NLMS system deepens the shallow potential well, require more energy to jump from this well to the other state. Making the shallow well deeper would hopefully make it easier to stay within it with the same amount of damping as Simulation 1, 2, and 3.

Simulations 6, 7, and 8, were conducted with Case 1 parameters in Table 5.2 for the SDOF NLMS system. This system has less asymmetry in its potential function than the Case 2 parameters used in Simulations 1, 2, and 3, which can be graphically seen in Figure 5.13.

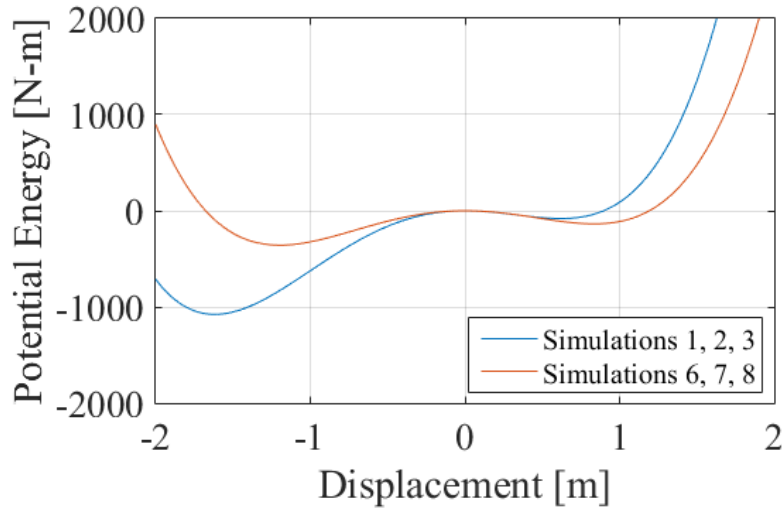


Figure 5.13 Potential Functions for Simulations 1, 2, and 3 and Simulations 6, 7, and 8

This could allow the switch from the deep potential well to the shallow potential well without increasing the damping on the SDOF NLMS system. Therefore, the damping matrix was reverted to that of Equation (5.22) and the linearized damping ratios for state 1 and state 2 of the SDOF NLMS-Beam system are shown in Equations (5.29) and (5.30), respectively.

$$[\zeta_{eq1}] = \begin{bmatrix} 0.001738 & 0 & 0 \\ 0 & 0.000334 & 0 \\ 0 & 0 & 0.021056 \end{bmatrix} \quad (5.29)$$

$$[\zeta_{eq2}] = \begin{bmatrix} 0.002029 & 0 & 0 \\ 0 & 0.000334 & 0 \\ 0 & 0 & 0.021611 \end{bmatrix} \quad (5.30)$$

The excitation parameters for Simulations 6, 7 and 8 are detailed in Table 5.6.

Table 5.6 Excitation Parameters used in Numerical Simulations

Simulation	Minimum Excitation Frequency $\Omega_{min} \left[\frac{rad}{s} \right]$	Step Excitation Frequency $\Omega_{step} \left[\frac{rad}{s} \right]$	Maximum Excitation Frequency $\Omega_{max} \left[\frac{rad}{s} \right]$	Excitation Amplitude $b [m]$
6	4.5	0.1	9.0	0.0005
7	4.5	0.1	9.0	0.00075
8	4.5	0.1	9.0	0.001

The excitation amplitudes progress similarly to those in Simulations 1, 2, and 3, gradually increasing from 0.0005 to 0.00075 and 0.001m for Simulations 6, 7, and 8 respectively. Simulation 6, like Simulation 1, has minimal excitation to observe approximately linear dynamics in each state. Simulation 7 provides a larger level of excitation, in which the bifurcation excitation amplitude has been exceeded, in order to induce snap-through from state 2 to state 1. Simulation 8 provides an even larger excitation amplitude to observe switching from any state and any inter-well oscillations that may occur.

The results of Simulation 6 are shown in Figures 5.14 and 5.15. Figures 5.14a and 5.14b provide the phase portrait and displacement time response of the system starting in state 1 for both the sweep up and the sweep down in frequency. Figure 5.14c and 5.14d also provide the phase portrait and displacement time response of the system, but starting in state 2 for both the sweep up and sweep down in frequency. Figure 5.15 describes the frequency response function for each frequency sweep. Similar to Simulation 1, the phase portraits for each sweep in Simulation 6 exhibit no nonlinear behavior and oscillate only around their fixed points. When starting in state 1 during Simulation 1 (Figures 5.14a and 5.14b), both the linearized natural frequencies can be seen for both the sweep up and sweep down in frequency. The same can be said for starting from state 2 in Simulation 1 (Figures 5.14c and 5.14d). None of the frequency sweeps contain any response levels that would cause snap-through. In the frequency response of Simulation 1 (Figure 5.13), all the peaks can be observed at the linearized natural frequencies detailed in Case 1 in Table 5.2. State 1 was not designed to match the linearized natural frequency of the 1st beam mode, thus leaving the 1st beam mode unchanged and the peak of the NLMS system exists between 7.4 and 7.5 rad/s. State 2 of Simulation 6, similar to state 2 of Simulation 1, splits the single peak into two new peaks around the original linearized natural frequency of the 1st beam mode.

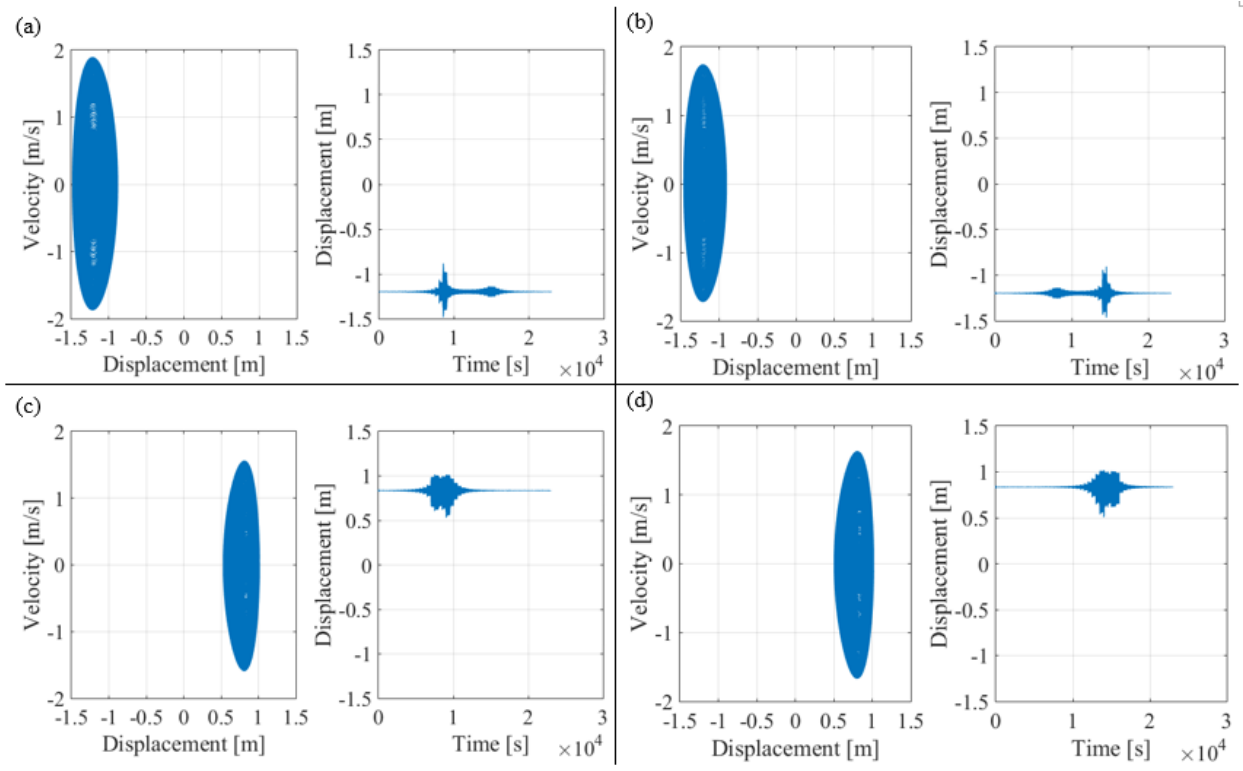


Figure 5.14 Phase Portrait (Left) and Time Response (Right) of Numerical Simulation 6 where (a) Begins in State 1 and Sweeps Up, (b) Begins in State 1 and Sweeps Down, (c) Begins in State 2 and Sweeps Up, (d) Begins in State 2 and Sweeps Down

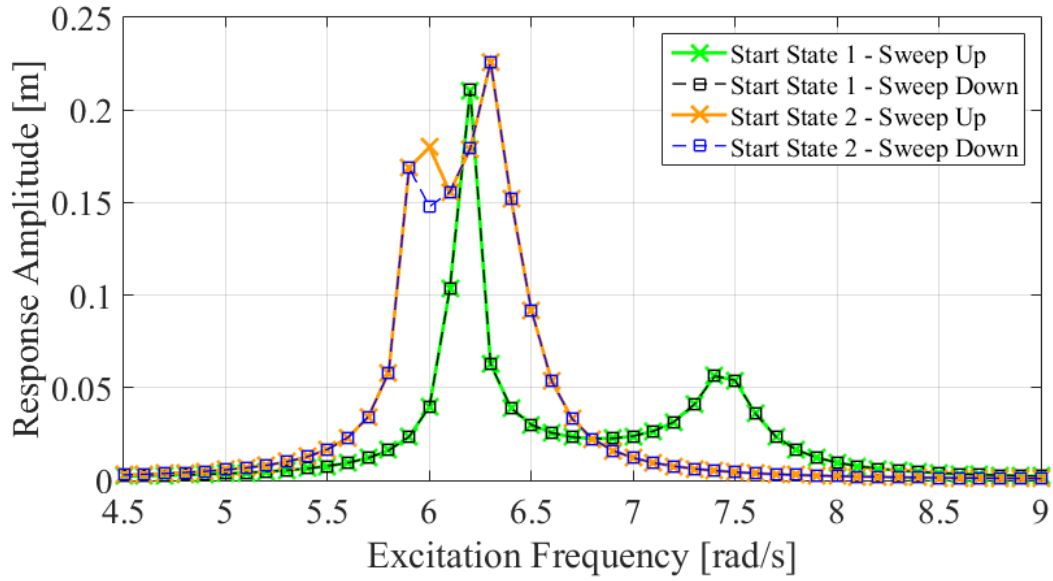


Figure 5.15 Frequency Response Function for Simulation 6 and Figure 5.12 Data

The phase portraits, displacement time response, and frequency response function of each sweep in Simulation 7 used an excitation amplitude of 0.00075m and can be seen in Figures 5.16 and 5.17. In Figure 5.16a, with the system starting in state 1 and stepping up in frequency, both the phase portrait and displacement time response show snap-through occurring with inter-well oscillations, and the displacement time response shows the system settling back into state 1. Figure 5.16b also shows inter-well oscillations are present for the sweep down in the phase portrait, however, the displacement time response shows the system settling in state 2, the shallow potential well. Starting in state 2 in Figure 5.16c, the system shows no snap-through in either the displacement time response or phase portrait when stepping up in frequency. In fact, this sweep looks nearly identical to the same sweep in Simulation 6. The step down in frequency in state 2, however, exhibits snap-through down to state 1 in the displacement time response, along with inter-well oscillations seen in the phase portrait of Figure 5.16d.

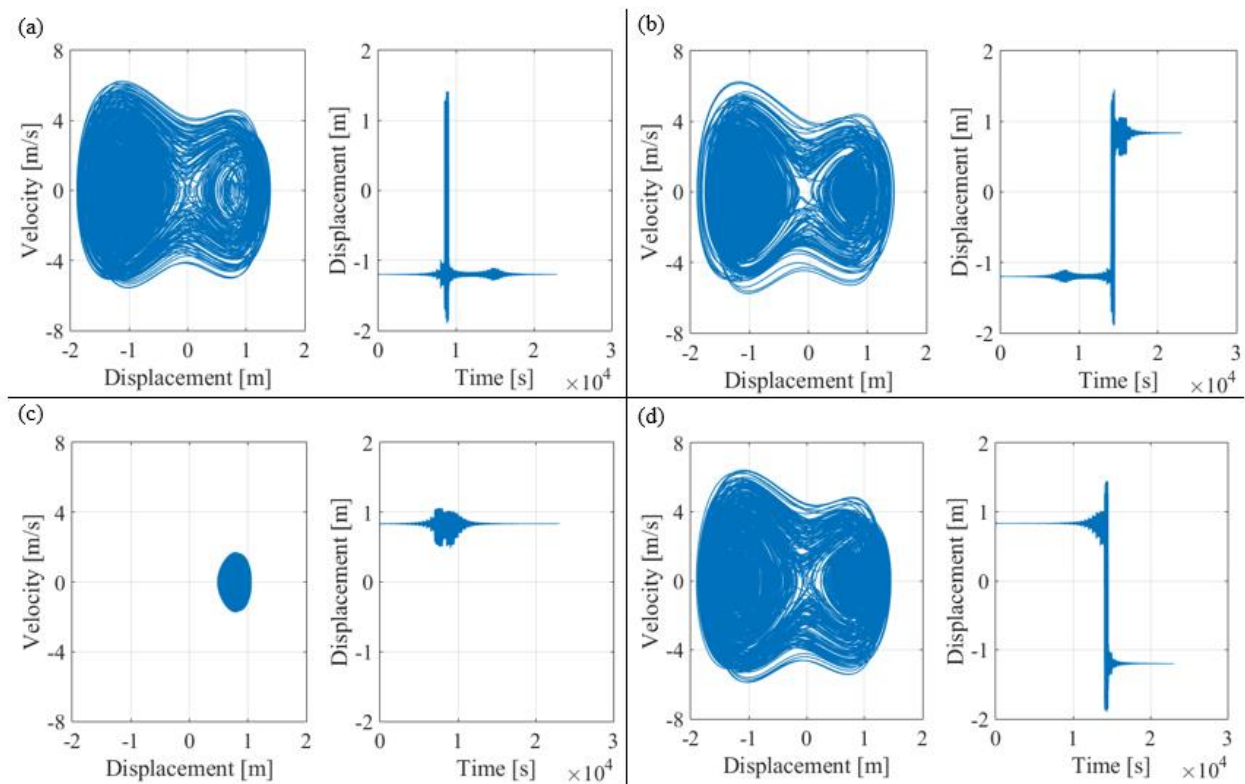


Figure 5.16 Phase Portrait (Left) and Time Response (Right) of Numerical Simulation 7 where (a) Begins in State 1 and Sweeps Up, (b) Begins in State 1 and Sweeps Down, (c) Begins in State 2 and Sweeps Up, (d) Begins in State 2 and Sweeps Down

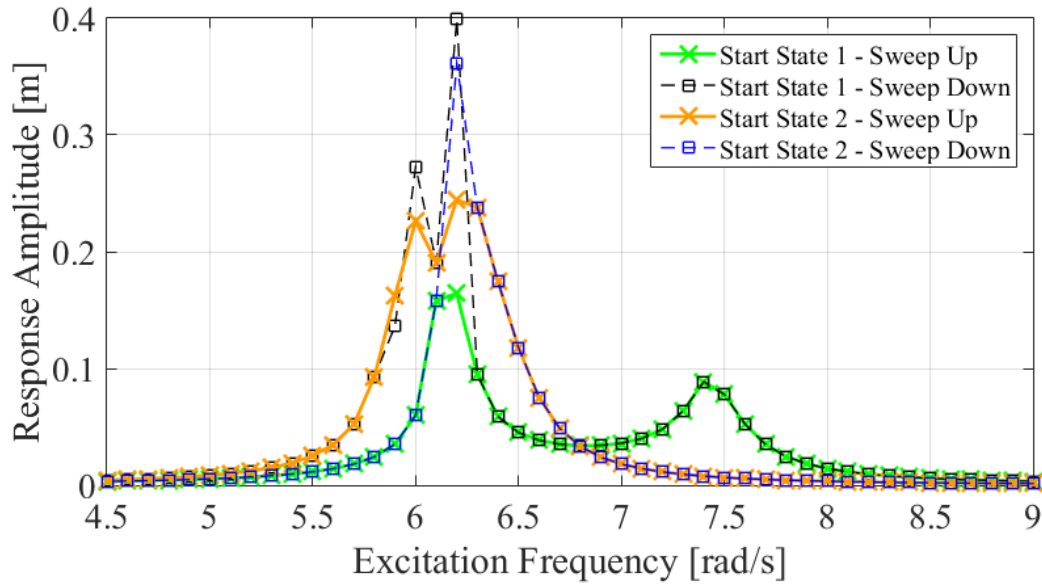


Figure 5.17 Frequency Response Function for Simulation 7 and Figure 5.14 Data

The frequency response function of Simulation 7 is captured in Figure 5.17. These frequency response curves display the snap to and from state 2 while sweeping up in state 1 (Figure 5.16a), the switch from state 1 to state 2 while sweeping down in frequency (Figure 5.16b), the lack of switching while sweeping up in state 2 (Figure 5.16c), and the switch from state 2 to state 1 during the sweep down that began in state 2 (Figure 5.16d). At this excitation level, the NLMS-Beam system does not dependently switch states but is shown to be capable of switching from the deep potential well to the shallow well.

Simulation 8 was conducted at an excitation amplitude of 0.001m to ensure switching will occur from state 2 to state 1 on the sweep up. Figures 5.18 and 5.19 capture the results of Simulation 8. Figure 5.18 provides the phase portraits and displacement time responses for each sweep and Figure 5.19 presents the frequency response function for each of the four sweeps. In Figure 5.18, snap-through does occur for all the frequency sweeps, but each sweep also contains inter-well oscillations. The displacement time response, sweeping up in state 1 (Figure 5.18a), still fails to settle into state 2 and contains even more inter-well oscillations than in the same displacement time response in Simulation 7 (Figure 5.16a). The displacement time response, sweeping down in state 1 (Figure 5.18b), which settled into state 2 on the sweep up in Simulation 7 (Figure 5.16b), now fails to stay in state 2 and immediately returns to state 1 at this excitation amplitude. In addition, snap-through now occurs in Simulation 8 while sweeping up in state 2 (Figure 5.18c)

where no switching was seen at the excitation amplitude used in Simulation 7 (Figure 5.16c). However, this switch fails to settle into state 1 and stays into state 2. The sweep down in state 2 for Simulation 8 (Figure 5.18d) also has larger inter-well oscillations than that same sweep in Simulation 7 (Figure 5.16d), but still successfully switches from state 2 to state 1. The frequency response function shed some light as to the reason for all the inter-well oscillations. The resonance at the 1st beam mode is overwhelming the NLMS system at the current excitation amplitude, making the system unpredictable and uncontrollable in switching to desired states. Regardless of this difficulty in control, the system is still stable as well as bistable.

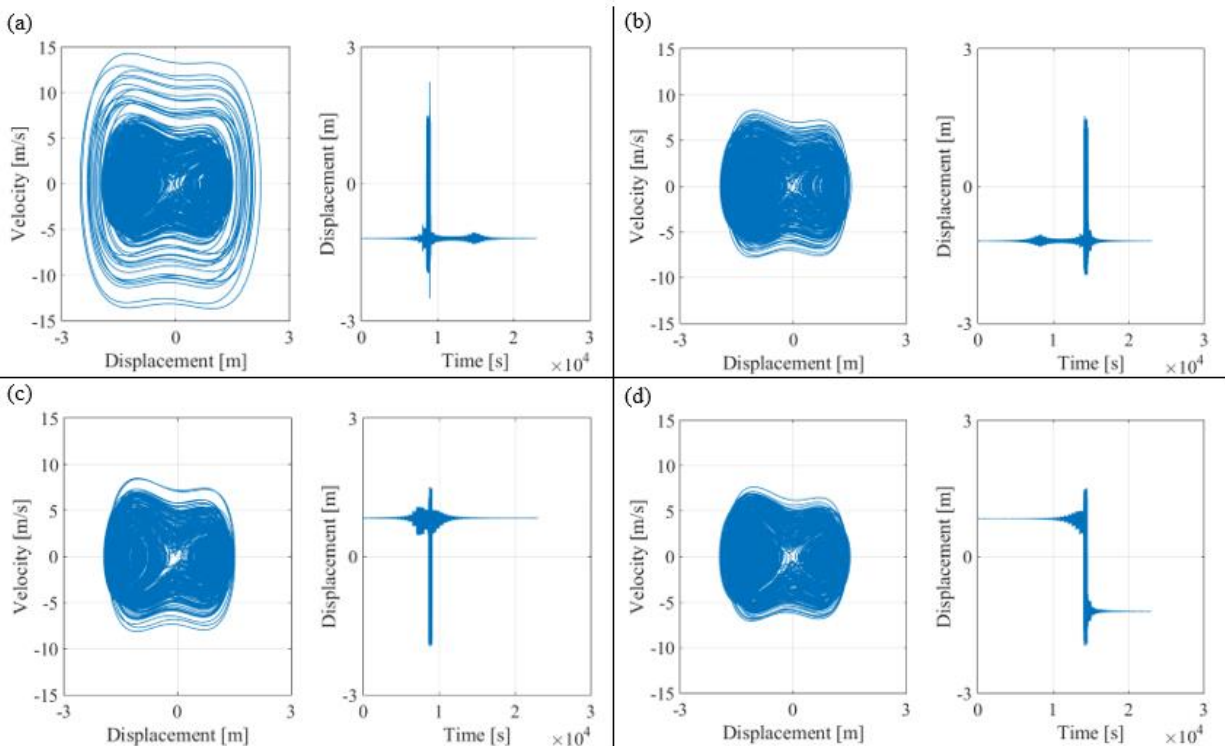


Figure 5.18 Phase Portrait (Left) and Time Response (Right) of Numerical Simulation 8 where (a) Begins in State 1 and Sweeps Up, (b) Begins in State 1 and Sweeps Down, (c) Begins in State 2 and Sweeps Up, (d) Begins in State 2 and Sweeps Down

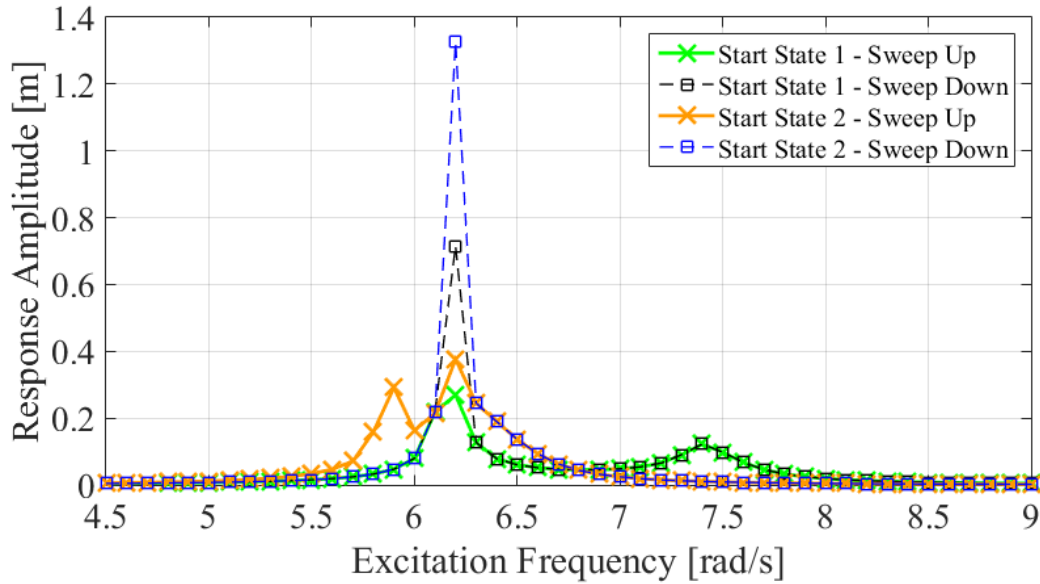


Figure 5.19 Frequency Response Function for Simulation 8 and Figure 5.16 Data

The problem with the SDOF NLMS is the extreme difficulty to snap from the deeper potential well to the shallow well stay there without a very large amount of damping. The studies conducted in this section indicate that increasing the damping may cause the structure to stay in the shallow potential well, but not without heavily impacting the transient dynamics. Furthermore, large damping would prevent the subsystem from switching until the overall structure is very near, if not in, resonance conditions, which is not optimal for a preventative, detuning approach. Beyond the difficulties in switching into the smaller potential well, the subsystem does not seem to be able to switch back to its original state after switching once. The reason this does not happen is the SDOF NLMS system only has one natural frequency in each state to excite. This means the system can only snap on one side of the targeted resonance, but not on the other side of the resonance. Therefore, the next structure this work considered was a coupled system with two masses, adding two DOF, and therefore, the possibility of being able to return the system to its original state after avoiding resonance.

6. COUPLED NONLINEAR MASS SPRING SYSTEM

With the SDOF NLMS-Beam system, Chapter 5 introduced the possibility of using multiple stable states that each have unique impact on the 1st mode of the cantilever beam to avoid resonance. However, the SDOF NLMS-Beam system had difficulties switching into the shallow potential well and could only switch states once during a frequency sweep. Chapter 6 replaces this nonlinear SDOF system with a coupled, nonlinear system with two DOF to add design flexibility and to additional natural frequency that could help produce a second snap-through during a frequency sweep. This chapter begins by introducing the model behind the Coupled NLMS system and the constraints required to ensure bistability. Then, numerical simulations were performed for the Coupled NLMS system without the beam to verify nonlinear behavior. After which, asymmetry was added into the potential functions of the nonlinear springs within the Coupled NLMS system to create different linearized natural frequencies for each state. Therefore, similar to the SDOF NLMS, each state of the Coupled NLMS system will have a unique impact on the 1st mode of the cantilever beam. Once the performance of the Coupled NLMS system was verified, it was attached to the end of the cantilever beam and numerical simulations were conducted to evaluate the effectiveness of the Coupled NLMS-Beam system at avoiding the 1st mode of the cantilever beam. Furthermore, the results were generalized to gain a better understanding of the entire systems' sensitivity to imperfection, modal discretization, and frequency content. The objective of this chapter is to evaluate the Coupled NLMS systems' capability to avoid resonance conditions around the 1st mode of the cantilever beam. The Coupled NLMS system presented in this chapter has two stable states with two different linearized natural frequencies in each state. Each state will have a unique impact on the overall system and switching between these states could effectively avoid the 1st mode of the cantilever beam.

6.1 Coupled Nonlinear Mass Spring Model

To more dependably snap from the deep potential well to the shallow potential well and switch back to the original state, the NLMS system was replaced with a coupled system with two DOF. This coupled system is an idealized mass-spring model of a bistable, composite plate used

for broadband energy harvesting [46]. The bistable plate has two length dimensions that offer design flexibility for multiple resonances. The coupled system achieves design flexibility with the addition of a second mass and second nonlinear spring. With two DOF and two nonlinear springs, each stable state will have two linearized natural frequencies. This system could also be designed to be bistable and used to avoid resonance.

6.1.1 Model

The idealized mass-spring model used here to capture the dynamics of the bistable plate from [46] can be seen in Figure 6.1. This model will be referred to as a Coupled NLMS system. The model consists of two masses, two linear springs, and two coupled nonlinear springs connected by a rigid massless rod.

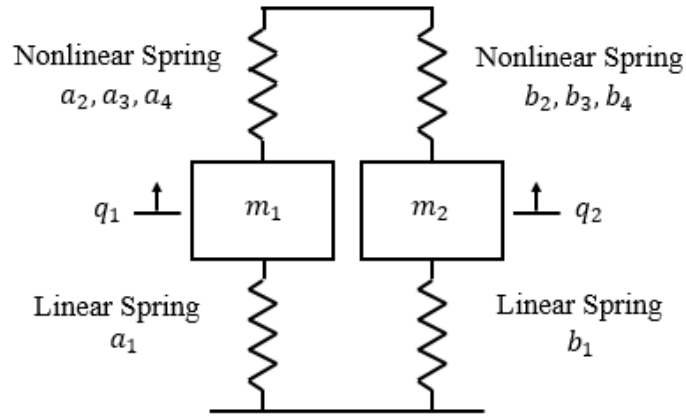


Figure 6.1 Coupled NLMS Model

The EOMs of the Coupled NLMS system are the following:

$$m_1 \ddot{q}_1 + \xi_1 \dot{q}_1 + A_1 q_1 + C q_1 q_2^2 + A_3 q_1^3 + A_4 q_1^2 = 0 \quad (6.1)$$

$$m_2 \ddot{q}_2 + \xi_2 \dot{q}_2 + B_1 q_2 + C q_1^2 q_2 + B_3 q_2^3 + B_4 q_2^2 = 0 \quad (6.2)$$

Dividing m_1 and m_2 into Equation (6.1) and Equation (6.2) respectively, the EOMs become the following

$$\ddot{q}_1 + \zeta_1 \dot{q}_1 + a_1 q_1 + a_2 q_1 q_2^2 + a_3 q_1^3 + a_4 q_1^2 = 0 \quad (6.3)$$

$$\ddot{q}_2 + \zeta_2 \dot{q}_2 + b_1 q_2 + b_2 q_1^2 q_2 + b_3 q_2^3 + b_4 q_2^2 = 0 \quad (6.4)$$

Where

$$\begin{aligned} \zeta_1 &= \frac{\xi_1}{m_1} & a_1 &= \frac{A_1}{m_1} & a_2 &= \frac{C}{m_1} & a_3 &= \frac{A_3}{m_1} & a_4 &= \frac{A_4}{m_1} \\ \zeta_2 &= \frac{\xi_2}{m_2} & b_1 &= \frac{B_1}{m_2} & b_2 &= \frac{C}{m_2} & b_3 &= \frac{B_3}{m_2} & b_4 &= \frac{B_4}{m_2} \end{aligned}$$

Similar to the NLMS system in Chapter 5, the EOMs can be written in first order form via a state space transform, from where the fixed points can be determined. Equation (6.5) summarizes the four state variables for this system.

$$\{\mathbf{x}\} = \begin{Bmatrix} x_1 \\ x_2 \\ x_3 \\ x_4 \end{Bmatrix} = \begin{Bmatrix} q_1 \\ \dot{q}_1 \\ q_2 \\ \dot{q}_2 \end{Bmatrix} \quad (6.5)$$

The state space form of the Coupled NLMS system is the following

$$\{\dot{\mathbf{x}}\} = \begin{Bmatrix} \dot{x}_1 \\ \dot{x}_2 \\ \dot{x}_3 \\ \dot{x}_4 \end{Bmatrix} = g(\mathbf{x}, t) = [A] \begin{Bmatrix} x_1 \\ x_2 \\ x_3 \\ x_4 \end{Bmatrix} + F(\mathbf{x}) \quad (6.6)$$

Where

$$[A] = \begin{bmatrix} 0 & 1 & 0 & 0 \\ -a_1 & -\zeta_1 & 0 & 0 \\ 0 & 0 & 0 & 1 \\ 0 & 0 & -b_1 & -\zeta_2 \end{bmatrix} \quad F(\mathbf{x}) = \begin{Bmatrix} 0 \\ -a_2 x_1 x_3^2 - a_3 x_1^3 - a_4 x_1^2 \\ 0 \\ -b_2 x_1^2 x_3 - b_3 x_3^3 - b_4 x_3^2 \end{Bmatrix}$$

The fixed points can be found by setting the right-hand side of Equation (6.6) equal to zero. Solving two coupled, third order equations symbolically results in a very long and complicated expression. Therefore, the exact expression will not be presented here, but the fixed points for a simpler example will be presented shortly. The Jacobian of the Coupled NLMS system can be derived using the same method detailed in both Chapter 4 and Chapter 5, as shown below.

$$G(x) = \begin{bmatrix} f_1(x_1, x_2, x_3, x_4) \\ f_2(x_1, x_2, x_3, x_4) \\ f_3(x_1, x_2, x_3, x_4) \\ f_4(x_1, x_2, x_3, x_4) \end{bmatrix} = [A] \begin{Bmatrix} x_1 \\ x_2 \\ x_3 \\ x_4 \end{Bmatrix} + F(x) \quad (6.7)$$

$$J|_{(x_1, x_2, x_3, x_4)} = \begin{bmatrix} \frac{\partial f_1}{\partial x_1} & \frac{\partial f_1}{\partial x_2} & \frac{\partial f_1}{\partial x_3} & \frac{\partial f_1}{\partial x_4} \\ \frac{\partial f_2}{\partial x_1} & \frac{\partial f_2}{\partial x_2} & \frac{\partial f_2}{\partial x_3} & \frac{\partial f_2}{\partial x_4} \\ \frac{\partial f_3}{\partial x_1} & \frac{\partial f_3}{\partial x_2} & \frac{\partial f_3}{\partial x_3} & \frac{\partial f_3}{\partial x_4} \\ \frac{\partial f_4}{\partial x_1} & \frac{\partial f_4}{\partial x_2} & \frac{\partial f_4}{\partial x_3} & \frac{\partial f_4}{\partial x_4} \end{bmatrix}$$

$$J|_{(x_1, x_2, x_3, x_4)} = \begin{bmatrix} 0 & 1 & 0 & 0 \\ -a_1 - a_2x_3^2 - 3a_3x_1^2 - 2a_4x_1 & -\zeta_1 & -2a_2x_1x_3 & 0 \\ 0 & 0 & 0 & 1 \\ -2b_2x_1x_3 & 0 & -b_1 - b_2x_1^2 - 3b_3x_3^2 - 2b_4x_3 & -\zeta_2 \end{bmatrix} \quad (6.8)$$

Finding the eigenvalues of the Jacobian evaluated at every fixed point will determine the stability of each fixed point. In order to design this system to be bistable, two stable fixed points must be present and separated by an unstable fixed point. With two nonlinear springs, the possibility for more than two stable states exist. Thus, specific constraint equations were introduced to ensure a bistable design.

6.1.2 Designing for Bistability

To illustrate these constraints clearly, a simplified form of Equations (6.3) and (6.4) will be used to derive the fixed points of the Coupled NLMS system. The following derivation will remove the quadratic nonlinearity, i.e., $a_4 = b_4 = 0$. Therefore, the EOMs of the Coupled NLMS become the following:

$$\ddot{q}_1 + \zeta_1 \dot{q}_1 + a_1 q_1 + a_2 q_1 q_2^2 + a_3 q_1^3 = 0 \quad (6.9)$$

$$\ddot{q}_2 + \zeta_2 \dot{q}_2 + b_1 q_2 + b_2 q_1^2 q_2 + b_3 q_2^3 = 0 \quad (6.10)$$

With the same state variables as Equation (6.5), the state-space equations of Equations (6.9) and (6.10) are

$$\{\dot{x}\} = \begin{Bmatrix} \dot{x}_1 \\ \dot{x}_2 \\ \dot{x}_3 \\ \dot{x}_4 \end{Bmatrix} = [A] \begin{Bmatrix} x_1 \\ x_2 \\ x_3 \\ x_4 \end{Bmatrix} + F(x) \quad (6.11)$$

Where

$$[A] = \begin{bmatrix} 0 & 1 & 0 & 0 \\ -a_1 & -\zeta_1 & 0 & 0 \\ 0 & 0 & 0 & 1 \\ 0 & 0 & -b_1 & -\zeta_2 \end{bmatrix} \quad F(x) = \begin{Bmatrix} 0 \\ -a_2 x_1 x_3^2 - a_3 x_1^3 \\ 0 \\ -b_2 x_1^2 x_3 - b_3 x_3^3 \end{Bmatrix}$$

The fixed points of the system can be determined by setting the right-hand side of Equation (6.11) equal to zero. For the Coupled NLMS system defined by Equations (6.9) and (6.10), there exist nine possible fixed points. For the system to be bistable, there must be three real fixed points.

$$x_{eq} = (x_1, x_2, x_3, x_4) \left[m, \frac{m}{s}, m, \frac{m}{s} \right]$$

$$x_{eq} = (0, 0, 0, 0)$$

$$x_{eq} = \left(-\frac{i\sqrt{a_1}}{\sqrt{a_3}}, 0, 0, 0 \right)$$

$$x_{eq} = \left(0, 0, -\frac{i\sqrt{b_1}}{\sqrt{b_3}}, 0 \right)$$

$$x_{eq} = \left(+\frac{i\sqrt{a_1}}{\sqrt{a_3}}, 0, 0, 0 \right)$$

$$x_{eq} = \left(0, 0, +\frac{i\sqrt{b_1}}{\sqrt{b_3}}, 0 \right)$$

$$x_{eq} = \left(-\frac{\sqrt{-a_2 b_1 + a_1 b_3}}{\sqrt{a_2 b_2 - a_3 b_3}}, 0, -\frac{\sqrt{-a_3 b_1 - a_1 b_2}}{\sqrt{a_2 b_2 - a_3 b_3}}, 0 \right)$$

$$x_{eq} = \left(-\frac{\sqrt{-a_2 b_1 + a_1 b_3}}{\sqrt{a_2 b_2 - a_3 b_3}}, 0, +\frac{\sqrt{-a_3 b_1 - a_1 b_2}}{\sqrt{a_2 b_2 - a_3 b_3}}, 0 \right)$$

$$x_{eq} = \left(+\frac{\sqrt{-a_2 b_1 + a_1 b_3}}{\sqrt{a_2 b_2 - a_3 b_3}}, 0, +\frac{\sqrt{-a_3 b_1 - a_1 b_2}}{\sqrt{a_2 b_2 - a_3 b_3}}, 0 \right)$$

$$x_{eq} = \left(+\frac{\sqrt{-a_2 b_1 + a_1 b_3}}{\sqrt{a_2 b_2 - a_3 b_3}}, 0, -\frac{\sqrt{-a_3 b_1 - a_1 b_2}}{\sqrt{a_2 b_2 - a_3 b_3}}, 0 \right)$$

The first constraint is defined by Equation (6.12).

$$a_2 b_2 = a_3 b_3 \quad (6.12)$$

This places the last four fixed points at positive and negative infinity, effectively removing those points from the physical focus of this system. This reduces the number of possible fixed points to five, four of which will not exist if they remain imaginary. To reduce from five fixed points down to three, one of the linear stiffness terms, i.e., a_1 or b_1 , must be negative. This will cause two of the four complex fixed points to become real-valued, and therefore exist in the physical system. Keeping the other linear stiffness term positive ensures this system will have only three fixed points. Therefore, if Equation (6.12) is held and $b_1 < 0$, for example, the fixed point of the system will be the following points.

$$x_{eq} = (0, 0, 0, 0) \quad (6.13)$$

$$x_{eq} = \left(0, 0, -\frac{i\sqrt{b_1}}{\sqrt{b_3}}, 0 \right) \quad (6.14)$$

$$x_{eq} = \left(0, 0, \frac{i\sqrt{b_1}}{\sqrt{b_3}}, 0 \right) \quad (6.15)$$

The Jacobian of the simplified form of the Coupled NLMS system, defined by Equations (6.9) and (6.10) is the following

$$J|_{(x_1, x_2, x_3, x_4)} = \begin{bmatrix} 0 & 1 & 0 & 0 \\ -a_1 - a_2 x_3^2 - 3a_3 x_1^2 & -\zeta_1 & -2a_2 x_1 x_3 & 0 \\ 0 & 0 & 0 & 1 \\ -2b_2 x_1 x_3 & 0 & -b_1 - b_2 x_1^2 - 3b_3 x_3^2 & -\zeta_2 \end{bmatrix} \quad (6.16)$$

It can be easily verified by finding the eigenvalues of the Jacobian that the positive and negative fixed points will be stable and the fixed point at $x_3=0$ will be unstable, indicating a bistable system. Similar to Chapter 5, the negative fixed point will be referred to as state 1 and the positive fixed point will be referred to as state 2.

Since one of the springs will have a positive linear stiffness and the other spring will have a negative stiffness, the structure possesses a monostable spring and a bistable spring. The nonlinear stiffnesses of both springs introduce hysteresis into the frequency response function of

the structure in the form of coexisting solutions. The coexisting solutions consist of a high-energy branch and a low-energy branch where the sweep up and sweep down exist on different branches for a given range of excitation frequencies. This provides the potential to shape the frequency response to encourage jumps between high and low energy branches. Ideally, a frequency response similar to that of Figure 6.2 is desired to induce snap-through between states. The desired frequency response exhibits both softening and hardening characteristics to ensure two jumps between energy branches will occur during a frequency sweep. With a hardening spring, the sweep up follows the high-energy branch until it jumps down to the low-energy branch, whereas the sweep down follows the low-energy branch until it jumps up to the high energy branch.

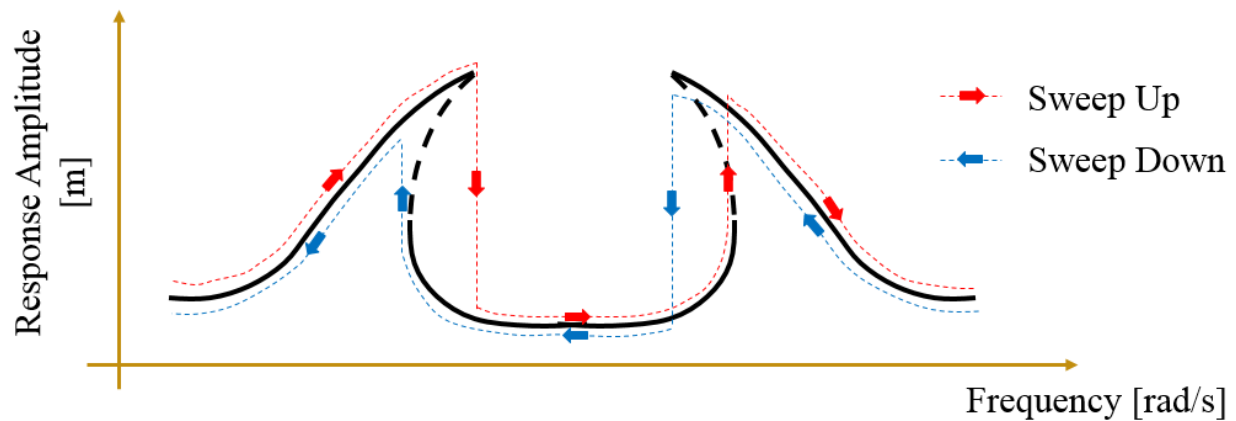


Figure 6.2 Desired Frequency Response

With a softening spring, the sweep up sits on the low-energy branch before jumping to the high-energy branch and the sweep down stays on the high-energy branch before finally jumping down to the low-energy branch. The desired frequency response will use a high-energy branch to induce the first snap-through, avoiding resonance, and a jump from a low-energy branch to a high-energy branch for a second snap-through back to the system's original state. Designing the hardening response to exist at a lower frequency than the softening response will produce this jump scheme for both the sweep up and sweep down in frequency.

Ignoring the coupling between the two masses, the monostable spring closely resembles a Duffing oscillator with a positive linear stiffness, in which the spring can exhibit a hardening behavior. On the other hand, the bistable spring closely resembles a Duffing oscillator with a

negative linear stiffness, which can only exhibit a softening behavior as solutions to the hardening case tend to infinity [47]. As this structure has two DOF, there will be two linearized natural frequencies in each stable state, one for each spring. In addition, the cubic nonlinear coupling between the two DOF indicates that one spring will begin to exhibit the hardening or softening characteristics of the other spring. With these possibilities in mind, the softening, bistable spring must show a larger absolute value linear stiffness than the hardening, monostable spring to produce the desired frequency response shown in Figure 6.2.

6.1.3 Base Excitation within Coupled NLMS Model

To verify the desired hardening and softening performance within the Coupled NLMS system, harmonic base excitation was added to the base of this model. This excitation term only factors into the linear restoring force of each spring, as it only has inertial effects on the system's dynamics. The following equations account for the harmonic excitation in the following EOMs, where b is the excitation amplitude and Ω is the excitation frequency.

$$\ddot{q}_1 + \zeta_1 \dot{q}_1 + a_1(q_1 - b \cos \Omega t) + a_2 q_1 q_2^2 + a_3 q_1^3 = 0 \quad (6.17)$$

$$\ddot{q}_2 + \zeta_2 \dot{q}_2 + b_1(q_2 - b \cos \Omega t) + b_2 q_1^2 q_2 + b_3 q_2^3 = 0 \quad (6.18)$$

With the addition of base excitation, the state equations of the Coupled NLMS system in Equation (6.11) become the following expression

$$\{\dot{x}\} = \begin{Bmatrix} \dot{x}_1 \\ \dot{x}_2 \\ \dot{x}_3 \\ \dot{x}_4 \end{Bmatrix} = [A] \begin{Bmatrix} x_1 \\ x_2 \\ x_3 \\ x_4 \end{Bmatrix} + F(x) + E(x) \quad (6.19)$$

Where

$$[A] = \begin{bmatrix} 0 & 1 & 0 & 0 \\ -a_1 & -\zeta_1 & 0 & 0 \\ 0 & 0 & 0 & 1 \\ 0 & 0 & -b_1 & -\zeta_2 \end{bmatrix} \quad F(x) = \begin{Bmatrix} 0 \\ -a_2 x_1 x_3^2 - a_3 x_1^3 \\ 0 \\ -b_2 x_1^2 x_3 - b_3 x_3^3 \end{Bmatrix} \quad E(x) = \begin{Bmatrix} 0 \\ a_1 b \cos \Omega t \\ 0 \\ b_1 b \cos \Omega t \end{Bmatrix}$$

Generating a frequency response would verify the presence of nonlinear hysteresis and switching of the bistable spring. Tables 6.1 and 6.2 summarize the mechanical parameters of the coupled system used for this verification.

Table 6.1 Mechanical Parameters for Coupled NLMS Model – Equation 6.9

$\zeta_1 \left[\frac{N \cdot s}{kg \cdot m} \right]$	$a_1 \left[\frac{N}{kg \cdot m} \right]$	$a_2 \left[\frac{N}{kg \cdot m^3} \right]$	$a_3 \left[\frac{N}{kg \cdot m^3} \right]$
0.05	100	10	100

Table 6.2 Mechanical Parameters for Coupled NLMS Model – Equation 6.10

$\zeta_2 \left[\frac{N \cdot s}{kg \cdot m} \right]$	$b_1 \left[\frac{N}{kg \cdot m} \right]$	$b_2 \left[\frac{N}{kg \cdot m^3} \right]$	$b_3 \left[\frac{N}{kg \cdot m^3} \right]$
0.05	-200	100	10

Two numerical simulations of Equation (6.19) with an excitation amplitude of 0.01 meters and excitation frequencies ranging from 15 rad/s to 22 rad/s by steps of 0.1 rad/s were conducted to verify the performance of the Coupled NLMS system. Unlike Chapter 5, each simulation was solved numerically with the 4th order Runge-Kutta method twice for a given state: once stepping up in frequency and once stepping down frequency. The first simulation began from the state 1 and the second simulation began from state 2. To verify the performance described in Section 6.1.2, both the displacement of m_1 and m_2 were studied. Per the Coupled NLMS parameters summarized in Tables 6.1 and 6.2, the mass m_1 is attached to the monostable spring and mass m_2 is attached to the bistable spring. The frequency responses starting from state 1 and from state 2 can be seen in Figure 6.3 and Figure 6.5 respectively. In Figures 6.4 and 6.6, the phase portraits and displacement time responses for both m_1 and m_2 are provided for the system starting from state 1 and state 2.

The frequency response function of the Coupled NLMS system starting in state 1 for both sweeping directions (Figure 6.3) exhibits nonlinear hysteresis with coexisting solutions. The hysteresis regions can be seen by comparing the sweep up and down plots for each mass. Specifically, for mass m_1 , the sweep up and sweep down map out coexisting solutions evident of a hardening spring around resonance.

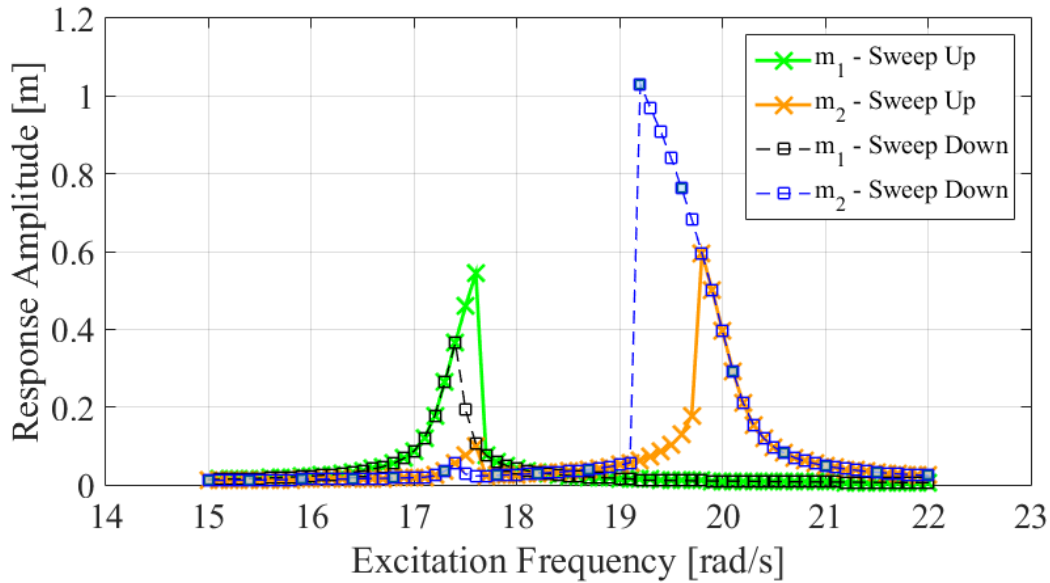


Figure 6.3 Frequency Response Curve of Base-Excited Coupled NLMS System with Mechanical Parameters Detailed in Table 6.1 and Table 6.2 – Starting with the Negative Fixed Point (State 1) for Both the Sweep Up and Sweep Down

For mass m_2 , the sweep up and sweep down represent a softening spring around resonance. In addition, hardening characteristics exist around the resonance of mass m_1 in the frequency response of mass m_2 due to the coupling between the two DOF in the EOM of the Coupled NLMS system. Since the coupling coefficient is much larger in Equation (6.18) than in Equation (6.17), the hardening characteristics are seen in mass m_2 and no softening characteristics are seen in mass m_1 .

The hardening and softening characteristics are also seen in the time displacement curves for each mass and each sweep. For mass m_1 , the displacement time response for the sweep up in frequency (Figure 6.4a) shows the sudden drop in oscillations indicative of the jump from the high-energy branch to the low-energy branch. The displacement time response for the sweep down (Figure 6.4b) also shows the increase in oscillation in the low-energy branch before jumping to the high-energy branch. For mass m_2 , the displacement time response for the sweep up (Figure 6.4c) shows the jump from high-energy to low energy branches first from the coupling of mass m_1 and then a jump from a low-energy branch to a high-energy branch. On the sweep down (Figure 6.4d), the displacement time response reverses this process, first jumping

from a high-energy branch to a low energy branch and then from a low-energy branch to a high-energy branch due to the coupling of mass m_1 .

The phase portraits of Figure 6.4 confirm the positions of the fixed points of the overall bistable system. Mass m_1 is attached to the monostable spring, whose fixed point is at zero displacement regardless of which stable state the Coupled NLMS system is in. The phase portrait of mass m_1 for both the sweep up (Figure 6.4a) and the sweep down (Figure 6.4b) in frequency show that the mass is purely oscillating around this equilibrium point. Mass m_2 is attached to the bistable spring. This simulation of the Coupled NLMS system begins in state 1, the negative fixed point, for all sweeps. For the sweep up (Figure 6.4c) and sweep down (Figure 6.4d) of mass m_2 , the mass is observed to oscillate around the negative fixed point. For the excitation amplitude provided in the simulation of state 1, no snap-through is observed in either the phase portraits nor the displacement time responses of mass m_2 (Figures 6.4c and 6.4d).

The second simulation began with the Coupled NLMS system in state 2 for both frequency sweeps. Figure 6.5 shows the frequency response functions for both mass m_1 and mass m_2 for both a sweep up and a sweep down in frequency. Figure 6.6 presents the phase portraits and the displacement time responses of each frequency sweep and each mass. Note how the frequency response function of the Coupled NLMS system that begins in state 2 (Figure 6.5) looks identical to that of the system when it begins in state 1 (Figure 6.3). This is because the system has a symmetric potential function.

Recall from Section 2.1.4, a symmetric potential function has the same linearized natural frequencies in either state. For the parameters used in this Coupled NLMS system, the quadratic nonlinearities were removed, which made the potential function symmetric. Thus, there is no difference in the linearized natural frequencies of mass m_1 or mass m_2 between state 1 and state 2, resulting in a frequency response function that is identical regardless of which state the system is in. As the excitation amplitude did not change from the simulation in state 1 (Figures 6.3 and 6.4), the jumps in the frequency response of state 2 (Figure 6.5) are strictly due to hysteresis and no snap-through occurs in any sweep.

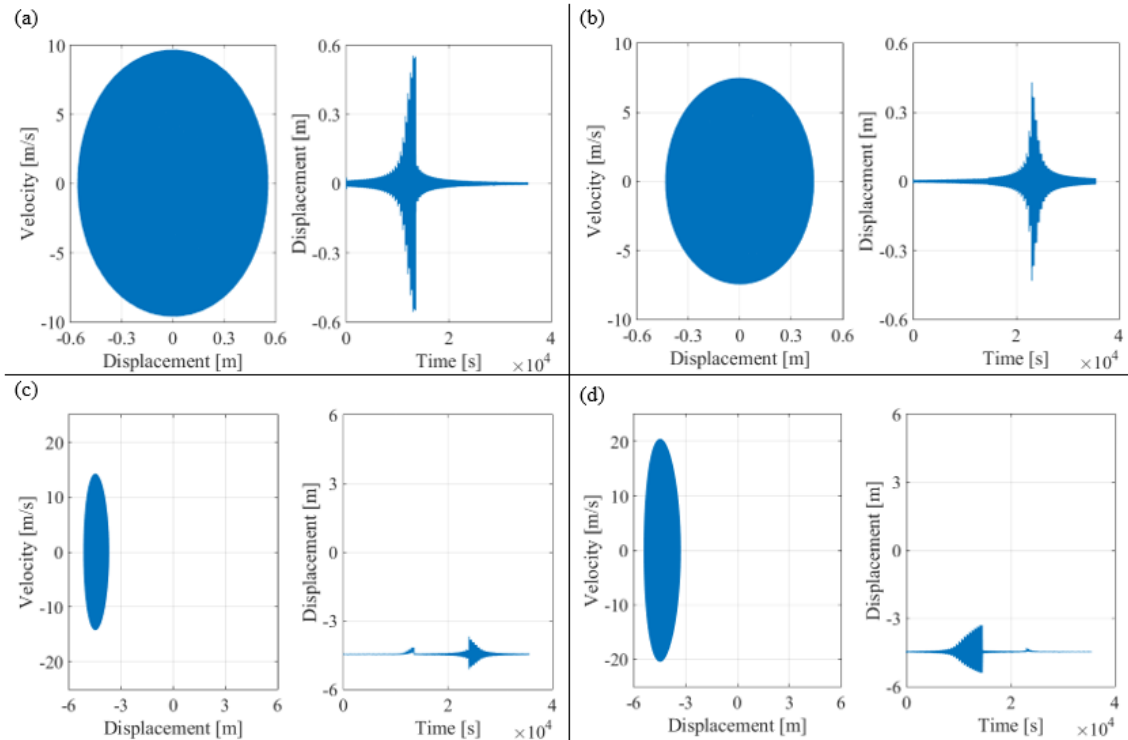


Figure 6.4 Phase Portrait and Displacement Time Response of (a) m_1 with a Monostable Spring during a Sweep Up from 15 to 22 rad/s (b) m_1 with Monostable Spring during a Sweep Down from 22 to 15 rad/s (c) m_2 with the Bistable Spring during a Sweep Up from 15 to 22 rad/s (d) m_2 with Bistable Spring during a Sweep Down from 15 to 22 rad/s – Starting with the Negative Fixed Point (State 1) for Both the Sweep Up and Sweep Down

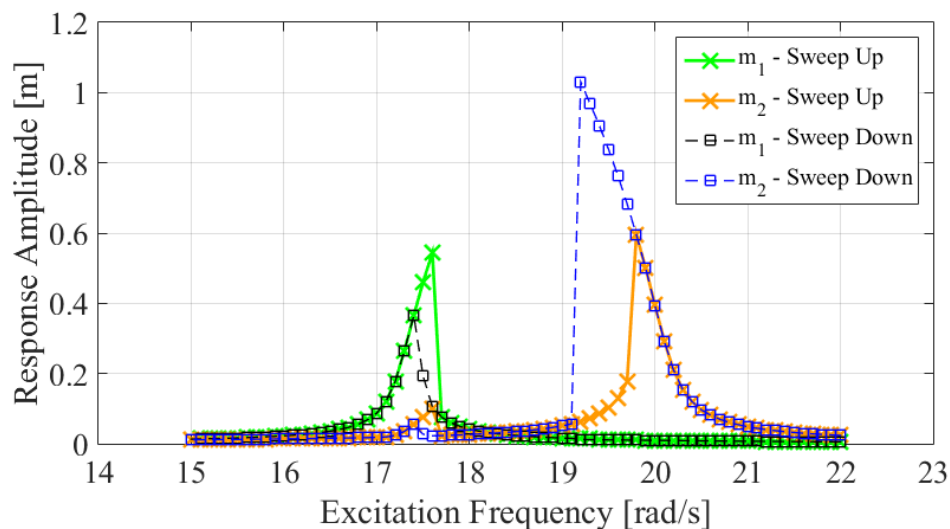


Figure 6.5 Frequency Response Curve of Base Excited Coupled NLMS System with Mechanical Parameters Detailed in Table 6.1 and Table 6.2 – Starting with the Positive Fixed Point (State 2) for Both the Sweep Up and Sweep Down

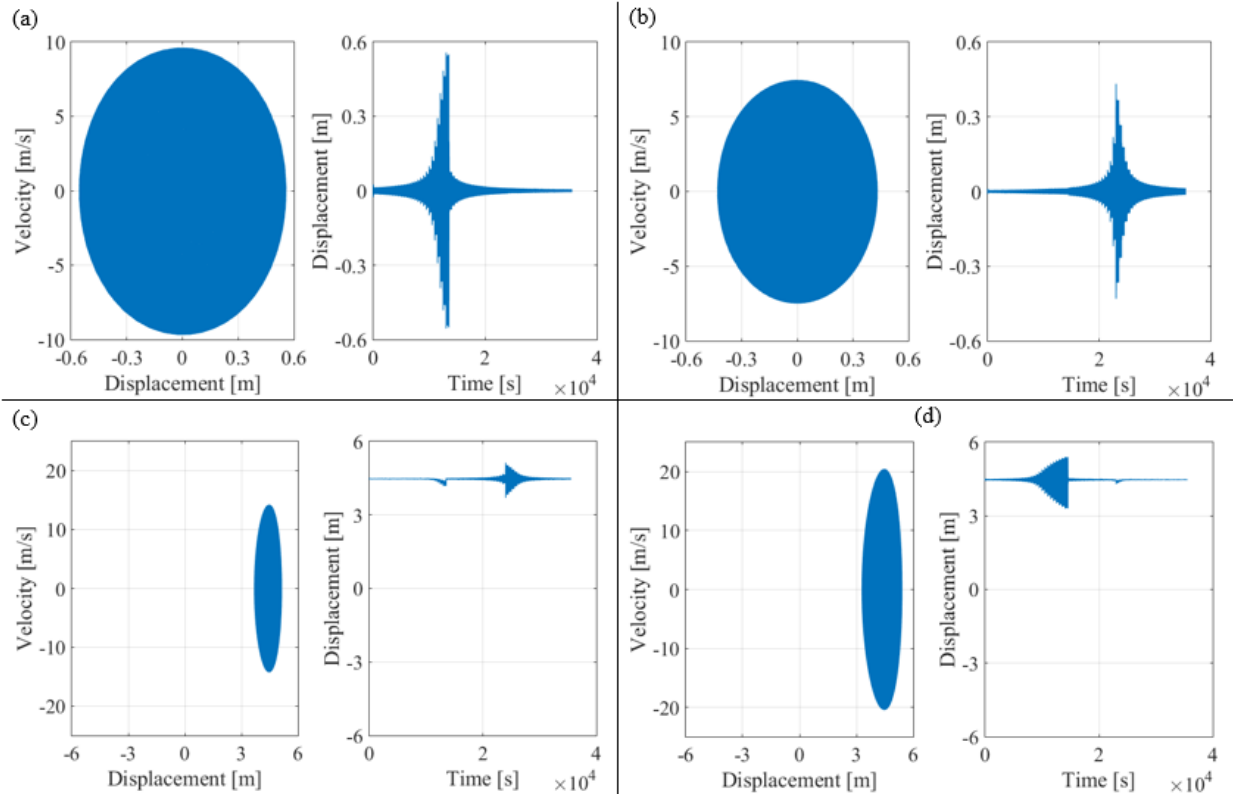


Figure 6.6 Phase Portrait and Displacement Time Response of (a) m_1 with a Monostable Spring during a Sweep Up from 15 to 22 rad/s (b) m_1 with Monostable Spring during a Sweep Down from 22 to 15 rad/s (c) m_2 with the Bistable Spring during a Sweep Up from 15 to 22 rad/s (d) m_2 with Bistable Spring during a Sweep Down from 15 to 22 rad/s – Starting with the Positive Fixed Point (State 2) for Both the Sweep Up and Sweep Down

The phase portrait and the displacement time responses for the sweep up and sweep down of mass m_1 in state 2 of the Coupled NLMS system (Figures 6.6a and 6.6b) are identical to those of state 1 of the Coupled NLMS system (Figures 6.4a and 6.4b) because the nonlinear spring attached to mass m_1 is monostable. Recall, the monostable spring has a single fixed point at zero displacement regardless of the state of the bistable spring. Thus, the phase portraits and displacement time responses of mass m_1 (Figures 6.6a and 6.6b) were expected to show the same jumps from one energy branch to another and the same oscillations around the single stable fixed point as in state 1 (Figures 6.4a and 6.4b). On the other hand, the bistable spring attached to mass m_2 has two stable fixed points. Therefore, when the Coupled NLMS system is excited in state 2, it is expected for mass m_2 to oscillate around state 2, the positive fixed point, instead of the negative fixed point. This behavior can be seen in both the phase portraits and the displacement time responses (Figures 6.6c and 6.6d). As mentioned with the frequency response

(Figure 6.5), the symmetry in this Coupled NLMS configuration means there is no difference in linearized natural frequency between state 1 and state 2, so the displacement time responses (Figure 6.6c and 6.6d) show the same jumps in energy branches for state 2 as in state 1 (Figures 6.4c and 6.4d). Note how the symmetry also reflects the displacement time response of state 1 about the unstable fixed point at zero displacement for state 2. In either state, the displacement response on the high-energy branch appears to drift towards the unstable fixed point before jumping down to the low-energy branch. In order to create a difference between state 1 and state 2, asymmetry in the form of both quadratic nonlinearities was brought back into the EOM for the Coupled NLMS system. In addition, the excitation amplitude was increased to ensure snap-through occurs in order to evaluate the possibility of avoiding resonance.

6.1.4 Addition of Asymmetry to Base Excited Model

Introducing a quadratic nonlinearity into the equations of motion alters the fixed points of the system. The stable fixed points are no longer symmetric about the unstable fixed point, creating stable states with their own unique linearized stiffnesses, and thus, their own unique linearized natural frequency values. Tables 6.3 and 6.4 detail the mechanical parameters used in Equations (6.3) and (6.4). Both the damping and the excitation amplitudes were increased to ensure snap-through was observed. In addition, the mechanical parameters of the Coupled NLMS system were adjusted to possess natural frequencies closer to that of the cantilevered beam. The coupling coefficients were adjusted to increase the influence of the hardening characteristics of the monostable spring on the bistable spring.

Table 6.3 Mechanical Parameters for Asymmetric Coupled NLMS Model – Equation 6.3

$\zeta_1 \left[\frac{N \cdot s}{kg \cdot m} \right]$	$a_1 \left[\frac{N}{kg \cdot m} \right]$	$a_2 \left[\frac{N}{kg \cdot m^3} \right]$	$a_3 \left[\frac{N}{kg \cdot m^3} \right]$	$a_4 \left[\frac{N}{kg \cdot m^2} \right]$
0.2	25	10	100	25

Table 6.4 Mechanical Parameters for Asymmetric Coupled NLMS Model – Equation 6.4

$\zeta_2 \left[\frac{N \cdot s}{kg \cdot m} \right]$	$b_1 \left[\frac{N}{kg \cdot m} \right]$	$b_2 \left[\frac{N}{kg \cdot m^3} \right]$	$b_3 \left[\frac{N}{kg \cdot m^3} \right]$	$b_4 \left[\frac{N}{kg \cdot m^2} \right]$
0.2	-50	250	25	25

As with the symmetric case in Section 6.1.3, two numerical simulations were performed: one for the Coupled NLMS system beginning in state 1 and one for the system beginning in state 2. For the asymmetric case, the two simulations were conducted with an excitation amplitude of 0.059 meters and excitation frequencies ranging from 3 rad/s to 14 rad/s by steps of 0.1 rad/s. In each state, a sweep up and a sweep down in frequency were performed. The dynamics of both masses m_1 and m_2 were studied. Figure 6.7 shows the phase portrait and displacement time response for the sweep up and down in frequency for mass m_1 and Figure 6.8 details the same for m_2 . As the frequency response of mass m_2 also exhibits hardening behavior due to the coupling to the monostable spring that is attached to mass m_1 , the frequency response of Figure 6.9 will only present the frequency response for mass m_2 .

The first simulation of the Coupled NLMS system begins in state 1. Studying the phase portraits of the sweep up (Figure 6.7a) and the sweep down (Figure 6.7b) of mass m_1 , it is clear the mass is still oscillating around the single fixed point. However, compared to the symmetric case (Figures 6.4a and 6.4b), the coupling to mass m_2 has slightly skewed the once elliptical shape towards the negative fixed point of the bistable spring. The displacement time responses for both the sweep up (Figure 6.7a) and the sweep down (Figure 6.7b) of mass m_1 exhibit rapid changes in response levels due to the snap-through of the bistable spring attached to mass m_2 . The snap-through in the bistable spring can be seen in the sweep up (Figure 6.8a) and sweep down (Figure 6.8b) of mass m_2 . During the sweep up (Figure 6.8a), snap-through is seen in the displacement time response, with the system switching from state 1 to state 2 at 8 rad/s. In the phase portrait (Figure 6.8b), there does appear to be one inter-well oscillation before the system settles into state 2.

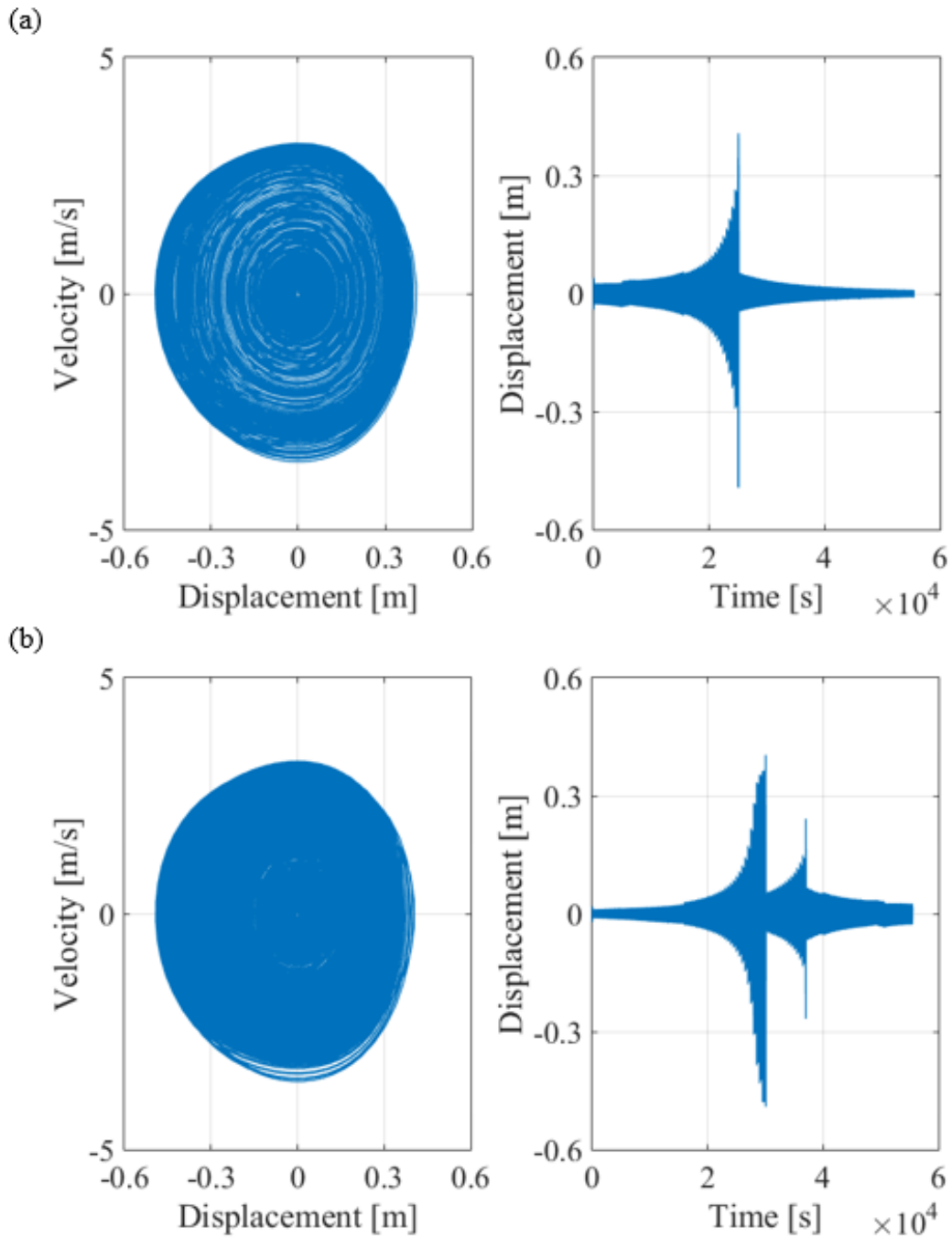


Figure 6.7 Phase Portrait and Displacement Time Response of m_1 , Starting from the Negative Fixed Point (State 1) of the Monostable Spring for (a) a Sweep Up from 3 to 14 rad/s and (b) a Sweep Down from 14 to 3 rad/s

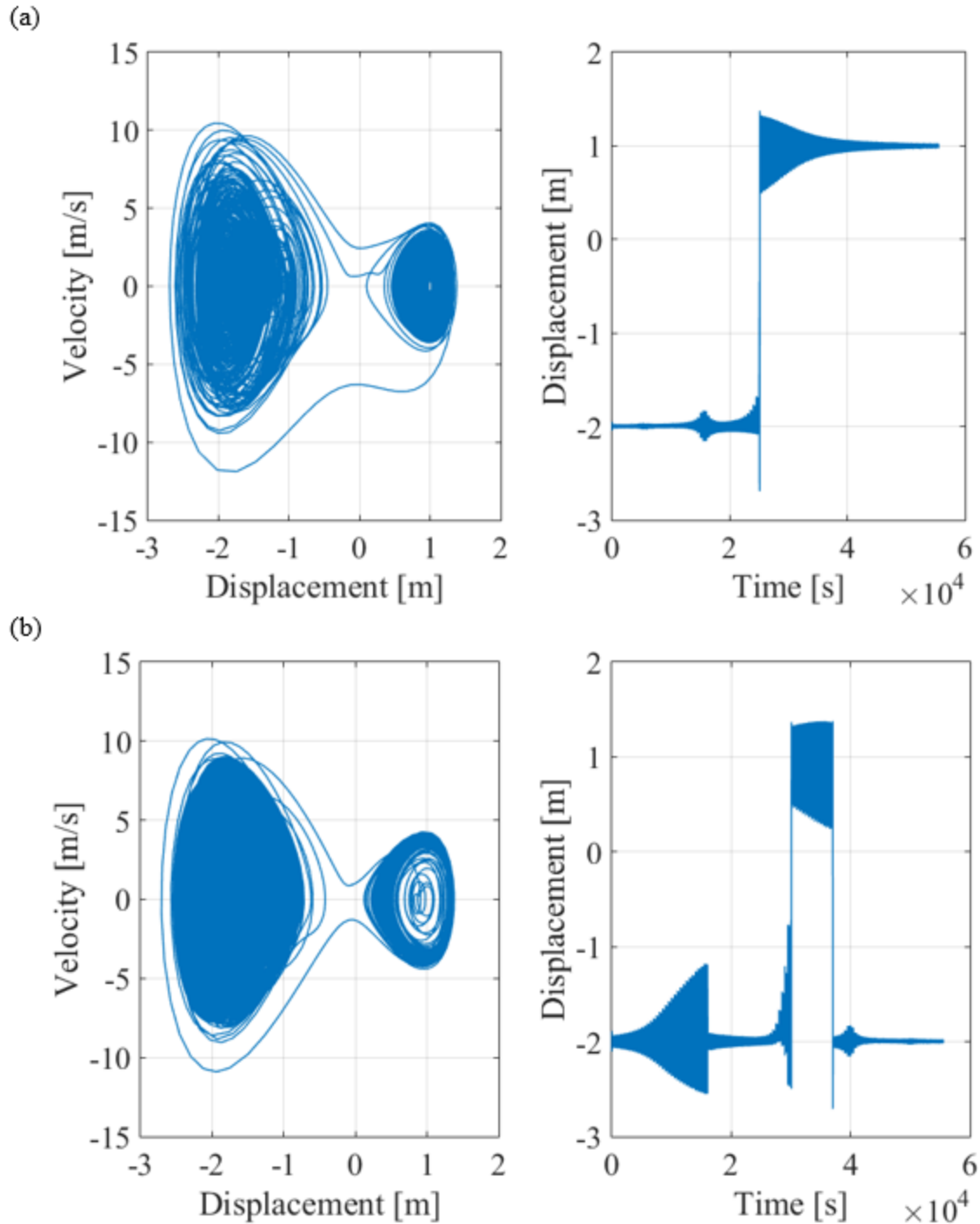


Figure 6.8 Phase Portrait and Displacement Time Response of m_2 , Starting from the Negative Fixed Point (State 1) of the Bistable Spring for (a) a Sweep Up from 3 to 14 rad/s and (b) a Sweep Down from 14 to 3 rad/s

The snap-through in the sweep up (Figure 6.8a) is an improvement from the SDOF NLMS system because it cleanly switches from the deep potential well to the shallow potential well with

minimal inter-well oscillations. This switch also avoid resonance, as the response decays to either side of the snap-through. This is only a single switch, however, meaning this sweep could not snap-through again to return to state 1. The sweep down, starting in state 1 (Figure 6.8b), does exhibit two snap-throughs in addition to one jump in energy level. Examining the phase portrait (Figure 6.8b) shows a jump from a high-energy branch to a low-energy branch, a snap-through at 8 rad/s to state 1, and another snap-through back to state 2 at 6.6 rad/s. The displacement time response also confirms that both snap-throughs occurred without any inter-well oscillations. Therefore, the sweep down from state 1 (Figure 6.8b) has the potential to switch around resonance to avoid larger response levels and to switch back to its original state for future resonance crossings.

The frequency response function loses clarity when nonlinear hysteresis and multiple stable states are present. It is difficult to determine whether a discontinuity in the frequency response is just a jump between high and low energy branches or a switch in stable state. Therefore, the frequency response amplitudes corresponding to a positive fixed point (state 2) are assigned a positive amplitude and the amplitudes corresponding to a negative fixed point (state 1) are assigned a negative amplitude. Figure 6.9 presents the modified frequency response of the Coupled NLMS system.

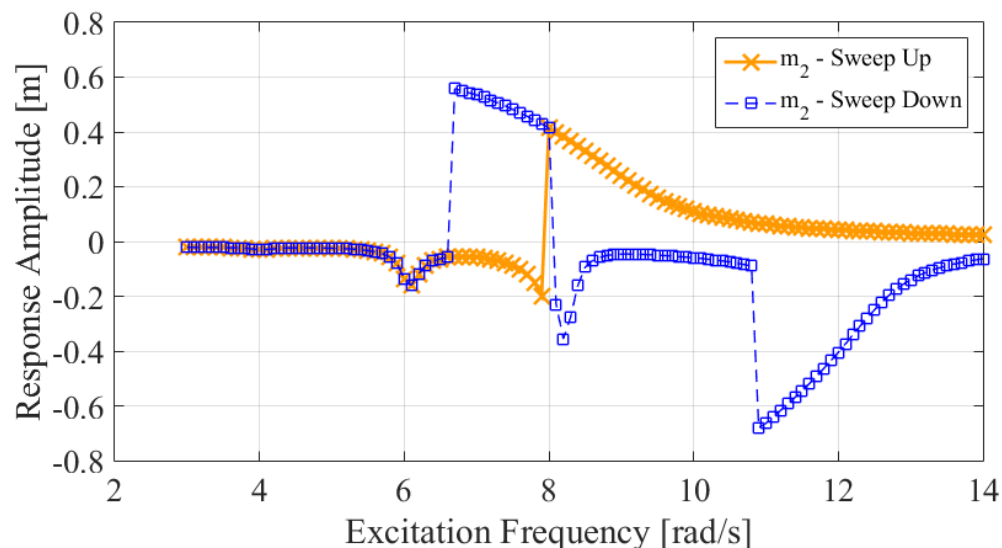


Figure 6.9 Modified Frequency Response of m_2 – Starting from the Negative Fixed Point (State 1) of the Bistable Spring for Both the Sweep Up and Sweep Down in Frequency

Stepping up through the frequencies exhibits one switch at 8 rad/s from state 1 to state 2, or the negative fixed point to the positive fixed point. This path also does not show any jumps

due to hysteresis. Stepping down in frequency exhibits one jump from a high-energy branch to a low-energy branch and two switches in state: one at 8 rad/s, from State 1 to State 2, and one at 6.6 rad/s, back to the negative fixed point (state 1).

For comparison, the same simulations were run with the asymmetric Coupled NLMS system starting in state 2. Figure 6.10 details the phase portrait and displacement time response for the sweep up and down in frequency for the mass m_1 , attached to the monostable spring and Figure 6.11 details the same for the mass m_2 , attached to the bistable spring. Figure 6.12 presents the modified frequency response, which is similar to the frequency response of the system starting in state 1, the negative fixed point (Figure 6.9). For this simulation, the excitation amplitude was adjusted slightly to 0.05825 meters to see switching in both the sweep up and sweep down. Studying the phase portraits of the sweep up (Figure 6.10a) and the sweep down (Figure 6.10b) of mass m_1 , it is clear the mass is still oscillating around the single fixed point. The coupling to mass m_2 still skewed the once elliptical shape of the phase portrait. The rapid changes in response levels seen in the displacement time responses (Figures 6.10a and 6.10b) occur at different points than when the system begins in state 1 (Figures 6.7a and 6.7b) due to the different linearized natural frequencies of state 2. Compared to state 1 (Figures 6.7a and 6.7b), the sweep up in state 2 (Figure 6.10a) possesses two snap-throughs and the sweep down (Figure 6.10b) has a single snap-through, indicated by the rapid changes in response levels. This is more clearly seen by studying the phase portraits and displacement time responses of mass m_2 . The displacement time response of the sweep up (Figure 6.11a) shows a jump from a low-energy branch to a high-energy branch, a snap-through to state 1 at 5.8 rad/s, and a second snap-through back to state 2 at 8.0 rad/s. The sweep down (Figure 6.11b) only has a single snap-through at 6.6 rad/s. Examining the phase portraits, the two snap-throughs in the sweep up (Figure 6.11a) have a small number of inter-well oscillations, while the snap-through on the sweep down (Figure 6.11b) does not exhibit any inter-well oscillations. The sweep up (Figure 6.11a) has shown to switch around resonance to avoid larger response levels and to switch back to its original state for future resonance crossings, making this configuration viable for avoiding resonance.

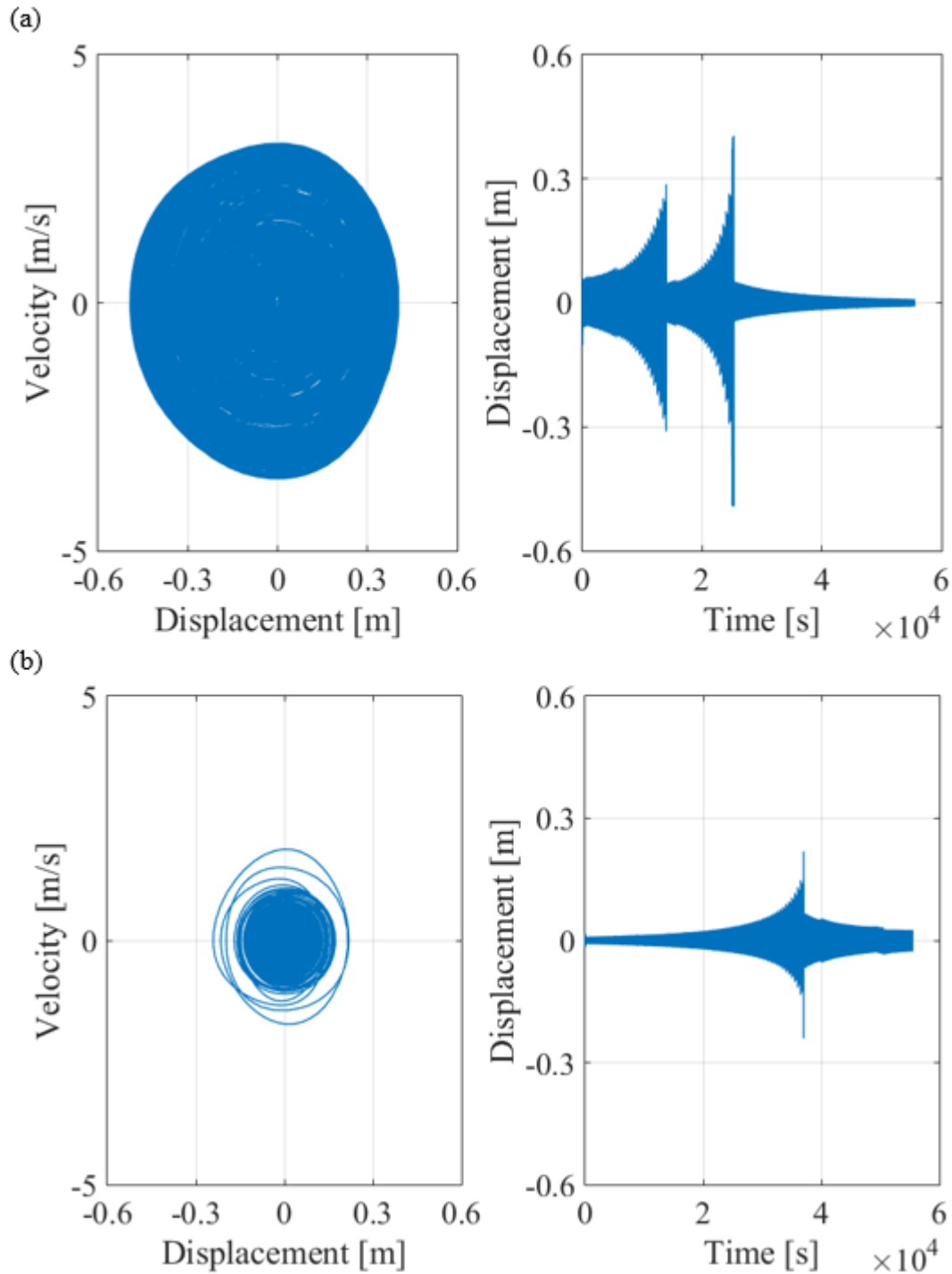


Figure 6.10 Phase Portrait and Displacement Time Response of m_1 , Starting from the Positive Fixed Point (State 2) of the Bistable Spring for (a) a Sweep Up from 3 to 14 rad/s and (b) a Sweep Down from 14 to 3 rad/s

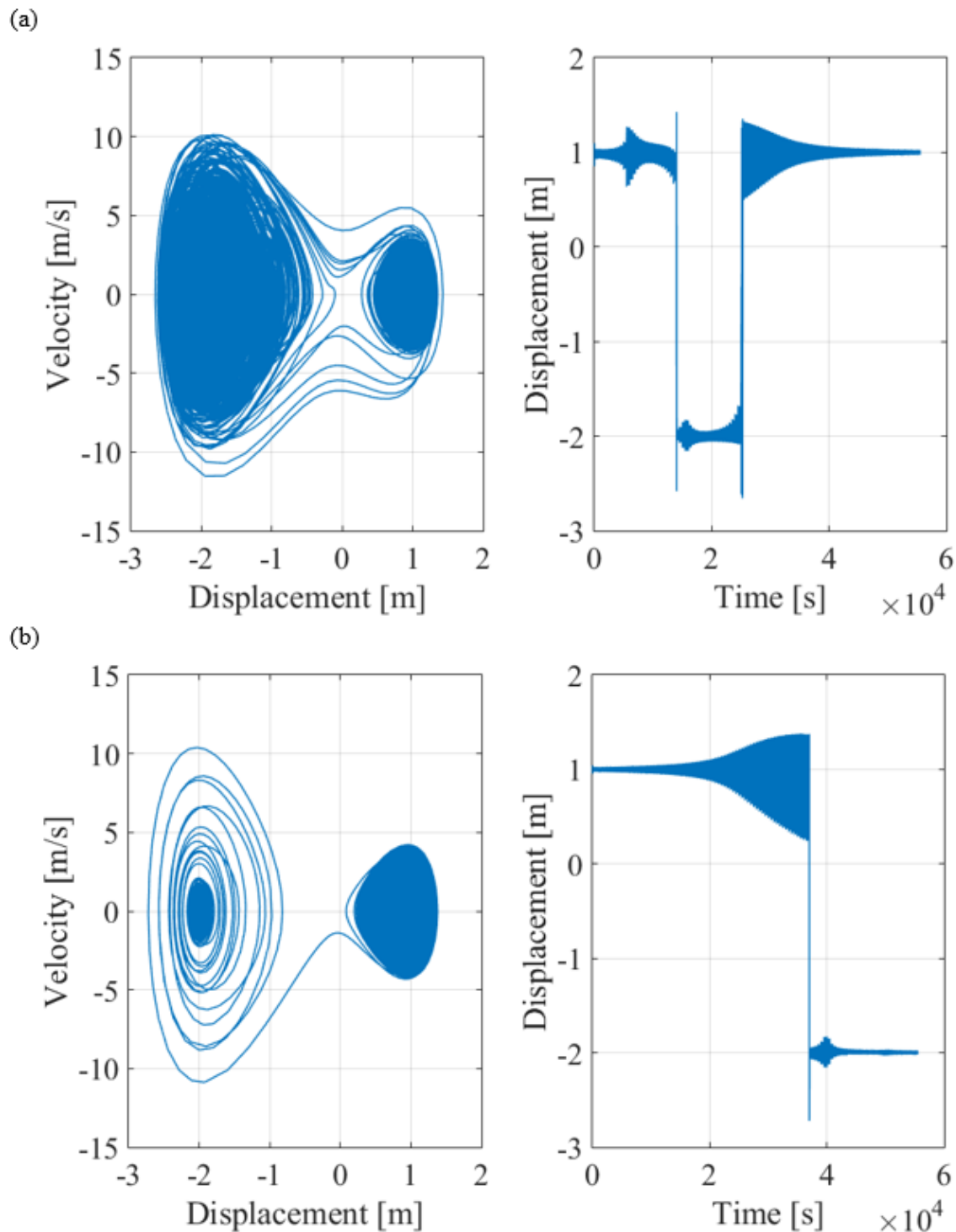


Figure 6.11 Phase Portrait and Displacement Time Response of m_2 , Starting from the Positive Fixed Point (State 2) of the Bistable Spring for (a) a Sweep Up from 3 to 14 rad/s and (b) a Sweep Down from 14 to 3 rad/s

The frequency response of the Coupled NLMS system, starting in state 2 for each frequency sweep, is presented in Figure 6.12.

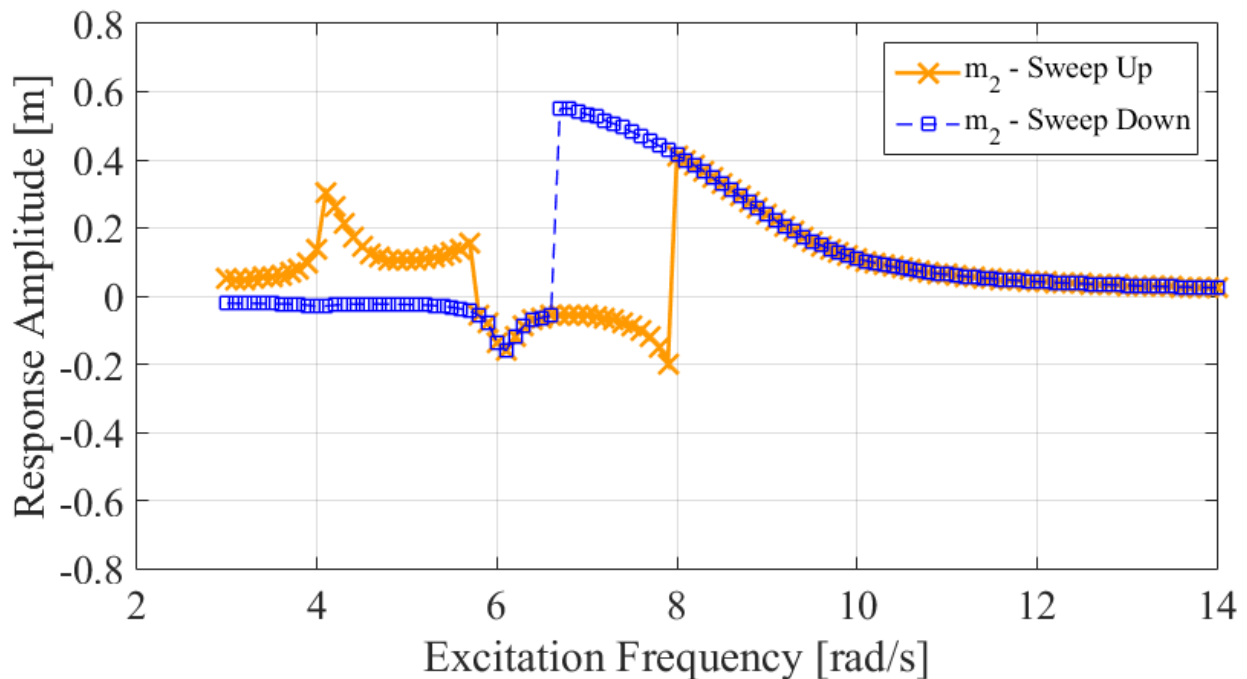


Figure 6.12 Modified Frequency Response of m_2 – Starting from the Positive Fixed Point (State 2) of the Bistable Spring for Both the Sweep Up and Sweep Down in Frequency

When stepping up in frequencies, a jump from a low-energy to high-energy branch is observed, as well as two switches: one at 5.8 rad/s from State 2 to State 1, and one from 8.0 rad/s, back to the original state. Stepping down in frequency reveals a single switch at 6.6 rad/s. Notice how the sweep up switches state when the system appears to rise into resonance, effectively avoiding resonance altogether.

Regardless of which state the asymmetric, Coupled NLMS system is initially set into, there exists a path in which two switches between states can occur and a path in which one switch occurs. The path stepping up in frequency, starting from the state 2, is the more promising path. Each switch occurs as the response rises into what could be a resonance, indicating that this system could avoid resonance if added to a target structure. In comparison, starting from state 1 and stepping down in frequency also achieves two switches that could avoid resonance. However, the dynamics after the switch from the negative fixed point to the positive fixed point lie on a high-energy branch, which could be undesirable, depending on its impact on

the target structure. As the asymmetric, coupled system has shown the desired two switches, we proceeded to study the Coupled NLMS system's impact on the cantilever beam.

6.2 Asymmetric Coupled NLMS System Added to Beam

Having achieved promising performance from the Coupled NLMS system, the next step is to attach the subsystem onto the target structure. As with the SDOF NLMS system, the Coupled NLMS is added to the end of the beam where the maximum displacement occurs for the first mode.

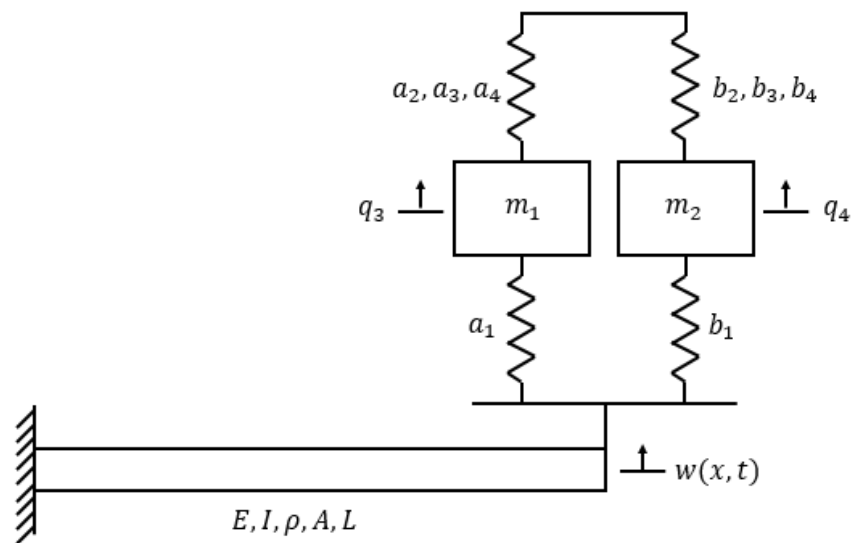


Figure 6.13 Coupled NLMS System Attached to Beam

With the addition of the Coupled NLMS system to the beam, the EOM of the combined system are detailed in Equations (6.20) to (6.23). Note the deflection of the beam is only coupled with the linear stiffness of both springs with the Coupled NLMS system.

$$\begin{aligned}
 & \int_0^L \rho A (\phi_1(x) \ddot{q}_1(t) + \phi_2(x) \ddot{q}_2(t)) (\phi_1(x)) dx \\
 & + \int_0^L EI (\phi_1''(x) q_1(t) + \phi_2''(x) q_2(t)) (\phi_1''(x)) dx \\
 & + a_1 (q_3(t) - \phi_1(L) q_1(t) - \phi_2(L) q_2(t)) (-\phi_1(L)) \\
 & + b_1 (q_4(t) - \phi_1(L) q_1(t) - \phi_2(L) q_2(t)) (-\phi_1(L)) = 0
 \end{aligned} \tag{6.20}$$

$$\begin{aligned}
& \int_0^L \rho A (\phi_1(x) \ddot{q}_1(t) + \phi_2(x) \ddot{q}_2(t)) (\phi_2(x)) dx \\
& + \int_0^L EI (\phi_1''(x) q_1(t) + \phi_2''(x) q_2(t)) (\phi_2''(x)) dx \\
& + a_1 (q_3(t) - \phi_1(L) q_1(t) - \phi_2(L) q_2(t)) (-\phi_2(L)) \\
& + b_1 (q_4(t) - \phi_1(L) q_1(t) - \phi_2(L) q_2(t)) (-\phi_2(L)) = 0 \tag{6.21}
\end{aligned}$$

$$m_1 \ddot{q}_3 + a_1 (q_3(t) - \phi_1(L) q_1(t) - \phi_2(L) q_2(t)) + a_2 q_3 q_4^2 + a_3 (q_3(t))^3 + a_4 (q_3(t))^2 = 0 \tag{6.22}$$

$$m_2 \ddot{q}_4 + b_1 (q_4(t) - \phi_1(L) q_1(t) - \phi_2(L) q_2(t)) + b_2 q_3^2 q_4 + b_3 (q_4(t))^3 + b_4 (q_4(t))^2 = 0 \tag{6.23}$$

These four EOM can be rewritten into matrix form, which can be seen below.

$$[M]\{\ddot{q}\} + [K]\{q\} + f(q) = \{0\} \tag{6.24}$$

Where

$$[M] = \begin{bmatrix} \int_0^L \rho A \phi_1^2(x) dx & 0 & 0 & 0 \\ 0 & \int_0^L \rho A \phi_2^2(x) dx & 0 & 0 \\ 0 & 0 & m_1 & 0 \\ 0 & 0 & 0 & m_2 \end{bmatrix}$$

$$[K] = \begin{bmatrix} \int_0^L EI (\phi_1''(x))^2 dx + a_1 \phi_1^2(L) + b_1 \phi_1^2(L) & \int_0^L EI \phi_1''(x) \phi_2''(x) dx + a_1 \phi_1(L) \phi_2(L) + b_1 \phi_1(L) \phi_2(L) & -a_1 \phi_1(L) & -b_1 \phi_1(L) \\ \int_0^L EI \phi_1''(x) \phi_2''(x) dx + a_1 \phi_1(L) \phi_2(L) + b_1 \phi_1(L) \phi_2(L) & \int_0^L EI (\phi_2''(x))^2 dx + a_1 \phi_2^2(L) + b_1 \phi_2^2(L) & -a_1 \phi_2(L) & -b_1 \phi_2(L) \\ -a_1 \phi_1(L) & -a_1 \phi_2(L) & a_1 & 0 \\ -b_1 \phi_1(L) & -b_1 \phi_2(L) & 0 & b_1 \end{bmatrix}$$

$$f(q) = \begin{pmatrix} 0 \\ 0 \\ a_2 q_3 q_4^2 + a_3 (q_3(t))^3 + a_4 (q_3(t))^2 \\ b_2 q_3^2 q_4 + b_3 (q_4(t))^3 + b_4 (q_4(t))^2 \end{pmatrix}$$

These EOM can also be written in state space form, which is amenable to numerical simulation. Incorporating the beam eigenfunctions will allow the fixed points of the system to be found. With four generalized coordinates in the Coupled NLMS-Beam system, there are now eight state variables.

$$\{\mathbf{x}\} = \begin{Bmatrix} x_1 \\ x_2 \\ x_3 \\ x_4 \\ x_5 \\ x_6 \\ x_7 \\ x_8 \end{Bmatrix} = \begin{Bmatrix} q_1 \\ \dot{q}_1 \\ q_2 \\ \dot{q}_2 \\ q_3 \\ \dot{q}_3 \\ q_4 \\ \dot{q}_4 \end{Bmatrix} \quad (6.25)$$

The state space form of the Coupled NLMS- Beam system is the following expression.

$$\{\dot{\mathbf{x}}\} = \begin{Bmatrix} \dot{x}_1 \\ \dot{x}_2 \\ \dot{x}_3 \\ \dot{x}_4 \\ \dot{x}_5 \\ \dot{x}_6 \\ \dot{x}_7 \\ \dot{x}_8 \end{Bmatrix} = [A] \begin{Bmatrix} x_1 \\ x_2 \\ x_3 \\ x_4 \\ x_5 \\ x_6 \\ x_7 \\ x_8 \end{Bmatrix} + F(x) \quad (6.26)$$

Where

$$[A] = \begin{bmatrix} 0 & 1 & 0 & 0 & 0 & 0 & 0 & 0 \\ \frac{1}{\int_0^L \rho A \phi_1^2(x) dx} \left(-\int_0^L EI (\phi_1''(x))^2 dx - a_1 \phi_1^2(L) - b_1 \phi_1^2(L) \right) & 0 & 0 & 0 & 0 & 0 & 0 & 0 \\ 0 & 0 & 0 & 1 & 0 & 0 & 0 & 0 \\ \frac{1}{\int_0^L \rho A \phi_2^2(x) dx} \left(-\int_0^L EI \phi_1''(x) \phi_2''(x) dx - a_1 \phi_1(L) \phi_2(L) - b_1 \phi_1(L) \phi_2(L) \right) & 0 & 0 & 0 & 0 & 0 & 0 & 0 \\ 0 & 0 & 0 & 0 & 0 & 1 & 0 & 0 \\ \frac{1}{m_1} (a_1 \phi_1(L)) & 0 & 0 & 0 & 0 & 0 & 0 & 0 \\ 0 & 0 & 0 & 0 & 0 & 0 & 0 & 1 \\ \frac{1}{m_2} (b_1 \phi_1(L)) & 0 & 0 & 0 & 0 & 0 & 0 & 0 \end{bmatrix}$$

$$\begin{array}{cccc}
0 & & & 0 \\
\frac{1}{\int_0^L \rho A \phi_1'^2(x) dx} \left(- \int_0^L EI \phi_1''(x) \phi_2''(x) dx - a_1 \phi_1(L) \phi_2(L) - b_1 \phi_1(L) \phi_2(L) \right) & & & 0 \\
0 & & & 1 \\
\frac{1}{\int_0^L \rho A \phi_2'^2(x) dx} \left(- \int_0^L EI (\phi_2''(x))^2 dx - a_1 \phi_2^2(L) - b_1 \phi_2^2(L) \right) & & & 0 \\
0 & & & 0 \\
\frac{1}{m_1} (a_1 \phi_2(L)) & & & 0 \\
0 & & & 0 \\
\frac{1}{m_2} (b_1 \phi_2(L)) & & & 0 \\
\\
0 & 0 & 0 & 0 \\
\frac{1}{\int_0^L \rho A \phi_1'^2(x) dx} (a_1 \phi_1(L)) & 0 & \frac{1}{\int_0^L \rho A \phi_1'^2(x) dx} (b_1 \phi_1(L)) & 0 \\
0 & 0 & 0 & 0 \\
\frac{1}{\int_0^L \rho A \phi_2'^2(x) dx} (a_1 \phi_2(L)) & 0 & \frac{1}{\int_0^L \rho A \phi_2'^2(x) dx} (b_1 \phi_2(L)) & 0 \\
0 & 1 & 0 & 0 \\
\frac{1}{m_1} (a_1) & 0 & 0 & 0 \\
0 & 0 & 0 & 1 \\
0 & 0 & \frac{1}{m_2} (b_1) & 0
\end{array}$$

$$F(x) = \left\{ \begin{array}{c} 0 \\ 0 \\ 0 \\ 0 \\ 0 \\ -\frac{a_2}{m_1} x_5 x_7^2 - \frac{a_3}{m_1} (x_5)^3 - \frac{a_4}{m_1} (x_5)^2 \\ 0 \\ -\frac{b_2}{m_2} x_5^2 x_7 - \frac{b_3}{m_2} (x_7)^3 - \frac{b_4}{m_2} (x_7)^2 \end{array} \right\}$$

From the state space equations, the fixed points and the Jacobian can be found to determine stability, linearize the nonlinear equations of motion, and find the linearized natural frequencies. The Jacobian can be determined using the following expression.

$$G(x) = \begin{bmatrix} f_1(x_1, x_2, x_3, x_4, x_5, x_6, x_7, x_8) \\ f_2(x_1, x_2, x_3, x_4, x_5, x_6, x_7, x_8) \\ f_3(x_1, x_2, x_3, x_4, x_5, x_6, x_7, x_8) \\ f_4(x_1, x_2, x_3, x_4, x_5, x_6, x_7, x_8) \\ f_5(x_1, x_2, x_3, x_4, x_5, x_6, x_7, x_8) \\ f_6(x_1, x_2, x_3, x_4, x_5, x_6, x_7, x_8) \\ f_7(x_1, x_2, x_3, x_4, x_5, x_6, x_7, x_8) \\ f_8(x_1, x_2, x_3, x_4, x_5, x_6, x_7, x_8) \end{bmatrix} = [A] \begin{Bmatrix} x_1 \\ x_2 \\ x_3 \\ x_4 \\ x_5 \\ x_6 \\ x_7 \\ x_8 \end{Bmatrix} + F(x) \quad (6.27)$$

$$J|_{(x_1, x_2, x_3, x_4, x_5, x_6)} = \begin{bmatrix} \frac{\partial f_1}{\partial x_1} & \frac{\partial f_1}{\partial x_2} & \frac{\partial f_1}{\partial x_3} & \frac{\partial f_1}{\partial x_4} & \frac{\partial f_1}{\partial x_5} & \frac{\partial f_1}{\partial x_6} & \frac{\partial f_1}{\partial x_7} & \frac{\partial f_1}{\partial x_8} \\ \frac{\partial f_2}{\partial x_1} & \frac{\partial f_2}{\partial x_2} & \frac{\partial f_2}{\partial x_3} & \frac{\partial f_2}{\partial x_4} & \frac{\partial f_2}{\partial x_5} & \frac{\partial f_2}{\partial x_6} & \frac{\partial f_2}{\partial x_7} & \frac{\partial f_2}{\partial x_8} \\ \frac{\partial f_3}{\partial x_1} & \frac{\partial f_3}{\partial x_2} & \frac{\partial f_3}{\partial x_3} & \frac{\partial f_3}{\partial x_4} & \frac{\partial f_3}{\partial x_5} & \frac{\partial f_3}{\partial x_6} & \frac{\partial f_3}{\partial x_7} & \frac{\partial f_3}{\partial x_8} \\ \frac{\partial f_4}{\partial x_1} & \frac{\partial f_4}{\partial x_2} & \frac{\partial f_4}{\partial x_3} & \frac{\partial f_4}{\partial x_4} & \frac{\partial f_4}{\partial x_5} & \frac{\partial f_4}{\partial x_6} & \frac{\partial f_4}{\partial x_7} & \frac{\partial f_4}{\partial x_8} \\ \frac{\partial f_5}{\partial x_1} & \frac{\partial f_5}{\partial x_2} & \frac{\partial f_5}{\partial x_3} & \frac{\partial f_5}{\partial x_4} & \frac{\partial f_5}{\partial x_5} & \frac{\partial f_5}{\partial x_6} & \frac{\partial f_5}{\partial x_7} & \frac{\partial f_5}{\partial x_8} \\ \frac{\partial f_6}{\partial x_1} & \frac{\partial f_6}{\partial x_2} & \frac{\partial f_6}{\partial x_3} & \frac{\partial f_6}{\partial x_4} & \frac{\partial f_6}{\partial x_5} & \frac{\partial f_6}{\partial x_6} & \frac{\partial f_6}{\partial x_7} & \frac{\partial f_6}{\partial x_8} \\ \frac{\partial f_7}{\partial x_1} & \frac{\partial f_7}{\partial x_2} & \frac{\partial f_7}{\partial x_3} & \frac{\partial f_7}{\partial x_4} & \frac{\partial f_7}{\partial x_5} & \frac{\partial f_7}{\partial x_6} & \frac{\partial f_7}{\partial x_7} & \frac{\partial f_7}{\partial x_8} \\ \frac{\partial f_8}{\partial x_1} & \frac{\partial f_8}{\partial x_2} & \frac{\partial f_8}{\partial x_3} & \frac{\partial f_8}{\partial x_4} & \frac{\partial f_8}{\partial x_5} & \frac{\partial f_8}{\partial x_6} & \frac{\partial f_8}{\partial x_7} & \frac{\partial f_8}{\partial x_8} \end{bmatrix} \quad (6.28)$$

The linearized equations of motion and the linearized natural frequencies can be determined from the Jacobian evaluated at each fixed point and accounting for the eigenfunctions of the cantilever beam.

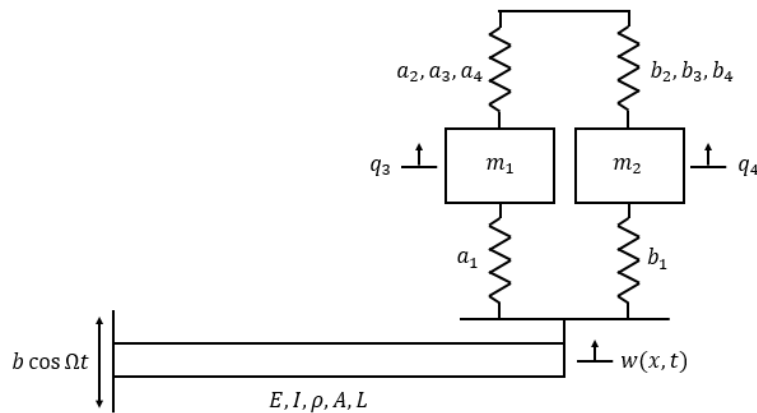


Figure 6.14 Coupled NLMS System Attached to Beam

As with the SDOF NLMS system, the base of the beam was excited. This excitation is illustrated in Figure 6.14. The addition of the base excitation is incorporated into the beam deflection, resulting the total deflection of the beam, described by Equation (5.14). The EOM become the following expressions.

$$[M]\{\ddot{q}\} + [K]\{q\} + f(q) = E(q) \quad (6.29)$$

Where

$$[M] = \begin{bmatrix} \int_0^L \rho A \phi_1^2(x) dx & 0 & 0 & 0 \\ 0 & \int_0^L \rho A \phi_2^2(x) dx & 0 & 0 \\ 0 & 0 & m_1 & 0 \\ 0 & 0 & 0 & m_2 \end{bmatrix}$$

$$[K] = \begin{bmatrix} \int_0^L EI(\phi_1''(x))^2 dx + a_1 \phi_1^2(L) + b_1 \phi_1^2(L) & \int_0^L EI \phi_1''(x) \phi_2''(x) dx + a_1 \phi_1(L) \phi_2(L) + b_1 \phi_1(L) \phi_2(L) & -a_1 \phi_1(L) & -b_1 \phi_1(L) \\ \int_0^L EI \phi_1''(x) \phi_2''(x) dx + a_1 \phi_1(L) \phi_2(L) + b_1 \phi_1(L) \phi_2(L) & \int_0^L EI(\phi_2''(x))^2 dx + a_1 \phi_2^2(L) + b_1 \phi_2^2(L) & -a_1 \phi_2(L) & -b_1 \phi_2(L) \\ -a_1 \phi_1(L) & -a_1 \phi_2(L) & a_1 & 0 \\ -b_1 \phi_1(L) & -b_1 \phi_2(L) & 0 & b_1 \end{bmatrix}$$

$$f(q) = \left\{ \begin{array}{c} 0 \\ 0 \\ a_2 q_3 q_4^2 + a_3 (q_3(t))^3 + a_4 (q_3(t))^2 \\ b_2 q_3^2 q_4 + b_3 (q_4(t))^3 + b_4 (q_4(t))^2 \end{array} \right\}$$

$$E(q) = \left\{ \begin{array}{c} -\int_0^L \rho A \phi_1(x) b \Omega^2 \cos \Omega t dx - a_1 \phi_1(L) b \cos \Omega t - b_1 \phi_1(L) b \cos \Omega t \\ -\int_0^L \rho A \phi_2(x) b \Omega^2 \cos \Omega t dx - a_1 \phi_2(L) b \cos \Omega t - b_1 \phi_2(L) b \cos \Omega t \\ a_1 b \cos \Omega t \\ b_1 b \cos \Omega t \end{array} \right\}$$

These EOMs can be written in state space form and used for numerical simulation. Section 6.3 details the results of several numerical simulations of Figure 6.14 and Equation (6.29).

6.3 Results

The parameters used for the cantilever beam are summarized in Table 6.5. These parameters are identical to those used in Table 5.1 with the exception of the length of the beam. In proving the effectiveness of the Coupled NLMS system, it was simpler to change the linearized natural frequency of 1st beam mode to match one of the linearized natural frequencies of the Coupled NLMS system. In reality, the parameters of the Coupled NLMS system would need to be designed to match the linearized natural frequency of the beam.

Table 6.5 Beam Parameters

Young's Modulus, E (N/m ²)	Second Area Moment of Inertia, I (m ⁴)	Density, ρ (kg/m ³)	Cross-Sectional Area, A (m ²)	Length, L (m)
180,000,000	0.0833	7700	1	4.3833

As the monostable spring has a single potential well and has no other stable state to switch to, there is no need for asymmetry within the monostable potential. Therefore, the quadratic nonlinearity was removed from the monostable spring, i.e. $a_4=0$, to simplify the Coupled NLMS model. In addition, the damping on both masses was decreased to encourage switching. Table 6.6 and Table 6.7 reflect this set of parameters for the coupled NLMS model.

Table 6.6 Mechanical Parameters for Asymmetric Coupled NLMS Model – Equation 6.3

$\zeta_1 \left[\frac{N \cdot s}{kg \cdot m} \right]$	$a_1 \left[\frac{N}{kg \cdot m} \right]$	$a_2 \left[\frac{N}{kg \cdot m^3} \right]$	$a_3 \left[\frac{N}{kg \cdot m^3} \right]$	$a_4 \left[\frac{N}{kg \cdot m^2} \right]$
0.1	25	10	100	0

Table 6.7 Mechanical Parameters for Asymmetric Coupled NLMS Model – Equation 6.4

$\zeta_2 \left[\frac{N \cdot s}{kg \cdot m} \right]$	$b_1 \left[\frac{N}{kg \cdot m} \right]$	$b_2 \left[\frac{N}{kg \cdot m^3} \right]$	$b_3 \left[\frac{N}{kg \cdot m^3} \right]$	$b_4 \left[\frac{N}{kg \cdot m^2} \right]$
0.1	-50	250	25	25

In Chapter 4, it was demonstrated that increasing the mass of an additional DOF increase its impact on the target structure. Using the mechanical parameters defined in Equations (6.3) and (6.4), the masses are assumed to be 1 kg. Thus, in order to increase the difference between states, the mass of the subsystem was increased. However, with two masses, each mass does not need to have the same mass. After many iterations, the preferable ratio between m_1 and m_2 was determined to be 25 to 1. To achieve a total mass of the Coupled NLMS system of approximately 2% the mass of the beam, the mass attached to the monostable spring, m_1 , was set to 650 kg and the mass attached to the bistable spring, m_2 , was set to 26 kg. The new mechanical parameters of the coupled NLMS system are reflected in Tables 6.8 and 6.9.

Table 6.8 Mechanical Parameters for Asymmetric Coupled NLMS Model – Equation (6.1)

$\xi_1 \left[\frac{N \cdot s}{m} \right]$	$A_1 \left[\frac{N}{m} \right]$	$A_2 \left[\frac{N}{m^3} \right]$	$A_3 \left[\frac{N}{m^3} \right]$	$A_4 \left[\frac{N}{m^2} \right]$
65	16250	6500	65000	0

Table 6.9 Mechanical Parameters for Asymmetric Coupled NLMS Model – Equation (6.2)

$\xi_2 \left[\frac{N \cdot s}{m} \right]$	$B_1 \left[\frac{N}{m} \right]$	$B_2 \left[\frac{N}{m^3} \right]$	$B_3 \left[\frac{N}{m^3} \right]$	$B_4 \left[\frac{N}{m^2} \right]$
2.6	-1300	6500	650	650

A parameter study was conducted to visualize how the linearized natural frequencies of each state change as the quadratic nonlinearity on the bistable spring is varied. The results of this parameter sweep are summarized in Figure 6.15. In each figure, the solid line represents the linearized natural frequencies of the system in state 1 and the dashed line corresponds to the linearized natural frequencies of the system in state 2. Figure 6.15a illustrates how the linearized natural frequencies of just the Coupled NLMS system change, and Figure 6.15b shows the linearized natural frequencies of the combined Coupled NLMS-Beam system. The 2nd beam mode is excluded from the combined system (Figure 6.15b) because it is not impacted by the addition of the Coupled NLMS system and does not change with any switch in state.

Figure 6.15 indicates the possibility for a larger difference between states by increasing asymmetry. However, as discussed in Chapter 5, there is a compromise between the damping of the subsystem and the asymmetry in order to effectively switch from the deeper potential well to the shallow well. Therefore, the quadratic nonlinearity was left at 650 N/m², leaving the possibility of optimization for future research. The linearized natural frequencies, computed from the values provided in Tables 6.5, 6.8 and 6.9 are summarized in Table 6.10.

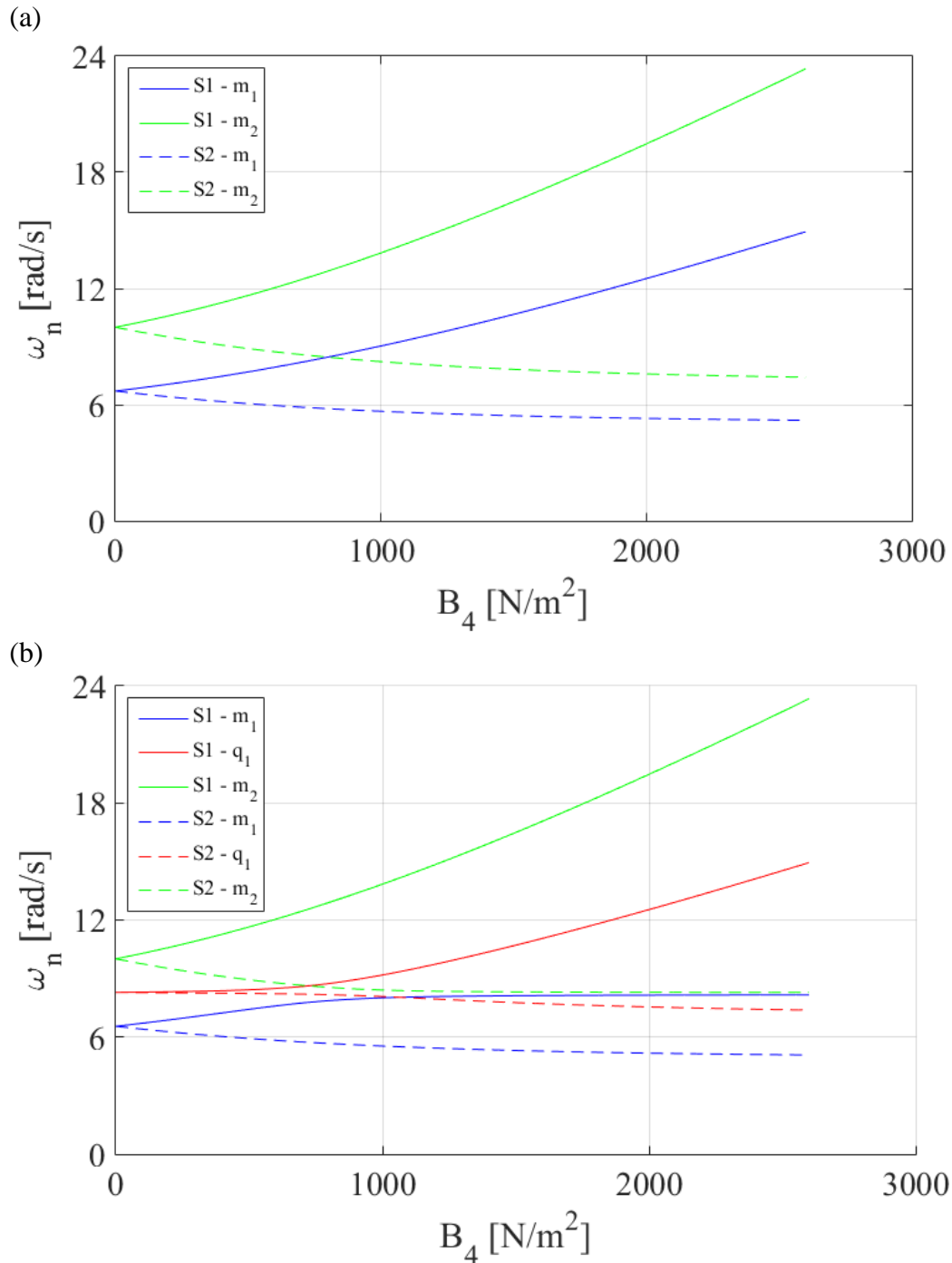


Figure 6.15 Linearized Natural Frequencies for Various Quadratic Nonlinearities, B_4 , in (a) the Coupled NLMS System and (b) the Coupled NLMS – Beam System (excluding the 2nd beam mode)

Table 6.10 Linearized Natural Frequencies of Coupled NLMS – Beam System with Table 6.5 Beam Parameters

Mode	Natural Frequencies (rad/s)	
	State 1 $x_{\text{eq}} = (0, 0, 0, 0, 0, 0, -2, 0)$	State 2 $x_{\text{eq}} = (0, 0, 0, 0, 0, 0, 0, 1, 0)$
m_1	7.6779	5.7911
1 st Beam Mode	8.5408	8.2139
m_2	12.251	8.7168
2 nd Beam Mode	50.6353	50.6353

The eigenvectors associated with each linearized natural frequency were also computed. The eigenvectors verify which mode is excited for a given linearized natural frequency. The first four linearized natural frequencies correspond to the negative fixed point, state 1, and the next four linearized natural frequencies correspond to the positive fixed point, state 2.

$$v = \begin{pmatrix} x_1 \\ x_3 \\ x_5 \\ x_7 \end{pmatrix} = \begin{pmatrix} 1st \text{ Beam Mode} \\ 2nd \text{ Beam Mode} \\ m_1 \text{ Mode} \\ m_2 \text{ Mode} \end{pmatrix}$$

State 1

$$\omega_{n1} = 50.6353 \text{ rad/s}$$

$$v_1 = \begin{pmatrix} 0 \\ 1.00 \\ 0 \\ 0 \end{pmatrix}$$

$$\omega_{n3} = 8.5408 \text{ rad/s}$$

$$v_3 = \begin{pmatrix} -0.75 \\ 0 \\ 0.65 \\ 0.03 \end{pmatrix}$$

$$\omega_{n2} = 12.2511 \text{ rad/s}$$

$$v_2 = \begin{pmatrix} 0.03 \\ 0 \\ 0 \\ 1.00 \end{pmatrix}$$

$$\omega_{n4} = 7.6779 \text{ rad/s}$$

$$v_4 = \begin{pmatrix} 0.65 \\ 0 \\ 0.75 \\ -0.02 \end{pmatrix}$$

State 2

$$\omega_{n1} = 50.6353 \text{ rad/s}$$

$$v_1 = \begin{pmatrix} 0 \\ 1.00 \\ 0 \\ 0 \end{pmatrix}$$

$$\omega_{n2} = 8.7168 \text{ rad/s}$$

$$v_2 = \begin{pmatrix} -0.33 \\ 0 \\ 0.06 \\ -0.94 \end{pmatrix}$$

$$\omega_{n3} = 8.2139 \text{ rad/s}$$

$$v_3 = \begin{pmatrix} -0.92 \\ -0.01 \\ 0.20 \\ 0.34 \end{pmatrix}$$

$$\omega_{n4} = 5.7911 \text{ rad/s}$$

$$v_4 = \begin{pmatrix} -0.20 \\ 0 \\ -0.98 \\ 0.01 \end{pmatrix}$$

The natural frequencies corresponding to the first beam mode shift by approximately 4% and the squared natural frequencies of the 1st beam mode shift by approximately 7.5%. The impact the coupled NLMS system has on the beam can be increased by increasing the mass of the subsystem, but at a certain point, the mass of the system will greatly impact the designed stiffness of the structure and would counteract any weight saving measures made in the design of the targeted structure. In the switching of RFD, which semi-actively switched between the open-circuit and short-circuit electrical boundary conditions, the largest coupling coefficient studied by Kauffman et al [43] was 5%. Recall that the coupling coefficient, k^2 , is equivalent to the difference in the squared natural frequencies between the short-circuit and open-circuit conditions. The Coupled NLMS system achieves a greater shift in the linearized natural frequency of the 1st beam mode of 7.5%, while being passive, with no need for external power or control, and purely mechanical, with no electrical circuitry necessary.

Numerical simulations were run with the combined Coupled NLMS – Beam system to determine the effectiveness of the Coupled NLMS system in avoiding resonance. The damping specified in Table 6.8 and Table 6.9 for each DOF of the Coupled NLMS system was incorporated into the modal damping matrix for the overall system. In order to avoid oversaturating the Coupled NLMS system, the damping on each beam mode was increased. The damping matrix can be seen in Equation (6.30).

$$[C] = \begin{bmatrix} 20000 & 0 & 0 & 0 \\ 0 & 20000 & 0 & 0 \\ 0 & 0 & 65 & 0 \\ 0 & 0 & 0 & 2.6 \end{bmatrix} \quad (6.30)$$

Using the linearized EOM for each fixed point with the damping matrix, the linearized damping ratios can be found.

$$[\zeta_{eq1}] = \begin{bmatrix} 0.00585 & 0 & 0 & 0 \\ 0 & 0.00585 & 0 & 0 \\ 0 & 0 & 0.00651 & 0 \\ 0 & 0 & 0 & 0.02418 \end{bmatrix} \quad (6.31)$$

$$[\zeta_{eq2}] = \begin{bmatrix} 0.00609 & 0 & 0 & 0 \\ 0 & 0.00585 & 0 & 0 \\ 0 & 0 & 0.00863 & 0 \\ 0 & 0 & 0 & 0.03399 \end{bmatrix} \quad (6.32)$$

Table 6.11 also summarizes the linearized damping ratios for each mode.

Table 6.11 Linearized Damping Ratios for the Coupled NLMS-Beam System

Mode	Linearized Damping Ratios	
	State 1 $x_{eq} = (0, 0, 0, 0, 0, 0, -2, 0)$	State 2 $x_{eq} = (0, 0, 0, 0, 0, 0, 1, 0)$
m_1	0.00651	0.00863
1 st Beam Mode	0.00585	0.00609
m_2	0.02418	0.03399
2 nd Beam Mode	0.00585	0.00585

For each simulation, the displacement time response and the phase portrait of mass m_2 was studied for both the sweep up (Figure 6.16a) and the sweep down (Figure 6.16b) of the combined system starting in state 2. In addition, a modified frequency response of mass m_2 (Figure 6.17) would indicate the difference between switches in state and jumps between energy branches. Finally, the frequency response function for the 1st beam mode (Figure 6.18) would verify that the target 1st beam mode resonance was successfully avoided.

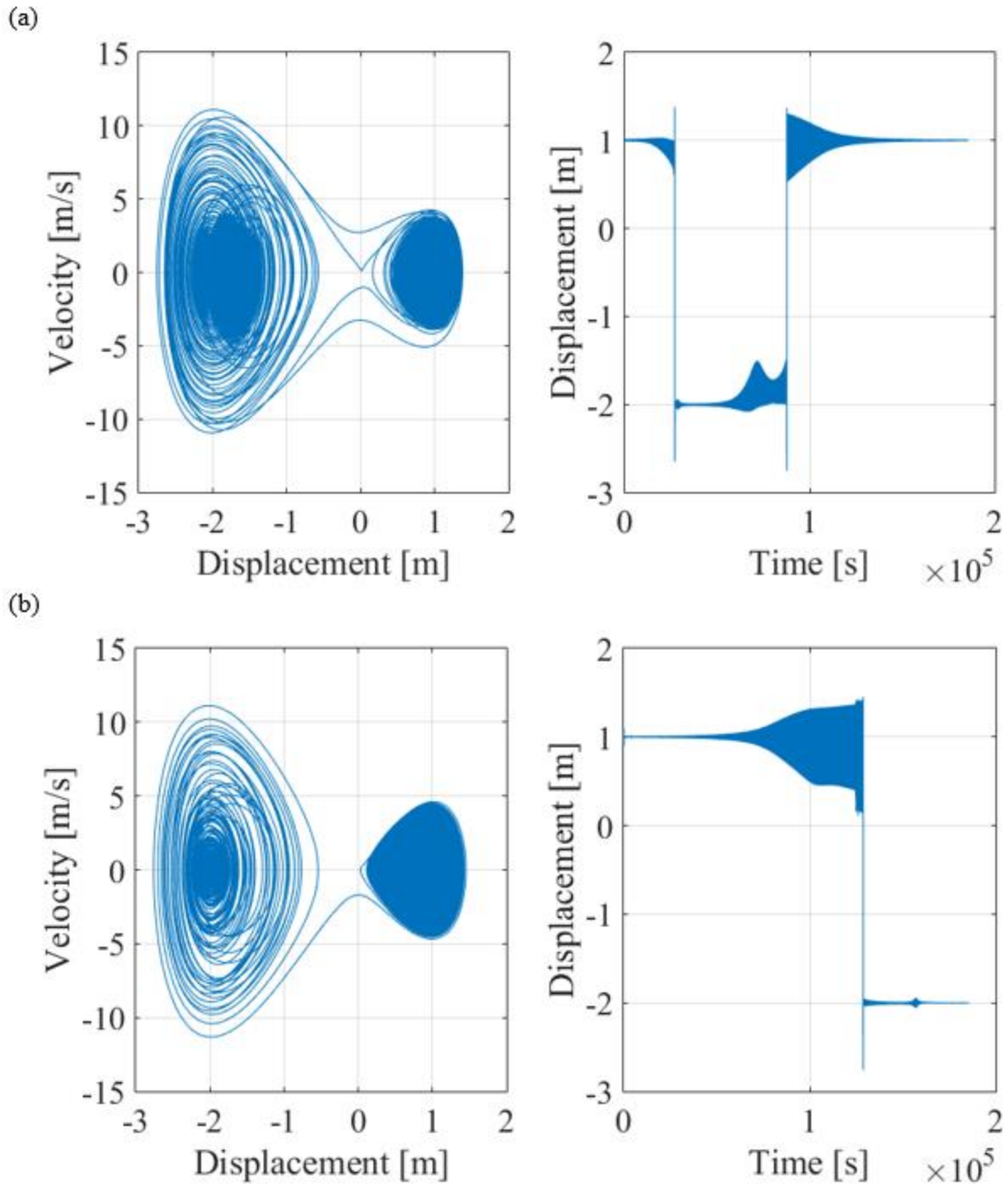


Figure 6.16 Phase Portrait and Displacement Time Response for m_2 , Starting from the Positive Fixed Point (State 2) of the Bistable Spring, (a) Sweeping Up 5 to 12.4 rad/s and (b) Sweeping Down 12.4 to 5 rad/s with an Excitation Amplitude of 0.00563 m

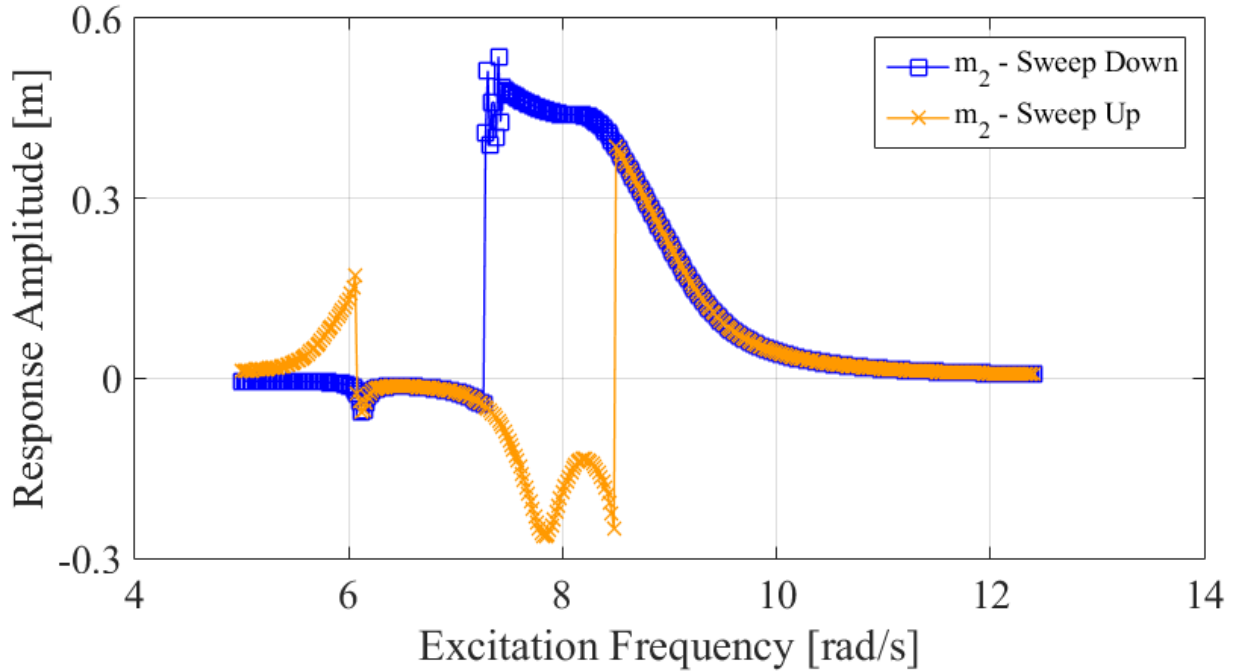


Figure 6.17 Modified Frequency Response for m_2 in the Coupled NLMS System and Beam – Starting from Positive Fixed Point (State 2)

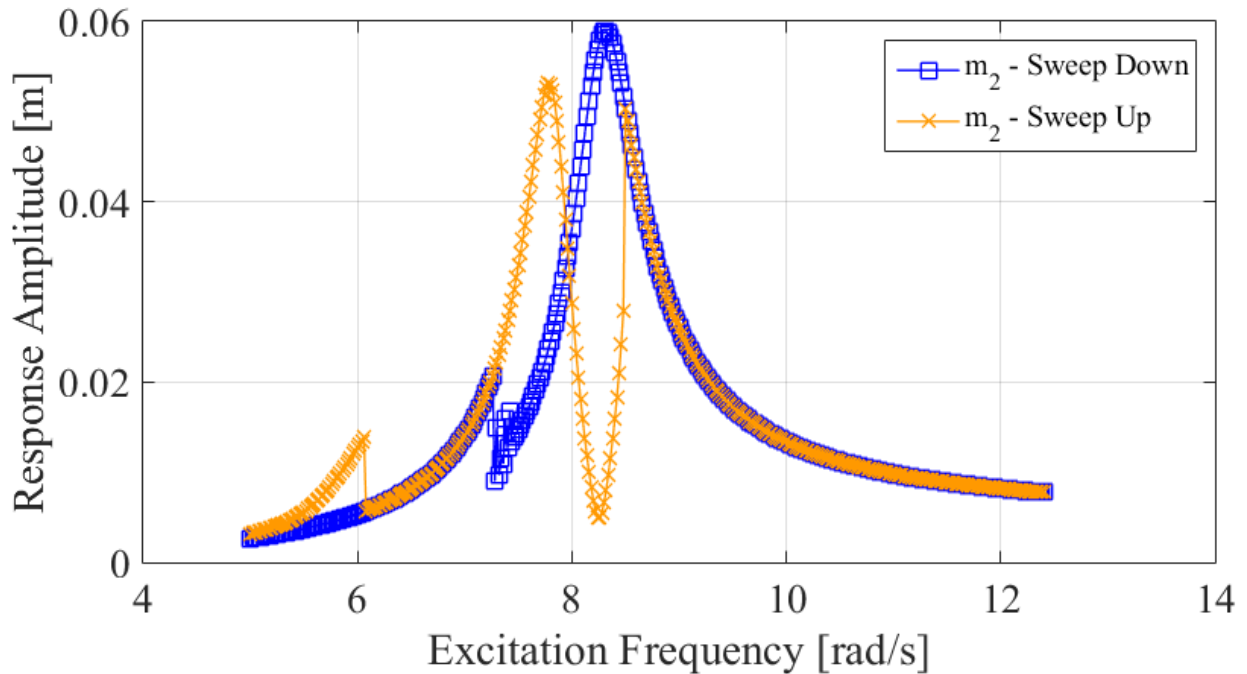


Figure 6.18 Frequency Response for 1st Beam Mode in the Coupled NLMS System and Beam – Starting from Positive Fixed Point (State 2)

The displacement time response, sweeping up in frequency (Figure 6.16a) shows snap-through from state 2 to state 1 at 6.08 rad/s and snap-through from state 1 back to state 2 at 8.50 rad/s. The response decreases on either side of each snap-through, indicating that high response levels are being avoided. The phase portrait shows that one of the switches has one inter-well oscillation. The displacement time response of the sweep down (Figure 6.16b) shows one snap-through occurring at 7.26 rad/s, switching from state 2 to state 1. The phase portrait confirms that this snap-through does not occur with any inter-well oscillations.

The modified frequency response function of mass m_2 (Figure 6.17) confirms each of these switches. Furthermore, the frequency response indicates there were no jumps between energy levels, as every switch proceeds from a positive to a negative amplitude or vice versa. The modified frequency response of the 1st beam mode (Figure 6.18) shows the results of the Coupled NLMS system's efforts to avoid resonance. In the sweep up, a switch from state 2 to state 1 at 6.08 rad/s avoids the 1st beam mode resonance in state 2 at 8.21 rad/s. The system proceeds through the resonance primarily exciting the mass m_1 in state 1 at 7.68 rad/s. Then, the system switches back to state 2 at 8.50 rad/s, avoiding the 1st beam resonance at 8.54 rad/s. After which, the response amplitude decreases for the remainder of the sweep. However, on the sweep down, the system does not switch from state 2 to state 1 until 7.26 rad/s, after the system has swept through the 1st beam mode's resonance at 8.21 rad/s. This produces larger response amplitudes in the 1st mode of the beam and even introduces some chaos in the response of mass m_2 before finally switching state. Based on this frequency response for the 1st beam mode (Figure 6.18), the combined Coupled NLMS-Beam system was successful at avoiding the resonance corresponding to the 1st beam mode when the system is excited by increasing frequencies.

Now that the performance of the Coupled NLMS system has been evaluated when the system begins in positive fixed point (state 2), the system was studied when each frequency sweep began in the negative fixed point (state 1). The phase portrait and the displacement time response for the sweep up and sweep down are shown in Figure 6.19a and Figure 6.19b respectively. Similar to the sweeps that start in state 2, both the modified frequency responses for both the mass m_2 (Figure 6.20) and the 1st beam mode (Figure 6.21) were examined to determine if resonance was indeed avoided. The displacement time response of the sweep up (Figure 6.19a) shows one snap-through at 8.50 rad/s and the phase portrait shows this snap-

through occurred with a single inter-well oscillation. The sweep down (Figure 6.19b) has one jump from a high-energy branch to a low-energy branch and two snap-throughs: one snap-through from state 1 to state 2 at 8.54 rad/s and one snap-through from state 2 to state 1 at 7.42 rad/s. These two snap-throughs occur with a total of five or six inter-well oscillations, which can be seen in the phase portrait.

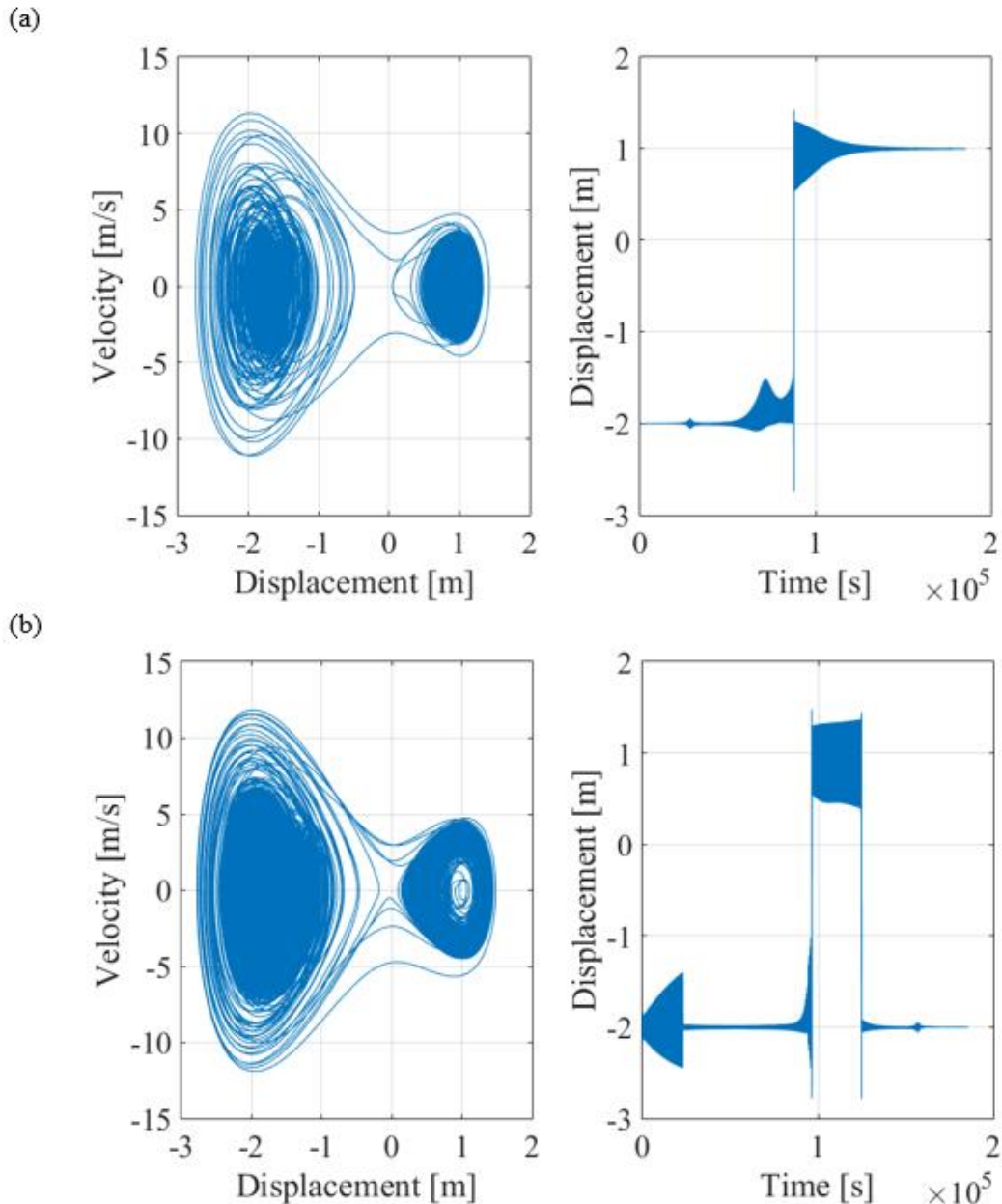


Figure 6.19 Phase Portrait and Displacement Time Response for m_2 , Starting from the Negative Fixed Point (State 1) of the Bistable Spring, (a) Sweeping Up 5 to 12.4 rad/s and (b) Sweeping Down 12.4 to 5 rad/s with an Excitation Amplitude of 0.00556 m and 0.00554 m respectively

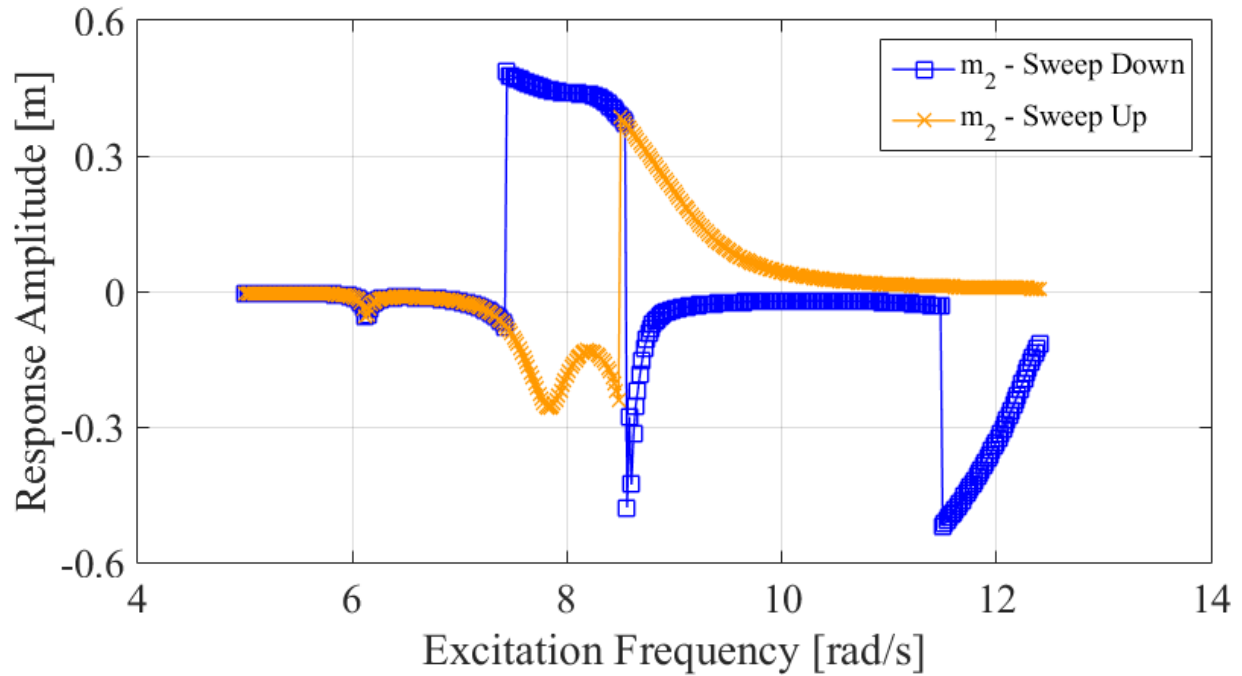


Figure 6.20 Modified Frequency Response for m_2 in the Coupled NLMS System and Beam – Starting from Negative Fixed Point (State 1)

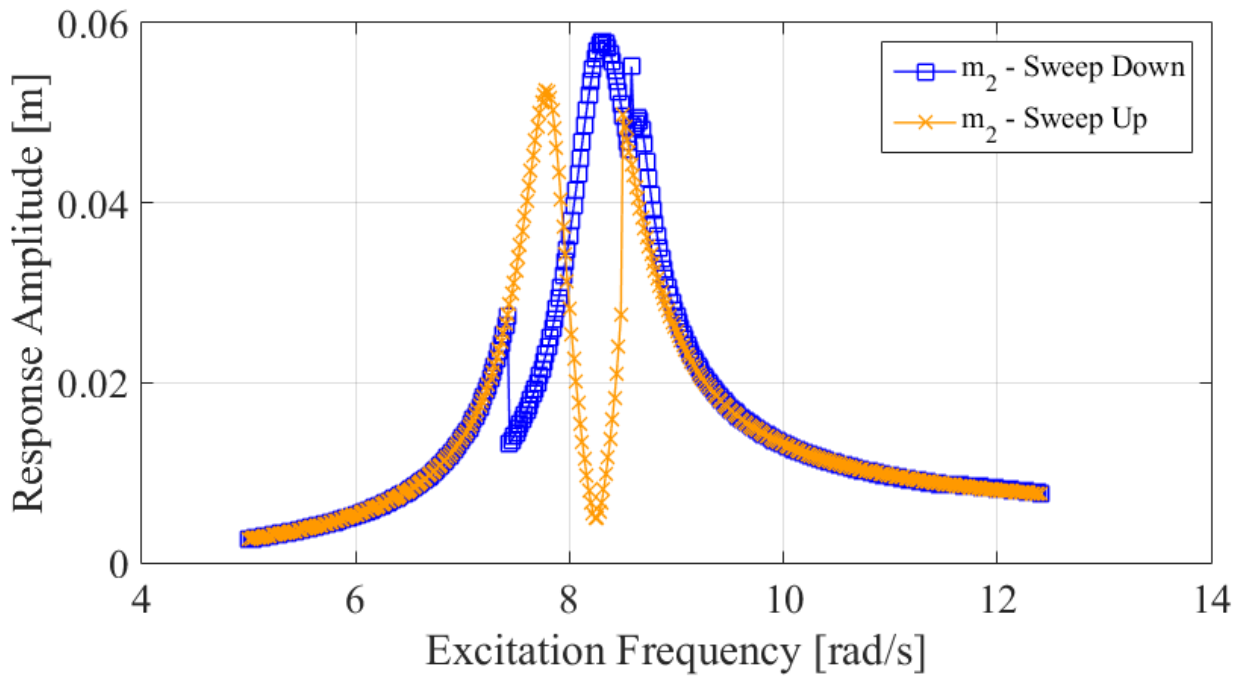


Figure 6.21 Modified Frequency Response for 1st Beam Mode in the Coupled NLMS System and Beam – Starting from Negative Fixed Point (State 1)

The modified frequency response of the mass m_2 (Figure 6.20) illustrates the three switches in state and the jump from a high-energy branch to low-energy branch without changing state. Each switch seen in the modified frequency response of the mass m_2 (Figure 6.20) is also reflected in the frequency response of the 1st beam mode (Figure 6.21). The sweep up progresses through the resonance primarily exciting the mass m_1 at 7.68 rad/s, then switches from state 1 to state 2 at 8.50 rad/s, avoiding the 1st beam mode resonance at 8.54 rad/s. This sweep is an example of how a single snap-through can avoid the resonance of the 1st beam mode. The sweep down switches from state 1 to state 2 at 8.54 rad/s before exciting the 1st beam mode at 8.21 rad/s. When the combined system is in state 1, the mass m_2 is experiencing large oscillations that continue to increase until the system switches back to state 1 at 7.42 rad/s. The sweep up in frequency is shown to do a better job at avoiding resonance than the sweep down. While the sweep down does switch twice, the system still sweeps thorough the resonance of the 1st beam mode. Therefore, sweep up is still the more optimal path to avoid resonance.

The results summarized in the frequency response functions of the systems starting in state 2 and starting in state 1 (Figures 6.18 and 6.21, respectively) reveal three important points. First, a purely mechanical, passive subsystem, can have a substantial impact on the natural frequencies of a targeted structure. Second, the combined system can switch to avoid resonance conditions. The optimal switching scheme occurs on the sweep up regardless of which state the combined system begins in, as either sweep down still sweeps through the resonance we are trying to avoid. Third, the subsystem can return to its original state to preserve the designed stiffness of the targeted structure when the system begins in state 2. This detuning procedure differs slightly from the switching Kauffman et al achieve. Kauffman's system begins in its stiffer state, switches to its softer state, and then returns to the stiffer state [42]. With the Coupled NLMS – Beam system, the switching best performs starting in the softer state. The subsystem switches to its stiffer state, avoiding the resonance of the softer state, then returns to the softer state before sweeping through the resonance of the stiffer state.

If the resonance conditions of the Coupled NLMS–Beam system were a result of the intersection of engine orders and natural frequencies, the switching scheme could be seen in a Campbell diagram similar to Figure 2.3a. The frequency response of the cantilever beam is not dependent on rotational speed, but projecting the switching procedure for each sweep of the Coupled NLMS-Beam system onto a Campbell diagram provides a graphical comparison

between the switching scheme of RFD and that of the Coupled NLMS–Beam system. This was performed with the Coupled NLMS-Beam system beginning in state 1 and state 2, which can be seen in the following figure.

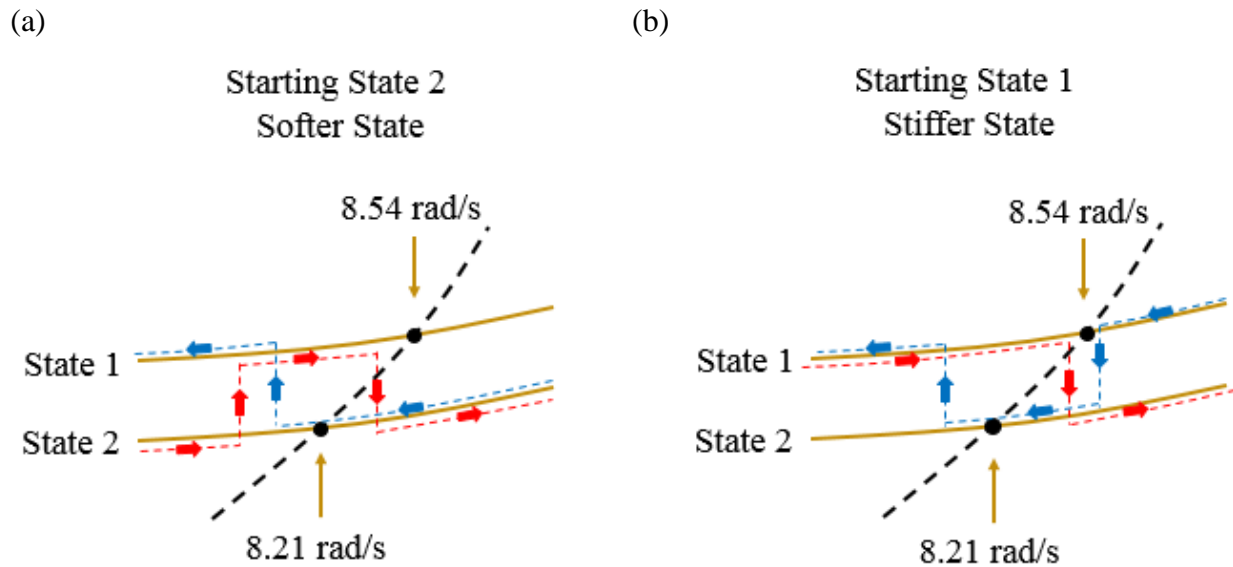


Figure 6.22 Campbell Diagram Interpretation of Coupled-NLMS – Beam Switching Scheme (a) Starting in State 2 for both the Sweep Up and Sweep Down in Frequency (b) Starting in State 1 for both the Sweep Up and Sweep Down in Frequency. The Dashed, Black Line Indicates an Engine Order that would exist in a Rotating Environment

The system could be optimized more to start in the stiffer state, following a switching procedure similar to that presented by Kauffman. This could be achieved by decreasing the damping of the Coupled NLMS system. This would cause less energy to be dissipated in the subsystem, making the subsystem more likely to switch from state 2 back to state 1 before sweeping through the resonance corresponding to the 1st beam mode. However, this reduces the excitation amplitude required to induce switching, causing the subsystem to be more susceptible to inter-well oscillations and acquiring too much energy to stay within the shallow well for any period of time. If either of these conditions occur, the model will not be able to avoid resonance properly. More information on future work regarding this research is presented in Section 7.1.

6.4 Generalization of Results: Sensitivity to System Imperfections

A few investigations were conducted to better understand and reinforce the success of the coupled system. These investigations include studying the systems sensitivity to mistuning, a

problem prevalent in turbomachinery blades, studying the impact of the coupled system on higher order modes of the cantilever beam, and inspecting the frequencies present in the response of the Coupled NLMS system to better understand the physics of the overall structure.

6.4.1 Impact of Detuning Mechanical Parameters

An important aspect of many systems designed to target particular natural frequencies is their susceptibility to mistuning, which is random variations with the target or designed structure. To study the impact of mistuning, two parameters of the cantilever beam were intentionally detuned: the length of the beam and the stiffness of the beam. In this research, the impact of the detuned parameter was measured by the percent difference between state 1 and state 2 of the linearized natural frequency of the 1st beam mode. This investigation studies how a change in this percent difference impacts the coupled NLMS system's ability to switch between states in order to avoid resonance. Figures 6.23 and 6.24 illustrate how the difference between the state 1 and state 2 linearized natural frequencies of the 1st beam mode changes as the length or stiffness of the beam is detuned from the designed value. Each parameter was altered from -20% to 20% of its designed value. Figure 6.23 presents the difference in terms of the squared natural frequency and Figure 6.24 presents the difference in terms of purely the linearized natural frequency.

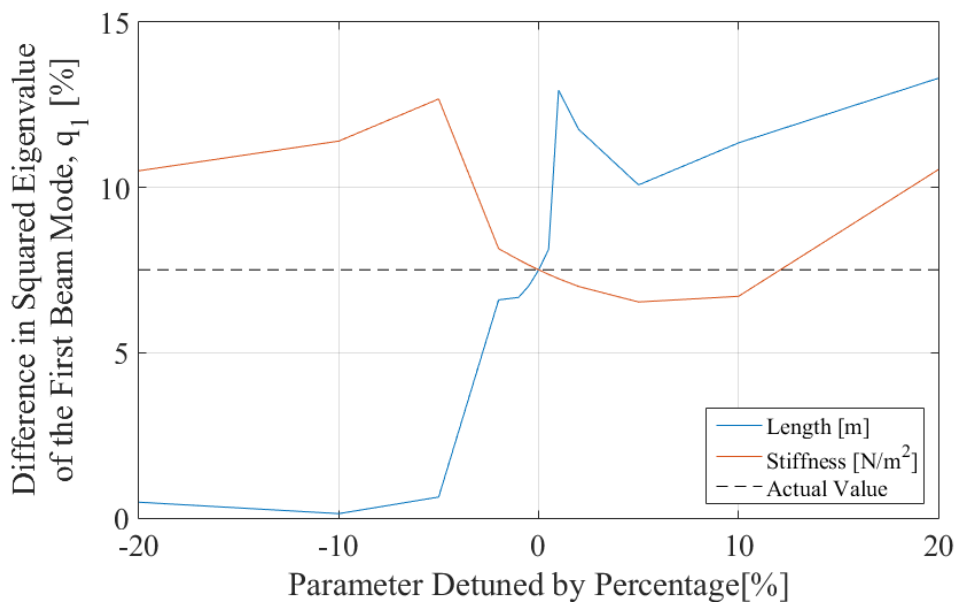


Figure 6.23 Difference in Squared Eigenvalue Corresponding to 1st Beam Mode between State 1 and State 2

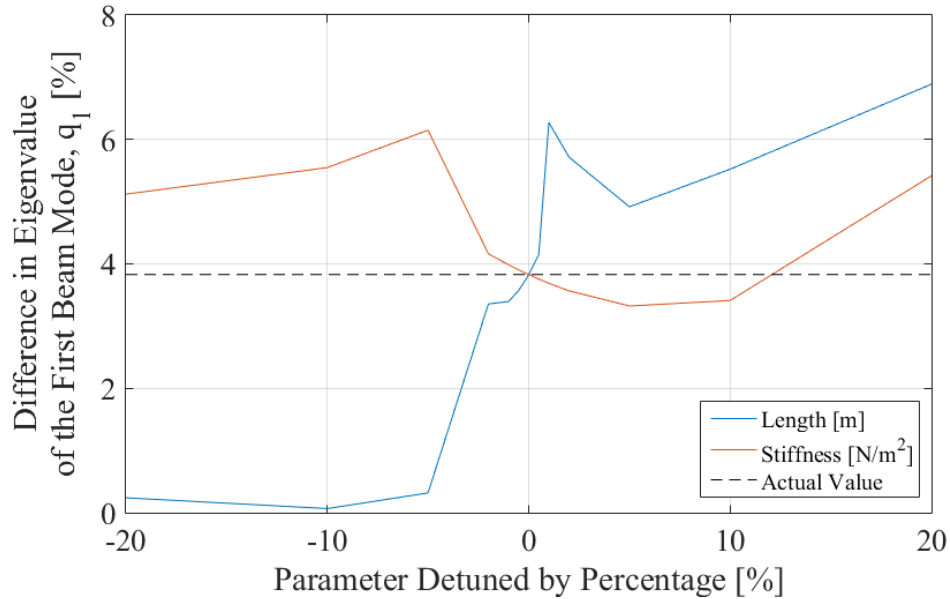


Figure 6.24 Difference in Eigenvalue Corresponding to 1st Beam Mode between State 1 and State 2

Based on the relationships presented in Figures 6.23 and 6.24, the length of the beam can be mistuned by $\pm 0.5\%$ before there is a significant change in the difference between state 1 and state 2. The same can be said for $\pm 2\%$ mistuning of the beam stiffness. The Coupled NLMS-Beam system parameters used in this investigation are summarized in Tables 6.5, 6.8 and 6.9, with the exception of the detuned parameter. The system was started in state 2 for any investigative sweep, as that provided best performance when avoiding resonance.

Figure 6.25 shows the displacement time response and phase portrait for the mass m_2 for the sweep up (Figure 6.25a) and the sweep down (Figure 6.25b) in frequency for the Coupled NLMS-Beam system with a 2% increase in the beam's stiffness. The displacement time response for the sweep up (Figure 6.25a) looks nearly identical to the results presented in Section 6.3 (Figure 6.16). However, examining the phase portrait (Figure 6.25a) reveals there are many more inter-well oscillations compared to single inter-well oscillation in the original system (Figure 6.16). The sweep down (Figure 6.25b) was impacted by the 2% increase in stiffness. The displacement time response shows that instead of snap-through, the system jumps from a high-energy branch to a low-energy branch. The system will still snap-through from state 2 to state 1 only after it has reached the natural frequency of the mass m_1 at around 5.79 rad/s. Since the sweep up (Figure 6.25a) is relatively unchanged, the system's ability to avoid resonance is

unhindered. Despite the change from a snap-through to a jump in energy branch, the system still sweeps through the 1st beam resonance on the sweep down (Figure 6.25b), thus, the effectiveness of this sweep remains relatively unaffected.

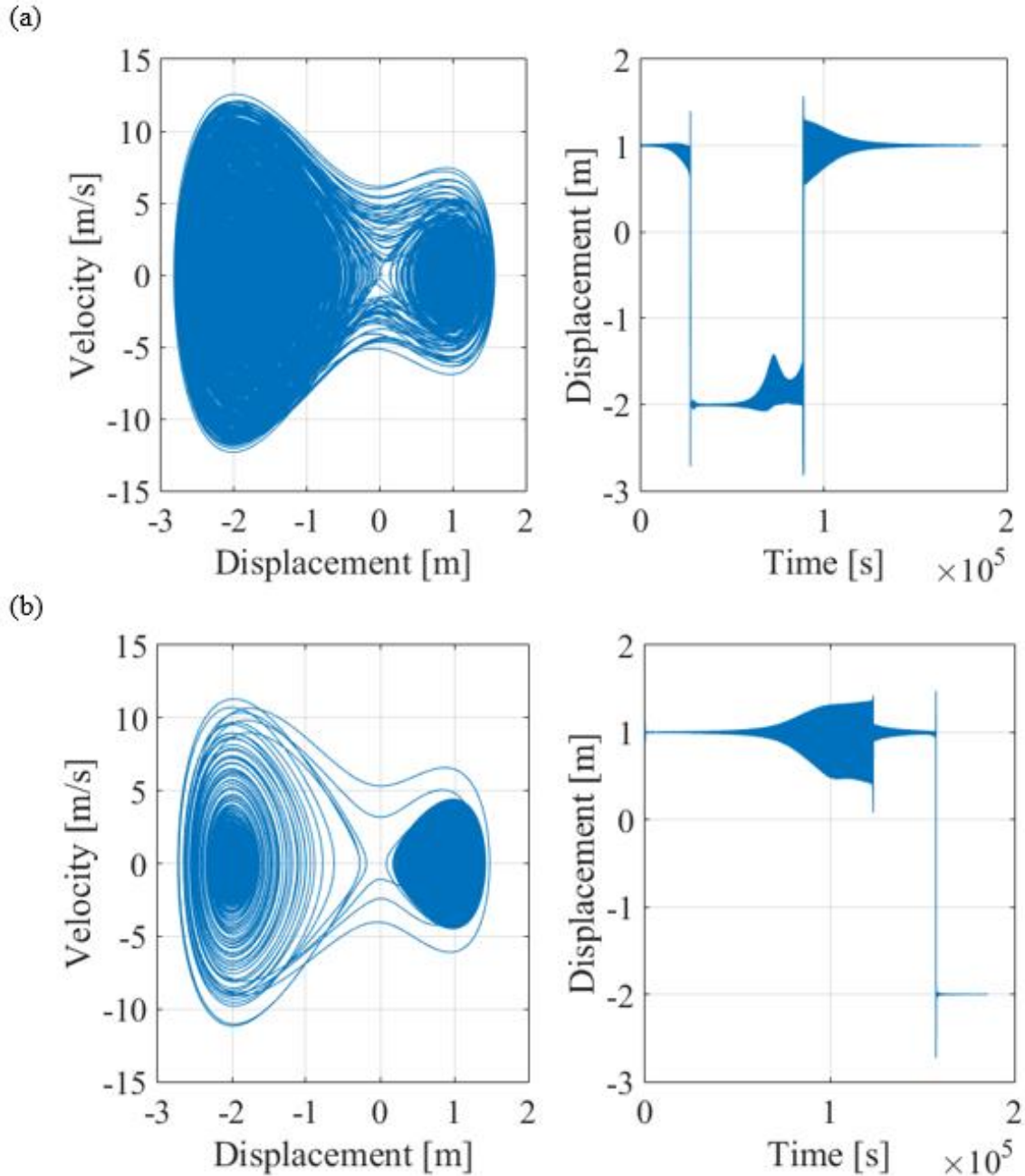


Figure 6.25 Phase Portrait and Displacement Time Response for m_2 , Starting from the Positive Fixed Point (State 2) of the Bistable Spring with +2% Stiffness Detuning, (a) Sweeping Up 5 to 12.4 rad/s and (b) Sweeping Down 12.4 to 5 rad/s with an Excitation Amplitude of 0.00564 m

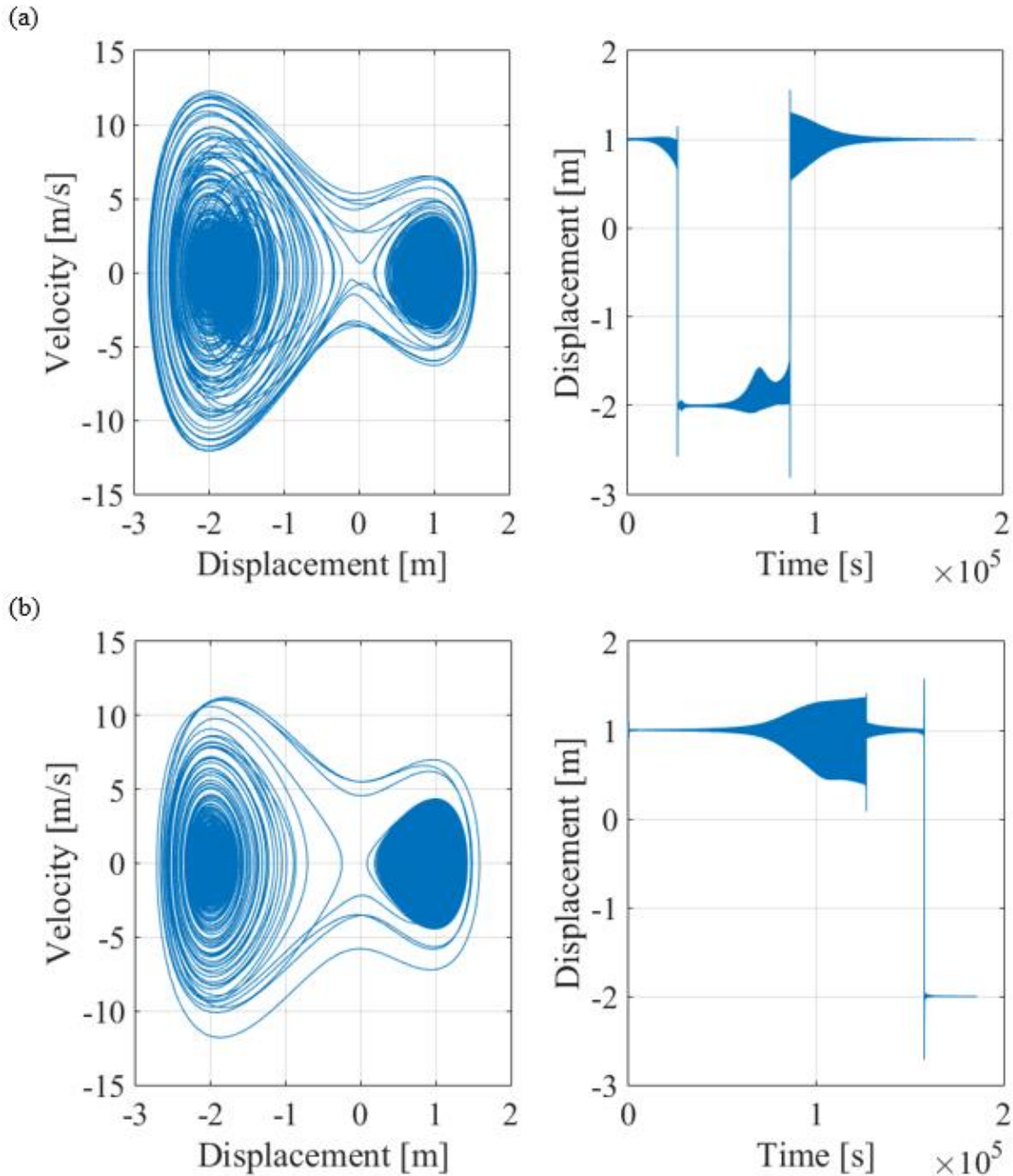


Figure 6.26 Phase Portrait and Displacement Time Response for m_2 , Starting from the Positive Fixed Point (State 2) of the Bistable Spring with -2% Stiffness Detuning, (a) Sweeping Up 5 to 12.4 rad/s and (b) Sweeping Down 12.4 to 5 rad/s with an Excitation Amplitude of 0.00562 m

Figure 6.26 shows the displacement time response and phase portrait for the mass m_2 for the sweep up (Figure 6.26a) and the sweep down (Figure 6.26b) in frequency for the Coupled NLMS-Beam system with a 2% decrease in the beam's stiffness. Compared to a 2% increase in

the beam's stiffness (Figure 6.25), the displacement time responses for the sweep up and sweep down look nearly identical. The phase portraits of the 2% decrease in stiffness (Figure 6.26) look similar to that of the 2% increase in stiffness, but the phase portrait of the sweep up (Figure 6.26a) has fewer inter-well oscillations than the same sweep with the 2% increase in stiffness (Figure 6.25a). Therefore, like for the 2% increase in stiffness, the 2% decrease in the beam's stiffness has little impact on the performance of the system.

Figure 6.27 shows the displacement time response and phase portrait for the mass m_2 for the sweep up (Figure 6.27a) and the sweep down (Figure 6.27b) in frequency for the Coupled NLMS-Beam system with a 0.5% increase in the beam's length. The displacement time response for the sweep up (Figure 6.27a) looks nearly identical to the results presented in Section 6.3 (Figure 6.16). However, examining the phase portrait (Figure 6.27a) reveals there are many more inter-well oscillations compared to single inter-well oscillation in the original system (Figure 6.16). For the sweep down (Figure 6.27b), the displacement time response and the phase portrait remain unchanged from the tuned set of parameters (Figure 6.16). Therefore, like for the 2% increase and decrease in stiffness, the 0.5% increase in the beam's length has little impact on the performance of the system.

For a 0.5% increase in the beam's length, the displacement time response for the sweep up (Figure 6.28a) looks nearly identical to the results presented in Section 6.3 (Figure 6.16), but the phase portrait (Figure 6.28a) endures more inter-well oscillations compared to single inter-well oscillation in the original system (Figure 6.16). For the sweep down (Figure 6.28b), the displacement time response remains relatively unchanged from the original system (Figure 6.16), but the phase portrait (Figure 6.28a) does show the addition of a single inter-well oscillation. Therefore, like for the 0.5% increase in the beam's length, the 0.5% decrease in the beam's length has little impact on the performance of the system.

Figures 6.25 to 6.28 were presented to show that for 2% mistuning of the beam's stiffness or for 0.5% mistuning of the beam's length, the performance of the Coupled NLMS-Beams system remains unaffected. As the mistuning goes beyond 0.5% for the length of the beam and 2% for the stiffness of the beam, the performance of the Coupled NLMS system degrades substantially.

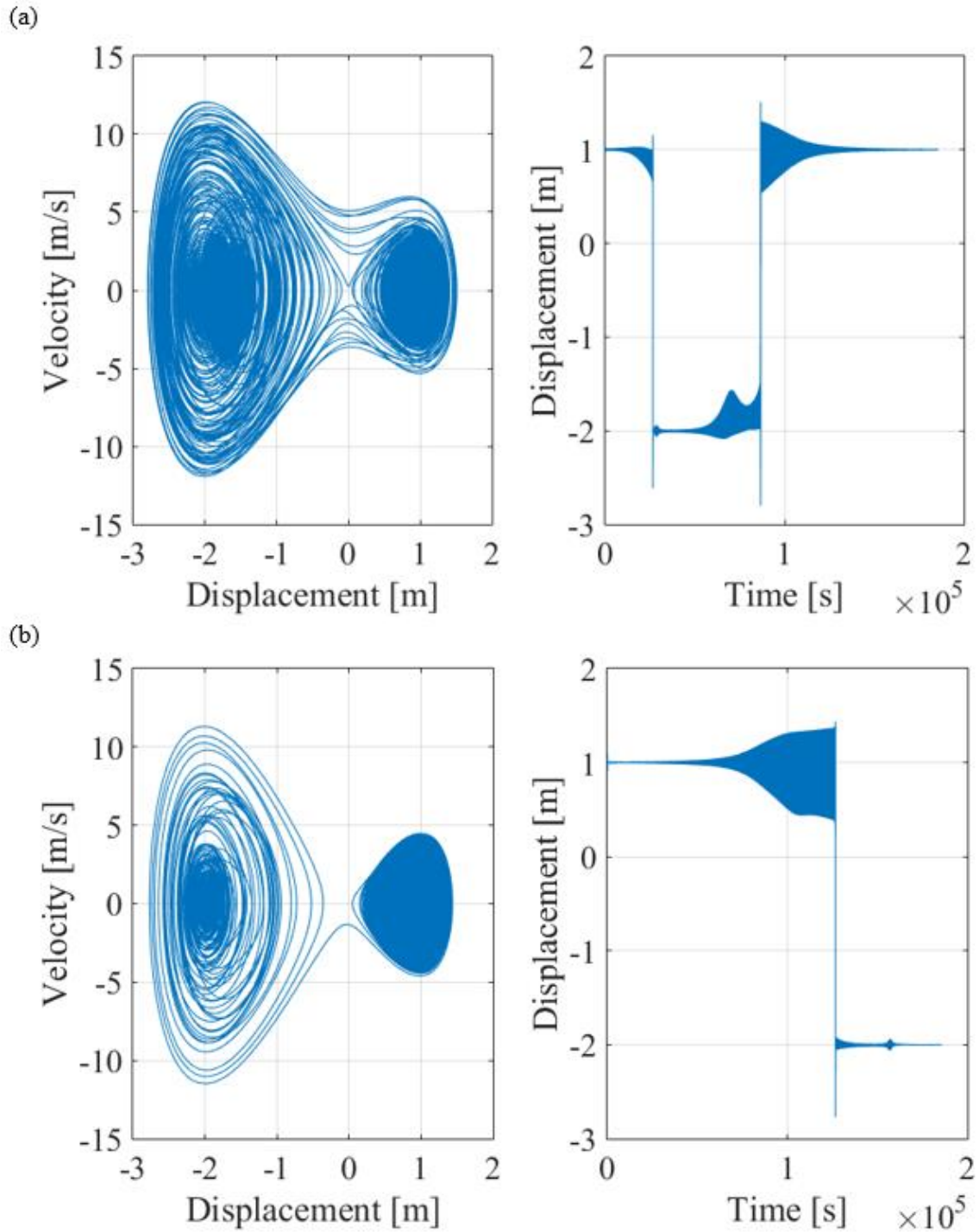


Figure 6.27 Phase Portrait and Displacement Time Response for m_2 , Starting from the Positive Fixed Point (State 2) of the Bistable Spring with +0.5% Length Detuning, (a) Sweeping Up 5 to 12.4 rad/s and (b) Sweeping Down 12.4 to 5 rad/s with an Excitation Amplitude of 0.00564 m

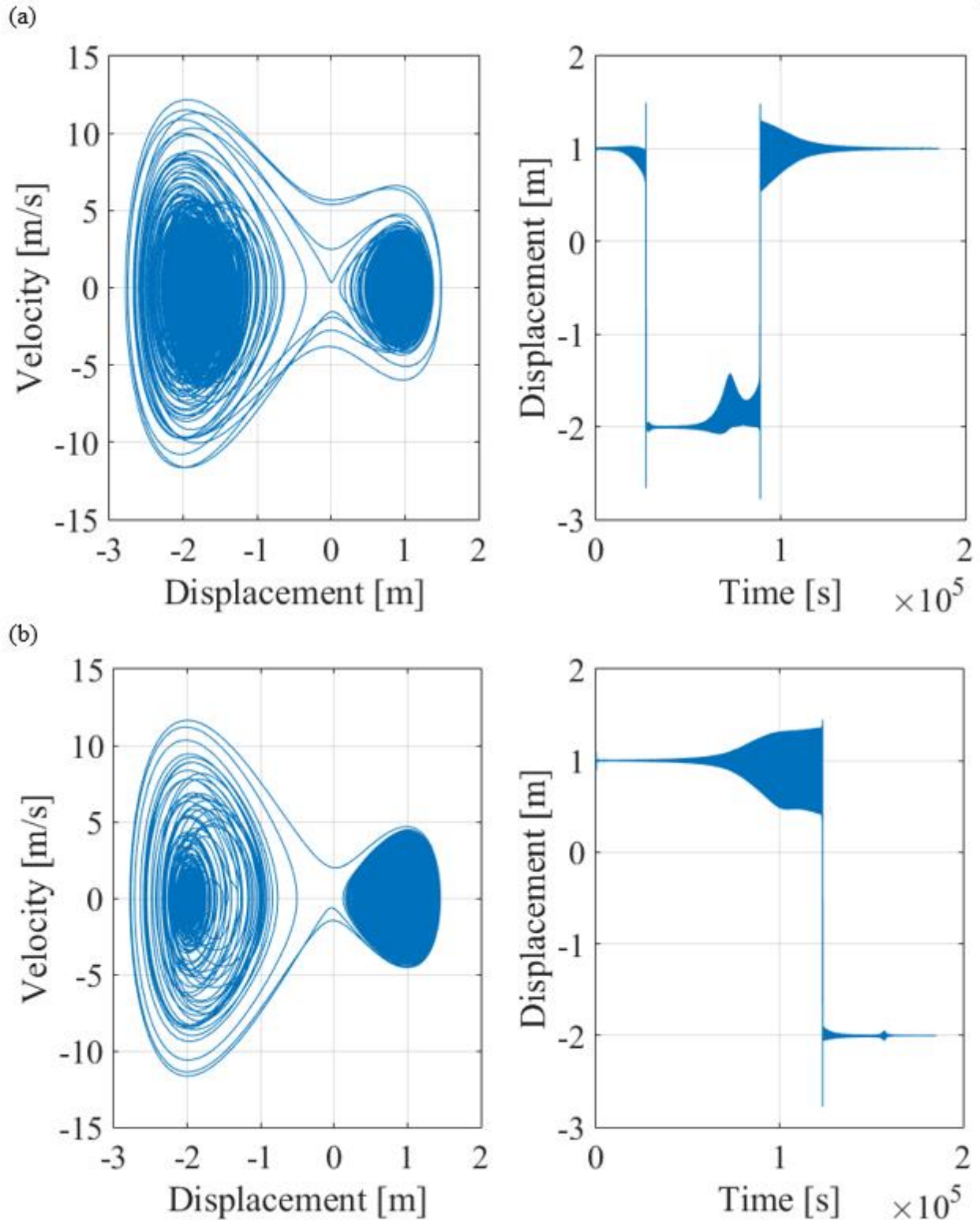


Figure 6.28 Phase Portrait and Displacement Time Response for m_2 , Starting from the Positive Fixed Point (State 2) of the Bistable Spring with -0.5% Length Detuning, (a) Sweeping Up 5 to 12.4 rad/s and (b) Sweeping Down 12.4 to 5 rad/s with an Excitation Amplitude of 0.00564 m

Figures 6.29, 6.30, and 6.31 present examples in which detuning a parameter by 5% impacts resonance avoidance by changing the switching dynamics. In these examples, the Coupled NLMS system fails to switch as resonance is approached. The failure to switch states causes the system to experience resonance conditions. For a 5% increase in the beams length (Figure 6.29) or a 5% decrease in the stiffness of the beam (Figure 6.31), the system still switches from the shallow potential well to the deeper potential well, but fails to switch from the deeper potential well to the shallow well. This causes the Coupled NLMS-Beam system to experience high response levels during resonance conditions from the 1st beam mode. In Figure 6.30, which corresponds to a 5% increase in the beam's stiffness, the system fails to switch even from the shallow potential well to the deeper well, experiencing high response levels for the remainder of the sweep.

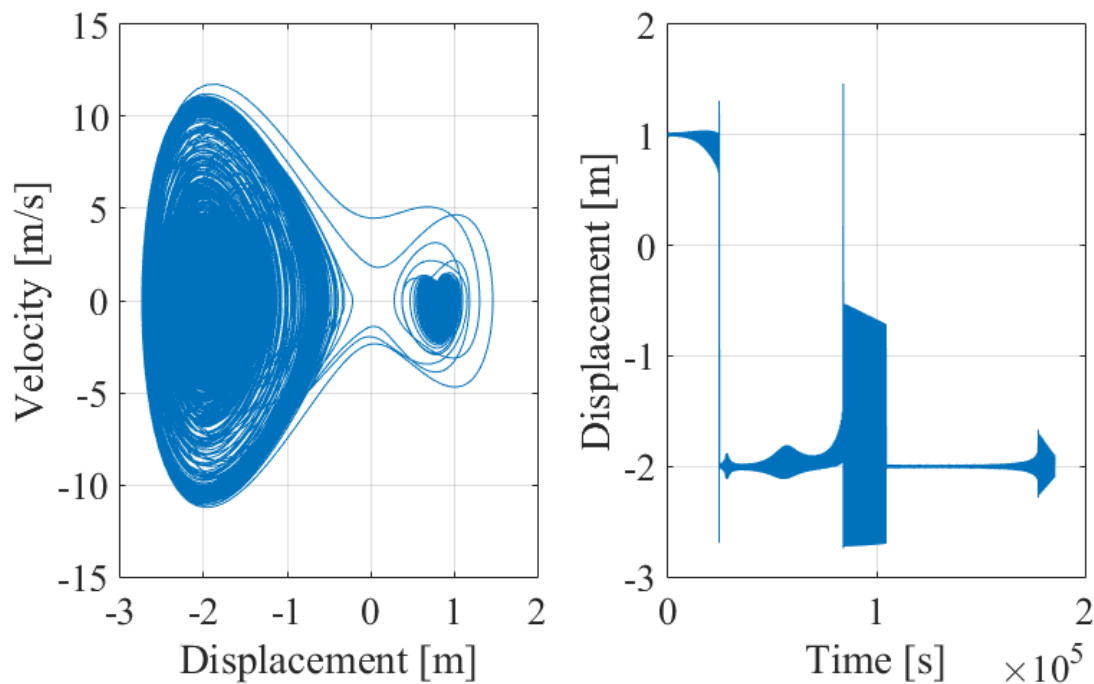


Figure 6.29 Phase Portrait and Displacement Time Response for m_2 , Starting from the Positive Fixed Point (State 2) of the Bistable Spring with +5% Length Detuning, Sweeping Up 5 to 12.4 rad/s with an Excitation Amplitude of 0.00564 m

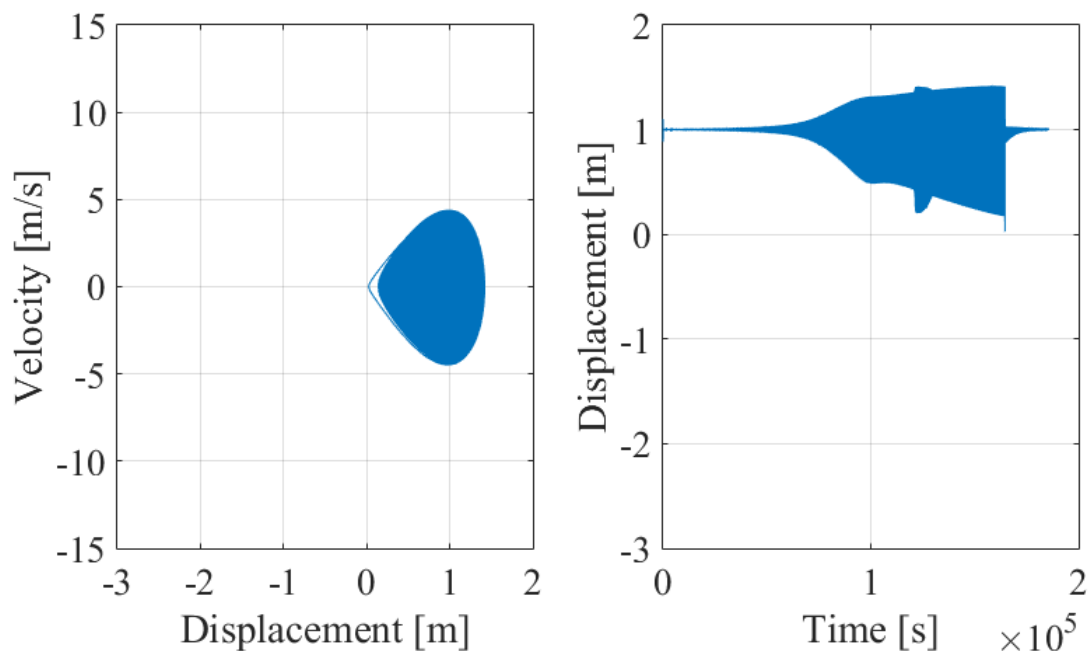


Figure 6.30 Phase Portrait and Displacement Time Response for m_2 , Starting from the Positive Fixed Point (State 2) of the Bistable Spring with +5% Stiffness Detuning, Sweeping Down 12.4 to 5 rad/s with an Excitation Amplitude of 0.00564 m

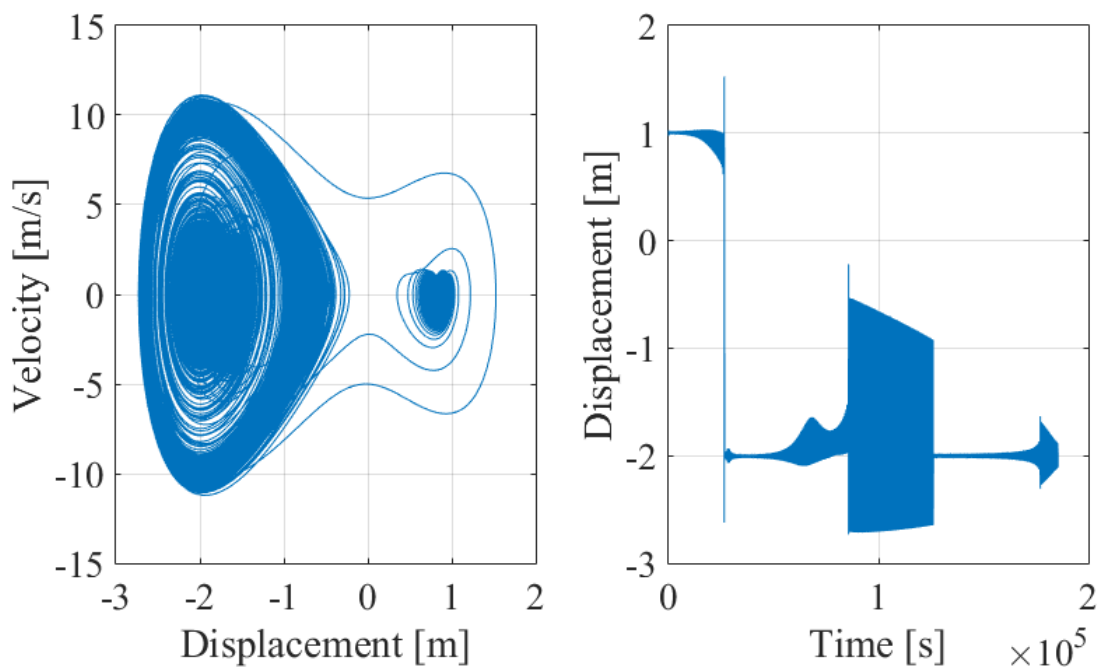


Figure 6.31 Phase Portrait and Displacement Time Response for m_2 , Starting from the Positive Fixed Point (State 2) of the Bistable Spring with -5% Stiffness Detuning, Sweeping Up 5 to 12.4 rad/s with an Excitation Amplitude of 0.00564 m

Despite robustness in mistuned mechanical parameters, the performance of the coupled NLMS system is very sensitive to the excitation amplitude. The modal damping applied to the beam must be substantial to avoid overwhelming the Coupled NLMS system. There is also very little margin of excitation levels between no switching, switching, and many inter-well oscillations. The damping and asymmetry in the Coupled NLMS – Beam system could be further optimized to reduce its sensitivity to excitation amplitude; this optimization is left to future research.

6.4.2 Effect of Modal Discretization: Higher Order Modes

A short investigation was conducted into the impact of using more than just two modes to approximate the deflection of the beam. This would help ensure that high frequency modes are not excited in the process of avoiding resonance. As any number of modes could be used, a 7-term modal expansion of the beam was chosen arbitrarily to compare with the 2-term modal expansion. For a 7-term modal expansion, Equation (4.26) is modified to the form expressed in Equation (6.33).

$$\begin{aligned}
 w(x, t) &= \sum_{i=1}^7 \phi_i(x)q_i(t) \\
 &= \phi_1(x)q_1(t) + \phi_2(x)q_2(t) + \phi_3(x)q_3(t) + \phi_4(x)q_4(t) + \phi_5(x)q_5(t) + \phi_6(x)q_6(t) + \phi_7(x)q_7(t) \quad (6.33)
 \end{aligned}$$

The equations of motion were determined using the Lagrange Equations as with Equations (6.20) to (6.23), however, the 7-term expansion was substituted for the 2-term expansion. This creates 9 EOMs, along with 9 generalized coordinates. The EOMs can be rewritten in state space form and used to solve for the fixed points of the system. The state variables of this system are defined in Equation (6.34), where the superscript T indicates the transpose of the vector.

$$\begin{aligned}
 \{\mathbf{x}\} &= \{x_1 \ x_2 \ x_3 \ x_4 \ x_5 \ x_6 \ x_7 \ x_8 \ x_9 \ x_{10} \ x_{11} \ x_{12} \ x_{13} \ x_{14} \ x_{15} \ x_{16} \ x_{17} \ x_{18}\}^T \\
 &= \{q_1 \ \dot{q}_1 \ q_2 \ \dot{q}_2 \ q_3 \ \dot{q}_3 \ q_4 \ \dot{q}_4 \ q_5 \ \dot{q}_5 \ q_6 \ \dot{q}_6 \ q_7 \ \dot{q}_7 \ q_8 \ \dot{q}_8 \ q_9 \ \dot{q}_9\}^T \quad (6.34)
 \end{aligned}$$

The fixed points were determined to be the same as the fixed points using the 2-term expansion.

$$x_{eq} = (x_1, x_2, x_3, x_4, x_5, x_6, x_7, x_8, x_9, x_{10}, x_{11}, x_{12}, x_{13}, x_{14}, x_{15}, x_{16}, x_{17}, x_{18}) \quad (6.35)$$

$$x_{eq} = (0, 0, 0, 0, 0, 0, 0, 0, 0, 0, 0, 0, 0, 0, 0, 0, -2, 0)$$

$$x_{eq} = (0, 0, 0, 0, 0, 0, 0, 0, 0, 0, 0, 0, 0, 0, 0, 0, 0, 0)$$

$$x_{eq} = (0, 0, 0, 0, 0, 0, 0, 0, 0, 0, 0, 0, 0, 0, 0, 0, 0, 1, 0)$$

As with the 2-term expansion, there are two stable states and one unstable state. State 1 will be the negative fixed point and State 2 will be the positive fixed point. The linearized natural frequencies and their associated eigenvectors were determined from the Jacobian of this Coupled NLMS – Beam system. The mechanical parameters in Tables 6.1, 6.8, and 6.9 were also used in this investigation. The eigenvectors indicate which mode is excited for a given linearized natural frequency.

$$v = \begin{pmatrix} x_1 \\ x_3 \\ x_5 \\ x_7 \\ x_9 \\ x_{11} \\ x_{13} \\ x_{15} \\ x_{17} \end{pmatrix} = \begin{pmatrix} 1st \text{ Beam Mode} \\ 2nd \text{ Beam Mode} \\ 3rd \text{ Beam Mode} \\ 4th \text{ Beam Mode} \\ 5th \text{ Beam Mode} \\ 6th \text{ Beam Mode} \\ 7th \text{ Beam Mode} \\ m_1 \text{ Mode} \\ m_2 \text{ Mode} \end{pmatrix}$$

Beginning with the 1st stable state, at the negative fixed point, the linearized natural frequencies and the eigenvectors of this state are as follows

$$\omega_{n1} = 956.4220 \text{ rad/s}$$

$$v_1 = \begin{pmatrix} 0 \\ 0 \\ 0 \\ 0 \\ 0 \\ -0.07 \\ -1.00 \\ 0 \\ 0 \end{pmatrix}$$

$$\omega_{n2} = 687.9150 \text{ rad/s}$$

$$v_2 = \begin{pmatrix} 0 \\ 0 \\ 0 \\ 0 \\ 0 \\ 1.00 \\ 0.10 \\ 0 \\ 0 \end{pmatrix}$$

$$\omega_{n3} = 459.1187 \text{ rad/s}$$

$$v_3 = \begin{pmatrix} 0 \\ 0 \\ 0 \\ 0 \\ -1 \\ 0 \\ 0 \\ 0 \\ 0 \end{pmatrix}$$

$$\omega_{n4} = 277.7385 \text{ rad/s}$$

$$v_4 = \begin{pmatrix} 0 \\ 0 \\ 0 \\ -1 \\ 0 \\ 0 \\ 0 \\ 0 \\ 0 \end{pmatrix}$$

$$\omega_{n5} = 141.7321 \text{ rad/s}$$

$$v_5 = \begin{pmatrix} 0 \\ 0 \\ 1 \\ 0 \\ 0 \\ 0 \\ 0 \\ 0 \\ 0 \end{pmatrix}$$

$$\omega_{n6} = 50.6353 \text{ rad/s}$$

$$v_6 = \begin{pmatrix} 0 \\ 1.00 \\ 0 \\ 0 \\ 0 \\ 0 \\ 0 \\ 0 \\ 0 \end{pmatrix}$$

$$\omega_{n7} = 12.2511 \text{ rad/s}$$

$$v_7 = \begin{pmatrix} 0.03 \\ 0 \\ 0 \\ 0 \\ 0 \\ 0 \\ 0 \\ 1.00 \end{pmatrix}$$

$$\omega_{n8} = 8.5407 \text{ rad/s}$$

$$v_8 = \begin{pmatrix} 0.75 \\ 0 \\ 0 \\ 0 \\ 0 \\ 0 \\ -0.66 \\ -0.03 \end{pmatrix}$$

$$\omega_{n9} = 7.6779 \text{ rad/s}$$

$$v_9 = \begin{pmatrix} -0.66 \\ 0 \\ 0 \\ 0 \\ 0 \\ 0 \\ -0.75 \\ 0.02 \end{pmatrix}$$

Moving onto the 2nd stable state, the positive fixed point, the linearized natural frequencies and the eigenvectors of this state are as follows

$$\omega_{n1} = 956.4220 \text{ rad/s}$$

$$v_1 = \begin{pmatrix} 0 \\ 0 \\ 0 \\ 0 \\ 0.07 \\ 1.00 \\ 0 \\ 0 \end{pmatrix}$$

$$\omega_{n2} = 687.9150 \text{ rad/s}$$

$$v_2 = \begin{pmatrix} 0 \\ 0 \\ 0 \\ 0 \\ 0 \\ -1.00 \\ -0.10 \\ 0 \end{pmatrix}$$

$$\omega_{n3} = 459.1187 \text{ rad/s}$$

$$v_3 = \begin{pmatrix} 0 \\ 0 \\ 0 \\ 0 \\ 1 \\ 0 \\ 0 \\ 0 \end{pmatrix}$$

$$\omega_{n4} = 277.7385 \text{ rad/s}$$

$$v_4 = \begin{pmatrix} 0 \\ 0 \\ 0 \\ 1 \\ 0 \\ 0 \\ 0 \\ 0 \end{pmatrix}$$

$$\omega_{n5} = 141.7321 \text{ rad/s}$$

$$v_5 = \begin{pmatrix} 0 \\ 0 \\ -1 \\ 0 \\ 0 \\ 0 \\ 0 \\ 0 \end{pmatrix}$$

$$\omega_{n6} = 50.6353 \text{ rad/s}$$

$$v_6 = \begin{pmatrix} 0 \\ 1.00 \\ 0 \\ 0 \\ 0 \\ 0 \\ 0 \\ 0 \end{pmatrix}$$

$$\omega_{n7} = 8.7167 \text{ rad/s}$$

$$v_7 = \begin{pmatrix} -0.33 \\ 0 \\ 0 \\ 0 \\ 0 \\ 0 \\ 0.06 \\ -0.94 \end{pmatrix}$$

$$\omega_{n8} = 8.2139 \text{ rad/s}$$

$$v_8 = \begin{pmatrix} -0.92 \\ 0 \\ 0 \\ 0 \\ 0 \\ 0 \\ 0.20 \\ 0.34 \end{pmatrix}$$

$$\omega_{n9} = 5.7909 \text{ rad/s}$$

$$v_9 = \begin{pmatrix} 0.20 \\ 0 \\ 0 \\ 0 \\ 0 \\ 0 \\ 0.98 \\ -0.01 \end{pmatrix}$$

For either stable state, there are no additional modes excited beyond the modes revealed to be coupled in the 2-term modal expansion. In fact, the last four linearized natural frequencies

and eigenvectors are nearly identical to the four linearized natural frequencies and the eigenvectors found with the 2-term modal expansion. The modes higher than the 2nd mode are also unaffected by the switching of the bistable spring within the coupled NLMS system. The 6th and 7th modes of the beam appear to possibly indicate coupling between to the two, but the amount of coupling is small. The absence of additional, unintentionally excited modes indicates that energy transferred from the beam to the coupled NLMS system is not returned to the beam in a higher order mode. The 1st beam mode, which the Coupled NLMS system is designed to avoid, is the only mode effected by a switch in state.

6.4.3 Frequency Content within Displacement Time Response

Fast Fourier transforms (FFTs) were performed on a displacement time response to obtain a better understanding of the dynamics at various excitation frequencies. The following figure illustrates the different points of the displacement time response that were sampled. This displacement time response starts from the positive fixed point, switches from state 2 to state 1 to avoid the 1st beam mode in state 2, and switches back to state 2 to both avoid the 1st beam mode in state 1 and to return to its original state for future resonance crossings. Point A is a point early in the sweep at a frequency far from resonance. Point B captures the response rising into resonance before the switch from state 2 to state 1 occurs and Point C observes the response after this switch. Points D and E study the response before and after the switch back to state 2, similar to points B and C for the 1st snap-through. Point F, similar to point A, captures the response away from resonance at the end of the frequency sweep.

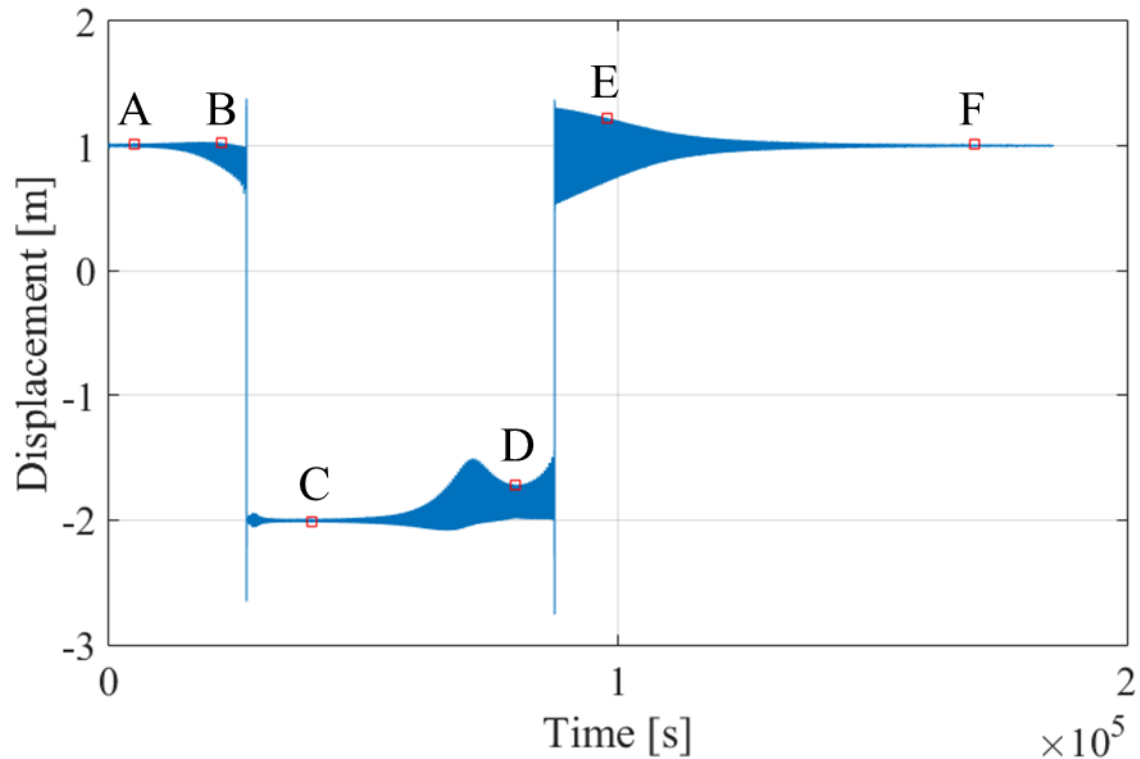


Figure 6.32 Points at which Periods were Sampled for Frequency Content

At each point, an FFT was performed on at least 10 periods of the signal. These approximately 10 periods were taken at steady state for a given excitation frequency. Each sampled signal was slightly different in length due to the number of data points needed to capture at least 10 periods at a given frequency. This changes the exact frequency range examined in each FFT. Table 6.12 summarizes the excitation frequencies at each of the sampled points and the frequency range inspected with the FFT.

Table 6.12 Sampled Points for FFTs

Sample Point	Excitation Frequency [rad/s]	Frequency Range Inspected [rad/s]
A	5.18	0 to 376
B	5.86	0 to 378
C	6.58	0 to 379
D	8.18	0 to 404
E	8.90	0 to 421
F	11.78	0 to 509

Figure 6.33 details the results of the FFTs and the frequencies present at each of the sample points. No frequency content was seen above 20 rad/s for every sample point.

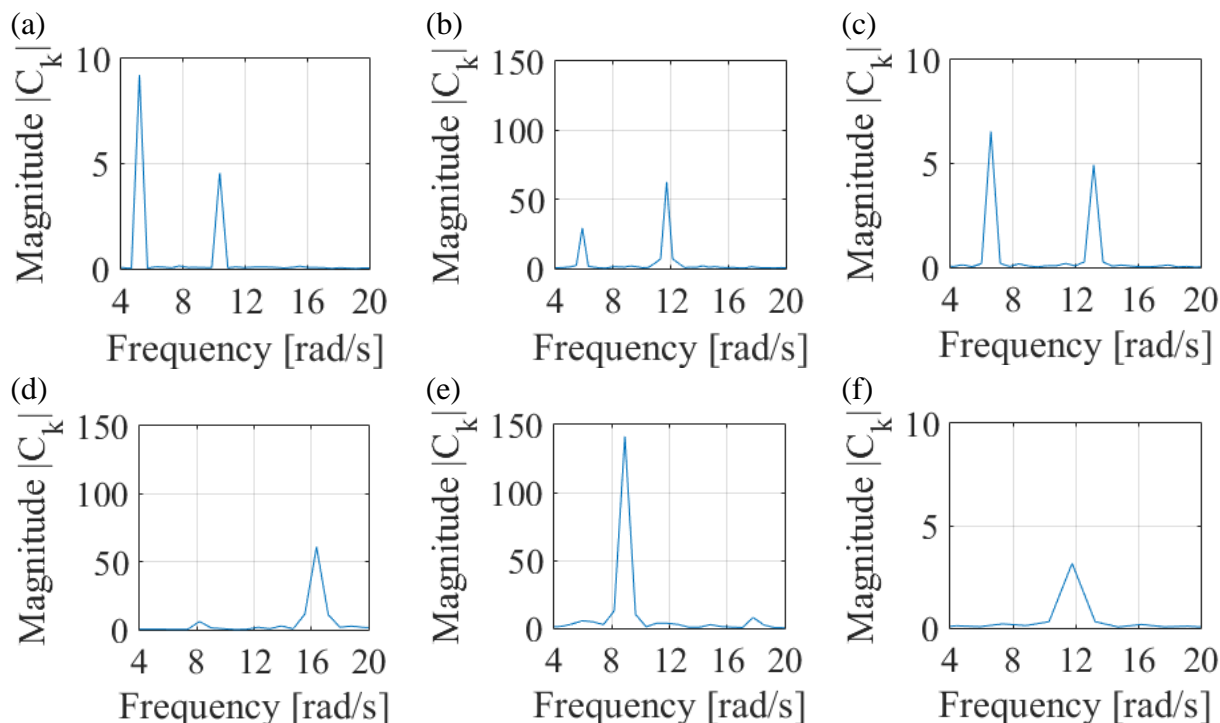


Figure 6.33 FFTs of at Least 10 Periods at (a) Point A, (b) Point B, (c) Point C, (d) Point D, (e) Point E, and (f) Point F

The displacement time response (Figure 6.32) at each point had two frequencies present with the exception of Point F, which only had a single frequency. The two frequencies present were the excitation frequency and a superharmonic at twice the excitation frequency. A superharmonic is any frequency that occurs at a multiple of a fundamental frequency, which is the forcing frequency in this case. Table 6.13 details each of the frequencies present at each sample point.

Table 6.13 Frequencies Present at Various Points in the Displacement Time Response

Sample Point	Excitation Frequency [rad/s]	Superharmonic Frequency [rad/s]
A	5.18	10.36
B	5.86	11.72
C	6.58	13.16
D	8.18	16.37
E	8.90	17.81
F	11.79	N/A

In the case of this system, the superharmonic frequencies do not align with the modes of either the cantilever beam or the coupled NLMS system. Thus, no additional modes are excited. In future designs of the coupled NLMS system to avoid resonance within a target structure, the possibility of superharmonics should be taken into account.

7. CONCLUSIONS

The goal of this thesis was to provide a passive, purely mechanical solution to mitigate resonance vibration in a structure with a two-switch scheme similar to that of RFD. From the results presented herein, a purely mechanical, bistable device proved capable of avoiding resonance with two switches per resonance crossing. Two devices were proposed in this thesis: a SDOF nonlinear mass spring model and a coupled 2DOF nonlinear mass spring model. The SDOF NLMS gave rise to the challenge of snapping from a stable state with a deep potential well to a state with a shallower potential well without overdamping the system. This solution also could not switch back to its original state to preserve the original, designed stiffness. The Coupled NLMS, constructed with a monostable, hardening spring and a bistable softening spring, was shown to snap between stable states to avoid the resonance of a cantilever beam. The coupled device, in the configuration presented, was able to shift the linearized natural frequency of the beam's 1st bending mode by approximately 4%, equivalent to a piezoelectric material with an electromechanical coefficient of about 7.5%. The combined Coupled NLMS – Beam system also demonstrated robustness to $\pm 0.5\%$ mistuning of the beam length and to $\pm 2\%$ mistuning of the beam stiffness, but it is still sensitive to changes in excitation amplitude. In additional investigations, targeting a resonance of the beam with the coupled 2DOF NLMS system did not impact any other modes of the beam, including those beyond the 2-term expansion used in numerical simulations. The displacement response of the overall system to base excitation was shown to contain a superharmonic frequency in addition to the excitation frequency, which should be considered in the design of the coupled 2DOF NLMS system. While further optimization could improve the performance of the coupled device, the coupled 2DOF NLMS proved to be a purely mechanical device that could avoid resonance with only two switches per resonance crossing, free of any constraints that piezoelectric shunt circuits or semi-active control methods require.

A purely mechanical, bistable device is applicable to physically constrained and highly-stressed environments, like turbomachinery. The Coupled NLMS system's switching capabilities was projected onto a Campbell diagram and proved to be a viable solution for avoiding resonance in a rotating environment without the constraints of external control or electrical circuitry. The Coupled NLMS system could also be implemented onto the disk of the

bladed-disk assembly to target disk modes or utilize blade-disk coupling to target blade modes without interfering with the flow of the turbine. In addition, replacing the Coupled NLMS system with a bistable geometry would allow the device to be directly integrated into the design of the bladed disk, but the task of designing such a geometry is left for future research.

7.1 Future Work

Elements of this research available for future work include the following:

1. Creating an optimization routine to further the performance and increase the robustness of the Coupled NLMS model.
2. Developing an analytical or numerical model of a strip resembling a bladed disk with zero blades and adapting the coupled 2DOF NLMS system to target the modes of the rotating strip. The model presented here is a planar model which does not include nor consider the rotational symmetry and modal diameters present within a rotating structure.
3. Adapting the idealized coupled NLMS system into a geometry that could be implemented into the strip to perform the two-switch per resonance crossing scheme as the coupled NLMS system. This will require full-field analysis techniques to ensure the geometry exhibits the same behavior as the coupled NLMS system.
4. Design and test a strip with the implemented bistable geometry to verify FEA and detuning of the structure. Eventually, the geometry can be implemented into a complete bladed disk and tested
5. A study into targeting more than a single mode. This research shows the passive vibration mitigation of a single mode of a targeted structure, but a possible parallel configuration could target multiple modes, similar to the tuned RL-shunts of piezoelectric material.

REFERENCES

- [1] Preumont, A. (1997). *Vibration Control of Active Structures* (Vol. 2). Dordrecht: Kluwer Academic Publishers.
- [2] Behrens, S., Fleming, A. J., & Moheimani, S. O. R. (2003). A broadband controller for shunt piezoelectric damping of structural vibration. *Smart Materials and Structures*, 12(1), 18.
- [3] Singh, D. A., & Vizzini, A. J. (1994). Structural integrity of composite laminates with interlaced actuators. *Smart Materials and Structures*, 3(1), 71.
- [4] Melnykowycz, M. M. (2008). *Long Term Reliability of Active Fiber Composites (AFC)* (Doctoral dissertation, ETH Zurich).
- [5] Larson, G. D., Rogers, P. H., & Munk, W. (1998). State switched transducers: A new approach to high-power, low-frequency, underwater projectors. *The Journal of the Acoustical Society of America*, 103(3), 1428-1441.
- [6] Delpero, T. (2014). *Design of adaptive structures with piezoelectric materials* (Doctoral dissertation, ETH Zurich).
- [7] Corr, L. R., & Clark, W. W. (2002). Comparison of low-frequency piezoelectric switching shunt techniques for structural damping. *Smart Materials and Structures*, 11(3), 370.
- [8] Corr, L. R., & Clark, W. W. (2003). A novel semi-active multi-modal vibration control law for a piezoceramic actuator. *Journal of Vibration and Acoustics*, 125(2), 214-222.
- [9] Liu, J., Li, L., Huang, X., & Jezequel, L. (2017). Dynamic characteristics of the blisk with synchronized switch damping based on negative capacitor. *Mechanical Systems and Signal Processing*, 95, 425-445.
- [10] Wagg, D., & Neild, S. A. (2016). *Nonlinear Vibration with Control*. Springer International Pu
- [11] Leo, D. J. (2007). *Engineering Analysis of Smart Material Systems* (pp. 232-290). Hoboken, NJ: John Wiley & Sons.
- [12] Forward, R. L. (1979). Electronic damping of vibrations in optical structures. *Applied Optics*, 18(5), 690-697.
- [13] Hagood, N. W., & von Flotow, A. (1991). Damping of structural vibrations with piezoelectric materials and passive electrical networks. *Journal of Sound and Vibration*, 146(2), 243-268.

- [14] Belloli, A., & Ermanni, P. (2007). Optimum placement of piezoelectric ceramic modules for vibration suppression of highly constrained structures. *Smart Materials and Structures*, 16(5), 1662.
- [15] Den Hartog, J. P., & Ormondroyd, J. (1928). Theory of the dynamic vibration absorber. *ASME J. Appl. Mech*, 50(7), 11-22.
- [16] Habib, G., Detroux, T., Viguié, R., & Kerschen, G. (2015). Nonlinear generalization of Den Hartog' s equal-peak method. *Mechanical Systems and Signal Processing*, 52, 17-28.
- [17] Den Hartog, J. P. (1985). *Mechanical Vibrations*. Courier Corporation.
- [18] Vakilinejad, M., Grolet, A., & Thomas, O. (2019). A Comparison of Robustness and Performance of Linear and Nonlinear Lanchester Dampers.
- [19] Babitsky, V. I., & Vepruk, A. M. (1993). Damping of beam forced vibration by a moving washer. *Journal of Sound and Vibration*, 166(1), 77-85.
- [20] Miller, L. M., Pillatsch, P., Halvorsen, E., Wright, P. K., Yeatman, E. M., & Holmes, A. S. (2013). Experimental passive self-tuning behavior of a beam resonator with sliding proof mass. *Journal of Sound and Vibration*, 332(26), 7142-7152.
- [21] Xu, Q., Niu, J., Yao, H., Zhao, L., & Wen, B. (2019). Nonlinear dynamic behavior and stability of a rotor/seal system with the dynamic vibration absorber. *Advances in Mechanical Engineering*, 11(1), 1687814018819578.
- [22] Grinberg, I., Lanton, V., & Gendelman, O. V. (2012). Response regimes in linear oscillator with 2DOF nonlinear energy sink under periodic forcing. *Nonlinear Dynamics*, 69(4), 1889-1902.
- [23] Ahmadabadi, Z. N., & Khadem, S. E. (2012). Nonlinear vibration control of a cantilever beam by a nonlinear energy sink. *Mechanism and Machine Theory*, 50, 134-149.
- [24] Georgiades, F., & Vakakis, A. F. (2009). Passive targeted energy transfers and strong modal interactions in the dynamics of a thin plate with strongly nonlinear attachments. *International Journal of Solids and Structures*, 46(11-12), 2330-2353.
- [25] Bab, S., Khadem, S. E., & Shahgholi, M. (2014). Lateral vibration attenuation of a rotor under mass eccentricity force using non-linear energy sink. *International Journal of Non-Linear Mechanics*, 67, 251-266.
- [26] Agnes, G. S. (1999, June). Piezoelectric coupling of bladed-disk assemblies. In *Smart Structures and Materials 1999: Passive Damping and Isolation* (Vol. 3672, pp. 94-104). International Society for Optics and Photonics.

- [27] Mokrani, B., Bastaits, R., Viguie, R., & Preumont, A. (2012, September). Vibration damping of turbomachinery components with piezoelectric transducers: Theory and experiment. In *ISMA2012 International Conference on Noise and Vibration Engineering, Leuven, Belgium* (Vol. 69).
- [28] Mokrani, B., Bastaits, R., Horodincea, M., Romanescu, I., Burda, I., Vigié, R., & Preumont, A. (2015). Parallel piezoelectric shunt damping of rotationally periodic structures. *Advances in Materials Science and Engineering*, 2015.
- [29] Mokrani, B., & Preumont, A. (2018). A numerical and experimental investigation on passive piezoelectric shunt damping of mistuned blisks. *Journal of Intelligent Material Systems and Structures*, 29(4), 610-622.
- [30] Zhou, B., Thouverez, F., & Lenoir, D. (2014). Vibration reduction of mistuned bladed disks by passive piezoelectric shunt damping techniques. *AIAA journal*, 52(6), 1194-1206.
- [31] Yu, H., & Wang, K. W. (2007). Piezoelectric networks for vibration suppression of mistuned bladed disks. *Journal of Vibration and Acoustics*, 129(5), 559-566.
- [32] Lopp, G. K., Kelley, C., & Kauffman, J. L. (2019). Effect of Turbomachinery Blade Root Flexibility on Electromechanical Coupling for Piezoelectric-Based Vibration Reduction. In *AIAA Scitech 2019 Forum* (p. 1636).
- [33] Liu, J., Li, L., Fan, Y., & Deng, P. (2018). Research on vibration suppression of a mistuned blisk by a piezoelectric network. *Chinese Journal of Aeronautics*, 31(2), 285-299.
- [34] Campos, R. O., & Nicoletti, R. (2015). Vibration reduction in vertical washing machine using a rotating dynamic absorber. *Journal of the Brazilian Society of Mechanical Sciences and Engineering*, 37(1), 339-348.
- [35] Alsuwaiyan, A. S., & Shaw, S. W. (2002). Performance and dynamic stability of general-path centrifugal pendulum vibration absorbers. *Journal of Sound and Vibration*, 252(5), 791-815.
- [36] Shaw, S. W., & Alsuwaiyan, A. (2000, April). Torsional vibration reduction using passive nonlinear absorbers. In *Smart Structures and Materials 2000: Damping and Isolation* (Vol. 3989, pp. 388-400). International Society for Optics and Photonics.
- [37] Hu, H. L., & He, L. D. (2017). Online control of critical speed vibrations of a single-span rotor by a rotor dynamic vibration absorber at different installation positions. *Journal of Mechanical Science and Technology*, 31(5), 2075-2081.
- [38] Theurich, T., Gross, J., & Krack, M. (2019). Effects of modal energy scattering and friction on the resonance mitigation with an impact absorber. *Journal of Sound and Vibration*, 442, 71-89.
- [39] Olson, B. J., Shaw, S. W., & Pierre, C. (2005). Order-tuned vibration absorbers for cyclic rotating flexible structures. *ASME Paper No. DETC2005-84641*.

- [40] Olson, B. J., Shaw, S. W., & Pierre, C. (2005). Order-tuned vibration absorbers for a rotating flexible structure with cyclic symmetry. In *Proceedings of the ASME International Design Engineering Technical Conferences and Computers and Information in Engineering Conference—DETC2005* (Vol. 1, pp. 2475-2484).
- [41] Ghaderi, A. A., Mohammadzadeh, A., & Bahrami, M. N. (2016). Optimum Design of Damped Vibration Absorber for Rotationally Periodic Structures. *Journal of Mechanics*, 32(4), 381-390.
- [42] Kauffman, J. L., & Lesieutre, G. A. (2012). Piezoelectric-based vibration reduction of turbomachinery bladed disks via resonance frequency detuning. *AIAA Journal*, 50(5), 1137-1144.
- [43] Kauffman, J. L., & Lesieutre, G. A. (2011, April). Performance of piezoelectric-based damping techniques for structures with changing excitation frequencies. In *Active and Passive Smart Structures and Integrated Systems 2011* (Vol. 7977, p. 79770D). International Society for Optics and Photonics.
- [44] Lopp, G. K., & Kauffman, J. L. (2016, April). State switching in regions of high modal density. In *Active and Passive Smart Structures and Integrated Systems 2016* (Vol. 9799, p. 97991X). International Society for Optics and Photonics.
- [45] Lopp, G. K., & Kauffman, J. L. (2017). Resonance frequency detuning in regions of high modal density. In *25th AIAA/AHS Adaptive Structures Conference* (p. 1439).
- [46] Arrieta, A. F., Hagedorn, P., Erturk, A., & Inman, D. J. (2010). A piezoelectric bistable plate for nonlinear broadband energy harvesting. *APPLIED PHYSICS LETTERS*, 97, 104102.
- [47] Kovacic, I., & Brennan, M. J. (2011). *The Duffing Equation: Nonlinear Oscillators and their Behaviour*. John Wiley & Sons
- [48] Inman, D. J. (2006). *Vibration with Control* (pp. 179-185). Chichester: Wiley.
- [49] Borino, G., & Muscolino, G. (1986). Mode-superposition methods in dynamic analysis of classically and non-classically damped linear systems. *Earthquake Engineering & Structural Dynamics*, 14(5), 705-717.
- [50] Inman, D. J., & Singh, R. C. (1994). *Engineering vibration* (Vol. 3). Englewood Cliffs, NJ: Prentice Hall.
- [51] Meirovitch, L. (1997). *Principles and Techniques of Vibrations* (Vol. 1). New Jersey: Prentice Hall.
- [52] Murray, R. M. (2017). *A Mathematical Introduction to Robotic Manipulation*. CRC Press.